

Alma Mater Studiorum - Università di Bologna

Dipartimento di Ingegneria Industriale - DIN

Dottorato di Ricerca

Meccanica e Scienze Avanzate dell'Ingegneria

Ciclo XXIV

Settore Concorsuale di afferenza: 09/C1

Settore Scientifico disciplinare: ING-IND/08

**Waste heat recovery systems:
numerical and experimental analysis of
organic Rankine cycle solutions**

Dott. Ing. Valentina Orlandini

Coordinatore Dottorato:
Prof. Nicolás Cavina

Relatore:
Prof. Andrea De Pascale

Esame Finale 2017

Abstract

In large-scale stationary power generation the dominant role is covered by the gas and steam cycle technologies. However, large variety of energy sources are not technically and/or economically exploitable through gas or steam cycles. When the temperature and the thermal power available are limited, the Organic Rankine Cycle (ORC) technology becomes an attractive power generation solution. The ORC architecture is similar to the conventional water steam Rankine cycle, but the working fluid is an organic component, characterized by a lower ebullition temperature than water, allowing power generation from low-grade heat sources. ORC is considered as an emerging technology for power generation through the exploitation of thermal sources at various temperatures. ORCs are commercially available in the range from few kW to MW. The total, worldwide ORC installed capacity is equal to 2.75 GW_{el} , considering all the various applications. The most common applications are: recovery of waste energy from industrial processes; conversion of renewable low-temperature heat sources into electricity (biomass, geothermal and solar sources); improving efficiency of power plants by waste heat recovery on the exhaust gases of gas turbines or engines. This technology nowadays plays a non-negligible role, due to the increasing interest on the environmental protection and the energy efficiency policies.

This thesis aims to present the ORC technology, its advantages and related problems. In particular, it provides an analysis of ORC waste heat recovery system in different and innovative scenarios, focusing on cases from the biggest to the lowest scale. Both industrial and residential ORC applications are considered. In both applications, the installation of a subcritical and recuperated ORC system is examined. Moreover, heat recovery is considered in absence of an intermediate heat transfer circuit. This solution allow to improve the recovery efficiency, but requiring safety precautions. Possible integrations of ORC systems with renewable sources are also presented and investigated to improve the non programmable source exploitation. In particular, the offshore oil and gas sector has been selected as a promising industrial large-scale ORC application. From the design of ORC systems coupled with Gas Turbines (GTs) as topper systems, the dynamic behavior of the GT+ORC innovative combined cycles has been analyzed by developing a dynamic model of all the considered components. The dynamic behavior is caused by integration with a wind farm. The electric and thermal aspects have been examined to identify the advantages related to the waste heat recovery system installation. Moreover, an experimental test rig has been realized to test the performance of a micro-scale ORC prototype. The prototype recovers heat from a low temperature water stream, which could be available for instance in industrial or residential waste heat. In the test bench, various sensors have been installed, an acquisitions system developed in Labview environment to completely analyze the ORC behavior. Data collected in real time and corresponding to the system dynamic behavior have been used

to evaluate the system performance based on selected indexes. Moreover, various operational steady-state conditions are identified and compared. Operation maps are realized for a completely characterization of the system and to detect the optimal operating conditions.

Index

Structure of the manuscript	vii
List of Figures	x
List of Tables	xv
Nomenclature	xvii
I Organic Rankine Cycle Technology: State of the Art	1
1 Introduction	2
1.1 Organic Rankine cycle technology	4
1.1.1 Working fluid	6
1.2 ORC applications	14
1.2.1 Geothermal ORC power plants	14
1.2.2 ORC biomass power plants	16
1.2.3 Waste heat recovery ORC applications	18
1.2.4 ORC in solar power plants	19
1.3 ORC world capacity	20
II Large-Scale Waste Heat Recovery: ORC Numerical Analysis	24
2 WHR from gas turbines exhaust: applications in the oil and gas sector	25
2.1 Case study	29
2.1.1 Other offshore power plant configurations	31

3	Integrated power system dynamic model	35
3.1	The gas turbine model	35
3.2	The organic Rankine cycle model	38
3.3	The offshore wind farm model	42
4	Power system sizing: the maximum allowable wind power	45
4.1	Plant reliability	47
5	Thermodynamic analysis	50
5.1	Integrated system thermodynamic performance	56
5.2	Waste heat recovery performance	59
6	Electrical, environmental and economic analysis	65
6.1	Plant flexibility	65
6.2	Fuel savings and emission reduction	68
III Micro-Scale Waste Heat Recovery: ORC Experimental Analysis		72
7	Small scale ORC technology	73
7.1	Expanders for small scale Rankine cycles	76
7.1.1	Scroll expanders	79
7.1.2	Screw expanders	80
7.1.3	Vane expanders	82
7.1.4	Piston expanders	83
7.1.5	Comparison between volumetric expander typologies	84
7.2	Reciprocating piston expanders	89
7.2.1	Losses in piston expanders	91
8	Experimental test facility	96
8.1	ORC prototype: main components	100
8.1.1	Evaporator and recuperator	100

8.1.2	Condenser	101
8.1.3	Expander	102
8.1.4	Pump	107
9	The test bench instrumentation and acquisition system	110
9.1	Selected and installed sensors	110
9.2	Developed acquisition system	113
9.3	Performance parameters	118
10	Test campaign	120
10.1	Steady state operational windows preliminary identification	121
10.2	Results and operational maps	123
10.2.1	Assessment of irreversibility	125
	Conclusions	135
	Appendix A	139
	Appendix B	140
	Appendix C	142
	Appendix D	145
	Bibliography	148

Structure of the manuscript

The organic Rankine cycle is an advanced power generation technology commonly used to convert low-grade heat into electricity, for a wide range of power values (scales from a fraction of kW_e to several MW_e). ORC technology results now robust and advantageous in many ways and it has shown a renewed interest over the last decades thanks to its flexibility and easy maintenance. At low temperatures, organic working fluids lead to higher cycle efficiency than water and organic fluids are preferable because the fluid mechanics leads to high turbine efficiency in both full and partial load. ORC are considered for a number of different applications, such as recovery of waste energy from industrial processes; conversion of renewable low-temperature heat sources into electricity (biomass, geothermal and solar sources); improving efficiency of power plants by waste heat recovery on the exhaust gases of gas turbines or engines. Therefore, ORC technology nowadays plays a non-negligible role, due to the increasing interest on the environmental protection and the energy efficiency policies. In this thesis two innovative scenarios of ORC Waste Heat Recovery (WHR) application are considered.

This thesis focuses on the WHR ORC systems in two different and innovative scenarios with the aim to identify advantages and problem related to the ORC technology applications. The cycles considered are subcritical and recuperated. Moreover, direct heat recovery is analyzed, setting safety precautions and improving the recovery efficiency. An industrial application of ORC as a large-scale waste heat recovery system to produce electricity is considered. The heat recovery market is still at an early stage but has long passed the demo/prototype phase (349.1 MW_{el} of installed capacity in the world). The main ORC WHR application in industrial sector is waste heat recovery from Diesel engines or gas turbines, correspondent to 66.8% of the ORC world installed capacity. The industrial sector selected is oil and gas and in particular, the innovative ORC application on offshore oil and gas platforms. Compactness, low weight, and dynamic flexibility are crucial aspects to identify the best WHR technology in this sector. Given their high modularity and simplicity, ORCs have been proposed to recover the thermal energy of offshore gas turbines. Moreover, the integration of the system with an offshore wind farm is considered. This integration causes a discontinuous waste heat flow, due to the variable nature of renewable source. ORC technology is flexible and can operate at partial load conditions (while steam cycles require more constant conditions). Therefore, offshore plant configuration with and without ORCs installation are compared to identify the advantages related to the ORC using.

Almost all the ORC units available on the market are in the medium to-high power range, while micro-small size systems are not so diffused yet. Micro-scale ORCs are still in demonstration phase, but their application could save primary energy and reduce pollutant emissions. Small and micro size ORCs are suitable for several applications, such as electric generation in remote houses and domestic CHP (Combined Heat and

Power) units. Therefore, small and micro-scale systems are studied in this thesis. A test rig has been developed with the aim to completely characterize the system and components behavior. Several sensors have been installed in the test bench and an acquisition system has been developed in Labview environment to monitor the system behavior in real time. Various parameters and the performance indexes are introduced from literatures to realize system operational maps and to identify the potential of micro-ORC applications. In particular:

Part I introduces the Organic Rankine Cycle (ORC) technology in comparison with the most conventional systems, such as water steam Rankine cycles. The configurations, the working fluids and their characteristics are described (Section 1.1). Section 1.2 bears an overview of the most diffuse ORC applications, based on the current ORC technology installations present all over the world.

Part II is focused on the large-scale Waste Heat Recovery (WHR) systems application in the industrial environment. The considered scenario is an offshore oil and gas facility with the aim to analyze the ORCs installation impact in a offshore power plant integrated to a renewable sources. In particular, Chapter 2 introduces and presents the interests and the advantages related to the waste heat recovery systems in the oil and gas sector and identifies the organic Rankine cycle as a much more promising system if compared to several WHR systems. Moreover, the offshore wind power application is described, highlighting the main critical aspects. Section 2.1 presents the case study, i.e. the upgrading of an existing offshore oil and gas platform located in the North Sea. The upgrading consists of coupling each gas turbine with a WHR ORC module and integrating the system with an offshore wind farm. Chapter 3 shows the developed dynamic model of the power system, based on first principles, realized in Modelica language. The model is integrated with a time series-based model of offshore wind mills power production. The loss of wind power is simulated to determine maximum frequency excursions and thus identify a reasonable size for the wind farm (see Chapter 4). A reliability analysis of the overall system is presented in Section 4.1 and two wind scenarios are obtained using the described wind farm model. Chapter 5 presents a thermodynamic study of the integrated power plant, showing the overall system and the recovery dynamic performance. Section 6.1 describes additional dynamic tests aimed at evaluating the electric grid stability and Section 6.2 presents the economic and environmental aspects of the ORC integration, comparing the integrated system with simpler power plant configurations.

Part III presents adoption of ORC as micro-scale WHR technology, an interesting sector still in demonstration phase. In particular, Chapter 7 introduces small and micro-scale ORC applications. Particular interest is given on the expander devices. Axial and radial turbines result not suitable for small size ORC systems, because rotational speed increases dramatically with decreasing output power and consequently the cost increases. Therefore, volumetric expanders are more appropriate in small scale ORC units. The main volumetric expander typologies are presented in Section 7.1, with a focus on the reciprocating piston expanders. The operation phases of this kind of expanders are described in Section 7.2. Results from literature reporting modeling and experimental

activities are introduced in Section 7.2.1 to present the typical losses that occur during the expansion phase, the behavior of the isentropic efficiency and the operational maps. Finally, Chapter 8 describes the experimental test rig developed to test the performance of the micro-ORC prototype installed in the laboratory. The components of the micro-ORC system are described in Section 8.1, while Chapter 9 presents the installed test bench instrumentation and the acquisition system developed to monitor the system real time behavior. The parameter and the performance indexes evaluated from the measured quantities are introduced and described in Section 9.3. Several experimental tests are considered and examined in this thesis to test different ORC conditions. Chapter 10 identifies the steady-state conditions starting from real-time data relating to the dynamic behavior of the ORC system. Section 10.2 presents the operational maps realized based on the data collected and identifies the characteristic curves of the micro-scale ORC under investigation.

Acknowledgments

I would like to thank my advisor Professor Andrea De Pascale to gave me the this opportunity and with him all the *energy systems* group of the Department of Industrial Engineer, in particular Professor Antonio Peretto, Professor Michele Bianchi, Prof. Francesco Melino, Lisa Branchini, Maria Alessandra Ancona and the new members Saverio Ottaviano, Luigi Scarponi e Jessica Rosati to support me during the PhD years. I wish to acknowledge Professor Fredrik Haglind and Leonardo Pierobon (DTU, Denmark) for giving me the opportunity to cooperate with their research groups as guest student. I also would to thank my *new and old* family.

List of Figures

1.1	Comparison between ORC and other micro/small size power systems versus hot source temperature (figure revised from [6]).	4
1.2	Diagram T-s for Figure 1.2(a) wet, isentropic and dry fluids [4] and diagram Figure 1.2(b) of water and various typical ORC fluids [9].	7
1.3	ORC configurations: with (left) and without (right) recuperator heat exchanger at the expander outlet [9].	8
1.4	The optimal selections of low temperature working fluids corresponding to the heat source temperature level [16].	10
1.5	T-s diagram of ORC subcritical cycle(1.5(a)) and ORC supercritical cycle (1.5(b)) [13].	13
1.6	Representation of ORC applications fields in the heat source temperature-power output plane (figure revised from [3]).	15
1.7	Schematic of a geothermal ORC binary plant [9].	16
1.8	Working principle of biomass ORC power plant (cogenerative case) [9].	17
1.9	Schematic of a solar ORC power cycle [9].	19
1.10	Market share, applications (2016) [23].	20
1.11	Installed capacity per year and per application (Figure 1.11(a)) and installed project per year and per application (Figure 1.11(b)) [23].	22
1.12	Heat recovery applications (projects size upper to 50 kW _{el}) [23].	23
2.1	percentage of CO ₂ emissions from petroleum activities distributed by source, 2011 [26].	26
2.2	Performance of selected commercially available ORC.	28
2.3	Layout of the power system considered as case study. Figure 2.3(a) Integration of GTs, ORC units and wind farm with the electric grid. 2.3(b) Combined cycle unit configuration.	30
2.4	Structure of the multi-objective algorithm [55].	32
2.5	Layout of <i>GT configuration</i> Figure 2.5(a) and layout of <i>GT configuration-no WIND</i> 2.5(b).	34
3.1	Object diagram of the gas turbine sub-system model.	36

3.2	Comparison between the model and the operational data as shown in [67]. The numbers in the y-axis are relative to the values at the design point.	39
3.3	Object diagram of the combined cycle unit.	40
3.4	Modelica object diagram of the once-through heat exchanger model.	41
3.5	Probability distribution of wind speed and probability of occurrence of 9 m s^{-1} and 15 m s^{-1} wind speed [70].	42
3.6	Wind speed behavior acting on the wind mills in scenario 1 (3.6(a)) and in scenario 2 (3.6(b)).	43
3.7	Wind turbines power production power in scenario 1 (3.7(a)) and in scenario 2 (3.7(b)).	44
4.1	Power plant load required variations in analyzed cases.	46
4.2	Frequency in per unit as a function of time for the analyzed cases.	46
4.3	Maximum temperature of the organic fluid in the thermodynamic cycle as a function of time for the analyzed cases.	47
5.1	Power of the electric generators connected to the grid as a function of time in scenario 1 (5.1(a)) and in scenario 2 (5.1(b)).	51
5.2	Gas turbine 5.2(a) and ORC 5.2(b) power production variations in the considered scenarios.	53
5.3	Gas turbine exhaust gas 5.3(a) and OTB outlet temperature variation 5.3(b).	54
5.4	Thermal power exchanged at the OTB evaluated at ORC and GT side in scenario 1 (5.4(a)) and scenario 2 (5.4(b)).	55
5.5	Thermal power available after the recovery, cooling down the gas to the ambient temperature.	55
5.6	Dynamics of the ORC unit main parameters: 5.6(a) maximum temperature and 5.6(b) pump rotational speed.	56
5.7	Dynamics of the ORC unit main parameters: 5.7(a) working fluid mass flow and 5.7(b) maximum pressure.	57
5.8	Dynamics performances indexes: 5.8(a) lambda value, 5.8(b) integrated system equivalent heat rate and 5.8(c) ORC efficiency.	60
5.9	Various configurations: electric efficiency comparison.	61
5.10	Available heat in the condenser 5.10(a) and in the exhaust gas 5.10(b).	61

5.11	GT+ORC combined cycle thermal efficiency.	62
5.12	Various configurations: thermal efficiency comparison.	62
5.13	Instantaneous PES index behavior.	63
5.14	Instantaneous PES index comparison.	64
6.1	Power of the electric generators connected to the grid as a function of time. 6.1(a): Two gas turbines, two organic Rankine cycle units and the wind mill in <i>GT+ORC configuration</i> . 6.1(b): Two gas turbines and the wind mill in <i>GT configuration</i>	66
6.2	Frequency in per unit as a function of time. In <i>GT+ORC configuration</i> , the gas turbines, the organic Rankine cycle units and the wind mill supply the electric grid. Conversely, <i>GT configuration</i> entails the use of the gas turbines and the wind mill.	66
6.3	Gas turbine and organic Rankine cycle mechanical power in <i>GT+ORC configuration</i> and gas turbine mechanical power in <i>GT configuration</i> as a function of time.	67
6.4	Variation of the mechanical power supplied by one gas turbine with respect to the steady-state value for <i>configuration GT+ORC</i> and <i>GT</i>	68
6.5	Fuel savings (6.5(a)) and carbon dioxide emissions (6.5(b)) of the gas turbines, the organic Rankine cycle units and the wind mill (<i>configuration GT+ORC</i>) and for the gas turbines and the wind mill (<i>configuration GT</i>). 69	69
6.6	Net present value for <i>configuration GT+ORC</i> and <i>GT</i> as a function of the fuel price variation respect the base case (in percentage): effects of the CO ₂ tax value decreasing.	71
6.7	Net present value for <i>configuration GT+ORC</i> and <i>GT</i> as a function of the fuel price variation respect the base case (in percentage): effects of the CO ₂ tax value increasing.	71
7.1	ORC function of power output [20].	75
7.2	Classification of volumetric expanders according to the type of motion of the rotors [94].	78
7.3	Scroll expander [95] (7.3(a)) and its principle of operation [96] (7.3(b)). . .	80
7.4	Photo of the screw-shaped components of the expander (Figure 7.4(a)) and the cross section of a screw expander with a symmetric profile during operation (Figure 7.4(b), Figure 7.4(c)) [96].	81
7.5	Single-screw expander[96].	81

7.6	Lysholm asymmetric profile [93] (7.6(a)) and working principle of Lysholm screw expander [96] (7.6(b)).	82
7.7	Working principle and components of vane expander [93].	82
7.8	Diagram of a rotary piston expander [96] (7.8(a)), gerotor [96] (7.8(b)), rolling [93] (7.8(c)) and free [97] (7.8(d)) piston expanders.	85
7.9	Turbine volumetric expansion ratio values of existing ORC turbines of different technology and with specified fluids [6].	86
7.10	Power ranges of major volumetric expander technologies [3].	86
7.11	Rotational speeds ranges of major volumetric expander technologies [3].	87
7.12	ORC and expander efficiency function of power output [20].	87
7.13	Performance map for different types of expander [98].	89
7.14	Indicator diagram of piston expanders [3].	90
7.15	Schematic representation of the overall expander model [103].	93
7.16	Impact of the different losses on the evolution of the isentropic effectiveness with the pressure ratio [92, 104].	94
7.17	Operating maps for piston expanders [92].	95
8.1	The micro-ORC internal layout.	97
8.2	The hot and cold water supply lines.	98
8.3	Pictures and scheme of the test bench layout.	99
8.4	ORC system 3D layout and size: frontal and lateral views.	100
8.5	PFB puffer picture fig. 8.5(a) and internal structure fig. 8.5(b).	101
8.6	Grundfos Magna1 40-180F operational curves.	102
8.7	Schematic layout of evaporator and recuperator heat exchangers.	103
8.8	Schematic layout of evaporator and recuperator heat exchangers [109].	104
8.9	Expander schemes, available in [106].	105
8.10	Expander valve scheme [110].	106
8.11	The expander without (8.11(a)) and with (8.11(b)) the insulation material.	106
8.12	Kinetic mechanism scheme fig. 8.12(a) and a detail of the kinetic mechanism in the considered expander fig. 8.12(b).	107
9.1	Thermostatic bath, reference temperature sensor Figure 9.1(a) and acquisition system Figure 9.1(b) used during calibration procedure.	111

9.2	Pressure and temperature sensors placed in the ORC [9.2(a)] and Coriolis mass flow rate measure [9.2(b)].	112
9.3	Electromagnetic volumetric flow sensors placed in the hot water [9.3(a)] and in the cold water sides [9.3(b)].	112
9.4	Printed circuit board installed.	113
9.5	Chassis NI c-RIO 9114 [9.5(a)] and controller NI c-RIO 9022 [9.5(b)]. . .	114
9.6	Scheme of the measure chain in the realized test bench.	115
9.7	The T,s diagram updated in real-time, based on the acquired temperature and pressure values measured.	115
9.8	Sensors measurement and positions on the system layout (picture extracted from the implemented real-time visualization panel).	116
10.1	ORC simplified layout.	120
10.2	Quantities variations during a carried out test.	126
10.3	Recuperator heat exchange (10.3(a)) and ORC gross efficiency (10.3(b)) behavior during a carried out test.	127
10.4	Operating point obtained during steady state conditions: hot sources temperature (10.4(a)) and ORC evaporation and condensation temperatures (10.4(b)) versus cold sources temperature.	128
10.5	ORC maximum and minimum pressures, p_2 and p_6 , (10.5(a)) and expander pressure ratio p_2/p_3 (10.4(b)) behavior versus the working fluid mass flow rate.	129
10.6	Electric power production (10.6(a)) and ORC gross efficiency (10.6(b)) versus expander pressure ratio p_2/p_3 ; electric power production (10.6(c)) and ORC gross efficiency (10.6(d)) versus superheated ΔT_{SH} ;	130
10.7	ORC pump consumption (10.7(a)) and ORC net efficiency (10.7(b)) behavior versus expander pressure ratio p_2/p_3	131
10.8	Expander characterization: electrical isentropic efficiency behavior versus the expander pressure ration (10.8(a)); fluid power ratio versus the expander rotational speed N_{EXP}	131
10.9	ORC thermal power characterization: comparison between inlet and outlet thermal power (10.9(a)); heat exchange at evaporator (10.9(b)) and condenser (10.9(c)); heat exchange at recuperator (10.9(d)).	132
10.10	Thermodynamic cycle (10.10(a)) and heat exchanged diagram in recuperator (10.10(b)), condenser (10.10(c)) and evaporator (10.10(d)) of the operating point at maximum electric power production.	133

10.11 Schematic representation of the overall expander model [5]. 134

10.12 Efficiency of the ideal reversible recuperation cycle (10.12(a)) and irreversibility recuperation cycle efficiency (10.12(b)) for the operational data. 134

List of Tables

1.1	Water thermodynamic characteristics [1].	3
1.2	Advantages and drawbacks of technologies [9].	6
1.3	Fluids properties comparison in steam and organic Rankine cycles [1, 4].	8
1.4	ORC fluids advantages and disadvantages [7, 3].	9
1.5	Pure working fluid candidates for ORC [7].	11
1.6	Pure working fluid candidates for ORC [continue]. [7]	12
1.7	Recommended ORC working fluid based on temperature and applications [9].	15
1.8	Comparison of different types of geothermal plants [1].	17
2.1	Power range and heat source temperature data for several ORC commercial units (mainly excerpted from [29]).	28
2.2	Design specifications provided by the manufacturer for the twin-spool gas turbine considered as topping unit.	30
2.3	Design variables and point specifications used to parametrize the dynamic model of the organic Rankine cycle system, obtained as described in [55].	33
4.1	Frequency values and variations obtained in the studied cases.	47
5.1	Wind, GT and ORC electric maximum and minimum power production and ramp rate.	52
7.1	Technical constrains inherent piston, screw and scroll expanders [93, 92].	87
8.1	Tatano Kalorina 2204 biomass boiler (8.1(a)) and storage puffer (8.1(b)) characteristics.	102
8.2	Evaporator and recuperator heat exchanger specifications.	103
8.3	Water condenser heat exchanger specifications [109].	103
8.4	Design specifications provided by the manufacturer for the electric generator.	107
9.1	ORC sensors main data.	111

9.2	PCBs settings.	112
9.3	Acquisition system specifications.	117
10.1	Tests operating conditions.	123
D.1	ORC data operation, case A1	145
D.2	ORC data operation, case B1	146
D.3	ORC data operation, case C1	147

Nomenclature

Abbreviations

BWR Built-in Volume Ratio

ABC Air Bottoming Cycle

BDC Bottom Dead Center

BEM Blade-Element-Momentum

CC Combustion Chamber

CFC Chloro-Fluoro-Carbons

CHP Combined Heat and Power

COND Condenser

EHS Environmental, Health and Safety

EVAP Evaporator

EXP Expander

FPGA Field Programmable Gate Array

FS Full Scale

G Electric Generator

GHG Green-House Gas

GT Gas Turbine

GWP Global Warming Potential

HC Hydrocarbons

HCFC Partially fluoro-substituted
straight chain hydrocarbons

HFC Hydro-Fluoro-Carbons

HPC High Pressure Compressor

HPT High Pressure Turbine

ICE Internal Combustion Engine

IEC International Electrotechnical Commission

LPC Low Pressure Compressor

LPT Low Pressure Turbine

NPV Net Present Value

NREL National Renewable Energy Laboratory

NREL National Renewable Energy Laboratory

ODP Ozone Depletion Potential

ORC Organic Rankine Cycle

OTB Once-Through Boiler

P ORC Pump

PCB Printed Circuit Board

PES Primary Energy Saving

PFC Perfluorocarbons

PT Power Turbine

PUMP Pump

PV Photovoltaics

R Resistance

REC Recuperator

SP Set Point

SRC Steam Rankine Cycle

T ORC Turbine

TDC Top Dead Center

TIT Turbine Inlet Temperature °C

UV Ultraviolet

VM Manual Valves

VNC Normally Closed Valves

VNO Normally Open Valves

WHR Waste Heat Recovery

WT Wind Turbine

Greek Symbols

ϕ Coefficient [-]

α Failure Rate

β Pressure Ratio [-]

Δ Variation

η Efficiency [-]

λ Specific power recovery [%]

ω Rotational Speed [rpm s⁻¹]

Φ Filling Factor

ρ Density kg m⁻³

Roman Symbols

\dot{P}_n Maximum Wind Power

\dot{V} Volumetric Flow Rate [m³ s⁻¹]

η_{II} Irreversibility Recuperation Efficiency

A Area [m²]

c Speed of Sound [m s⁻²]

c_p Specific Heat Capacity [J kg⁻¹ K⁻¹]

c_{ng} Natural Gas price [\$]

C_T Stodola Constant [-]

D Expander Diameter [m]

D_s Specific Diameter [-]

F Fuel Chemical Power [kW]

F Veres Coefficient [-]

f Frequency

F_{cu} Copper Loss Fraction [kW]

H Head [m]

h Enthalpy [kJ kg⁻¹]

h_u Capacity Factor [h/]

HR Heat Rate [%]

I Shaft Inertia [N]

i Working Cycle Frequency [Hz]

I_t Turbulence Intensity [-]

I_{TOT} Total Investment Cost [\$]

k Heat Transfer Coefficient [W m⁻² K⁻¹]

L Mechanical Power Input [p.u.]

l Parallel Number of Components

LHV Lower Heating Value [MJ kg⁻¹]

m Series Number of Components

M_a Operating and Maintenance Costs Coefficient [-]

N Shaft rotation speed [rpm]

n Equipment Lifespan []

n Flow Coefficient [-]

N_s Specific Speed [-]

P Power [kW]

q Interest Factor [-]

R Annual Income [\$/]

$R(t)$ Reliability

RR Power Ramp Rate [MW s⁻¹]

t Time [s]

t_{rise}	rise time [s]	ev	Evaporation
V	Volume [m ³]	ex	Expansion Process
V	Wind Speed Velocity [m·s ⁻¹]	f	fuel
V_s	Machine Swept Volume [m ³]	fluid	Organic Fluid
v_{st}	Fuel Specific Volume [Sm ³]	g	gas
W	Power [kW]	gross	Gross Value
P	Pressure [bar]	hot	Hot Side
s	Entropy [kJ kg ⁻¹ K ⁻¹]	i	instantaneous
T	Temperature [°C]	in	inlet
Superscripts		is	Isentropic
el	Electric	l	Liquid
max	maximal	loss	Losses
$parallel$	Parallel Configuration	m	mechanical
ref	Reference	min	Minimum
S	Static Conditions	net	Net Value
$series$	Series Configuration	ng	Natural Gas
T	Total Conditions	out	outlet
th	Throat	Q	Thermal Power [kW]
WT	Wind Turbine	rec	Recovered Thermal Power [kW]
a	air	rr	Reversible Recuperation
amb	Ambient	SH	Superheated
ava	Available	su	Suction Process
C	Carnot	th	Thermal
c	Critical	th	theoretical
CC	Combustion Chamber	TOT	Total
cd	Condensation	U	Internal Energy [kJ]
cold	Cold Side	v	Vapour
COND	Thermal Power at Condenser [kW]		
des	Design		

Part I

Organic Rankine Cycle Technology: State of the Art

CHAPTER 1

Introduction

***Summary.** In this chapter the Organic Rankine Cycle (ORC) technology is introduced and compared to the most conventional systems, such as steam water Rankine cycles. A focus on the ORC configurations, organic fluids and their characteristics are performed. The problem of the working fluid selection is presented. Methods and information available in literature to select the right working fluid based on the ORC application and hot source characteristics are described. This chapter presents also an overview of the current state of the art in the ORC applications and of the worldwide capacity installation.*

The steam Rankine cycle is one of the most important ways to transform on large scale thermal energy into power. Main components of a steam power cycle are: boiler, expander, condenser and pump. In this cycle, water is used as working fluid and it has the thermodynamic characteristics reported in Table 1.1. Advantages presented by water as working fluid, according to [1], are:

- very good thermal/chemical stability and consequently no risk of decomposition;
- low viscosity, therefore low pumping work required;
- good energy carrier, due its high latent and specific heat;
- non-toxic, non-flammable and no threat to the environment: it presents zero Ozone Depletion Potential (ODP) and Global Warming Potential (GWP);
- cheap and abundant: it is available almost everywhere on earth.

However, many problems are encountered using water in a power cycle, as:

- need of superheating to prevent condensation during expansion;
- risk of erosion of turbine blades;
- excess pressure in the evaporator and low pressure in the condensation phase (frequently under ambient pressure);
- complex architecture and, consequently, expensive turbines.

Table 1.1: Water thermodynamic characteristics [1].

Water	
Molecular weight	18 kg kmol ⁻¹
Boiling point	373.15 K, 101.325 kPa
Freezing point	273.15 K, 101.325 kPa
Triple point	273.15 K, 0.611 kPa
Critical point	647 K, 22.06 kPa
Latent Heat	2256.6 kJ kg ⁻¹ , 101.325 kPa
Specific heat	4.18 kJ kg ⁻¹ K ⁻¹

Environmental Impact Indexes

Among the main environmental effects, identified by the standards (as by European Commission in [2]), there are global warming and ozone depletion related with the ORC operation. To evaluate the effects of each substance, two indexes are used:

- **Global Warming Potential (GWP):**

it represents the impact of a molecule of a certain compound on the greenhouse effect, which is considered the main cause of global warming. In particular, GWP index compares the amount of heat trapped by a certain mass of gas in question to the amount of heat trapped by an equal mass of carbon dioxide (GWP is expressed as kg of CO₂ equivalent).

- **Ozone Depletion Potential (ODP):**

it represents the potential of a molecule of a certain compound to deplete the ozone (O₃) layer that protect us from UV radiation. More in details, it is defined as the ratio of global loss of ozone due to given substance over the global loss of ozone caused by the release of the same mass of CFC-11 [2, 3].

Because of the aforementioned reasons, in particular of the higher boiling point value, water is more suitable for high temperature applications and large centralized systems [1]. Moreover, in case of renewable energy sources, such as solar thermal and geothermal, and in many small-medium size industrial applications, the amount of thermal power discharged, commonly at moderate temperature, is not compatible with conventional power generation methods. Consequently, a large amount of low-grade heat is simply wasted [4]. For instance, an internal combustion engine can provide exhaust gases at temperature values typically between 300 °C to 450 °C, a gas turbine is characterized by exhaust temperature 400 °C to 550 °C and micro gas turbines can give 250 °C to 350 °C. Other industrial heat fluxes, e.g. exhaust from ceramic desiccant ovens, concrete kiln gas, leather or food industry discharge heat, can provide similar temperature values, ranging from 200 °C to 500 °C depending on the process operation [5]. Vari-

ous thermodynamic cycles such as the Organic Rankine Cycle (ORC), Stirling engine, thermo-electric systems, supercritical Rankine cycle, Kalina cycle and trilateral flash cycle have been proposed and studied in literature for the conversion of low-grade heat sources into electricity. For instance, Figure 1.1 compares different micro/small size power systems, based on available or under development technologies, operating with various hot source temperatures [6]. The view presented in the figure constantly evolves, due to the innovative nature of the considered systems. However, compared to the cited systems, ORC has a simple structure, high reliability, requires less maintenance and for these reasons this technology is currently recognized as the most promising for exploitation of low/medium temperature heat sources [5, 7]. Moreover, micro-scale ORC results an interesting technology, due to the capacity of exploitation also temperatures lower than 100 °C.

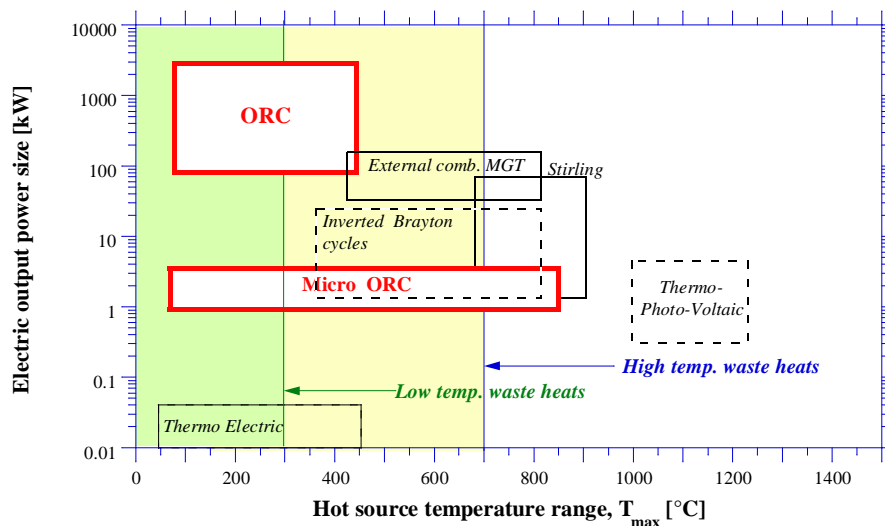


Fig. 1.1: Comparison between ORC and other micro/small size power systems versus hot source temperature (figure revised from [6]).

1.1 Organic Rankine cycle technology

ORC basic cycle architecture is similar to the traditional steam Rankine cycle, but it takes advantages of organic working fluids to recover heat from lower temperature heat sources. Therefore, the system performs a closed thermodynamic cycle, based on the sequence of: (i) evaporation, exploiting the heat provided by the hot source; (ii) expansion, producing output power; (iii) condensation, discharging unused residual heat and (iv) fluid pressure augmentation, through a pumping system. Based on the available heat source and its temperature, the influence of the working fluid and the corresponding

operating conditions are fundamental. The working fluids could be categorized according to the saturation vapor curve, which is one of the most crucial characteristics of the working fluids in an ORC [8]. As shown in Figure 1.2(a), there are generally three types of vapor saturation curves in the temperature-entropy (T,s) diagram: a dry fluid with positive slope, a wet fluid with negative slope, and an isentropic fluid with nearly infinitely large slope. Water is an example of wet fluid. This characteristic causes a high liquid content in the later stages of expansion and consequently the previous mentioned risk of turbine blades erosion. The water steam must therefore be superheated at the turbine inlet, temperatures are generally higher than 450 °C in case of steam cycle, to avoid turbine damages. This leads to a higher cost and to higher thermal stresses in the boiler and on the turbine blades [9]. However, the limitation of the vapor quality at the end of the expansion process disappears in case of dry and isentropic fluids. Therefore, there is no need to superheat the dry or isentropic fluid to avoid droplets presence at the expander discharge. However, the use and size of superheating depends on cycle performance evaluation, as efficiency and power output [10]. Due to the positive slope of the saturation vapor curve of dry fluid, a strongly superheated vapor exits the expander. The absence of condensation also reduces the risk of corrosion on the turbine blades and extends its life time to 30 years instead of 15 years to 20 years for steam turbines [11]. As a consequence, the load on the condenser increases and installing a recuperator could make even better use of the energy from the expanded vapor, preheating the pump fluid that will enter the evaporator [7, 9, 12]. Based on the presence of this heat exchanger, the ORC system configurations are classified as simple or recuperated as shown in Figure 1.3. Essentially, the presence of recuperator increases the ORC thermal efficiency, because it allows to reduce the amount of heat needed from the hot source to vaporize the fluid. Moreover, the use of recuperator reduces the heat released to the environment through the condenser. On the other side, if there is no limitation on the hot source temperature cooling, the net power output will not increase by adding a recuperator, and the net work output will approximately be the same. In more details, in some ORC applications there is a higher cooling limit of the hot sources. For instance, flue gases, containing water and sulfur trioxide, can not be cooled below the acid dew point, because the sulfuric acid vapor can condense. These acids potentially lead to corrosion and damage of the heat exchanger and should be avoided. The temperature of the acid dew point varies with the composition of the flue gas (typical values range from 100 °C to 130 °C) [13]. Furthermore, generally the increased pressure drop and the extra cost of the recuperator are negligible [13]. The choice of the cycle architecture depends on cost-benefit concerns and a variety of advanced cycle architectures are described and analyzed in literature to identify the advantages in comparison to the complexity [6, 13].

Figure 1.2(b) presents the saturation curves of water and of a few typical organic fluids in the T-s diagram, where the entropy difference between saturated liquid and saturated vapor appears lower for organic fluids compared to water. Indeed, for a given thermal power input at the evaporator, the organic fluids mass flow rate increases compared to the generated water flow rate. As a consequence, the increase of mass flow rate,

in addition to the higher liquid volume flow rate and pressure ratio typical for organic fluids, leads to a higher pump consumption [9]. More in details, in steam cycle the high pressure is nearly 60 bar to 70 bar, increasing the thermal stresses, complexity and cost of the boiler, while the condensing pressure is generally lower than 100 mbar. The reduction of the condensing pressure leads to a higher power production with advantages for cycle performances but, on the other hand, it entails a larger condenser surface, a more complex turbine, a higher auxiliary consumption and the increase of air leakage concerns [3]. In an ORC, pressure generally does not exceed 30 bar and, to avoid air infiltration in the cycle, condensing pressure higher than atmospheric pressure is advisable [9]. The choice of the condensing pressure depends on the characteristics of the organic working fluid. For instance organic fluids with a higher critical temperature result subatmospheric at ambient temperature, requiring condensing pressures lower than the atmospheric pressure. For several ORC fluids, the relatively high pressures at the condenser allow the use of air coolers. Such dry condensing system has a relevant energy consumption, but there is no water consumption and it fits well to the application in remote sites and extremely cold weather, where water management becomes a major issue [3]. Based on the aforementioned characteristics, advantages of the ORC systems can be summarized, as shown in Table 1.2. Moreover, Table 1.3 lists the comparison of steam and organic fluids properties.

Table 1.2: Advantages and drawbacks of technologies [9].

Advantages of ORC	Advantages of water steam cycle
No need of superheating	Fluid characteristics
Lower turbine inlet temperature	High efficiency
Compactness (higher fluid density)	Pump consumption
Lower evaporating pressure	
Lower evaporating temperature	
No water-treatment system	
Turbine design	
Low temperature heat recovery	

1.1.1 Working fluid

Working fluid selection is extremely important for an ORC system: the choice of fluid affects the thermodynamic cycle (as maximum and minimum bearable temperatures and pressures), the performance, the cost of components, the plant layout (expanders or turbines design), the safety requirements, etc.. More requirements of power sectors on fluid selection are the same for refrigerant and air-conditioning industries. More in details, the working fluid should be: commercially available, at a reasonable cost, non flammable and toxic, compatible with materials and environmental safety [3].

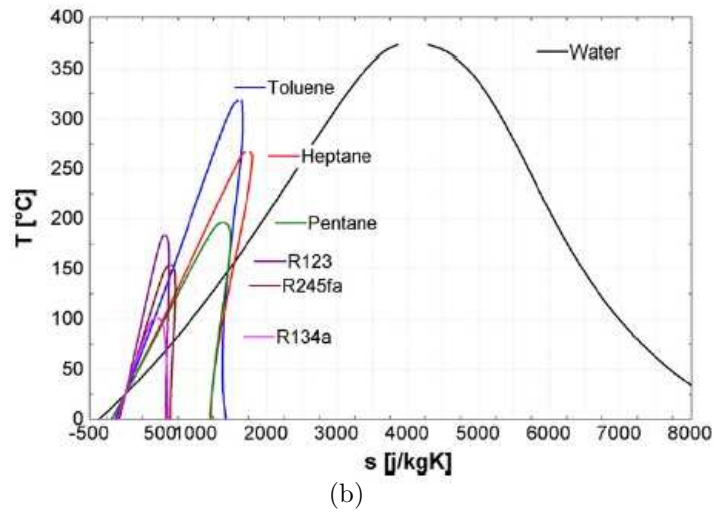
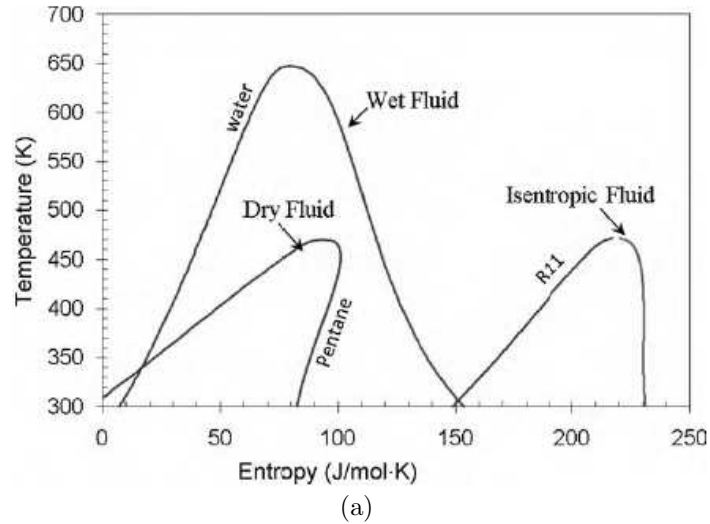


Fig. 1.2: Diagram T-s for Figure 1.2(a) wet, isentropic and dry fluids [4] and diagram Figure 1.2(b) of water and various typical ORC fluids [9].

Pure working fluids, as organic and inorganic fluids, could be used in ORC systems. From the structural point of view and type of atoms in the fluid molecule, the ORC working fluids can be categorized under various main classes, according to [3, 7]:

- Hydrocarbons (HC) including linear (n-butane, n-pentane), branched (isobutane, isopentane) and aromatic hydrocarbons (toluene, benzene);
- Perfluorocarbons (PFC);
- Siloxanes (MM/MDM/MD2M);
- Chloro-Fluoro-Carbons (CFC);

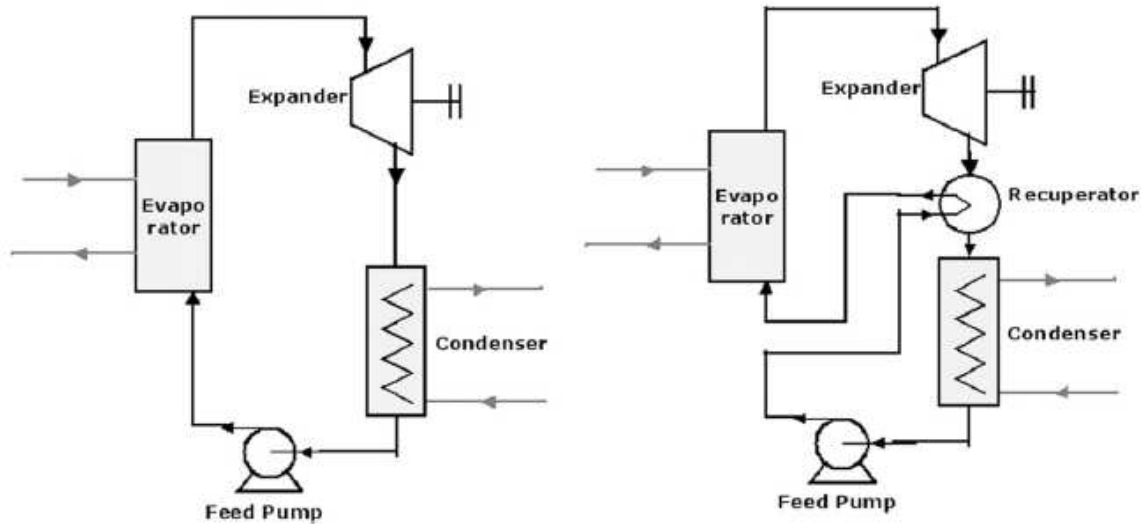


Fig. 1.3: ORC configurations: with (left) and without (right) recuperator heat exchanger at the expander outlet [9].

Table 1.3: Fluids properties comparison in steam and organic Rankine cycles [1, 4].

Fluid	Steam cycle	Organic Rankine cycle
	Water	Organic compound
Critical pressure	High	Low
Critical temperature	High	Low
Boiling point	High	Low
Condensing pressure	Low	Acceptable
Specific heat	High	Low
Viscosity	Low	Relatively high
Flammability	No	Yes
Toxicity	No	Yes
Environmental impact	No	High and depends on fluid
Availability	Available	Supply problem
Cost	Cheap	Expensive
Chemical stability	Yes	Deterioration and decomposition at high temperature
Corrosive	No	Depends on fluid and material

- Hydro-Fluoro-Carbons (HFC);
- Partially fluoro-substituted straight chain hydrocarbons (HCFC);
- Ethers and fluorinated ether;
- Alcohols;
- Inorganics.

Table 1.4 lists advantages and disadvantages of each fluid class presented above.

Table 1.4: ORC fluids advantages and disadvantages [7, 3].

<i>Fluid class</i>	<i>PRO</i>	<i>CONS</i>
HC	desirable thermodynamic properties	flammability issues
PFC	extremely inert; extremely stable	extreme molecular complexity; thermodynamically undesirable
Siloxanes	low toxicity level; low flammability level; high molecular mass; prolonged use as a high temperature heat carrier	available as mixtures; isobaric condensation and evaporation not isothermal and exhibit a certain glide
CFC	not flammable; not toxic; low cost; good thermodynamic characteristics	high ODP values
HFC	zero ODP; nonflammable; recyclable; low toxicity	GWP not zero
HCFC	several zero ODP fluids	
Ethers		flammable; thermodynamically undesirable toxic
Alcohols		flammable; soluble in water; thermodynamically undesirable
Inorganics	extensive and inexpensive; small environmental impact	some operation problems

Actually, there is no a best working fluid that satisfies all the previously cited requirements, but compromises must be made during the fluid selection, considering the application, external conditions and risk concerns. In most cases, the ORC manufacturers renounce to some of the qualities listed above. The refrigerant and air-conditioning industry adopted for many decades CFC, commonly known as "freons", which were ideal for many aspects, but they were progressively banned because of their large ODP. In general, halogeen compounds were widely used in the 1970s and 1980s as refrigerant fluids, due to their good thermodynamics properties. However, they have been banned since 1996 in most developed countries because of their high ODP values. Based on environmental safety concerns, the new family of HFC refrigerants was developed. These fluids are used worldwide, but new legislations are asking for GWP much lower than those exhibited by HFCs. However, refrigerant fluids with a high GWP are not yet banned from ORC applications, but Europe has forbidden the use of R134a in the auto-

motive sector (for A/C application) since 2013, whereas the USA is going to discourage its use after 2016 [3]. For this reason, great efforts have been invested in producing low-GWP drop-in fluids for the refrigerants R134a and R245fa, which are called R1234yf and R1233zd, respectively [14, 15].

Tables 1.5 and 1.6 exhibit pure working fluid candidates for organic Rankine cycle, grouped in the cited classes, with specification of critical pressure (P_c) and critical temperature (T_c) values. It can be seen that all kinds of organic and inorganic fluids could be used in an ORC system. However, the critical point of a working fluid suggests the proper operating temperature range for the working fluid of liquid and vapor forms and it becomes an important data for fluid selection given a thermal source [4]. Based on the critical temperature value, Tchanché et al. [1] group the fluids in three categories:

- high temperature fluids, with $T_c > 250^\circ\text{C}$;
- medium temperature fluids, with $150^\circ\text{C} < T_c < 250^\circ\text{C}$;
- low temperature fluids, with $T_c < 150^\circ\text{C}$.

For instance, Figure 1.4 presents the optimal low temperature working fluids selection corresponding to the heat source temperature level. For each presented fluid, the critical temperature results lower than the source temperature level.

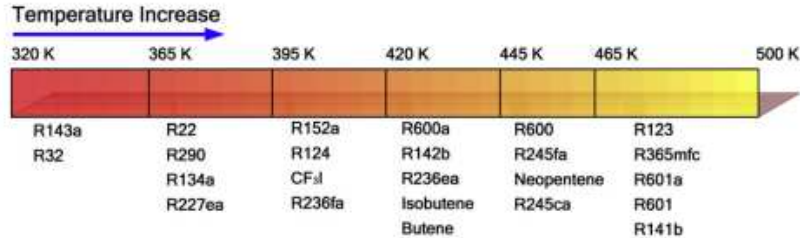


Fig. 1.4: The optimal selections of low temperature working fluids corresponding to the heat source temperature level [16].

The logic shown above is useful in case of *subcritical cycle*, i.e. a ORC cycle with a maximum pressure lower than the working fluid critical pressure (T-s diagram visible in Figure 1.5(a)). Subcritical cycles are the most common configuration applied in several ORC applications. If the working fluid has a critical temperature higher than the heat source maximum temperature, the use of superheating is generally detrimental since it entails a reduction of the working fluid mass flow rate and the power production. In this case, the saturated cycle is the optimal solution from both a thermodynamic and economic point of view. On the contrary, if a low critical temperature fluid is used, superheating is strongly recommended because it allows, if good optimized, an increase in the average temperature in the heat introduction process without limiting

Table 1.5: Pure working fluid candidates for ORC [7].

Classes and name	Alt. name	Pc [bar]	Tc [°C]
<i>Hydrocarbons (HCs)</i>			
Ethane	R-170	48.7	32
Propene	R-1270	45.3	91
Propane	R-290	41.8	96
Cyclopropane	HC-270	54.8	124
Propyne		56.3	129
Isobutane	R-600a	36.4	135
Isobutene		39.7	144
N-butane	R-600	37.9	152
Neopentane		31.6	160
Isopentane	R-601a	33.7	187
N-pentane	R-601	33.6	196
Isohexane		30.4	225
N-hexane		30.6	235
N-heptane		27.3	267
Cyclohexane		40.7	280
N-octane		25	296
N-nonane		22.7	321
N-decane		21	345
N-dodecane		17.9	382
Benzene		48.8	298
Toluene		41.3	319
p-Xylene		34.8	342
Ethylbenzene		36.1	344
N-propylbenzene		32	365
N-butylbenzene		28.9	388
<i>Perfluorocarbons (PFCs)</i>			
Carbon-tetrafluoride	R-14	36.8	-46
Hexafluoroethane	R-116	30.5	20
Octafluoropropane	R-218	26.8	73
Perfluoro-N-pentane	PF-5050	20.2	149
Decafluorobutane	R-3-1-10	23.2	113
Dodecafluoropentane	R-4-1-12	20.5	147
<i>Siloxanes</i>			
Hexamethyldisiloxane	MM	19.1	245
Octamethyltrisiloxane	MDM	14.4	291
Decamethyltetrasiloxane	MD2M	12.2	326
Dodecamethylpentasiloxane	MD3M	9.3	354
Octamethylcyclotetrasiloxane	D4	13.1	312
Decamethylcyclopentasiloxane	D5	11.6	346
Dodecamethylcyclohexasiloxane	D6	9.5	371
<i>Chlorofluorocarbons (CFCs)</i>			
Trichlorofluoromethane	R-11	43.7	197
Dichlorodifluoromethane	R-12	39.5	111

Table 1.6: Pure working fluid candidates for ORC [continue]. [7]

Classes and name	Alt. name	Pc [bar]	Tc [°C]
Trichlorotrifluoroethane	R-113	33.8	213
Dichlorotetrafluoroethane	R-114	32.4	145
Chloropentafluoroethane	R-115	30.8	79
<i>Hydrofluorocarbons (HFCs)</i>			
Trifluoromethane	R-23	48.3	26
Difluoromethane	R-32	57.4	78
Fluoromethane	R-41	59	44
Pentafluoroethane	R-125	36.3	66
1,1,1,2-Tetrafluoroethane	R-134a	40.6	101
1,1,1-Trifluoroethane	R-143a	37.6	73
1,1-Difluoroethane	R-152a	44.5	112
1,1,1,2,3,3,3-Heptafluoropropane	R-227ea	28.7	101
1,1,1,3,3,3-Hexafluoropropane	R-236fa	31.9	124
1,1,1,2,3,3-Hexafluoropropane	R-236ea	34.1	139
1,1,1,3,3-Pentafluoropropane	R-245fa	36.1	153
1,1,2,2,3-Pentafluoropropane	R-245ca	38.9	174
Octafluorocyclobutane	RC-318	27.8	114
1,1,1,2,2,3,3,4-Octafluorobutane	R-338mccq	27.2	159
1,1,1,3,3-Pentafluorobutane	R-365mfc	32.7	187
<i>Hydrochlorofluorocarbons (HCFCs)</i>			
Dichlorodifluoromethane	R-21	51.8	178
Chlorodifluoromethane	R-22	49.9	96
1,1-Dichloro-2,2,2-trifluoroethane	R-123	36.6	183
2-Chloro-1,1,1,2-tetrafluoroethane	R-124	36.2	122
1,1-Dichloro-1-fluoroethane	R-141b	42.1	204
1-Chloro-1,1-difluoroethane	R-142b	40.6	137
<i>Fluorinated ethers</i>			
Pentafluorodimethylether	RE125	33.6	81
Bis-difluoromethyl-ether	RE134	42.3	147
2-Difluoromethoxy-1,1,1-trifluoroethane	RE245	34.2	170
Pentafluoromethoxyethane	RE245mc	28.9	134
Heptafluoropropyl-methyl-ether	RE347mcc	24.8	165
<i>Alcohols</i>			
Methanol		81	240
Ethanol		40.6	241
<i>Ethers</i>			
Dimethyl-ether	RE170	53.7	127
Diethyl-ether	R-610	36.4	193
<i>Inorganics</i>			
Ammonia	R-717	113.3	132
Water	R-718	220.6	374
Carbon dioxide	R-744	73.8	31

the exploitation of the heat source [3]. Meanwhile, a *supercritical or transcritical cycle* is a cycle with a maximum pressure higher than the critical one, as shown in Figure 1.5(b). Working fluid is heated up from subcooled liquid to superheated vapor with a smooth transition above the critical point. The phase change is gradual and all the physical and thermodynamic properties vary without discontinuity in the heat introduction process. Supercritical cycles are interesting because they can achieve a higher efficiency compared to the subcritical ones if a finite heat capacity source is available, but they require more expensive devices. For instance, multistage centrifugal pumps are used and their power consumptions can strongly affect the cycle net efficiency. Furthermore, the cost of the heat exchanger is increased because of the higher thickness of metal required [3]. Other problems are the safety concerns, due to the excess pressure in the evaporator [1].

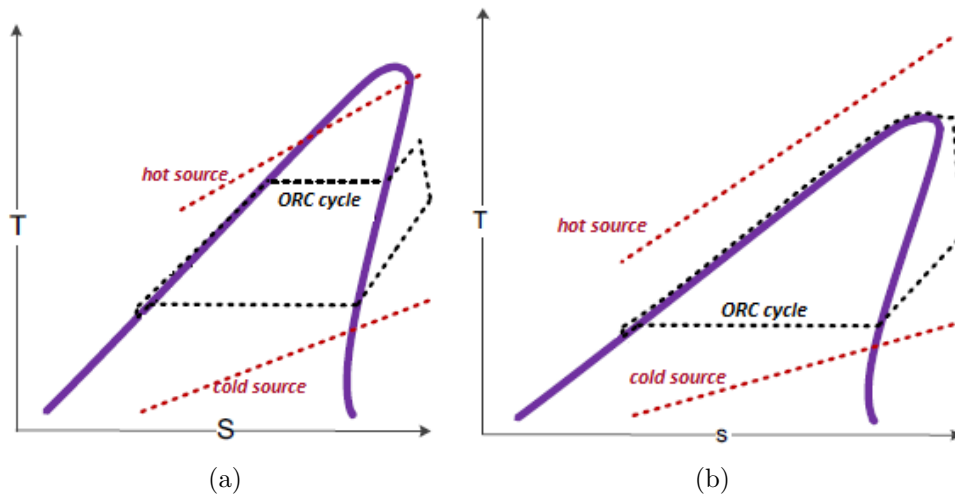


Fig. 1.5: T-s diagram of ORC subcritical cycle(1.5(a)) and ORC supercritical cycle (1.5(b)) [13].

In some applications, the use of a mixture of fluids, instead of pure fluids, allows to obtain a higher efficiency and a higher power production: due to the varying temperature for the heat source, the thermal performances of such cycles are quite poor, since pure fluids have the properties of boiling and condensing at constant temperature, which leads to large temperature differences in the vapor generator and condenser and in turn inevitably increases the irreversibility. Therefore, more interest is growing on the advantages of using mixtures as a working fluid in the power generation systems instead: heat can be supplied or rejected at variable temperature levels but still at constant pressure, since the boiling temperature can vary during the phase change and the binary mixture evaporates over a wide range of temperature, depends on the fluids present in the mixture selected [3, 7]. The use of fluids mixtures in ORC systems has been investigated in various studies [17, 18], with the aim to highlight the potential advantage of a nonisothermal phase transition in efficiency increase. Anyway, the use of a mixture working fluid in an ORC is still limited because of a number of difficulties which make these solutions less practical and affordable than the use of pure fluids, as

composition variation and reduction of heat transfer coefficient. In more detail, in case of leakage, the vapor vented to the environment presents a high concentration of the more volatile component. Therefore a differential refill is required in order to restore the original composition in the cycle, causing additional cost for the fluid analysis, a more expensive fluid storage area, and possible malfunctioning of the plant. Meanwhile, the heat transfer coefficient during evaporation and condensation results lower for mixtures than for pure fluids. Moreover, for any new mixture a detailed bibliographic review is required but, unfortunately, there is a very little availability of experimental data on transport properties, which entails relevant difficulties in a reliable estimation of heat exchangers cost. [3].

1.2 ORC applications

Figure 1.6 presents the most common applications of ORC technology in the heat source temperature and power output plane. The lowest temperature presented in the figure corresponds to low temperature geothermal applications (80 °C [9]), while the upper temperature limit is related to the organic fluids thermal stability. Moreover, a gray area is also drawn, correspondent to the temperature-power zone where the installation of a steam cycle could be convenient respect to an ORC system. Generally, for temperature higher than 450 °C, the use of a steam water Rankine cycle is better [19].

The main ORC applications are following described. Table 1.7 presents the recommended fluids (considering subcritical cycles) depending on ORC applications and temperatures sources (data from literatures [9]). The highest power is producible by geothermal or large waste heat recovery ORC systems, while the lowest ORC power is interesting for domestic applications and it is an evolving limit. In the figure an area of prototypical small and micro-ORC application has been added in the low power-low temperature zone. Several prototypes have been studied in the last decade and various are described in literature [20]. However, only few models have reached the market at the present time, or are close to it. More information and details are available in Chapter 7.

1.2.1 Geothermal ORC power plants

The Earth is increasingly warmer the deeper one goes. This underground energy emitted from the center of the earth and usually called geothermal energy can be used for heating processes and/or electricity generation. The average geothermal gradient near the Earth's surface is about 300 K km⁻¹, not equally distributed and some locations are more suitable for geothermal applications than other [1]. Geothermal heat sources are available over a broad range of temperatures, from a few ten of degrees up to 300 °C. The technical lower bound for power generation is about 80 °C (as previously shown in Figure 1.6). Below this limit the conversion efficiency becomes too small and geothermal plants result not economical [9].

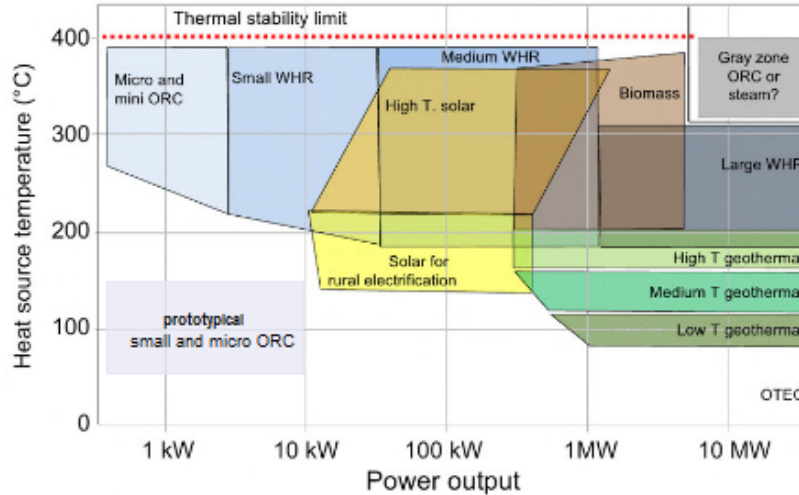


Fig. 1.6: Representation of ORC applications fields in the heat source temperature-power output plane (figure revised from [3]).

Table 1.7: Recommended ORC working fluid based on temperature and applications [9].

Application	Tcd [°C]	Tev [°C]	Recommended fluids
WHR	30/50	120	R113
	30	150/200	Benzene, Toluene, HCFC-123
	35	60/100	HCFC-123, n-pentane
	25	100/210	R113
	25	145*	R236EA
	40	120	Toluene, Benzene
	50	80/220	HCFC-123, R113
	2787	327*	R11, R141b, R113, HCFC-123, HFC-245fa, R245ca
<i>ICE WHR</i>	n/a	277*	HCFC-123
<i>ICE</i>	35	96/221	Benzene
CHP	55	60/150	R245-ca, isopentane
	90*	250/350*	ButylBenzene
Geothermal	50	170	Ethanol
	30*	70/90	Ammonia
	30	100	RE134, RE245, R600, HFC-245fa, R245ca, R601
	25	80/115	Propylene, R227ea, HFC-245fa
Solar	35	60/100	R152a, R600, R290
	45	120/230	n-dodecane
	30	150	R245fa, SES36

* Max and min temperature of heat/cold source instead of evaporating and condensing temperature

Major types of geothermal power plants are: dry steam, single-flash, double-flash and binary-cycle plants. Generally, flash systems are used for moderate and liquid-dominant resources, dry steam plants for dry-steam resources and binary cycles are well adapted

for low temperature liquid-dominant sites. Table 1.8 reports the comparison between the plants characteristics. For low temperature geothermal fluids below 150 °C, the binary option is the sole solution, because the flash steam plants not result economically feasible [1]. Low temperature geothermal plants present relatively high auxiliary consumption (about 30 % to 50 % of the gross power output) and consequently low efficiency values [9].

The thermal energy can be exploited by drilling deep wells (several thousand meters deep depending on the geological formation [9]) and pumping the hot brine trapped in the sub-layers to the surface via production well. The hot brine can transfer its heat directly to an organic fluid through the evaporator (as in Figure 1.7) or to a secondary working fluid via a second heat exchanger, increasing the safety, but reducing the efficiency. The brine then returns to the injection well at low temperature. The organic working fluid receives heat, evaporates and expands, passes the recuperator and the condenser before being pumped to the evaporator. The cooling system could be an air cooler, surface water cooling system, wet-type or dry-type cooling towers [1]. The choice is influenced by the geothermal site and water sources availability. In the case of high temperature (>150 °C) geothermal heat sources enable combined heat and power generation: the condensing temperature is generally set to a higher level (e.g. 60 °C). This solution allows to use the cooling water for heating, increasing the overall energy, but at the expense of a lower electrical efficiency and power production [9].

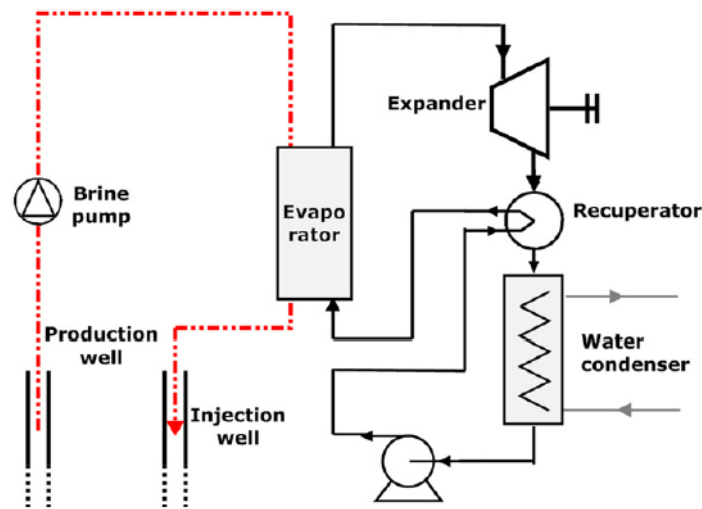


Fig. 1.7: Schematic of a geothermal ORC binary plant [9].

1.2.2 ORC biomass power plants

Biomass is widely available from several agriculture and industrial processes, such as wood industry or agricultural waste [9]. This abundant resource could be converted by combustion into heat. Generally, biomass fuel is burned through a process close to that

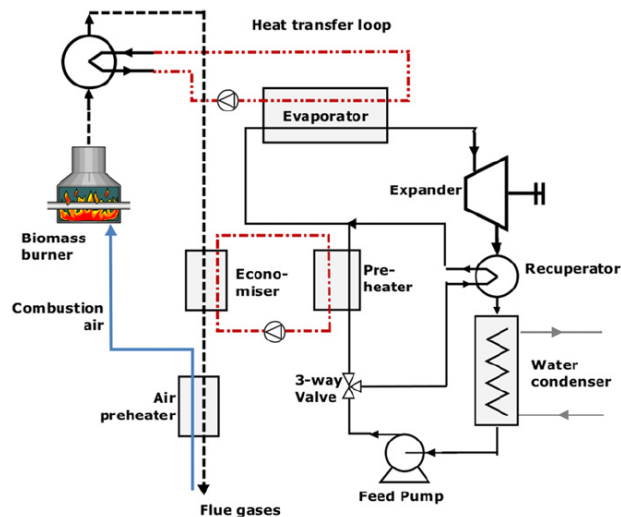
Table 1.8: Comparison of different types of geothermal plants [1].

Type	Resource temperature [°C]	Utilization efficiency [%]
Double-flash	240-320	35-45
Dry-steam	180-300	50-65
Single-flash	200-260	30-35
Basic binary	125-165	25-45

used in conventional steam boilers. The available heat is transferred via the flue gas to the ORC evaporator to vaporize the organic working fluid. To reduce the heat losses in the flue gas, it could be cooled down to the lowest possible temperature, without reach the acid dew point, installing various heat transfer loops: in Figure 1.8, the evaporator, economizer loops and the air preheater are shown.

Generally, an intermediate heat transfer loop is used (as visible in Figure 1.8), because it allows to reduce the pressure into the evaporator, to increase the inertia and consequently the insensitivity to the load change. Therefore, the control and the operation of the cycle result safer and simpler.

The condensation heat is frequently used to produce hot water at a temperature between 80°C to 120°C [1], suitable for space heating, as district heating, or other industrial thermal processes, such as wood drying or sorption cooling. The possibility to use heat as a by-product is an important asset of biomass ORC, highlighting the importance of a local heat demand. Due to the heat difficult transport across long distance, the biomass Combined Heat and Power (CHP) are usually driven by the heat demand rather than by the electricity demand. Most of the time, biomass CHP plant are limited to 6 MW to 10 MW thermal power, corresponding to 1 MW to 2 MW electrical power [9].

**Fig. 1.8:** Working principle of biomass ORC power plant (cogenerative case) [9].

Biomass ORC CHP plants at medium scale (1500 kW) have been successfully demon-

strated and are commercially available, while small scale systems of few kW are still under development. Examples of experimental studies of biomass-fired micro-CHP system based on the recuperated ORC for domestic applications are available in literature [21].

1.2.3 Waste heat recovery ORC applications

Waste heat is the unused heat generated during a combustion process or any other reaction/thermal process and directly exhausted to the environment. Industrial energy intensive processes as well as thermal engines and mechanical equipments produce overabundant heat, not entirely reintegrable on-site and rejected to the atmosphere [9]. The sources could be liquid or solid streams, hot air and flue/process gases, pressurized water, wastewater or exhaust vapor and fundamental information about Waste Heat Recovery (WHR) are: stream matter state, mass flow rate, heat temperature, stream composition and availability. The essential parameter is the heat source temperature and base on this value the waste heat sources are classified in: low for temperatures $<230\text{ }^{\circ}\text{C}$; medium for temperatures range between $230\text{ }^{\circ}\text{C}$ to $650\text{ }^{\circ}\text{C}$; high for temperature $>650\text{ }^{\circ}\text{C}$ [1]. A comparison between ORC and other waste heat recovery technologies, such as Stirling engine, Thermo Electric and Inverted Brayton Cycle is provided in literature [5] and it highlights that ORC is the best performing technology for heat recovery and power generation using heat sources at temperature ranges between $200\text{ }^{\circ}\text{C}$ to $400\text{ }^{\circ}\text{C}$. Moreover, waste heat flows are discontinuous, thus the cycle needs to be flexible. ORC systems already in function can operate at partial load conditions up to 10 %, while water steam cycle need more constant conditions [22].

The ORC technology could be adopted for fuel efficiency and environmental protection in various areas and processes, as power plant, manufacturing processes, cooling of technical equipment, automotive industry, maritime transportation, etc.. Recover waste heat from exhausted gas of Gas Turbines (GTs) in a Bryton cycle or of Internal Combustion Engines (ICEs) to produce energy is actually a common practice. Some industrial sector potentially interesting for ORC waste heat recovery applications are identify by Campana et al. in [22], in which the oil and gas sector results as a potential market for ORC technology as waste heat recovery system from GTs.

Some innovative ORC WHT applications are presented in literature. An example are the on-board ORCs in ICEs, i.e. the using of ORC systems as WHR for automotive application [19]. Generally spark ignition ICE releases heat through the radiation (temperature close to $80\text{ }^{\circ}\text{C}$ to $100\text{ }^{\circ}\text{C}$) and via exhaust gas ($400\text{ }^{\circ}\text{C}$ to $900\text{ }^{\circ}\text{C}$). The electricity generated from on-board ORC can be used for supplying auxiliary units such as the air conditioning or recharging the batteries. One of the main issues is the strong transient behavior of the system which requires complex controlling schemes in order to maintain acceptable efficiency and performance levels. An other innovative example, is the ORC for small WHR application with micro-gas turbines, that present power capacity lower

than 500 kW and exhaust temperature less than 400 °C, in order to increase the overall efficiency [19].

1.2.4 ORC in solar power plants

Energy from the sun can be utilized in electricity generation directly, through PV cells, or indirectly, as the solar thermal. Solar thermal power generation using concentrating collectors is a well-proven technology: the sun is tracked and its radiation reflected onto a linear or punctual collector, transferring heat to a fluid at high temperature. This heat is then used in a power cycle to generate electricity, as presented in Figure 1.9. The main concentrating solar power technology are the parabolic dish, the solar tower and the parabolic trough [9].

ORCs are promising technology to decrease investment costs at small scale: they can work at lower temperatures and the total installed capacity can be scaled down to the kW levels. The power from a solar ORC can be useful also to island microgrid and cogenerations for community. Typical uses are: grid connected power generation, distributed power generation, desalination, irrigation and using in hybrid system, i.e. involving another energy source in addition to solar.

A drawback of solar power is its intermittent nature, causing the imbalance between consumer demand and heat source availability. Therefore, the adding of thermal energy storage is considered to shift the excess energy from high-insolation periods to nighttime or periods of unfavorable conditions. This solutions increase efficiency, reliability and flexibility of the system.

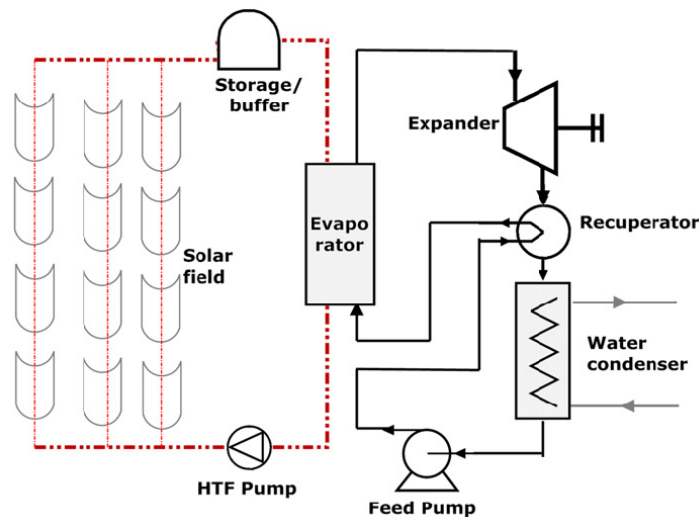


Fig. 1.9: Schematic of a solar ORC power cycle [9].

1.3 ORC world capacity

On a worldwide scale, the total ORC installed capacity is equal to 2749.1 MW_{el}, split into 563 power plants [23], considering all the possible applications. In Figure 1.10 geothermal is the most diffuse applications for ORC and it contributes to 76.5% of all ORC installed capacity worldwilde. Biomass follows with 10.7%. Heat recovery from gas turbines (e.g. compressor stations along pipelines) and stationary Diesel power plants have a similar share with 8.5%. All other heat recovery applications represent 4.2%, while solar thermodynamic applications remain negligible.

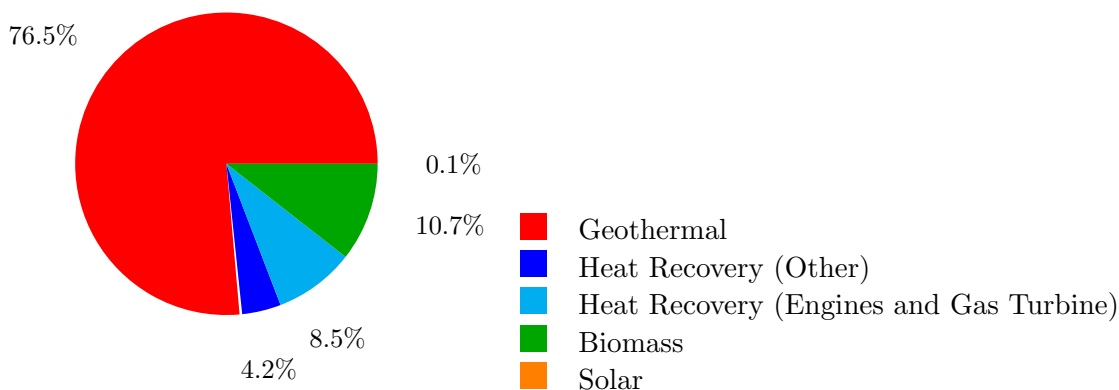
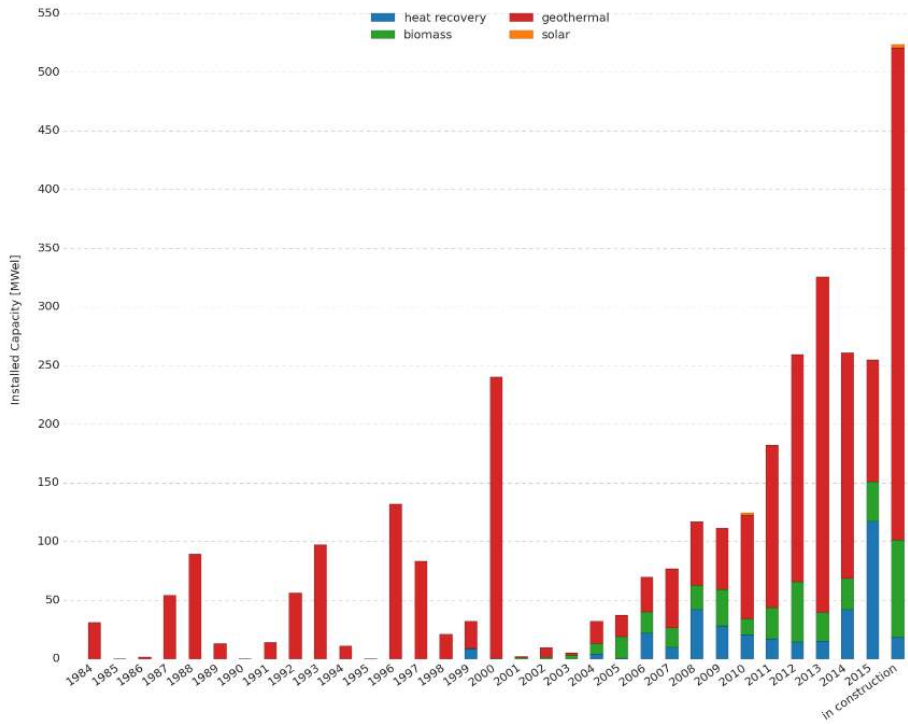


Fig. 1.10: Market share, applications (2016) [23].

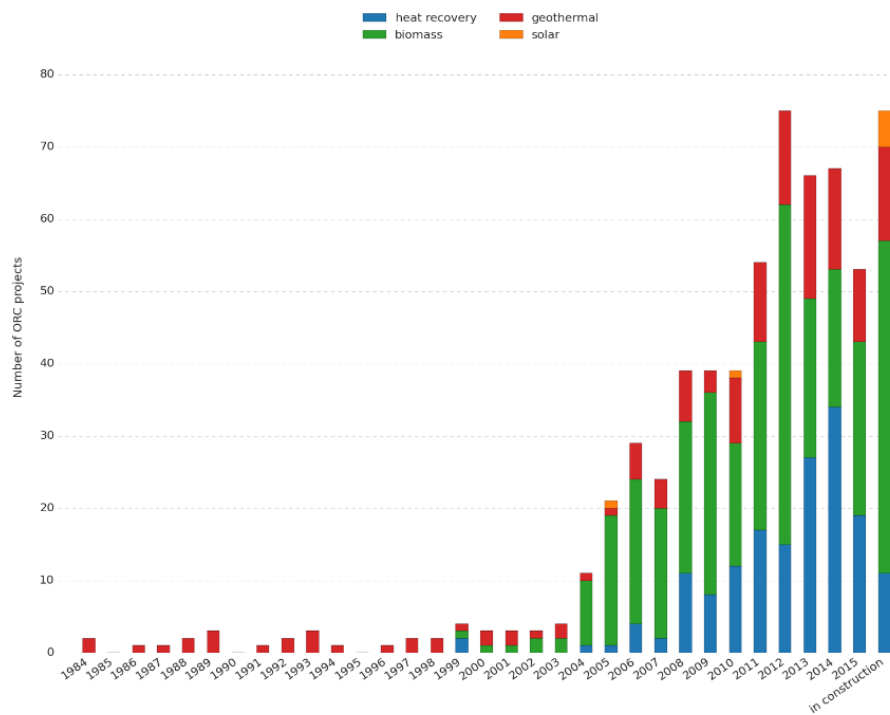
Figure 1.11 presents the installed capacity and installed projects in the period 1984-2016 divided per application. Figure 1.11(a) shows how the diffusion of the ORC technology is related to the geothermal applications, nevertheless first commercial plants (1952-1984) were used also in solar and waste heat recovery applications [3]. Moreover, the comparison between Figure 1.11(a) and Figure 1.11(b) highlights a common high size of the geothermal plants. Figure 1.11(a) shows also a peak of the ORC market in 2013, with 325.5 MW_{el} of new capacity installed [23]. Since then, there was a slowdown in 2014 and 2015, with roughly 250 MW_{el} being installed each year [23]. This may be due to a decline in geothermal applications, related to low natural gas prices and competition against solar and wind. The comparison between the figures shows also how the number of biomass installation increases from 2004, but the characteristic systems size are limited. The heat recovery market has grown significantly over the last three years, from 14.5 MW in 2013 to 116.8 MW up in 2015 [23]. The diffusion of this ORC application is probably related to the increasing interest in environmental impact and efficiency improvements. The heat recovery market is still at an early stage but has long passed the demo/prototype phase (349.1 MW_{el} of installed capacity in the world). The results shown in [24], that identify the cement, glass, steel and oil and gas industries as the most suitable processes for heat recovery to power applications, are confirmed by the market trend (see Figure 1.12). The main application is waste heat recovery from Diesel engines or gas turbines, correspondent to 66.8% of the installed capacity (i.e. 41 projects) [23]. These units are mostly installed on compressor stations along gas pipeline, or on Diesel

power plants [23]. Cement and lime plants result the first industrial application, with 10 projects and a total installed power of 29 MW_{el} . Waste to energy and metal industries (steel, aluminum, foundries, etc.) have similar shares with respectively 12 and 24 projects [23]. Biogas and landfill gas engines together account for 6.2 MW_{el} of installed capacity within 35 projects (projects below 50 MW_{el} not considered).

This thesis focuses on the waste heat recovery application of ORC systems in two different and innovative scenarios. With reference to Figure 1.6, an industrial application of ORC as a large-scale waste heat recovery system to produce electricity is considered. The industrial sector selected is oil and gas and in particular the innovative ORC application on offshore oil and gas platforms. Compactness, low weight, and dynamic flexibility are crucial aspects to minimize the installation costs. Thereby, the yearly energy conversion efficiency of offshore power stations is typically low, ranging between 20% to 30%. Given their high modularity and simplicity, ORCs have been proposed to recover the thermal energy of offshore gas turbines. The dynamic behavior of the ORC coupled with gas turbine is analyzed. The dynamic behavior is caused by the integration with an offshore wind farm. The electrical, thermal and economic aspects are studied to identify the feasibility of the ORC installation. The other innovative ORC application as waste heat recovery system considered in this thesis is the domestic sector. Domestic ORC technology is still under development and not presented in Figure 1.6. The optimal size for a domestic ORC depends on many factors. Considering the cost and the need to dissipate a large amount of heat, from sources with temperatures ranging between 60°C to 100°C , a power output from 300 W to 5 kW appears to be a good choice for most cases in the residential application [3]. The experimental rig developed to test the micro-ORC prototype is presented and the experimental campaign carried out on the micro-ORC prototype is described: from real-time data, collected through appropriately installed sensors and representing the dynamic behavior of the system, the ORC operational maps are realized under different conditions, with the aim to identify performance behavior of the system.



(a)



(b)

Fig. 1.11: Installed capacity per year and per application (Figure 1.11(a)) and installed project per year and per application (Figure 1.11(b)) [23].

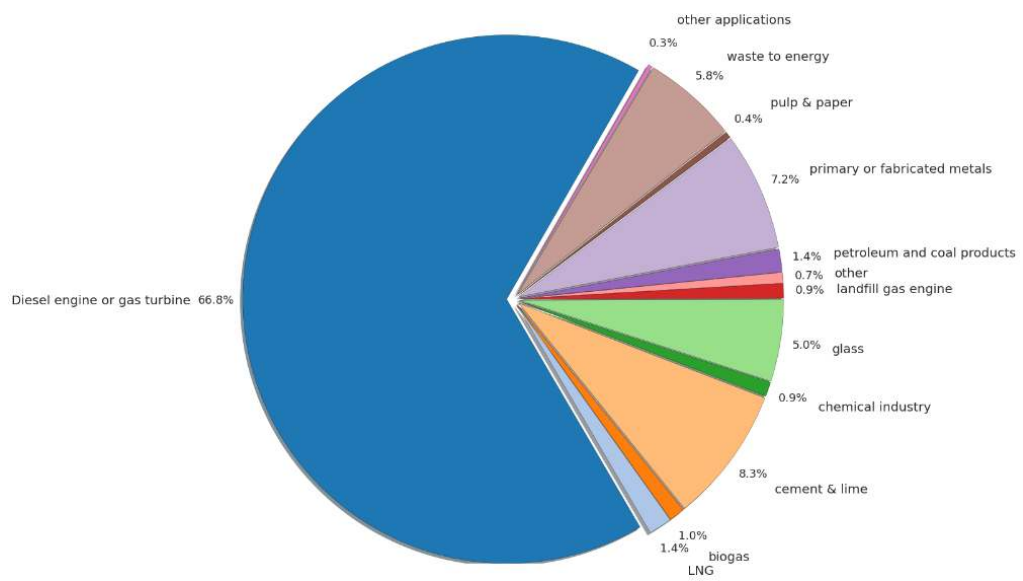


Fig. 1.12: Heat recovery applications (projects size upper to 50 kW_{el}) [23].

Part II

Large-Scale Waste Heat Recovery: ORC Numerical Analysis

CHAPTER 2

WHR from gas turbines exhaust: applications in the oil and gas sector

Summary. This chapter focuses on the large waste heat recovery ORC system applications in the industrial sector. The innovative scenario considered is an offshore oil and gas platform. Typical gas turbines installation arrangement on platforms consists of multiple gas turbine units, operating under part-load conditions, to guarantee a reserve power and safe operation of the engine. Due to this power system configuration, high quantity of heat is available in the exhaust gas. From a literature analysis, the ORC technology results the much more promising systems if compared to several WHR systems in the considered sector, allowing an efficiency improve and a reduction of the pollutants emissions. Therefore, the case study is presented and described in Section 2.1. The innovative aspect investigated are the using of ORC as WHR system and the integration with a offshore wind farm, to identify the ORC presence effects on the system behavior. Other simpler configuration are introduced to comparison purpose and to identify the advantages of the innovative power plant analyzed.

Gas turbine is a widely used prime mover for power generation and mechanical drive applications on offshore oil and gas production facilities as the gas fuel is easily available and in many cases free for operational cost, unless it could be monetized. Environmental, Health and Safety (EHS) issues are not only critical but very important for the oil & gas industry and considerable resources are allocated for EHS related aspects as negligence can be very costly as was evident from the incident of BP Deepwater Horizon project (on 20 April 2010). As noted in the EHS guidelines [25], all efforts shall be made to maximize energy efficiency and use cost effective approaches for reducing emissions. The main source of air emissions for offshore facilities is the combustion process for power and thermal energy generation and other drivers for large power consuming compressors and pumps among other factors. Particularly relevant are the CO₂ emissions which depend on type of fuels and efficiency of used prime movers. In a recent report prepared on the Norwegian Petroleum Sector, it is noted that 78.4% of the total CO₂ emissions by the oil & gas sector is attributed to the GTs and gas production related operations, as shown in Figure 2.1 [26]. Moreover, one of the requirements set in the 20-20-20 targets in March 2007 by the Commission of the European Communities [27] for the year 2020 is to achieve 20% reduction in the Green-House Gas (GHG) emissions relative to the 1990s levels. Therefore, in some particularly oil producing countries, such as Ireland and Norway, a carbon tax is introduced to promote effective energy utilization through Waste Heat Recovery and reducing the GHG emissions [28].

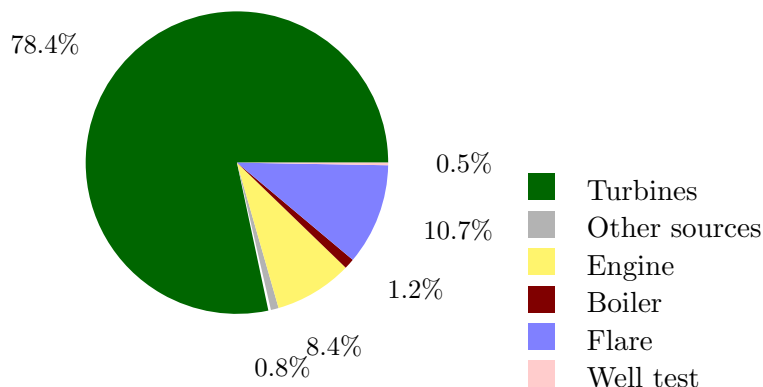


Fig. 2.1: percentage of CO₂ emissions from petroleum activities distributed by source, 2011 [26].

To meet the offshore electric power demand, the typical GTs installation arrangement consists of multiple gas turbine units with a potential of operating under part-load conditions. On offshore facilities, the power generation system operates in an island mode and the redundant installed capacity ensures the necessary reserve power and the safe operation of the engines. Moreover, due to weight and space constraints, the configurations are mostly simple cycle GTs with WHR system to meet thermal energy needs and the gas turbine selection for the offshore applications is focused more on reliability and compactness rather than GT electric efficiency and operating usually at less than 35% with few exceptions [29, 30]. The high levels of GHG emissions are related with the low operating efficiency of GTs and high temperature wasted heat. Nguyen et al. conduct the exergy analysis in [31] of a generic oil and gas platform and suggest that the power generation system alone is responsible for 62-65% of the total exergy losses. A direct remedy could be the removal of on-board power generators by relying on conveyance of electricity from onshore. Recent surveys [32, 33] and operational experience on actual facilities (e.g. the Troll A platform in the North Sea [34]) prove the economic feasibility of high-voltage direct current systems for low transportation ranges (≈ 300 km). Capturing and storing the CO₂ is also a solution to reduce emissions offshore. Floating plants with large power outputs (up to 450 MW) for offshore electrification integrating compression, pre-conditioning and CO₂ capture are under investigation [35, 36]. A drawback is that the sequestration process penalizes the energy conversion efficiency (up to 9%-points [35]). Furthermore, this process does not cope with the removal of other pollutants such as sulfur and nitrogen oxide. A viable solution to increase overall efficiency of the offshore energy systems is to utilize bottoming power cycle by recovering the waste heat energy from the GT exhaust gases and subsequently reduce pollutants emissions. A mature technology is the Steam Rankine Cycle (SRC). Kloster describes in [37] the existing SRC units in the Oseberg, Eldfisk and Snorre B offshore installations. However, adoption of the conventional bottoming cycles using steam on the offshore platforms is difficult because of weight and space requirements. Therefore, the use of different innovative approach consisting of a small size waste heat

recovery system could be considered as a possible solution. Bianchi and De Pascale [5] analyze the performance of several bottoming cycle solutions for low and medium waste heat energy sources. Specially, the examined systems are ORC, micro Rankine cycle, Stirling engine, inverted Bryton cycle and thermo-electric systems. Their detailed study of various bottoming cycles identifies the ORC technology as the most performing, from thermodynamic perspective, in order to exploit low-medium temperature waste heat sources. Pierobon et al. [38] evaluate and compare ORC, SRC and Air Bottoming Cycle (ABC) as waste energy recovery systems downstream of the SGT-500 gas turbine for the Draugen oil and gas offshore platform located in the North Sea. The interest on ABCs is related to: (i) the use of a non-toxic and inflammable working fluid; (ii) no need for a condenser section since these cycles operate as open-cycles; (iii) high compactness and (iv) low weight. Moreover, the results presented in various studies [39, 40, 41] prove a low gain in performance despite the low weight and short pay-back time. However, the investigation in [38] shows that the ORC system, despite requiring the highest weight, allows to obtain the highest net power output and net present value compared to the other analysed technologies. The ORC system considered in their study consists of the Turboden model 65-HRS, coupled with an intermediate heat transfer fluid loop between the GT exhaust gas and the organic fluid. In a recent study, Carcasci et al. [10] carry out a parametric evaluation of the ORC system for waste energy recovery considering effects of organic fluid type, its pressure and temperature at inlet to the expander including ORC fluid superheating in combination with the effects of maximum temperature of the intermediate heat transfer fluid. Their main observations include the following: performance of the ORC system depends on the selected organic fluid and the maximum temperature of the intermediate heat transfer fluid. Moreover, superheating of the ORC fluid is not always beneficial in improving performance of the ORC system. Bhargava et al. [42] compare the cogenerative performance of a topping GT cycle integrated with different bottoming cycles: Brayton bottoming cycle (another name for ABC), inverted Bryton cycle and ORC. Their study, similar to the work of Pierobon [30], shows that among the different bottoming cycles, the ORC offers better results in terms of the primary energy saving index and the overall electric efficiency for the analyzed system. More in details, with ORCs, improvements of the energy conversion efficiency range from 10% to 20%, with an additional specific weight of 15 - 20 t · MW⁻¹. Campana et al. [22] estimate the potential of the ORC as the waste heat recovery system in different industrial scenarios. In the oil & gas industry, gas turbines used for gas compressor stations and gas storage facilities are considered as the waste energy source for the ORC systems. Besides energy recovery and cost saving, 3.7 million metric tons of GHG emissions are avoided considering 8000 operational hours per year.

Commercially available and selected ORC units in terms of ORC electric efficiency, power size and most common applications/heat source temperature ranges are shown in Figure 2.2 and Table 2.1. It must be mentioned that the reported GE ORegenTM is a two loops ORC system, specially developed for the oil & gas industry applications [43]. As evident from Figure 2.2 and Table 2.1, GE offers the largest power rated ORC unit (up to 15 MW) specifically developed for the waste heat recovery from GT

Table 2.1: Power range and heat source temperature data for several ORC commercial units (mainly excerpted from [29]).

Manufacturer	Application	Power range [kWe]	Heat source temperature range [°C]
ORMAT	Geothermal, WHR, solar	200-7200	150-300
Turboden	CHP, geothermal	200-2000	100-300
GE	WHR	7000-15000	450-5250
Adoratech	CHP	315-1600	300
Infinity Turbine	WHR	250	>80
Vericorp	Geothermal, WHR, solar	20-115	150-300
TriOgen	WHR	160	>350
GMK	WHR, Geothermal, CHP	50-2000	120-350
Electratherm	WHR	50	>93

units with waste energy temperature ranging from 450 °C to 550 °C in line with typical GTs exhaust gas temperature values [29]. Whereas, Turboden commercial models are currently rated for the highest electric efficiency values. Furthermore, various studies

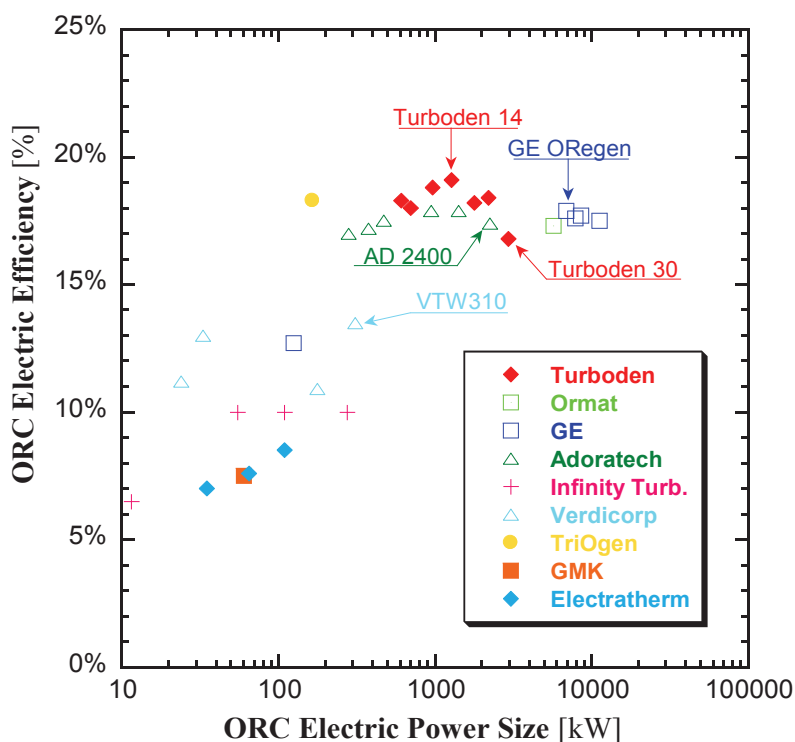


Fig. 2.2: Performance of selected commercially available ORC.

focus on the integration of wind power and gas turbines for on-shore applications, due to the increasing of wind power installed capacities. Moreover, the dynamic modeling of conventional systems takes a new meaning, caused by the unpredictable variability of

the renewable sources. For instance, [44] shows how the flexibility of GTs is somewhat limited by partial load efficiencies and accessible ramp rates. Hence, some units are sometimes required not to fulfill the firm power objective, but to meet steep ramp rates. Moreover, Branchini et al. [45] demonstrate how maintain many turbines working at full load for most of the analyzed time is hard, as wind speeds vary randomly throughout the each day. Research efforts focus on integrating wind power in oil and gas facilities. The rapid development of offshore wind power technologies enables designing floating turbines for water depths up to 700 m [46] and distances from the coast of around 100 km (case of BARD Offshore 1 [47]). The solution is attractive due to the uniform distribution of wind speed and space availability. The integration does not require additional weight and space compared to the implementation of waste heat recovery units or carbon capture technologies. On the other hand, additional challenges related to the stability of the electric network arise, due to the variability of this renewable source. As an example, Årdal et al. [48] and Marvik et al. [49] study how the presence of wind turbines could improve the stability of an offshore oil and gas platform using voltage controllers. Similarly, He et al. [50] investigate the integration between an offshore oil and gas platform and an offshore wind farm. However, in all previous studies addressing the integration of wind farms on offshore platforms, the platform power plants consist of gas turbines only working, as common in the oil and gas sector, at partial load, thus excluding the problems identified in the on-shore features.

2.1 Case study

This study considers the upgrading of an existing offshore oil and gas platform located in the North Sea. As previously introduced, the power plants installed on the offshore facilities generally present low values of electric efficiency. To improve the platform performance, without increase the fuel consumption, the innovative solution here presented consists in the integration between the conventional GT prime movers, ORCs as waste heat recovery systems and exploiting offshore wind as renewable sources. The integrated power system realized aim to guarantee the constant electric load required by the oil and gas offshore platform and heat regaining to meet thermal energy needs is analyzed.

In more details, the on board power plant consists of three combined cycle systems, as shown in Figure 2.3(a). Each one comprises a GT topping module and an ORC bottoming cycle unit. Figure 2.3(b) shows the detailed layout of the combined cycle unit. The ORC turbogenerator recovers the heat from the GT exhaust gases. The SGT-500 gas turbine is considered as topping unit. This engine has been widely adopted and commonly installed on offshore platforms requiring high fuel flexibility and reliability [51]. The turbine blades are uncooled. The engine employs two coaxial shafts coupling the Low Pressure Compressor (LPC in Figure 2.3(b)) with the Low Pressure Turbine (LPT) and the High Pressure Compressor (HPC) with the High Pressure Turbine (HPT). The Power Turbine (PT) transfers mechanical power through a dedicated shaft to the elec-

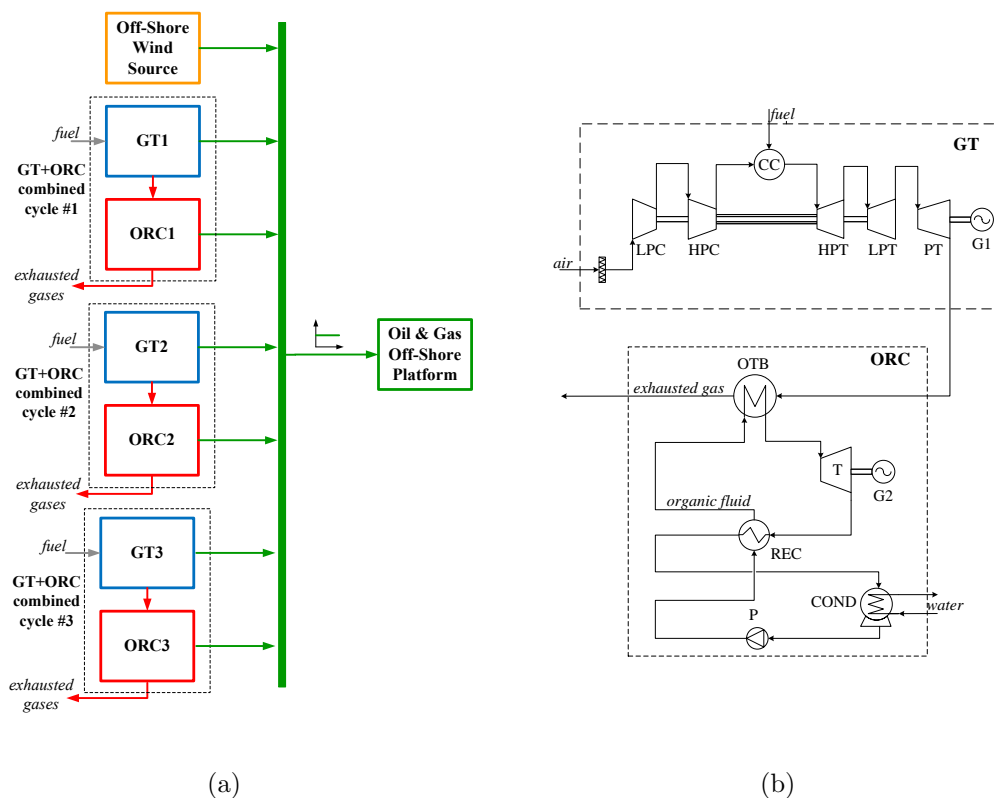


Fig. 2.3: Layout of the power system considered as case study. Figure 2.3(a) Integration of GTs, ORC units and wind farm with the electric grid. 2.3(b) Combined cycle unit configuration.

tric generator (G1 in Figure 2.3(b)). Natural gas is the fuel used in the Combustion Chamber (CC). Table 2.2 reports the design-point specifications of the gas turbines as provided by the manufacturer for the C-version launched in the 80's.

Table 2.2: Design specifications provided by the manufacturer for the twin-spool gas turbine considered as topping unit.

Model	Siemens SGT-500
Fuel	Natural gas
Turbine inlet temperature	850 °C
Exhaust gas temperature	379.2 °C
Exhaust gas mass flow	91.5 kg · s ⁻¹
Electric power output	16.5 MW
Electric efficiency	31.3 %

The ORC unit comprehends the single-pressure non-reheat Once-Through Boiler (OTB), the Turbine (T), the sea-water cooled shell-and-tube condenser (COND) and the feed-water Pump (P). The working fluid is benzene (molecular weight 78.11 g · mol⁻¹, critical

temperature and pressure 288.9 °C and 49.9 bar). This compound is widely adopted for operating ORC systems in this range of temperature [52, 53, 5]. The high resonance stabilization energy of the aromatic structure ensures its chemical stability up to 315 °C [54]. The saturation curve of benzene is positive (dry fluid as described in Chapter 1). A shell-and-tube recuperator is added to decrease the energy contained in the superheated vapor exiting the ORC expander. The simulation tool available in literature and developed by Pierobon et al. [55] has been used to design the ORC unit. The software allows identifying the thermodynamic states at the inlet and outlet of each ORC component applying basic energy and mass balances, once defined the boundary conditions, hot source inlet temperature, fluid, external conditions, etc.. Subsequently, the design of the plant equipment is carried out automatically, ultimately leading to the evaluation of the chosen performance metrics. An iterative procedure, based on the genetic algorithm method explores the design space, looking for optimal design configurations. Figure 2.4 presents the structure of the multi-objective algorithm. The optimization routine involves the ORC solver, the Nelder-Mead direct search optimizer, the shell and tube designer, and the volume and economic evaluations. Generally, a multi-objective optimization involves minimizing or maximizing simultaneously two or more functions subjected to a set of constraints. In contrast to single-objective optimization, a solution to a multi-objective problem is a range of optimal points. Use the genetic algorithm allows to avoid the calculation of derivatives and enabling the search of global optima. The genetic algorithm parameters are: population size 1000, generation size 200, crossover fraction 0.8 and migration fraction 0.2. The selected numerical values ensure the repeatability of the solution when different simulations are performed. The genetic algorithm stops when the maximum number of generations is reached or when the average change in the spread is lower than the specified tolerance (set equal to 10^3). Table 2.3 reports the main parameters assumed for the considered ORC system, according to the described methodology. More information could be found in [55].

The floating wind turbines are connected to the stand alone electric grid, see Figure 2.3(a). The wind turbine considered in this work is a reference generator developed at the National Renewable Energy Laboratory (NREL) [56]. The wind turbine is a three-blade upwind variable-speed and variable blade-pitch-to-feather-controlled turbine. The NREL together with the Massachusetts Institute of Technology is studying a tension leg platform for a floating wind turbine. Pretensioned mooring lines anchored to the seabed by suction piles [57] will connect the corners of the platform, designed for water depths from 60 m to 200 m and for a 5 MW turbine.

2.1.1 Other offshore power plant configurations

The presented configuration is named as *GT+ORC configuration* and its performance will be analyzed and compared in the following chapters to the performance of simpler power plant configurations. The comparison aims to identify the advantages related to the ORC installation and the wind farm integration.

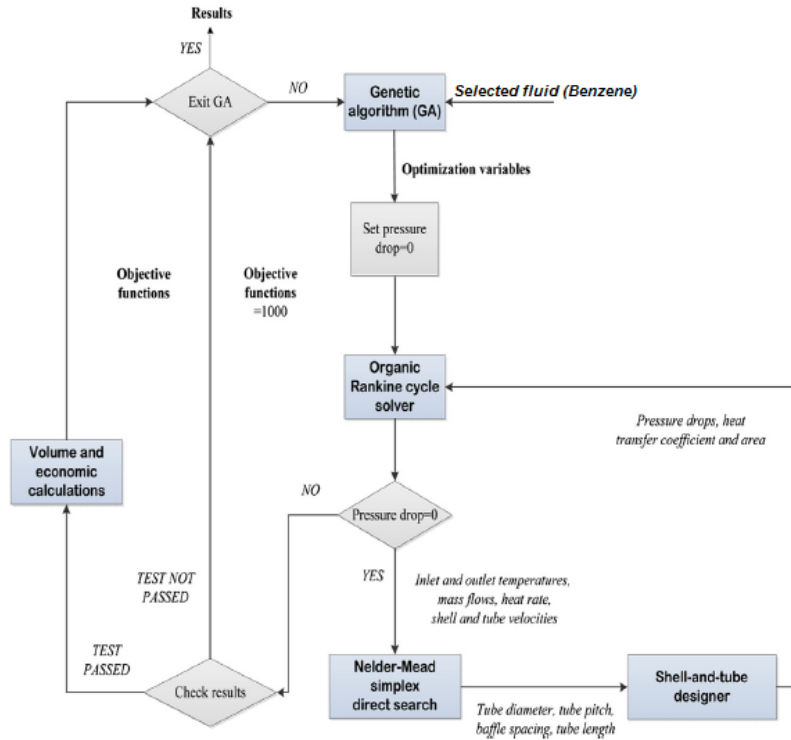


Fig. 2.4: Structure of the multi-objective algorithm [55].

The first case, named *GT configuration*, consists of the integration between wind farm and three gas turbines located on the platform, as reported in Figure 2.5(a). Meanwhile, the second considered configuration, called *GT configuration-no WIND*, is visible in Figure 2.5(b).

In both cases, the gas turbines have the same characteristics of GTs in *GT+ORC configuration* and two GTs are maintained in operation, while the third is back-up unit. The electric load required by the platform has been set equal to 30 MW in all cases.

In *GT configuration* each GT in operation guarantees the 50% of the remaining load, once considered the wind power production. In case of *GT configuration-no WIND*, the load required by the platform is completely satisfied by two gas turbines. Therefore, each GT produces 15 MW and they work constantly in off-design conditions (refer to design values reported in Table 2.2).

Table 2.3: Design variables and point specifications used to parametrize the dynamic model of the organic Rankine cycle system, obtained as described in [55].

Component	Parameters
Organic fluid	Benzene
Electric efficiency	21.8 %
ORC power output	4.8 MW
Mass flow	38.7 kg · s ⁻¹
Maximum pressure	28.9 bar
Minimum pressure	0.4 bar
Expander inlet temperature	266.5 °C
<i>Once-through boiler</i>	
Volume (cold side)	10.3 m ³
Volume (hot side)	51.5 m ³
Weight (metal walls)	45.4 t
UA-value	420.7 kW · K ⁻¹
<i>Recuperator</i>	
Volume (cold side)	1.18 m ³
Volume (hot side)	13.24 m ³
Weight (metal walls)	10.23 t
UA-value	390 kW · K ⁻¹
<i>Turbine</i>	
Throat flow passage area	0.040 m ²
Isentropic efficiency	81.6 %
Electric generator efficiency	98 %
<i>Pump</i>	
Delivery pressure	2928 kPa
Inlet pressure	36 kPa
Isentropic efficiency	72 %
Power consumption	0.2 MW

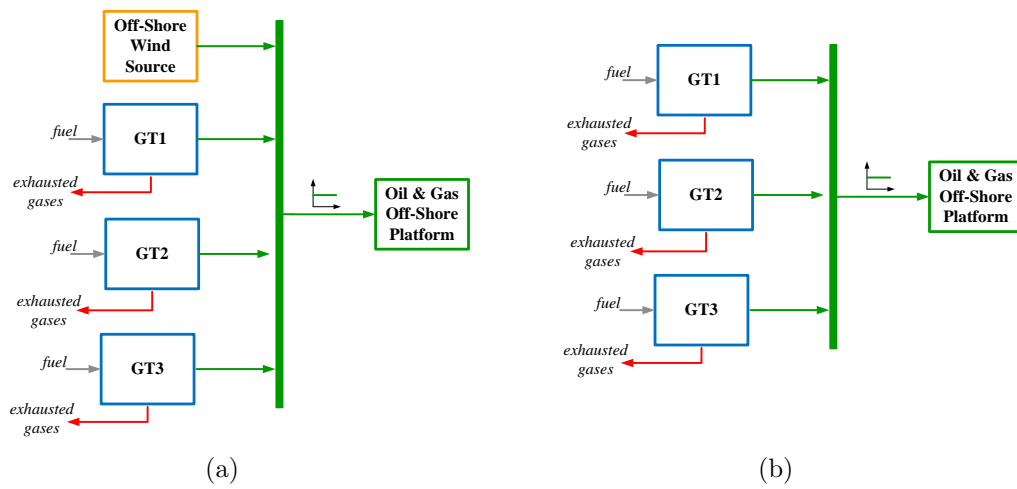


Fig. 2.5: Layout of *GT* configuration Figure 2.5(a) and layout of *GT* configuration-no WIND 2.5(b).

CHAPTER 3

Integrated power system dynamic model

Summary. This part chapter gives an overview of the adopted modeling language and of the dynamic model of integrated system components. In more details, the dynamic model of the power system is developed using components from existing Modelica packages. Modelica is an object-oriented modeling language that allows building dynamic models using an equation-based modular approach. The gas turbines model is described in Section 3.1 and data validation of this model are collected from literature. The GT sub-system model is built by exploiting basic components included in the ThermoPower library [58]. Section 3.2 introduced the ORC system model, that adopts software objects from the Modelica ORC package [59], with suitable adaptations regarding the heat transfer coefficients and flow configuration in the once-through boiler. Section 3.3 introduces the wind speed profiles and wind turbines power productions in two different scenarios. These data has been introduced into the dynamic model of the integrated system as a time series-based model.

3.1 The gas turbine model

Figure 3.1 shows the Modelica object diagram of the gas turbine. Compressors and turbines are multi-stage machines modeled as zero-dimensional components using steady-state and off-design characteristics. The low and high pressure compressors are modeled based on maps of axial compressors provided by Kurzke [60]. These maps, originally from Carchedi and Wood [61], use tables that state values for flow coefficient, pressure ratio, isentropic efficiency and speed of revolution for the complete operating range. The maps are scaled following the methodology proposed by Kurzke [62]. The equation proposed by Stodola [63] is employed for modeling the low pressure, high pressure and power turbines. Equation (3.1) expresses the relation between the inlet and outlet pressure (p_{in} and p_{out}) of the expander with the mass flow rate \dot{m}_g and the turbine inlet temperature T_{in} in off-design conditions.

$$C_T = \frac{\dot{m}_g \sqrt{T_{in}}}{\sqrt{p_{in}^2 - p_{out}^2}} \quad (3.1)$$

Meanwhile, the turbine off-design efficiency is predicted with the correlation proposed by Schobeiri [64]. In particular, eq. (3.2) relates the isentropic efficiency η_{is} and the

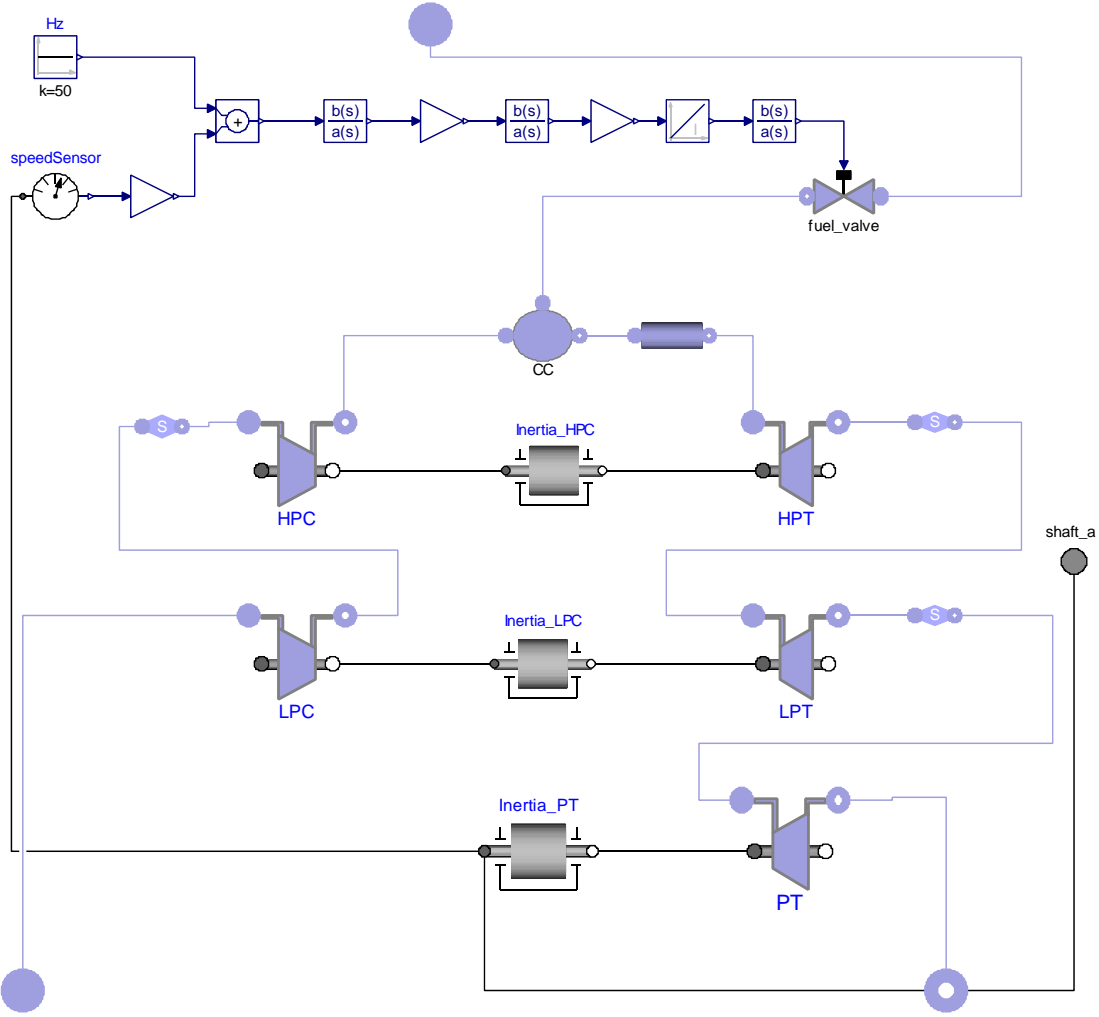


Fig. 3.1: Object diagram of the gas turbine sub-system model.

non-dimensional flow coefficient n . This coefficient is evaluated as shown in eq. (3.3), where N represents the shaft rotation speed [rpm] and Δh_{is} is the isentropic enthalpy drop. The subscript des refers to the variable calculate at design point.

$$\eta_{is} = \eta_{is,des} \frac{n}{n_{des}} \left(2 - \frac{n}{n_{des}} \right) \quad (3.2)$$

$$n = \frac{N}{\sqrt{2\Delta h_{is}}} \quad (3.3)$$

The combustion chamber (CC) unit is built assuming complete and adiabatic combustion process. In the component, mass and energy conservation (as shown respectively in eqs. (3.4) and (3.5)) are expressed including the dynamic terms. As suggested by Camporeale et al. [65], the mass and the internal energy are computed using the thermodynamic properties of the combustion products exiting the burner. Furthermore, it is assumed that the combustion process and the mixing action take place at constant

volume V_{CC} . In detail, ρ_{CC} represents the density inside the combustion chamber; U_{CC} is internal energy; \dot{m}_a , \dot{m}_f and \dot{m}_g are the air, fuel and gas mass flow rates respectively, while h_a , h_f , h_g the correspondent enthalpy values. LHV is the Lower Heating Value of the used fuel, in the considered case natural gas. This parameter is set according to the data provided by the gas turbine manufacturer. The pressure drops are lumped in an external device. In off-design conditions, a quadratic dependence to the volumetric flow rate \dot{V} is assumed, as visible in eq. (3.6).

$$V_{CC} \frac{d\rho_{CC}}{dt} = \dot{m}_a + \dot{m}_f - \dot{m}_g \quad (3.4)$$

$$\frac{dU_{CC}}{dt} = \dot{m}_a h_a + \dot{m}_f (h_f + LHV) - \dot{m}_g h_g \quad (3.5)$$

$$\frac{\Delta p}{\Delta p_{des}} = \left(\frac{\dot{V}}{\dot{V}_{des}} \right)^2 \quad (3.6)$$

The shaft dynamic balance (eq. (3.7)) is used to model the dynamics of each spool. The values of the inertia of the rotating masses (shaft, blades, generator) are set according to data provided by the gas turbine manufacturer.

$$\frac{d\omega}{dt} = \frac{\sum_{i=1}^n (P_{in,i} - P_{out,i})}{I\omega} \quad (3.7)$$

ω is the rotational speed in [rad/s], I is the inertia of the shaft, $P_{in,i}$ is the mechanical power given to the shaft and $P_{out,i}$ is the mechanical power provided by the shaft.

The part-load performance of the electric generator is predicted using eq. (3.8) proposed by Haglind and Elmegaard [66], where the electric efficiency in off-design is evaluated as function of mechanical power input in per unit L and of the copper loss fraction F_{cu} .

$$\eta_{el} = \frac{L\eta_{el,des}}{L\eta_{el,des} + (1 - \eta_{el,des})[(1 - F_{cu}) + F_{cu}L^2]} \quad (3.8)$$

Figure 3.1 shows (on the topside) the control system of the SGT-500 engine as given by the manufacturer. The compressors are not equipped with variable inlet guide vanes. The load of the engine can be adjusted by varying the opening of the fuel valve. The control system blocks are deeply described by Pierobon et al. [67]. The cited reference presents also a primary validation of the dynamic model of the SGT-500 engine by comparison with a reference model provided by the gas turbine manufacturer. More in details, the off-design steady-state behavior of the gas turbine model is compared to the part-load characteristics given by the manufacturer in 10 % and 100 % range. The mass flow rate and temperature of the exhaust gases, fuel mass flow rate and pressure in the combustion chamber are considered. The quantity showing the larger mismatch is the mass flow rate of the combustible. The relative error is about 3 % for loads larger than 60 % and it increases up to 15 % when the load decreases to 10 %. Meanwhile, Figure 3.2

present the results obtained in [67] from the comparison between real operational data of a SGT-500 gas turbine and the results of the developed dynamic model. The real data correspond to the operational data of gas turbine B of the Draugen oil and gas platform, located in the North Sea. In Figure 3.2(f) is visible how they consider a gas turbine operation initially at 45 % of the nominal power while the load decreases first to 41 % in 10 s and subsequently to 38 % in 20 s. The variables presented in [67] for the comparison are the rotational speeds of the LPC and HPC shafts, the fuel flow, the PT outlet temperature and the pressures at the outlet of the HPC and LPT. They evaluate the a LPC rotational speed relative error between 3.2 % to 6 %. An average relative error of around 10 % is found for the prediction of the pressure at the outlet of the high pressure compressor. The rotational speed of the high pressure compressor is estimated with a maximum error lower than 1.3 %. The highest average relative error, equal to 19.8 % occurs in the evaluation of the pressure at the outlet of the LPT. The relative error related to the fuel flow ranges from 0.1 % to 7.7 %, while the outlet temperature of the power turbine exhibits an average relative error of 0.6 % [67]. Based on these results, the developed gas turbine model is able to reproduce both the steady-state and the dynamic behavior of the components with reasonable accuracy, over the entire range of loads encountered during real operation [67].

3.2 The organic Rankine cycle model

The model of the ORC system is made of software objects acquired from a library that was developed to model a 150 kW ORC turbogenerator using toluene as the working fluid and it has been adapted to the considered case. This was successfully validated for dynamic operation against experimental data [59]. The model of the bottoming cycle unit is, therefore, deemed reliable, considering the similarity of the application at hand with the one presented in the cited reference.

The once-through boiler, shown in the object diagram of Figure 3.3, is implemented by combining basic ThermoPower modules. Figure 3.4 shows the 1D flow models for the gas side (top) and fluid side (bottom of the figure), and the 1D thermal model for the tube bundle (middle). The exchange of thermal power is modeled with so-called 1D thermal ports (in orange in the figure). The counter-current model establishes the topological correspondence between the control volumes on the tube walls, and the control volumes on the gas flow model. The tube metal wall of the boiler is modeled by a 1D dynamic heat balance equation, discretized by finite volumes. The flow models contain one-dimensional dynamic mass and energy balance equations, discretized by the finite volume method, assuming a uniform pressure distribution. The relatively small friction losses are lumped in an external component. The pressure drops in off-design conditions are estimated assuming a quadratic dependency with the volumetric flow rate (as previously shown in eq. (3.6)). The thermal resistance in the radial direction and thermal diffusion in the axial direction are neglected due to the relatively small contribution, as described by Casella et al. [59]. The heat transfer coefficient between

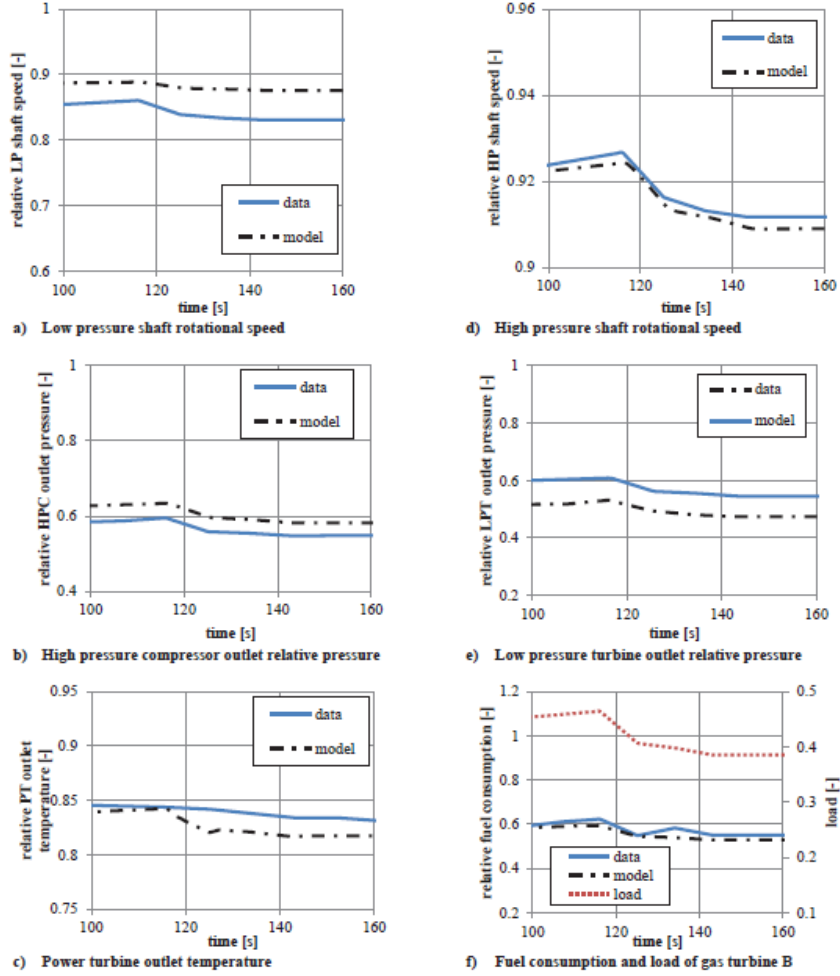


Fig. 3.2: Comparison between the model and the operational data as shown in [67]. The numbers in the y-axis are relative to the values at the design point.

the gas and the outer pipe surface is much lower than the one between the inner pipe surface and the ORC working fluid. Therefore, the overall heat transfer is essentially dependent on the flue gas side only. The heat transfer coefficient at the interface between the flue gas and the metal wall, in off-design conditions, is evaluated with the eq. (3.9) proposed by Incropera et al. [68].

$$k = k_{T,des} \left(\frac{\dot{m}}{\dot{m}_{des}} \right)^n \quad (3.9)$$

In Equation (3.9), k represents the heat transfer coefficient, \dot{m} is the mass flow rate and the subscript des refers to the value at nominal operating conditions. The variable n , taken equal to 0.6, is the exponent of the Reynolds number in the heat transfer correlation. The thermal interaction between the wall and the working fluid is described by specifying a sufficiently high constant heat transfer coefficient.

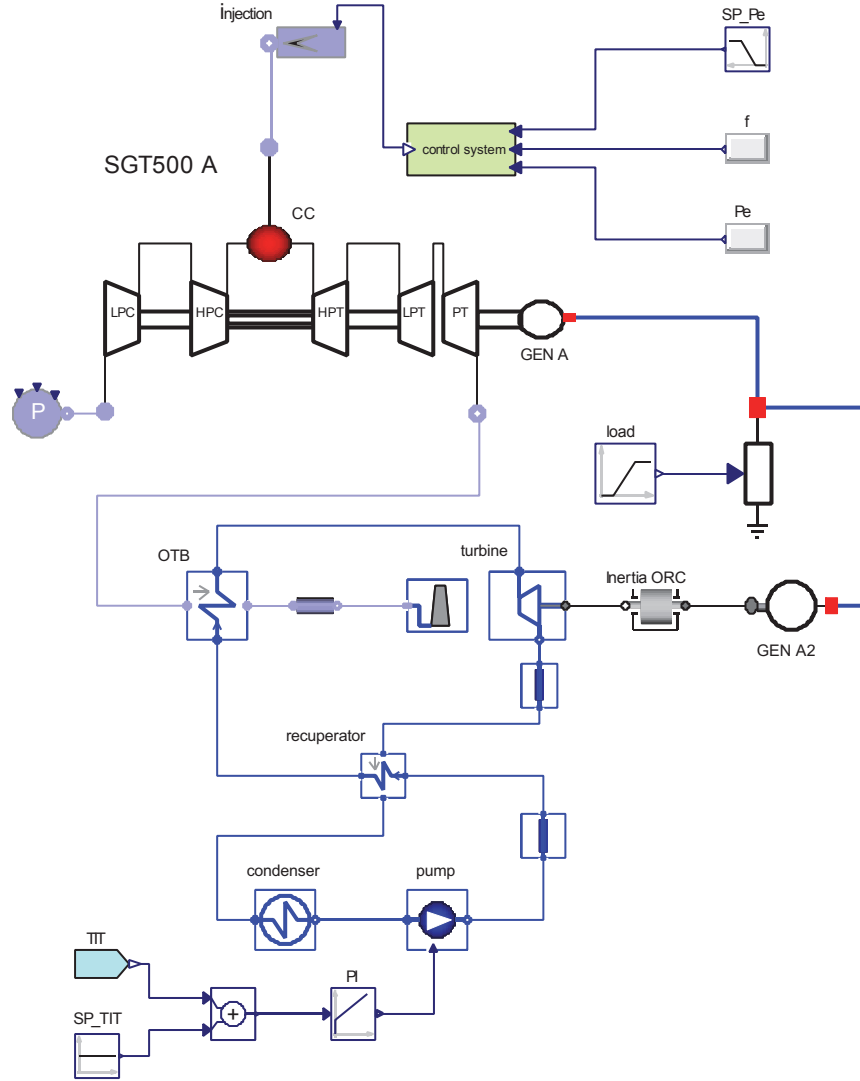


Fig. 3.3: Object diagram of the combined cycle unit.

The ORC turbine is modeled as an equivalent choked de Laval nozzle. The throat flow passage area is the sum of the throat areas of the nozzles that constitute the first stator row. An isentropic expansion is assumed from the inlet section to the throat, where sonic conditions are attained. The corresponding system of equations is listed below.

$$\begin{cases} s_{\text{in}} = s(p_{T,\text{in}}, T_{T,\text{in}}) \\ h_{S,\text{th}} = h_{T,\text{in}}(p_{T,\text{in}}, T_{T,\text{in}}) - \frac{1}{2} \cdot c(h_{S,\text{th}}, s_{\text{in}})^2 \\ \dot{m} = \rho_{S,\text{th}}(h_{S,\text{th}}, s_{\text{in}}) \cdot c(h_{S,\text{th}}, s_{\text{in}}) \cdot A_{\text{th}} , \end{cases} \quad (3.10)$$

where s_{in} is the specific entropy at the turbine inlet; the subscripts “S,th” and “T,in” indicate static conditions in the throat section and total conditions in the expander inlet section (i.e. total inlet pressure $p_{T,\text{in}}$ and total temperature $T_{T,\text{in}}$), respectively.

The specific enthalpy and the speed of sound are named h and c . The variables \dot{m} , ρ and A_{th} are the mass flow rate through the nozzle, the density and the flow passage area. The throat passage area is a fixed parameter obtained from the design calculation. Equation eq. (3.10) relates to the mass flow rate and the turbine inlet conditions at part-load. The off-design isentropic efficiency is predicted with the correlation proposed by Schobeiri [64] (see eq. (3.2)).

The recuperator is modeled by the counter-current connection of 1D ThermoPower modules, as the once-through boiler (see Figure 3.4). The heat transfer on the vapor side dominates. Therefore, the overall heat transfer coefficient is taken equal to that at the interface between the organic vapor and the metal wall. The overall heat transfer in off-design conditions and the pressure drops are modeled as for the OTB.

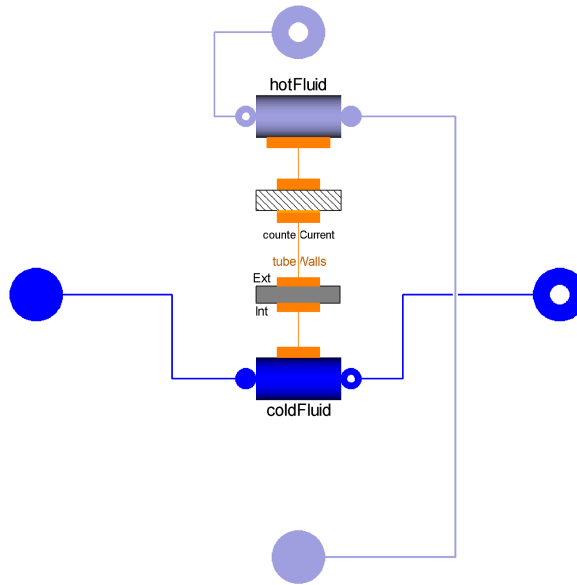


Fig. 3.4: Modelica object diagram of the once-through heat exchanger model.

The condenser is modeled as a fixed pressure component. This assumption is justified considering the large availability of sea-water. The cooling circuit can thus be controlled in such a way that the condenser pressure is nearly constant. For simplicity, the condensate is assumed to leave the component in saturated conditions (no subcooling) with no pressure losses.

The pump model is based on a head-volume flow curve derived by fitting the data of an existing centrifugal pump designed for similar volumetric flows and heads. The curve, given as a function of $\phi = \dot{m}/\rho \cdot \rho_{\text{des}}/\dot{m}_{\text{des}}$ and the rotation speed of the shaft N , is expressed as shown in eq. (3.11).

$$H = H_{\text{des}} \cdot (b_1 + b_2 e^\phi) \cdot \left(\frac{N}{N_{\text{des}}} \right)^2 \quad (3.11)$$

H is the head, $b_1 = 2.462$, and $b_2 = -0.538$. The exponential functional form is selected in order to result in a monotonic relation. This formulation increases the model robustness compared to polynomial expressions. The isentropic efficiency of the pump is expressed as a function of the coefficient $F = \phi \cdot N_{\text{des}}/N$, using the methodology proposed by Veres [69]. The off-design electric efficiency of the ORC generator is calculated similarly to the gas turbine generator (eq. (3.8)). The electro-mechanic efficiency of the pump motor is evaluated by assuming a quadratic dependency on the ratio between the actual load and its nominal value.

Figure 3.3 shows also the ORC control system, consisting of a proportional-integral (PI) controller. This component adjusts the speed of the pump to maintain the temperature at the inlet of the expander (TIT in Figure 3.3) equal to the design-point value (SP_TIT in Figure 3.3, the value is reported in Table 2.3). This strategy, currently used in ORC turbogenerators [59], ensures safe activities by tracking the hottest fluid temperature of the thermodynamic cycle.

3.3 The offshore wind farm model

Figure 3.5 reports the wind speed probability curve representative for the North Sea and available in [70]. The data are representative for the North Sea. Two wind speed scenario are considered: in the first one, a wind speed of $9 \text{ m} \cdot \text{s}^{-1}$ is chosen as average wind speed, since it has the highest probability of occurrence, as shown in Figure 3.5; while, in the second scenario, a wind speed of $15 \text{ m} \cdot \text{s}^{-1}$ is selected, because a commonly reference wind speed value. The turbulent wind is created by the IEC Turbulence Simulator in

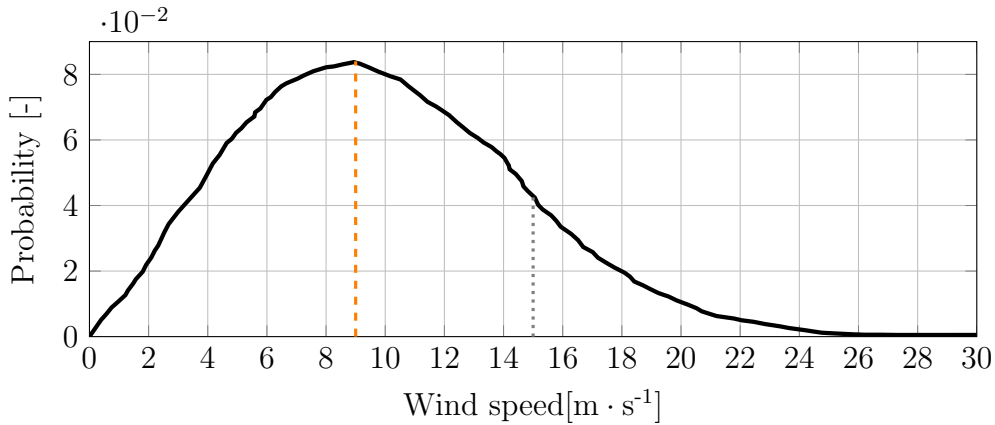
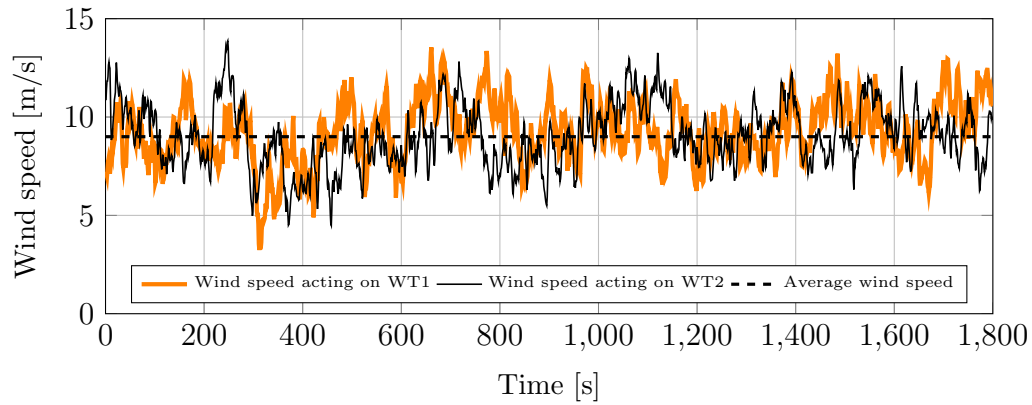


Fig. 3.5: Probability distribution of wind speed and probability of occurrence of $9 \text{ m} \cdot \text{s}^{-1}$ and $15 \text{ m} \cdot \text{s}^{-1}$ wind speed [70].

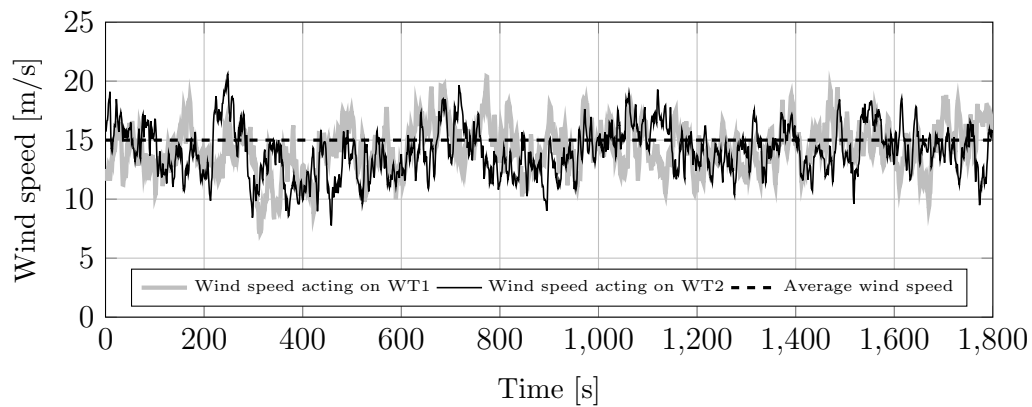
the WAsP Engineering model using the Mann model [71]. The turbulence intensity, I_t , is calculated using the normal turbulence model [72], as presented in eq. (3.12).

$$I_t = \frac{I_{\text{ref}}(0.75 \cdot V + 5.6[\text{m/s}])}{V} \quad (3.12)$$

V represents the wind speed velocity in $\text{m}\cdot\text{s}^{-1}$ and $I_{\text{ref}} = 0.14$ is the expected value of the turbulence intensity at a wind speed of $15 \text{ m}\cdot\text{s}^{-1}$ for medium turbulence characteristics [72]. Hence, at $9 \text{ m}\cdot\text{s}^{-1}$, I_t results equal to 0.19. The data of wind instantaneous speed acting on wind generators are obtained with the presented model for 1 h, considering a time step equal to 0.02 s. These data have been processed to consider a wind farm: the data collected for the first 30 min are used to reproduce the wind speed acting on only one wind turbine, while the data collected for the remaining time are considered as the wind acting on a second wind turbine. Figures 3.6(a) and 3.6(b) report the wind profiles obtained through the described model. In particular, Figure 3.6(a) shows the wind speed acting on the mills in the first considered scenario, under an average wind speed equal to $9 \text{ m}\cdot\text{s}^{-1}$, while fig. 3.6(b) reports the profile in the second scenario under a wind characterized by an average speed of $15 \text{ m}\cdot\text{s}^{-1}$, the commonly reference speed (see Figure 3.5). In each diagram are reported two curves, represent the wind acting on two different wind turbines.



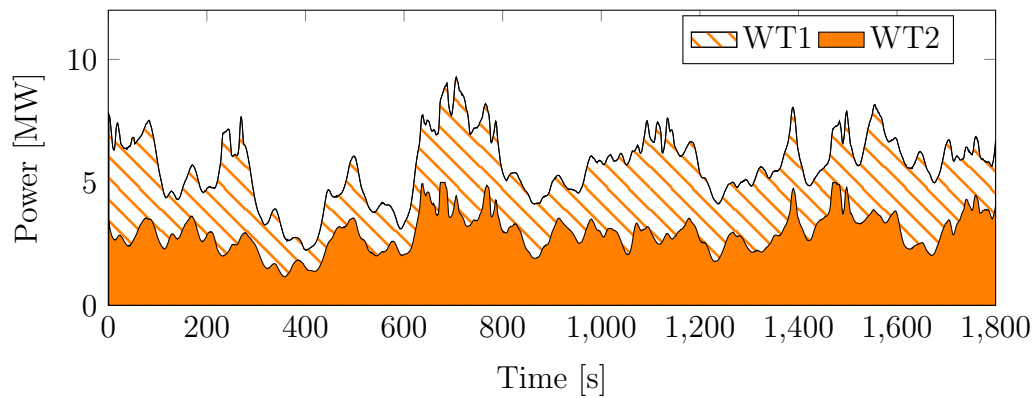
(a)



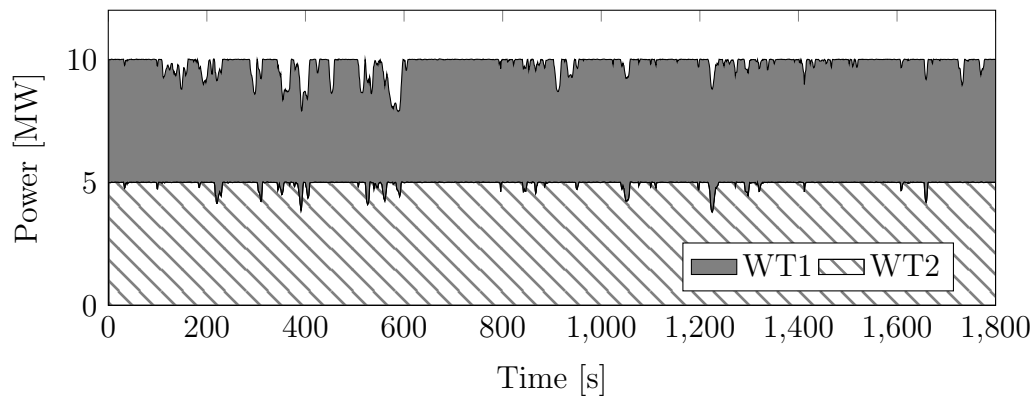
(b)

Fig. 3.6: Wind speed behavior acting on the wind mills in scenario 1 (3.6(a)) and in scenario 2 (3.6(b)).

Considering a NREL 5 MW wind turbine, the output power is calculated by the aeroelastic code Flex5 [73]. This code is widely used in the industry to model the dynamics of the wind turbine and monopile foundation. The aerodynamic loads on the blades are calculated by the unsteady Blade-Element-Momentum (BEM) method, more information are available in [70]. Under the presented wind speeds and considering two wind mills, the method described allows to obtain the power production reported in Figures 3.7(a) and 3.7(b). The figures highlight the production of each wind mill (named WT1 and WT2). In each diagram, the analyzed time range and the time step are equal to 30 min and 1 s respectively. Figure 3.7(a) shows how in the first scenario, the overall wind power production results widely intermittent: the wind power varies between 2.2 to 9.3 MW, meanwhile, in Figure 3.7(b) the wind power results more stable, ranging between 7.9 to 10 MW (Figure 3.7(b)), despite the wind speed high variability. These data of offshore wind mills has been introduced into the dynamic model of the integrated system as a time series-based model.



(a)



(b)

Fig. 3.7: Wind turbines power production power in scenario 1 (3.7(a)) and in scenario 2 (3.7(b)).

CHAPTER 4

Power system sizing: the maximum allowable wind power

Summary. This chapter presents the applied method to identify a reasonable size for the wind farm. The considered configuration consists of gas turbines, ORC systems integrated with wind mills. The loss of the total wind power installed is simulated to determine maximum frequency excursions in three different cases. The variations are compared to standard values to identify the number of wind turbines installable in the offshore wind farm. A reliability analysis of the overall system is presented in Section 4.1.

This section presents the simulation results used to identify the maximum wind power installable on-board. The selection criteria are based on the standards specified for offshore stand-alone electric grids. The electric power required by the oil and gas platform is assumed constant and equal to 30 MW. This nominal demand is reasonable for offshore facilities in the North Sea [31]. The power system on board (three combined cycle units) has a total installed capacity of 64 MW. Two combined cycle units run at a time covering 50 % of the load each. The third unit is on stand-by. Having an excess power capacity allows the platform operator to: i) minimize the risk of failure of the plant and causing a halt of oil production, and ii) cope with possible variations in the power demand during the reservoir lifetime. The platform under investigation produces gas exported via a gas pipeline to the coast and oil, which is first stored in tanks at the bottom of the sea and then exported via a shuttle tanker. This plant arrangement is commonly adopted in offshore power stations in order to enhance the system reliability and ensure the necessary reserve power for peak loads. The sudden loss of wind power is the worst possible scenario the plant has to withstand without compromising the functionality of the power system. The scenario implies that the wind turbines provide their maximum power output and the two combined cycle plants supply the remaining power until 200 s, when, in 1 s, the wind power production drops to zero. As a consequence, the GT+ORC systems have to increase the load to match the total power demand and stabilize the grid frequency. The maximum absolute frequency change has to be lower than 5 %, as imposed by the NORSOK standard [74]. This dynamic metric is thus used to identify the maximum wind power, \dot{P}_n , installable on board. The possible scenarios, visible in Figure 4.1, are:

- case 1: one wind turbine installed ($\dot{P}_n = 5$ MW),
- case 2: two wind turbines installed ($\dot{P}_n = 10$ MW),

- case 3: three wind turbines installed ($\dot{P}_n = 15 \text{ MW}$).

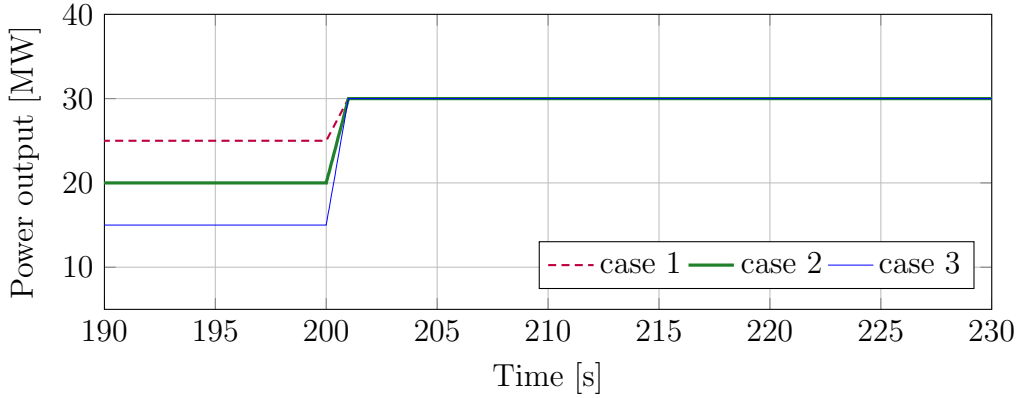


Fig. 4.1: Power plant load required variations in analyzed cases.

Figure 4.2 shows the frequency dynamics for the three test cases. The plot reports also the maximum allowable undershooting (red dotted line). All curves exhibit an undershooting, caused by the increased load demand. The minimum achieved frequency values (f_{min}) and the corresponding variations (Δf) are listed in Table 4.1.

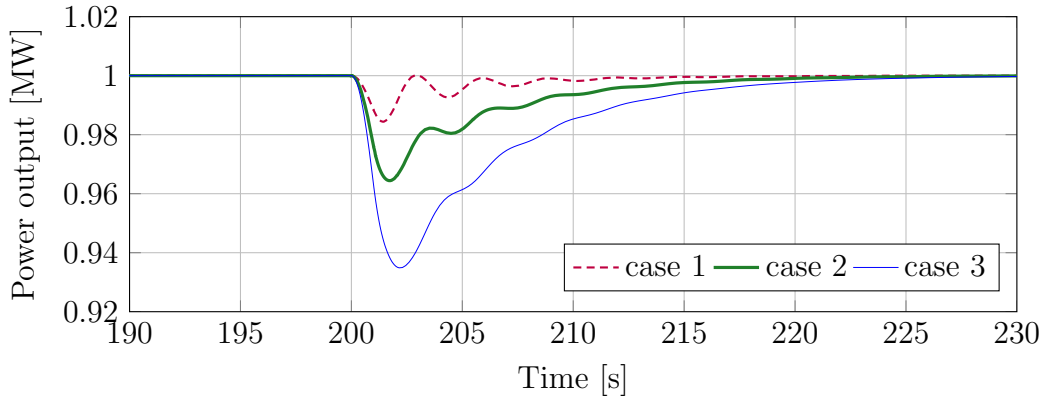


Fig. 4.2: Frequency in per unit as a function of time for the analyzed cases.

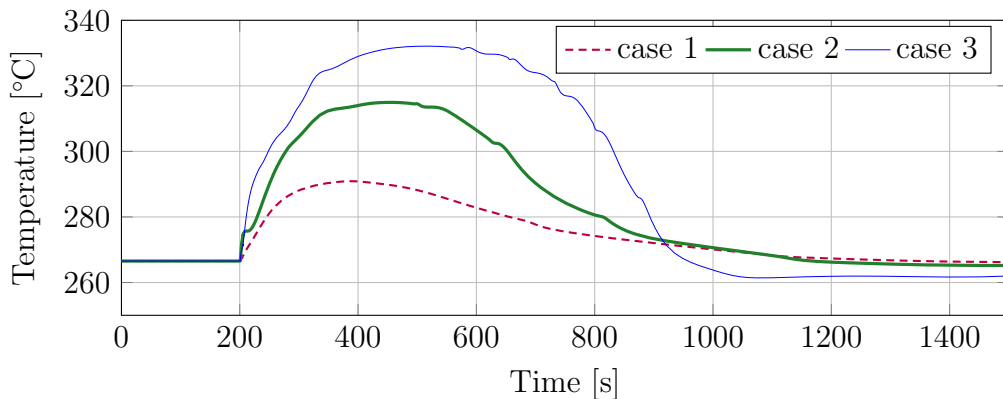
Figure 4.2 demonstrates that case 3 is not feasible as the frequency exceeds the prescribed threshold. Therefore, the integration of three wind turbines is not acceptable for the stability of the grid. The second dynamic metric used to compare the three cases is the rise time. This quantity is defined as the time required for the frequency to return back to 99% of the value at steady-state (50 Hz). Case 1 and 2 present faster responses than case 3, with a rise time equal to 2s and 8s, respectively. Case 3 presents a rise time of 11s, as visible in Figure 4.2. Two wind turbines are installable since they can supply one third of the electric load on the platform (30 MW) without compromising the stability of the electric grid. The optimal ratio strongly depends on the: i) maximum frequency tolerance, ii) control system of the gas turbine, and iii) size of the wind

Table 4.1: Frequency values and variations obtained in the studied cases.

Case	f_{min} [Hz]	Δf [%]	t_{rise} [s]
case 1	49.22	-1.56	2
case 2	48.22	-3.56	8
case 3	46.74	-6.52	11

turbine. The load required by the platform and the load condition of the gas turbines indirectly influence the control system. The results obtained in this study are generally applicable to the North Sea region given the selected grid specifications and the adopted offshore wind turbines.

Figure 4.3 shows the trend of the temperature at the inlet of the ORC expander during the loss of the wind power in the three analyzed cases. This variable is of paramount importance, being closely related to the maximum temperature reached by the ORC working fluid. Moreover, the time interval visible in Figure 4.3 is higher than the interval presented in Figures 4.1 and 4.2. The thermal quantities have high inertia and consequently their variations result slower respect to the electric quantities variations. Its thermal stability is a major concern in the design of ORC systems. The fluid decom-

**Fig. 4.3:** Maximum temperature of the organic fluid in the thermodynamic cycle as a function of time for the analyzed cases.

position can compromise the integrity and the performance of the components. The plot demonstrates that the peak value of the temperature in case 2 is equal to 314.9 °C. This is acceptable for the thermal stability of benzene. Andersen et al. [54] demonstrated that the decomposition is negligible for operating temperatures lower than 315 °C.

4.1 Plant reliability

The sizing of the wind farm following the methodology previously described allows to get an integrated system, consists of gas turbines, ORCs and two wind turbines, able

to satisfy at each time the required load. Moreover, as a result of Chapter 4, the power plant operation results independent from the wind turbines failures. In the reliability analysis the reliability of a single component $R(t)$ is defined as the probability that it does not fail in a considered time range t , assuming that it is working at the beginning of that time interval [75]. Generally, $R(t)$ can be calculated using the failure rate α , as shown in eq. (4.1) [76]. A parallel system configuration can work as long as not all components of the system fail. Conceptually, in a parallel configuration the total system reliability is higher than the reliability of any single system component. The reliability of a system placed in a parallel configuration $R(t)_{parallel}$ can be evaluated following eq. (4.2) [75], where n is the number of installed components. Meanwhile, a series system is a configuration such that, if any one of the system components fail, the entire system fails. Conceptually, a series system is one that is as weak as its weakest link [76]. The reliability of a series system $R(t)_{series}$ is evaluated based on eq. (4.3), where m is the number of components set in series. Moreover, the failure rate of the entire system is equal to the sum of the components failure rates. Meanwhile eq. (4.4) evaluates the reliability of a redundant-parallel system consist of l components, supposing a perfect switch between the different conditions [75].

$$R(t) = e^{-\alpha t} \quad (4.1)$$

$$R(t)_{parallel} = 1 - \prod_{i=1}^n (1 - R_i(t)) \quad (4.2)$$

$$R(t)_{series} = \prod_{i=1}^m R_i(t) \quad (4.3)$$

$$R(t)_{redundant-parallel} = e^{-\alpha t} \cdot \left(1 + 2\alpha t + \frac{(\alpha t)^2}{2!} + \dots + \frac{(\alpha t)^l - 1}{(l-1)!} \right) \quad (4.4)$$

While a full reliability analysis is out of the scope of this study, a few simplified considerations will be highlight in this section, following the existing literature which provides statistical information on the components failure rates. From the definition of reliability $R(t)$, the platform power plant and the wind farm could be viewed as two different systems in a reliability analysis. Indeed, as previously described, in the case of the sudden loss of wind power the platform power plant is able to withstand without compromising the functionality. An estimation of wind turbines and combined cycles reliability can be performed. The yearly failure rate α_{WT} of each wind turbine can be set equal to 2.38 (failures per year) according to Prez et al. [77], mainly related to faults in the electrical, control, sensors and hydraulic systems. This quite high value among data for wind turbines available in literature can be considered because larger wind turbines tend to fail more frequently than smaller ones [77]. The reliability of the overall wind farm in the analyzed case can be evaluated considering the wind turbines placed in a parallel configuration, because the wind farm results out of service when both the mills are broken. Thus, the wind farm yearly reliability results equal to 0.177. The platform power

plant operational configuration, shown in fig. 2.3, can be schematically considered as three series of two combined cycle (i.e. the series are combined cycle 1 and 2, combined cycle 2 and 3, combined cycle 1 and 3) set in parallel. The failure rate of each combined cycle α_{CC} is set equal the GT failure rate. The gas turbine critical failure rate per 10^6 hours is reported in literature between 460 and 1700 according to statistical data on real machines [78]. Therefore, considering a low yearly GT failure rate equal to 4.03, the reliability of two gas turbines set in series results equal to $3.16 \cdot 10^{-4}$. For the entire platform power plant the reliability is equal to 0.013 and considering a perfect switching between configuration, due to the presence of the third GT+ORC combined cycle unit maintained in stand-by. Finally, the wind farm and the combined cycle reliability values could be evaluated considering more variables, as the electrical infrastructure generally split in three subsections, e.g. export cables, inter-array cables and the offshore substation. The offshore substations are used to reduce electrical line losses and improve the overall electrical efficiency by increasing the voltage level from the collection system and then exporting the power. Moreover, they contains the necessary switching panels and other electrical facilities (e.g., power factor correction systems) [79].

CHAPTER 5

Thermodynamic analysis

Summary. *A thermodynamic analysis of the integrated power system is assessed in this chapter. The wind power scenarios previously introduced are considered and various performance indexes selected to evaluate the effects of renewable source intermittance nature. A comparison between the behavior of the integrated power system and simpler configurations are performed to identify the benefits due to the ORC installation and the exploiting of wind source.*

This chapter aims to examine the GTs, ORCs and wind power integrated system under a thermodynamic point of view. A focus on the CHP performance of the system is carried out, taking into account the dynamic behavior under variable wind condition. In particular, both the wind power scenarios, shown in Section 3.3, have been considered and compared. The wide time range allows to better observe the off-design system performance and the effect caused by wind power variations.

Figure 5.1 presents the power generation of the integrated system, consist of gas turbines, ORCs and wind mills under the two wind scenario presented in Section 3.3. The time interval analyzed is equal to 1800s, needing to appreciate the variation of the thermodynamic quantities, generally characterized by a low inertia. Considering also in this study a constant load required by the platform equal to 30 MW, the GT+ORC combined cycle in the first scenario has to satisfy a higher percentage of the overall requested load. In more detail, in scenario 1, the gas turbines satisfy the 62.40% of the load, while both ORCs and wind mills produce the 18.80% of the overall load. In scenario 2, the gas turbines satisfy the 51.30% of required load, the ORCs guarantees the 16.01% and the wind mills the 32.69%. Table 5.1 reports the maximum and minimum electric load produced by the components with the correspondent instants considering the 30 min analyzed: the GT power production, evaluated as the difference between the maximum and minimum values, varies in a power range equal to 3.33 MW and 1.1 MW respectively in scenario 1 and 2. Meanwhile, the ORC power variation is 370 W in scenario 1 and 120 W in scenario 2. Table 5.1 reports also the maximum ramp-rate values (RR) define as in eq. (5.1). It represents the maximum power production variation of each component considering a time step of 1 s. This value allows to appreciate how in scenario 2 the wind power production varies in a lower power range, but it presents steeper local variation. This profile causes higher local variations of GTs and ORC power production than in in scenario 1, as visible in Figure 5.2. Moreover, the results shown in table and the behaviors in figure allow to observe how the production peak values of the integrated system components do not appear related each other, due

to the inertia and the control strategy described in Section 3.1.

$$RR = \frac{dP}{dt} \quad (5.1)$$

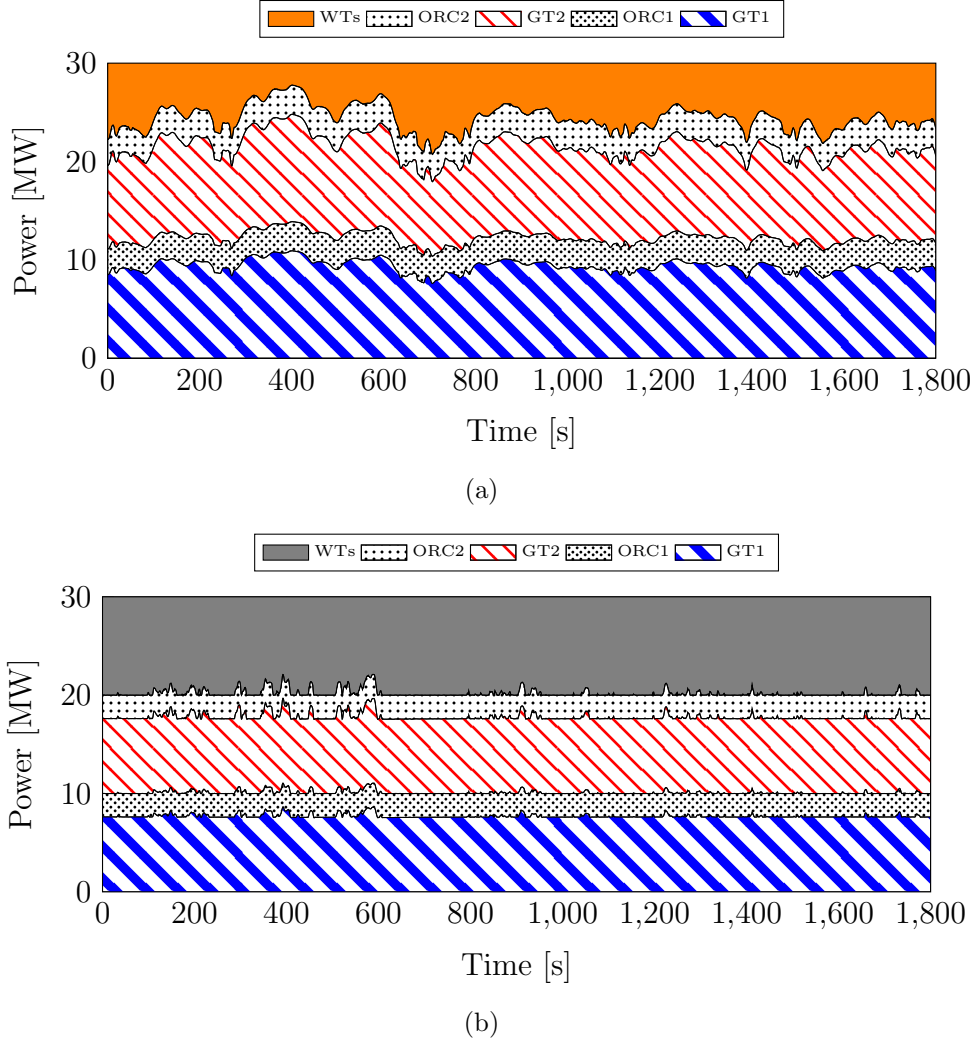


Fig. 5.1: Power of the electric generators connected to the grid as a function of time in scenario 1 (5.1(a)) and in scenario 2 (5.1(b)).

Several thermodynamic parameters are reported in the following figures to identify the effects of the wind power intermittance on the ORC behavior. Figure 5.3 shows the temperature variations of the GT exhaust gas and the gas temperature at the OTB outlet, i.e. after the waste heat recovery. More in details, the figure reports the difference between the punctual data and the start values. These data allow to compare and examine the variations. In scenario 1, the GT exhaust gas temperature start value results

Table 5.1: Wind, GT and ORC electric maximum and minimum power production and ramp rate.

	scenario 1	value	instant	RR
WIND	Maximum	9.28 MW	606 s	0.44 MW s ⁻¹
	Minimum	2.24 MW	302 s	
GT	Maximum	10.92 MW	401 s	0.23 MW s ⁻¹
	Minimum	7.59 MW	706 s	
ORC	Maximum	2.99 MW	433 s	0.03 MW s ⁻¹
	Minimum	2.62 MW	82 s	
	scenario 2	value	instant	
WIND	Maximum	10 MW	488 s	0.78 MW s ⁻¹
	Minimum	7.88 MW	572 s	
GT	Maximum	8.64 MW	392 s	0.36 MW s ⁻¹
	Minimum	7.54 MW	460 s	
ORC	Maximum	2.47 MW	603 s	0.07 MW s ⁻¹
	Minimum	2.35 MW	1413 s	

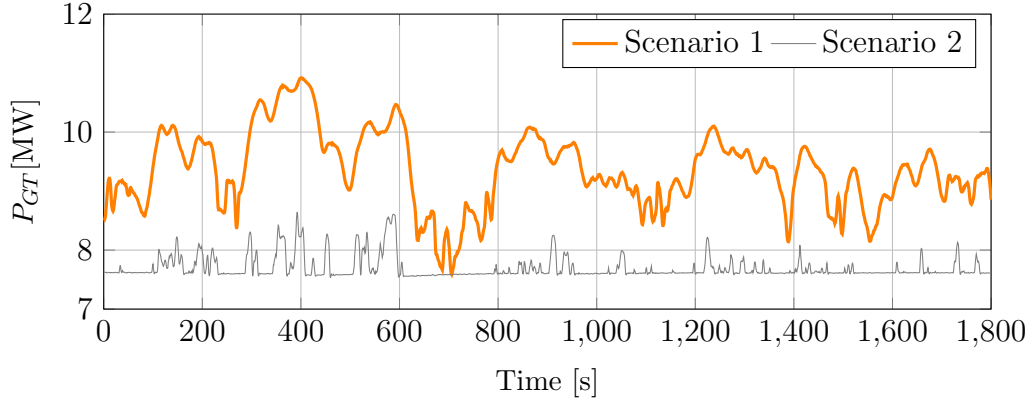
equal to 320.1 °C, while in scenario 2 it is equal to 312.1 °C. The comparison between Figure 5.3(a) and Figure 5.3(b) allows to appreciate how the temperature variations after the waste heat recovery through the OTB results less intermittent, highlighting the heat exchanger inertia. For instance, the OTB exhaust gas temperature variation between 700s and 900s in scenario 1, is caused by the GT exhaust gas drop at 700s. The delay is related to OTB dynamic model described in Section 3.2, that considers the delay caused by the wall and the heat stored in heat exchanger volume, used to produce the steam. Figure 5.4 presents the comparison between the thermal power evaluated at the gas turbine side as shown in eq. (5.2) and at the ORC side as shown in eq. (5.3). The behavior of the thermal power in the considered scenarios is affected by the wind power variations.

$$Q_{GAS} = \dot{m}_{GAS} \cdot c_{p,GAS} \cdot (T_{OTB,in} - T_{OTB,out}) \quad (5.2)$$

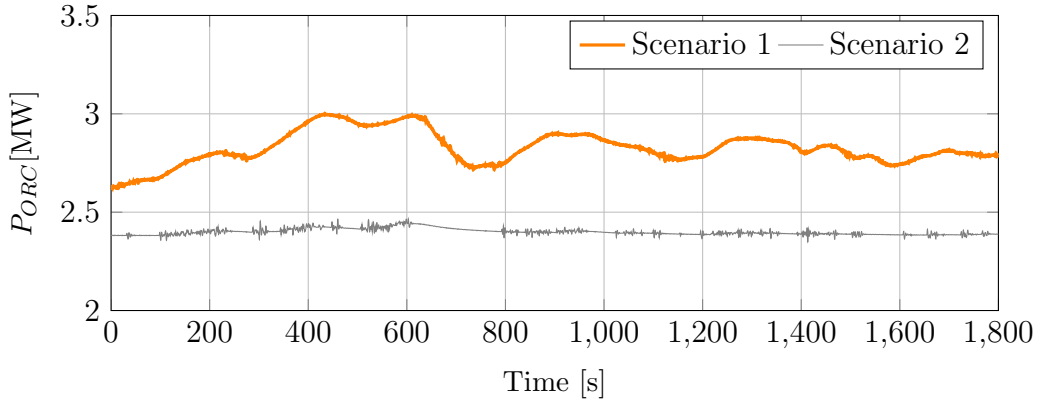
$$Q_{ORC} = \dot{m}_{ORC} (h_{OTB,out_{ORC}} - h_{OTB,in_{ORC}}) \quad (5.3)$$

where \dot{m}_{GAS} is the exhaust gas mass flow rate, $c_{p,GAS}$ is the gas specific heat capacity at constant pressure, $T_{OTB,in}$ and $T_{OTB,out}$ the gas temperatures at the inlet and outlet of the OTC heat exchanger. Meanwhile in Equation (5.3), \dot{m}_{ORC} represents the organic working fluid mass flow rate, $h_{OTB,out_{ORC}}$ and $h_{OTB,in_{ORC}}$ the enthalpy values of the ORC fluid at the OTB.

Due to the high temperatures of the exhaust gas at the OTB outlet, a primary evaluation on the discharged heat could be done through the Q_{ava} parameter. It is calculated as shown in eq. (5.4) and it represents the thermal power that could be ideally extracted



(a)



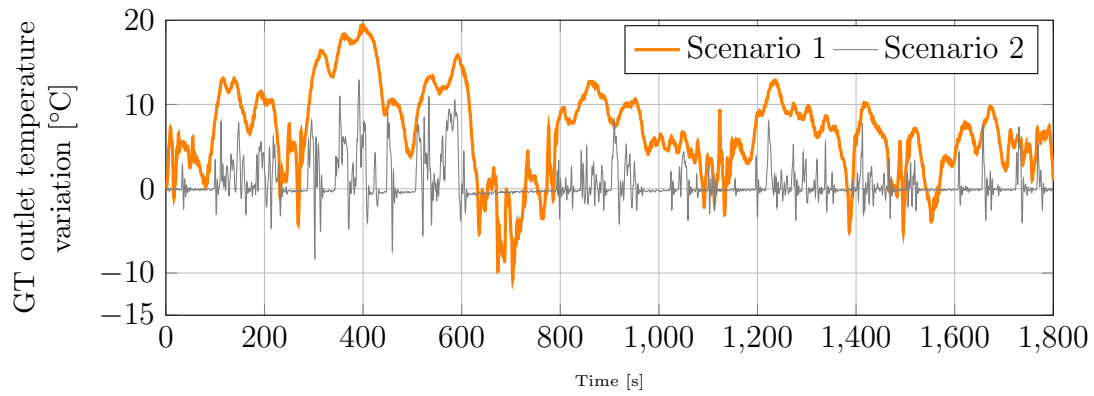
(b)

Fig. 5.2: Gas turbine 5.2(a) and ORC 5.2(b) power production variations in the considered scenarios.

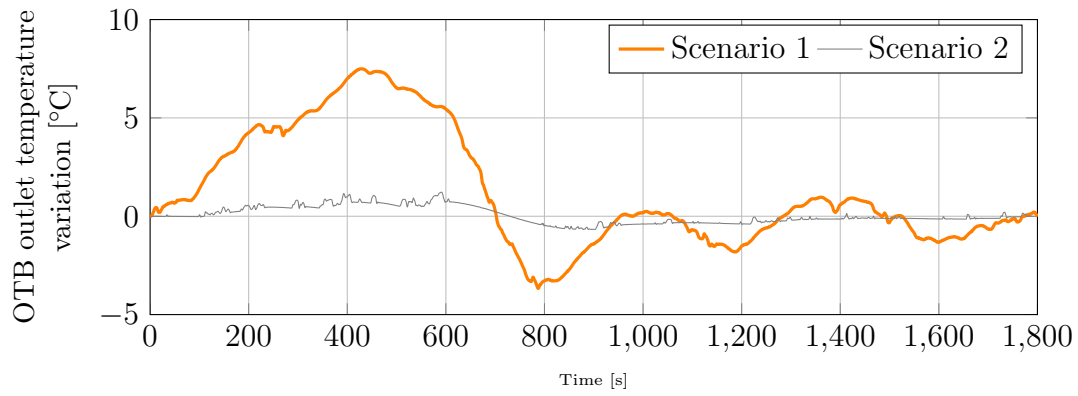
from the OTB exhaust gas in each instant, cooling down the gas to the ambient temperature (set equal to 15 °C). Figure 5.5 shows how in scenario 1 the exhaust gas still contains a sufficiently high waste heat available for cogenerative applications.

$$Q_{ava} = \dot{m}_{GAS} \cdot c_{p,GAS} \cdot (T_{OTB,out} - T_{amb}) \quad (5.4)$$

Figures 5.6 and 5.7 show the behaviors of the ORC parameters related to the control system, which adjusts the speed of the pump to maintain the maximum temperature equal to the design-point value (set equal to 266.54 °C). In particular, the examined parameters are: (i) the variations of the ORC maximum temperature, i.e. the ORC expander inlet temperature; (ii) the working fluid mass flow; (iii) the pump rotational speed and (iv) the ORC maximum pressure deviations respect to the start value. Figure 5.6(a) shows how the temperature value swings around the design value in both cases due to the control system action. Consequently, the ORC mass flow rate and the ORC maximum pressure vary. Finally, the ORC main parameters behaviors are not

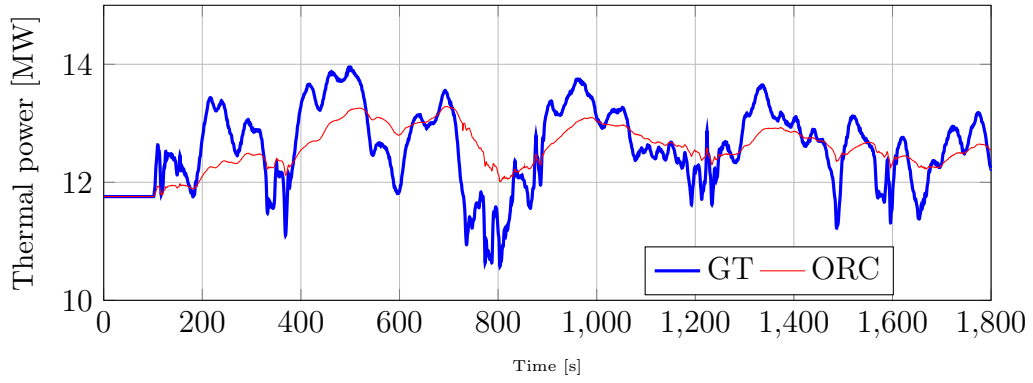


(a)

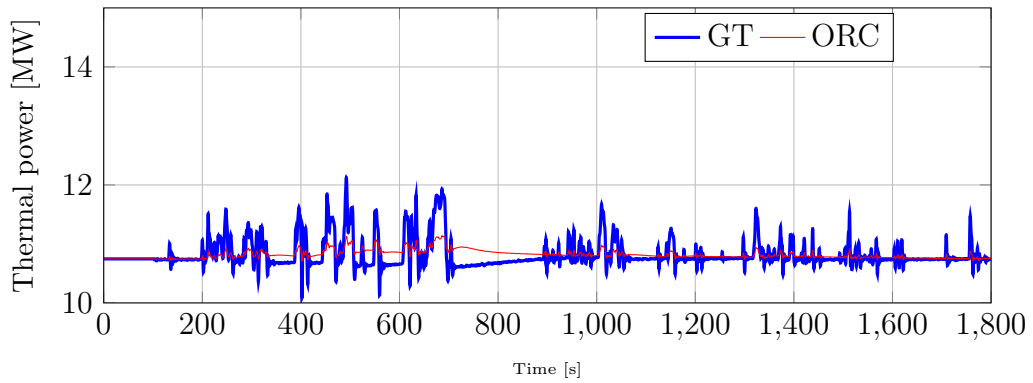


(b)

Fig. 5.3: Gas turbine exhaust gas 5.3(a) and OTB outlet temperature variation 5.3(b).



(a)



(b)

Fig. 5.4: Thermal power exchanged at the OTB evaluated at ORC and GT side in scenario 1 (5.4(a)) and scenario 2 (5.4(b)).

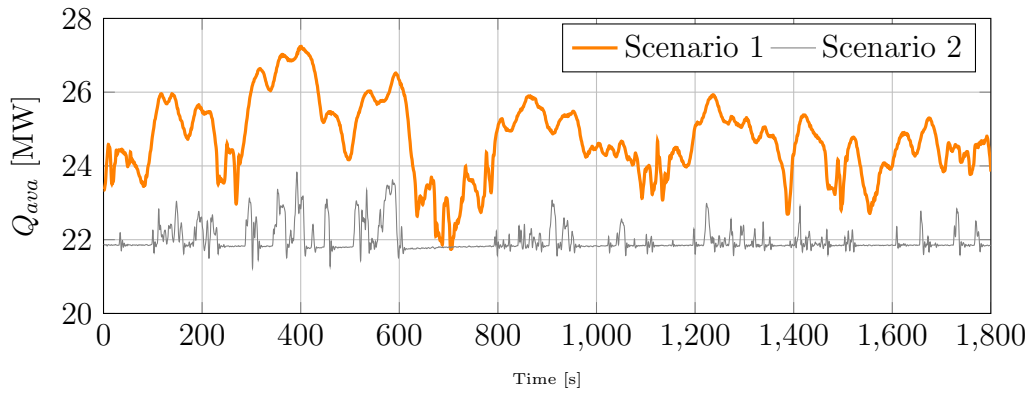
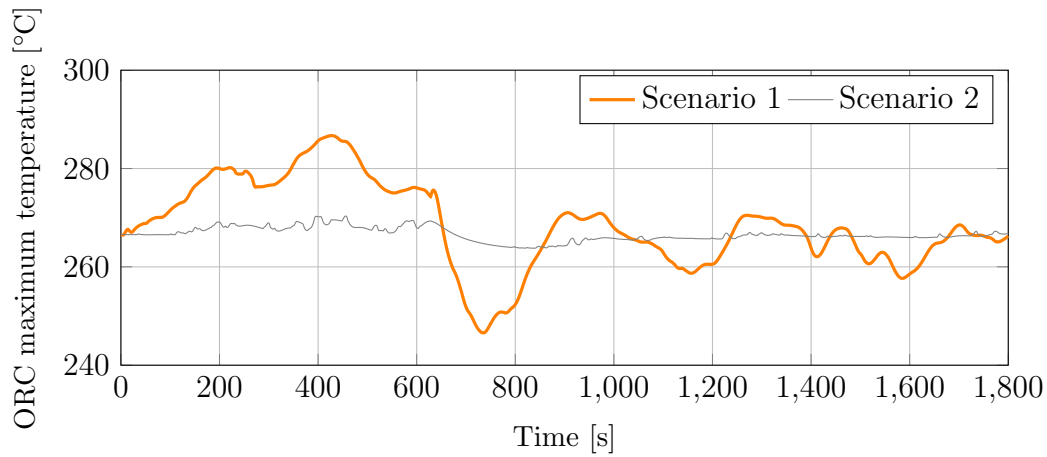
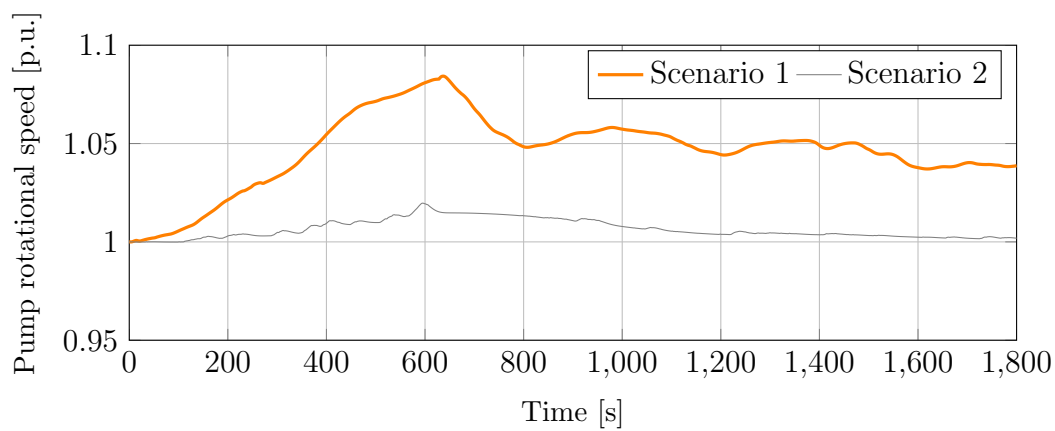


Fig. 5.5: Thermal power available after the recovery, cooling down the gas to the ambient temperature.

significantly related with the gas turbine outlet temperature variations (fig. 5.3(a)).



(a)



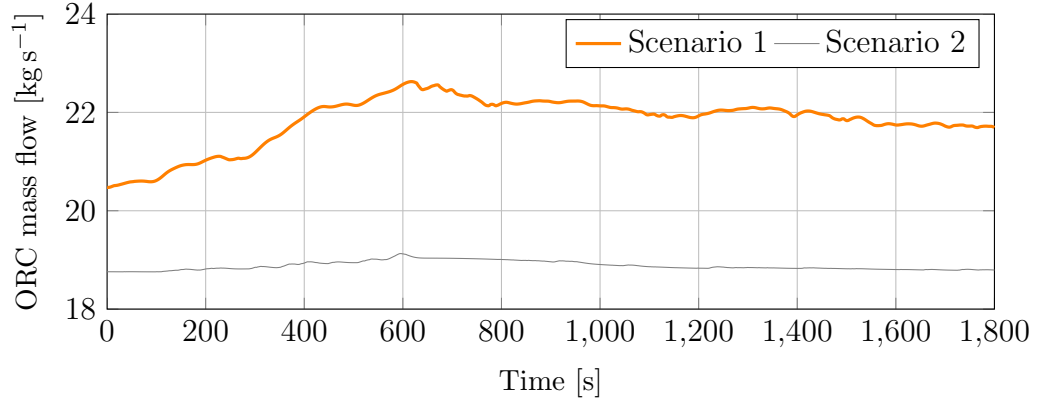
(b)

Fig. 5.6: Dynamics of the ORC unit main parameters: 5.6(a) maximum temperature and 5.6(b) pump rotational speed.

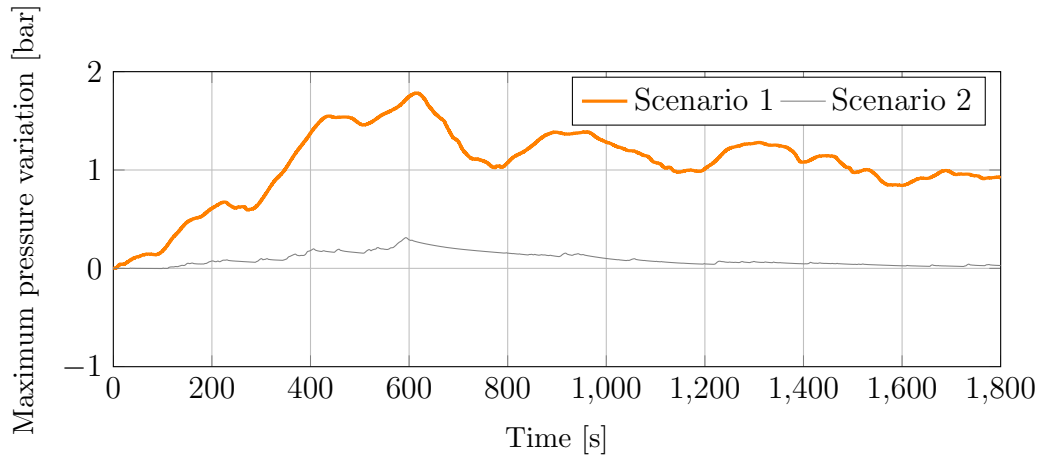
5.1 Integrated system thermodynamic performance

The performance of the entire WIND+GT+ORC integrated system are evaluated in this section under the wind scenarios previously introduced. The indexes used to define the performance are described in [51] and briefly listed below:

Specific power recovery (λ) represents the ratio between the electric power output recovered in the bottoming ORC system (P_{ORC}) and the GT electric power output (P_{GT}), as shown in eq. (5.5). In particular, P_{ORC} represents the net power available at the ORC electric generator after taking into account the auxiliary power required by



(a)



(b)

Fig. 5.7: Dynamics of the ORC unit main parameters: 5.7(a) working fluid mass flow and 5.7(b) maximum pressure.

the pump in the bottoming cycle.

$$\lambda = \frac{P_{ORC}}{P_{GT}} \quad (5.5)$$

Equation (5.6) introduces the **Heat Rate (HR)**, commonly defined as the ratio between the chemical power introduced into the combustion chamber with the fuel and the electric power produce by the GT+ORC combined cycle. This parameter gives indirectly information about fuel consumption and pollutant emissions variations under the considered wind profiles.

$$HR = \frac{F}{P_{GT} + P_{ORC}} \quad (5.6)$$

ORC electric efficiency (η_{el_ORC}) is the ratio between the ORC electric power output and the thermal power recovered from the exhaust gas (Q_{rec}), as shown in eq. (5.7).

$$\eta_{el_ORC} = \frac{P_{ORC}}{Q_{rec}} \quad (5.7)$$

Combined cycle electric efficiency (η_{el_GT+ORC}) is defined as the ratio between the gas turbine and ORC electric power output and the chemical power introduced as fuel into the GT combustion chamber (indicated as F in eq. (5.8)).

$$\eta_{el_GT+ORC} = \frac{P_{GT} + P_{ORC}}{F} \quad (5.8)$$

Figures 5.8 and 5.9 present the instantaneous behaviors of the listed parameters in the considered scenarios. The λ values (Figure 5.8(a)) are ranging between 26.12% and 35.91%, with an average value equal to 29.65% in scenario 1, while between 27.21% and 32.05% under the wind scenario 2, with an average value of 30.54%. Figure 5.8(b) shows the GT+ORC combined cycle heat rate progress in the analyzed period under the considered wind scenario: in scenario 2 the combined cycle HR results higher than in scenario 1, due to the strong wind power contribution. Meanwhile, the η_{el_ORC} average value (Figure 5.8(c)) results equal to the design value (equal to 21.8% as shown in Table 2.3) in both scenarios: in the first case the efficiency ranging between 19.65% and 26.58%, while in the second case it varies between 19.42% and 23.78%. Therefore, the ORC control system allows to maintain the ORC electric performance near the name-plate value. Moreover, Figure 5.8 shows how the λ and the η_{el_ORC} values increase under a decreasing of the thermal power introduced in OTB as shown the HR behavior. In fact, it gives information about the chemical power introduced into the GT combustion chamber, but also indirectly about the discharged thermal power.

Figure 5.9 shows the combined cycle electric efficiency behavior: η_{el_GT+ORC} results lower in the second case due to the low load required to the GT+ORC system.

In the same figure the values of this parameter are compared to the efficiency of various power plant configurations, introduced in Section 2.1.1 and briefly following described:

1. *GT+ORC configuration* corresponds to the combined cycle presented in the previous chapter integrated with two wind turbines;
2. *GT configuration* consists of the integration between two wind turbines and two gas turbines (each one guarantees the 50% of the remaining load) with the same characteristics of gas turbine in the *GT+ORC configuration*. The figure reports the efficiency values of a GT under the same wind scenarios presented in figs. 3.6(a), 3.6(b), 3.7(a) and 3.7(b);
3. *GT configuration-no WIND*, the load required by the platform (equal to 30 MW) is completely satisfied by two gas turbines. Therefore, each GT produces 15 MW

and the data reported in Figure 5.9 result constant and lower than the design electric efficiency value (see Table 2.2).

Figure 5.9 shows how the ORC introduction allows to increase the electric efficiency values in comparison with simpler configurations. The *GT configuration* results less convenient than the GT+ORC configuration, due to the high fuel consumption and off-design operation.

5.2 Waste heat recovery performance

In this section, two different cogenerative solutions are compared under the described wind scenarios. More in detail, the thermal power available at the condenser and in the exhaust gas at the outlet of the OTB have been estimated as shown in eqs. (5.9) and (5.10). More in details, Q_{COND} is evaluated as the thermal power contained into the organic fluid mass flow and exchanged at the condenser, while Q_{GAS} represents the thermal power that could be extracted from the GT exhaust, if gases were cooled down to a reference low temperature (set equal to 110 °C).

Figure 5.10 reports the value referred to a GT+ORC combined cycle. The figures show the Q_{COND} and Q_{GAS} behavior in the observed 30 min under the considered wind scenarios. In each time instant the thermal power available at the condenser is higher than Q_{GAS} in both shown scenarios. This solution is more interesting than the exhaust gas heat recovery, due to the size and weight limits commonly imposed in offshore applications.

$$Q_{COND} = \dot{m}_{ORC}(h_{COND,in} - h_{COND,out}) \quad (5.9)$$

$$Q_{GAS} = \dot{m}_{GAS}(h_{OTB,out} - h_{ref}) \quad (5.10)$$

The above parameters allow to evaluate the **thermal efficiency** of the GT+ORC combined cycle in cogenerative application (η_{th_GT+ORC}). It is defined as the ratio between the whole thermal power recoverable (through the condenser and from the exhaust gas) and the fuel power input into a GT unit (see eq. (5.11)). The behavior of this parameter is reported in fig. 5.11.

$$\eta_{th_GT+ORC} = \frac{Q_{COND} + Q_{GAS}}{F} \quad (5.11)$$

Figure 5.12 presents the thermal efficiency behavior also for the other simpler configurations previously introduced. In these power plant configurations, Q_{COND} results equal to zero, due to the waste heat recovery system absence. Therefore, the thermal efficiency evaluation is based exclusively on the thermal power that could be extracted from the

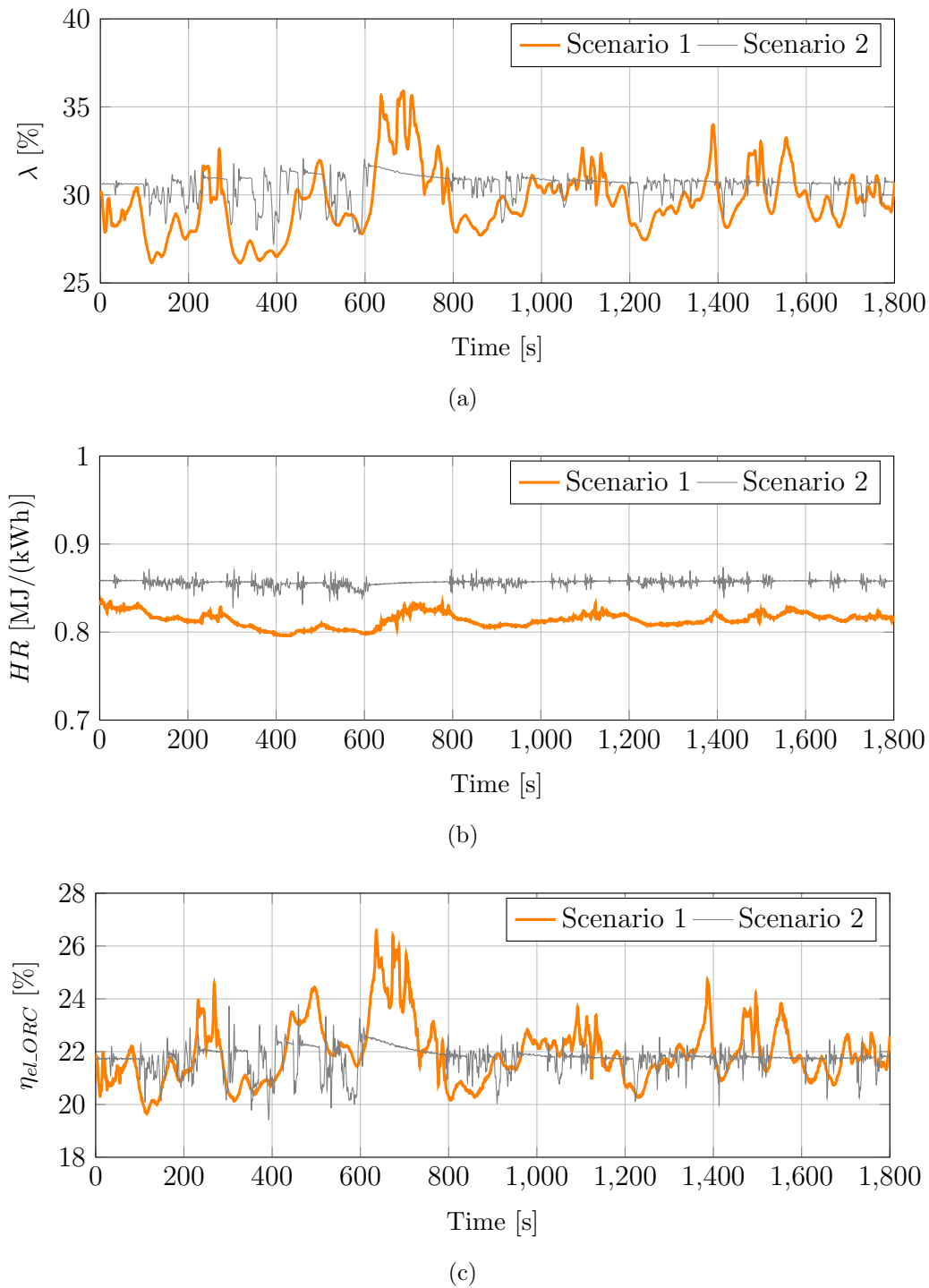


Fig. 5.8: Dynamics performances indexes: 5.8(a) lambda value, 5.8(b) integrated system equivalent heat rate and 5.8(c) ORC efficiency.

GT exhaust gas, Q_{GAS} . The comparison between Figures 5.11 and 5.12 shows how the ORC waste heat recovery system causes a decreasing of thermal performances. The GT

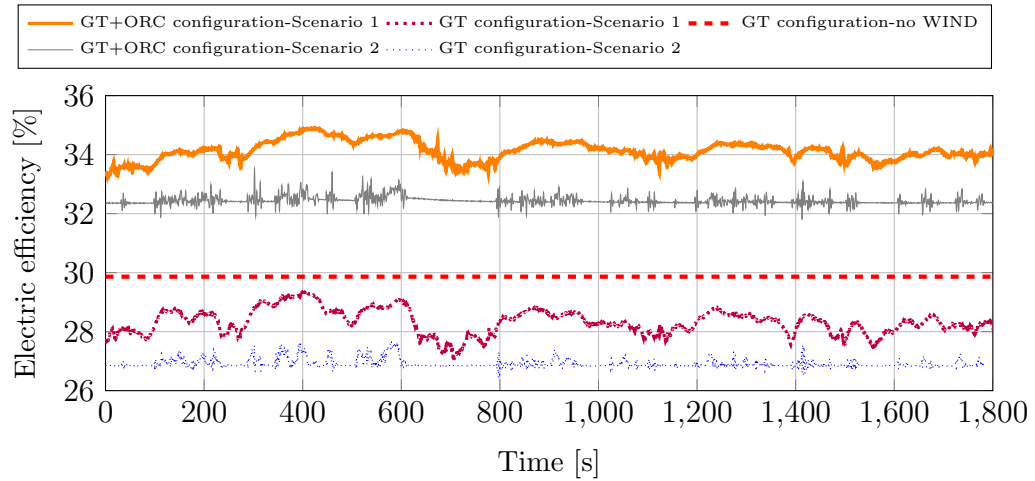
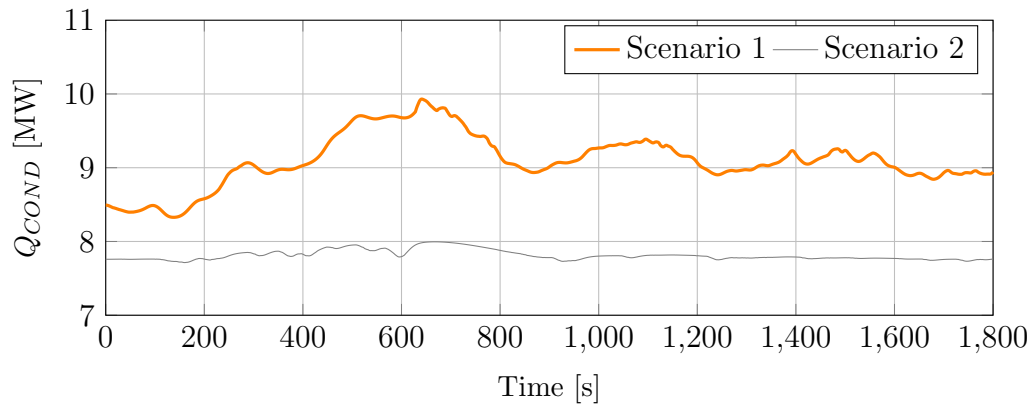
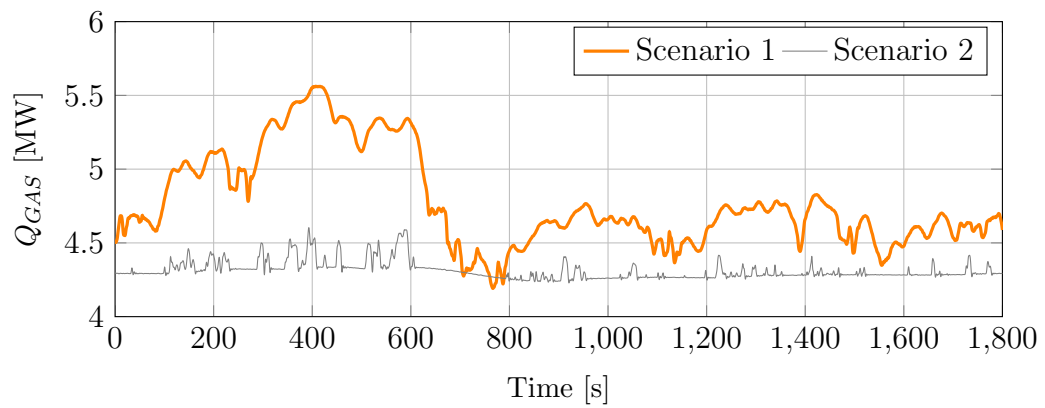


Fig. 5.9: Various configurations: electric efficiency comparison.



(a)



(b)

Fig. 5.10: Available heat in the condenser 5.10(a) and in the exhaust gas 5.10(b).

configuration, without the integration of wind source, allows to reach the highest thermal efficiency values. Meanwhile, the WIND+GT configuration presents comparable thermal performance under different wind scenarios.

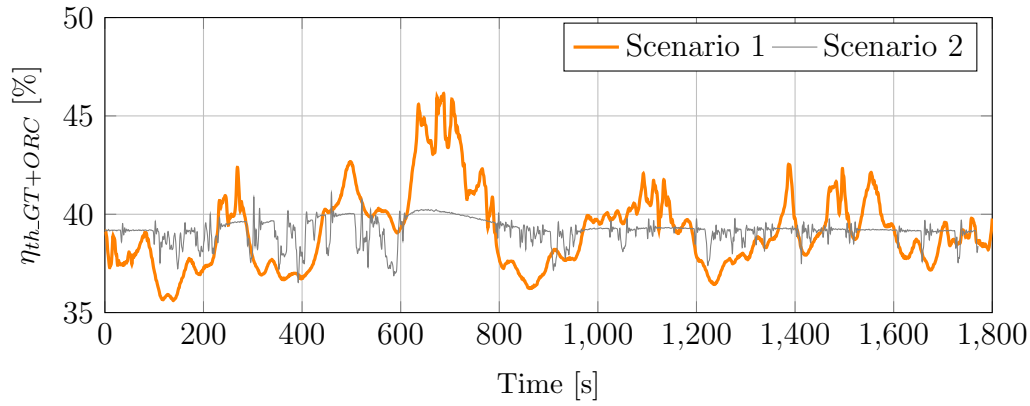


Fig. 5.11: GT+ORC combined cycle thermal efficiency.

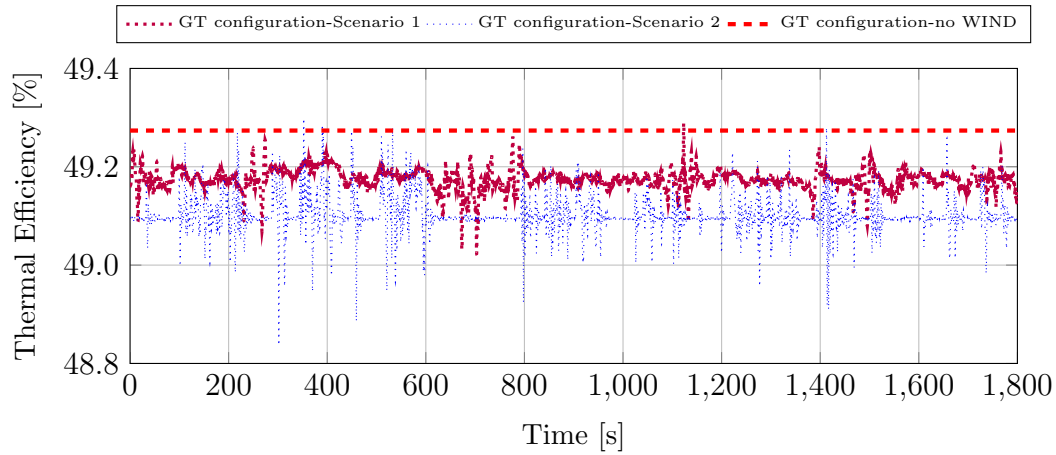


Fig. 5.12: Various configurations: thermal efficiency comparison.

The **instantaneous Primary Energy Saving** (PES_{is}) is also evaluated, as shown in eq. (5.12) [80].

$$PES_{is} = 1 - \frac{1}{\frac{\eta_{el_GT+ORC}}{\eta_{el_ref}} + \frac{\eta_{th_GT+ORC}}{\eta_{th_ref}}} \quad (5.12)$$

The PES_{is} parameter represents the instantaneous energy savings of the considered cogenerative GT+ORC combined cycle with respect to a conventional steam based combined cycle system having an electric efficiency (η_{el_ref}) equal to 52.5% and a standalone steam generator with thermal efficiency (η_{th_ref}) equal to 90% [81]. The data reported in fig. 5.13 could be compared with PES value available in literature. For instance, the PES_{is} performance in scenario 1 are comparable with the results illustrated in [51], where different configurations of GT+ORC combined cycles, using SGT-500 gas

turbine model as topper, are considered. Nevertheless, the GT+ORC combined cycle performance drops drastically under the wind scenario 2, due to the high wind power contribution. However, in both scenarios the PES_{is} results positive, demonstrating the capability of the WIND+GT+ORC integrated system to save primary energy.

In addition, fig. 5.14 presents the instantaneous PES index values in the *GT configuration* and *GT configuration-no WIND* in comparison with the *GT+ORC* base case. Figure 5.14(a) shows that the ORC presence allows to reach higher PES values under particular wind power conditions.

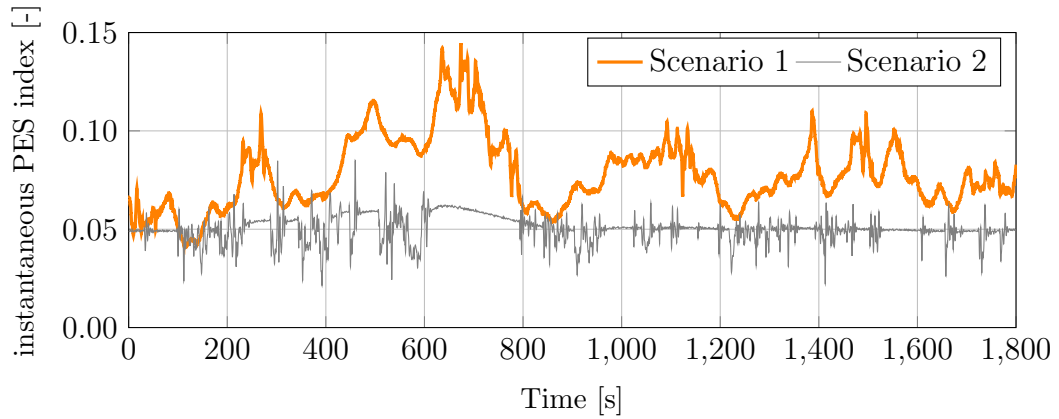
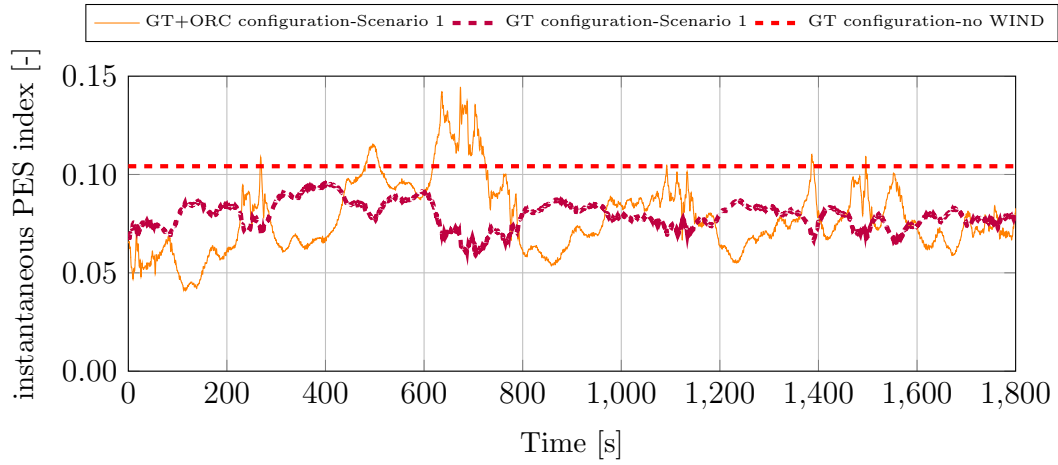
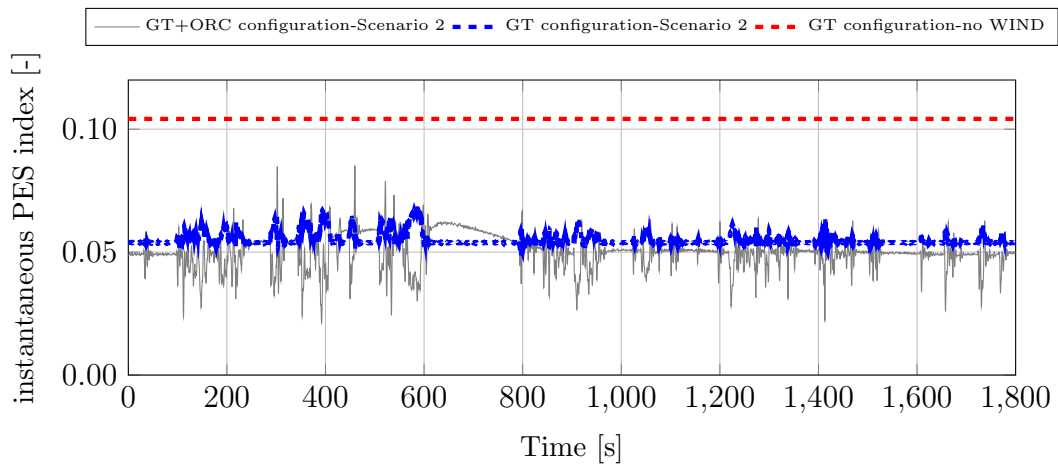


Fig. 5.13: Instantaneous PES index behavior.



(a)



(b)

Fig. 5.14: Instantaneous PES index comparison.

CHAPTER 6

Electrical, environmental and economic analysis

Summary. The electrical aspects of the integrated system, working in island mode, are investigated in this chapter. A reduce time interval of the first wind scenario is analyzed, due to the rapid behaviors of electric quantities. A comparison between a simpler configuration, consists of gas turbines and wind farm, is assessed to identify the benefits of ORCs installation. In this scenario environmental and economic evaluations are performed. The economic analysis considers both the fuel consumption and carbon dioxide emissions. The influence of the fuel price and carbon tax variations are identify through the net present value method.

6.1 Plant flexibility

This section aims to evaluate the capability of the *GT+ORC configuration* power system to rapidly adapt to an electric grid with varying production of wind power. Only 200 s of the shown wind power production profile in Section 3.3 has been considered. This time is long enough to evaluate the electrical and mechanical dynamics aspects of the analyzed integrated system. The dynamics of the power system is also assessed for the three gas turbines without waste heat recovery unit, i.e. the *GT configuration* described in Section 2.1.1. The comparison allows quantifying the impact of the ORC units on the dynamic flexibility of the system. The two plant configurations under investigation are:

- *GT+ORC configuration*: the wind farm is coupled to three combined cycle units,
- *GT configuration*: the wind farm is integrated with three gas turbines.

In both cases, two units run at the same time covering 50 % of the required power each. The third engine is back-up unit. The power demand on board is constant and equal to 30 MW in the two configurations. Figure 6.1(a) shows the power produced by the five electric generators connected to the grid (*GT+ORC configuration*). The gas turbines and the ORC modules produce 62 % and 18 % respectively of the total demand. The wind mill supplies the remaining 20 %. Figure 6.1(b) shows that the gas turbines have to cover around 80 % of the total required power as for *GT configuration*.

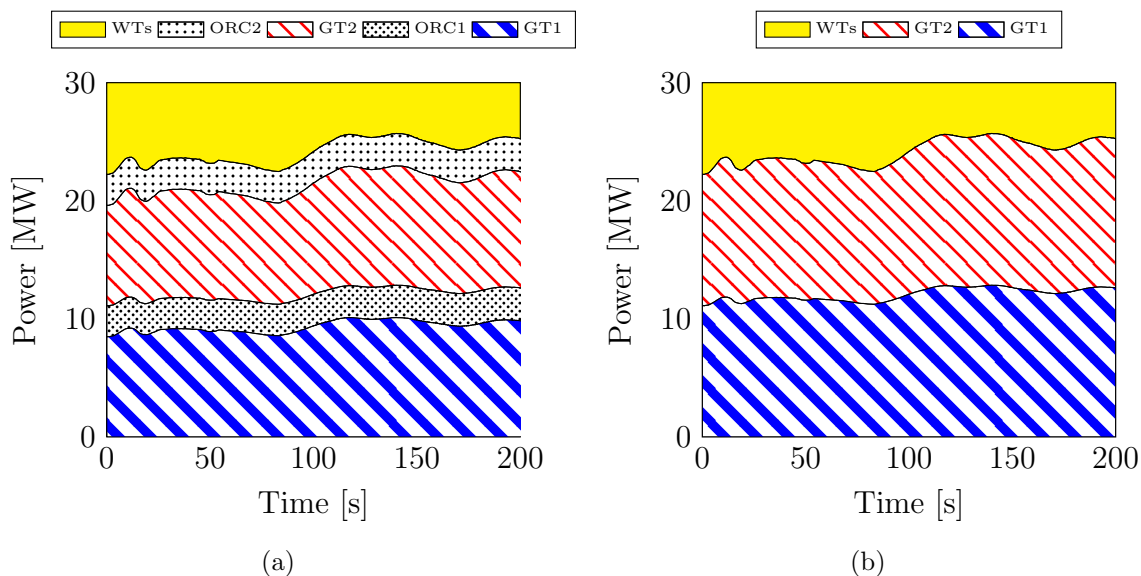


Fig. 6.1: Power of the electric generators connected to the grid as a function of time. 6.1(a): Two gas turbines, two organic Rankine cycle units and the wind mill in *GT+ORC configuration*. 6.1(b): Two gas turbines and the wind mill in *GT configuration*.

Figure 6.2 shows the frequency trends of the two configurations as a function of time. The presence of the organic Rankine cycle units reduces the small frequency oscillations compared to the use of two gas turbines alone. On the other hand, the maximum frequency variations are higher in case of ORCs installation.

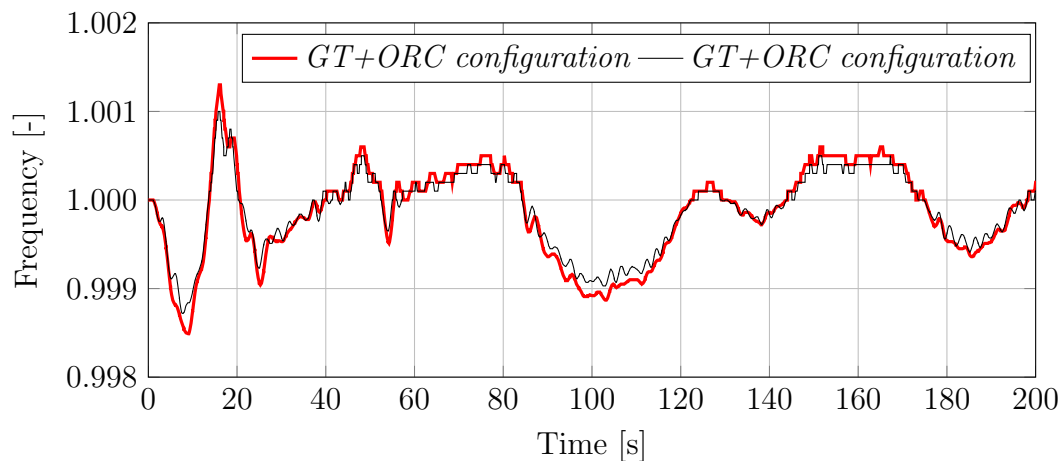


Fig. 6.2: Frequency in per unit as a function of time. In *GT+ORC configuration*, the gas turbines, the organic Rankine cycle units and the wind mill supply the electric grid. Conversely, *GT configuration* entails the use of the gas turbines and the wind mill.

Meanwhile, Figure 6.3 reports the mechanical power produced by the topping and bottoming units, i.e. $\dot{P}_{m,GT-(GT+ORC)}$ and $\dot{P}_{m,ORC-(GT+ORC)}$, considering *GT+ORC configuration*, and the mechanical power produced by the gas turbine, i.e. $\dot{P}_{m,GT-(GT)}$, considering *GT configuration*. The reported data refer to one combined cycle unit in *GT+ORC configuration* and to one gas turbine in *GT configuration*.

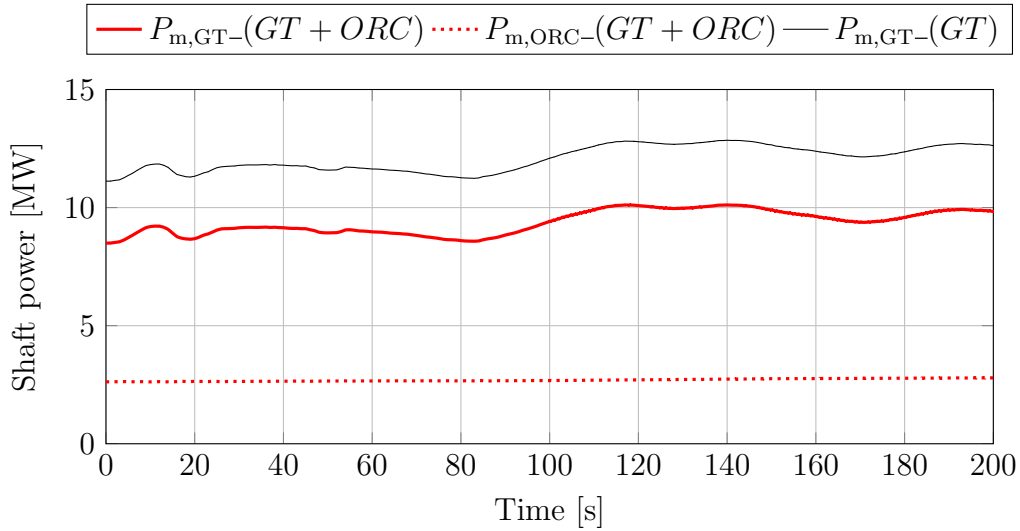


Fig. 6.3: Gas turbine and organic Rankine cycle mechanical power in *GT+ORC configuration* and gas turbine mechanical power in *GT configuration* as a function of time.

The plot pinpoints that the fluctuations of wind power do not influence the power produced by the ORC turbine. The maximum $\dot{P}_{m,ORC-(GT+ORC)}$ variation is lower than 0.2 MW considering all the time interval of 200 s. This trend is due to the inertia of the heat transfer equipment included in the ORC turbogenerator. The GTs are thus responsible for satisfying the load demand and cope with the wind power variability. Figure 6.4 shows the variation of the mechanical power produced by the gas turbines with respect to the steady-state value for configuration *GT+ORC* and *GT*.

In Figure 6.4, the area under the red and black curves is equal to 176 MJ and 191 MJ. These values are related with the kinetic energy stored into the rotating masses. The use of the ORC units enables reducing the variation of the mechanical power produced by the gas turbines, but it reduces the kinetic energy stored in the system. This smooths the dynamics of the fuel valve and reduces the smallest oscillations of the frequency. Note that the manufacturer designed the control system for the operations of the sole gas turbines. The implementation of the ORC turbogenerators may require a further tuning of the controller, thus improving the system dynamics. Moreover, the reliability of the system in *configuration GT+ORC* could be a problem with respect to the system in *configuration GT*, due its more complexity.

All the presented results suggest that the ORC systems enable decreasing the amplitude of the valve regulation. For the given load change, the response of gas turbines in

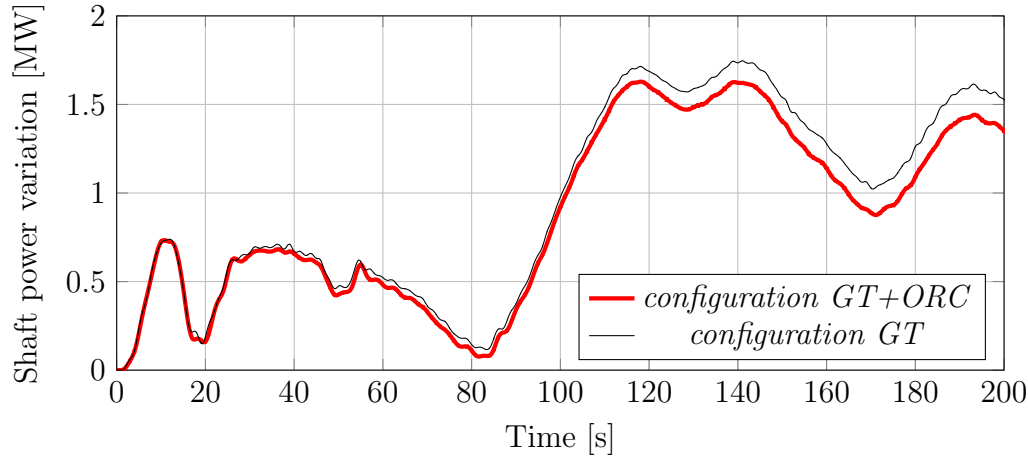


Fig. 6.4: Variation of the mechanical power supplied by one gas turbine with respect to the steady-state value for *configuration GT+ORC* and *GT*.

configuration GT is quicker than in *configuration GT+ORC*. Therefore, the integrated system in configuration A is less capable to follow the wind fluctuations compared to the plant in *configuration GT*.

6.2 Fuel savings and emission reduction

Figure 6.5 shows the fuel consumption and the actual CO₂ emissions of the two power systems (*configuration GT+ORC* and *configuration GT*). The CO₂ emissions are calculated according to [58], assuming perfect combustion and no heat losses to the environment. The difference between two configurations demonstrates that the implementation of the waste heat recovery systems can reduce the fuel consumption and CO₂ emissions by more than 15%. Namely, the use of ORC units (*configuration GT+ORC*) enables the saving of more than 60 kg of fuel and more than 160 kg of CO₂ in a time period of 200 s.

An economic assessment is possible based on the fuel and CO₂ savings. The economic evaluation is based on the Net Present Value (NPV) method. The NPV is calculated considering the equipment lifespan n , the interest factor q , the total investment cost I_{TOT} and the annual income R_i . Moreover, M_a in eq. (6.1) is a non-dimensional factor that accounts for operating and maintenance costs.

$$NPV = \sum_{i=1}^n M_a \frac{R_i}{(1+q)^i} - I_{TOT} \quad (6.1)$$

The major sources of annual incomes are associated with the fuel savings and with the avoided CO₂ taxes, respectively named R_{ng} and R_{CO_2} , evaluated as

$$R_{ng} = c_{ng} v_{st} \Delta \dot{m}_{ng} h_u, \quad (6.2)$$

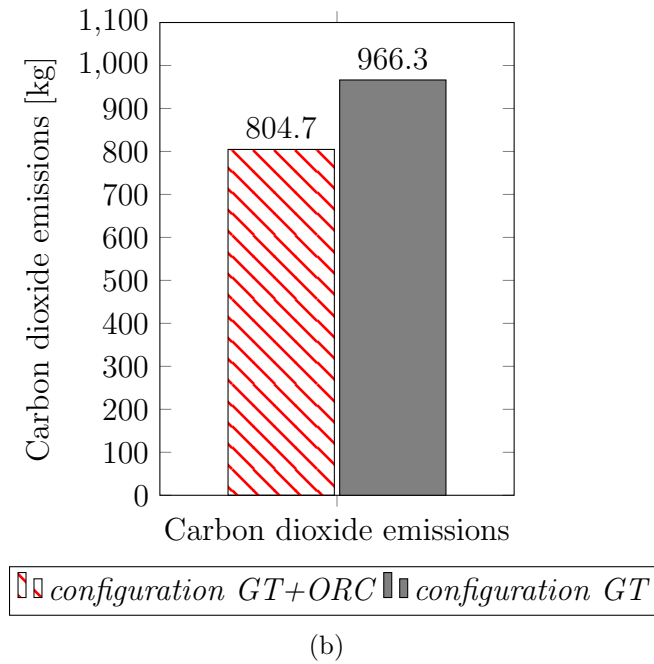
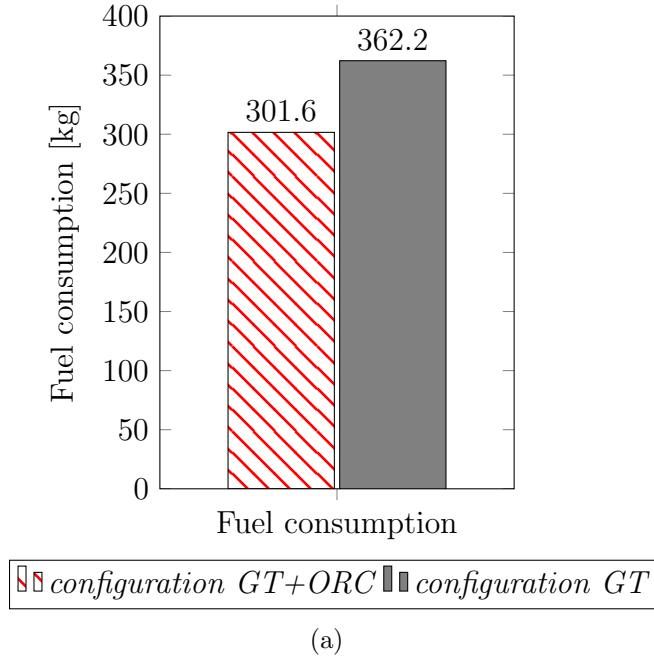


Fig. 6.5: Fuel savings (6.5(a)) and carbon dioxide emissions (6.5(b)) of the gas turbines, the organic Rankine cycle units and the wind mill (*configuration GT+ORC*) and for the gas turbines and the wind mill (*configuration GT*).

$$R_{CO_2} = c_{CO_2} \Delta \dot{m}_{CO_2} h_u, \quad (6.3)$$

where c_{ng} is the price of natural gas, v_{st} is the fuel specific volume calculated at 15 °C

and 1.013 bar, $\Delta\dot{m}_{ng}$ is the fuel saving and h_u represents the capacity factor in h/yr. In eq. (6.3), c_{CO_2} represents the carbon dioxide tax and $\Delta\dot{m}_{CO_2}$ is the avoided CO₂ emission.

The NPV method is used to assess the economic feasibility of the waste heat recovery units and wind mill. Based on information provided by platform operator, reasonable figures for the discount rate and the life-time of the investment are 6% and 30 years. The operating and maintenance costs are also accounted with an appropriate coefficient (M_a in set equal 0.9). The two sources of annual incomes are associated with the fuel savings and with the avoided CO₂ taxes respect to the use of gas turbines only. A fuel price of $0.09\text{\$} \cdot \text{Sm}^{-3}$ and a carbon dioxide tax of $55.9\text{\$} \cdot \text{t}^{-1}$ [82] is assumed. The yearly demand of electricity is calculated assuming a constant duty of 30 MW and a capacity factor of 7000 hours per year. The investment cost of the wind turbines per unit of power is equal to 5\\$/W [83], while a specific price of 3\\$/W is considered for the ORC units. The evaluated NPVs are equal to 5.85 M\\$ and 3.05 M\\$ for *configuration GT+ORC* and *GT*

Figures 6.6 and 6.7 show the net present value for *configuration GT+ORC* and *GT* as a function of the fuel price and CO₂ tax. The horizontal axis reports the fuel price as a percentage of base case fuel price (100% correspond to $0.09\text{\$} \cdot \text{Sm}^{-3}$). In particular, Figure 6.7 shows the effect of CO₂ tax increase in comparison with the reference CO₂ tax value scenario, while Figure 6.6 presents the effect of the CO₂ tax decreasing. In fig. 6.7 the solid lines refer to the tax scenario in the base case (named respectively *base case-configuration GT+ORC* and *base case-configuration GT*). The dotted and dashed lines refer respectively to a no-tax scenario and to a 50% tax scenario for the considered configurations. Similarly, the solid lines in fig. 6.6 refer to the base case tax scenario, while the dotted and dashed lines present respectively the results of an increase of the 50% and of the 100% of the CO₂ tax. The plots show how *configuration GT+ORC* becomes more convenient with respect to *configuration GT* when the fuel cost increases. However, in a no-tax scenario or in the case of a low fuel price, *configuration GT* is more attractive, due to the high investment cost of the ORC units. As reported in Figure 6.7, increasing the carbon tax price give an opposite trend: the NPV achievable using *configuration GT+ORC* are higher than using *configuration GT* also for cheap fuel scenarios.

Due to the increasing interest in the oil and gas sector on the environmental impact, emission reducing and the improving of efficiency, other studies have been developed on the possible using of ORC technology. More details and information could be find in the complete text of the presented studies attached in Chapter A.

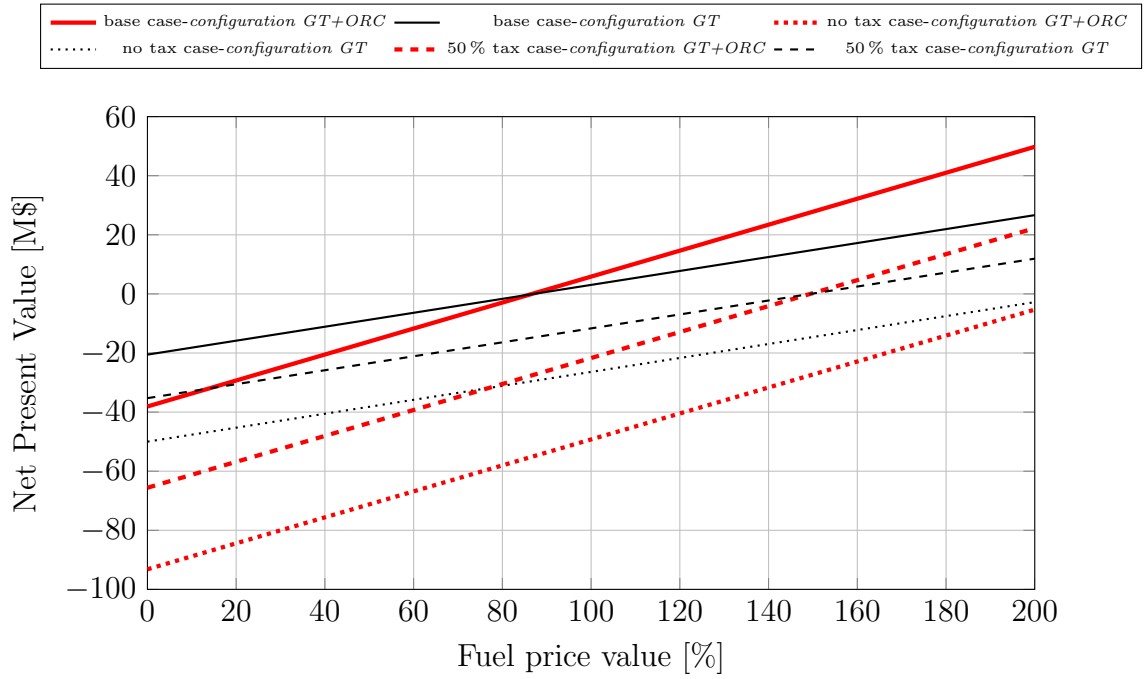


Fig. 6.6: Net present value for *configuration GT+ORC* and *GT* as a function of the fuel price variation respect the base case (in percentage): effects of the CO₂ tax value decreasing.

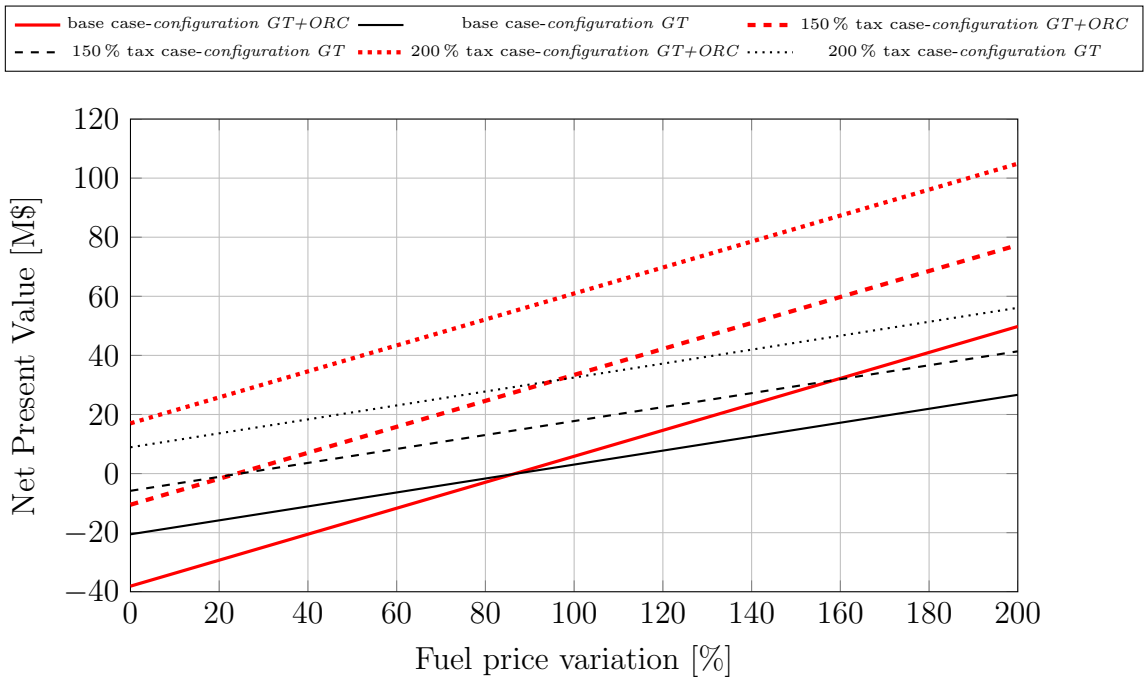


Fig. 6.7: Net present value for *configuration GT+ORC* and *GT* as a function of the fuel price variation respect the base case (in percentage): effects of the CO₂ tax value increasing.

Part III

Micro-Scale Waste Heat Recovery: ORC Experimental Analysis

CHAPTER 7

Small scale ORC technology

Summary. This chapter is focused on the small scale ORC systems, with particular interest on the expander devices. Axial and radial turbines result not suitable for small size ORC systems, because rotational speed increases dramatically with decreasing output power and consequently the cost increases. Therefore, volumetric expanders are more appropriate in small scale ORC units. The main volumetric expander typologies are presented in this chapter and particular attention is put on the reciprocating pistons. From literature, performance parameters are introduced and operating data collected. The considerations will be useful in the following chapters to better evaluate the experimental performance of the ORC prototype system under investigation.

The organic Rankine cycle is an advanced power generation technology commonly used to convert low grade heat into electricity, for a wide range of power values (scales from a fraction of kW_e to several MW_e). ORC technology results now robust and advantageous in many ways and it has shown a renewed interest over the last decades thanks to its flexibility and easy maintenance. At low temperatures, organic working fluids lead to higher cycle efficiency than water and organic fluids are preferable because the fluid mechanics leads to high turbine efficiency in both full and partial load. ORC are considered for a number of different applications, such as heat recovery from industrial streams at medium-to-low temperatures, biomass-fed cogenerators, low temperature solar cycles or small geothermal plants. Almost all the units available on the market are in the medium to-high power range, while micro-small size systems are not so diffused yet. Micro scale ORCs are still in demonstration phase, but their application could save primary energy and reduce pollutant emissions [3]. Small and micro size ORCs are suitable for several applications, such as electric generation in remote houses, domestic CHP units or trigeneration applications, and thermally driven heat pumps.

Small-scale and micro-scale CHP systems

There is no strict size definition of *micro* and *small* size of power systems and the limits are not clear and standardized.

According to [21], the concept *small-scale CHP* means combined heat and power generation systems with electrical power less than 100 kW, while *micro-scale CHP* is also often used to denote CHP systems with an electric capacity smaller than 15 kW_e.

Meanwhile, Beith in [84], defines *micro-CHP* the systems with power size between 2 kW to 10 kW, generally used in domestic applications; whereas he indicates that *small-CHP* plants cover a wider range of applications from 50 kW up to a few MW and commonly applied in larger establishments.

In Italy and Europe, the standard defines as *microl-scale CHP* systems with electrical power size lower than 50 kW and *small-scale CHP* system with electrical power size lower than 1 MW [80].

Small-scale and micro-scale CHP systems are particularly suitable for applications in commercial buildings, such as hospitals, schools, industrial premises, office building blocks, and domestic buildings of single or multifamily dwelling houses [21]. Small-scale and micro-scale CHP systems can help to meet a number of energy and social policy aims, including the reduction in greenhouse gas emissions, improved energy security, investment saving resulted from the omission of the electricity transmission and distribution network, and the potentially reduced energy cost to consumers. A micro-/small-scale CHP system is also able to provide a higher degree of reliability since the system can be operated independent of the grid. Currently, micro-scale and small-scale CHP systems are undergoing rapid development and are emerging on the market with promising prospects for the near future [21].

For instance, biomass is a interesting solution for decentralized, small-scale and micro-scale CHP systems due to its intrinsic properties. On one hand, small-scale and micro-scale biomass CHP systems can reduce transportation cost of biomass and provide heat and power where they are needed. With the continual rise in gas and electricity prices and the advances in the development of biomass technologies and biomass fuel supply infrastructure, biomass-fuelled CHP systems will become more economically competitive [21]. However, today in the distributed electricity generation from natural gas, the prominent technologies are the Internal Combustion Engines (ICE) and gas turbines. The heat rejected by the prime movers could be exploited for cogenerative purposes, increasing the overall efficiency, the economic profitability and energy sustainability of systems [85]. Referring to small size gas turbine, the flow rate of the flue gases and their temperature make ORC the most suitable choice for the bottoming cycle [85]. Various studies are available in literature on micro-GT and ORC coupling [86, 87, 88]. ORCs can also recover the waste heat from combustion gases and/or from cooling systems of the ICE. Several investigations aimed to analyzing the behavior of such processes [89, 90, 91] to investigate problem and advantages. In domestic applications, also the integration

with solar energy, as an alternative solution to Stirling engines [12]. Another possible application for micro and small ORC is the *cascade application*, i.e. couple an ORC either to a conventional Rankine cycle or to another ORC, where the condenser of one acts as an evaporator of the next and so on, in a cascade.

Therefore, recently there have been many experimental realizations of small scale ORC and particular interest is given on: operating conditions, performances achieved for components and complete cycle, components type and size used in the set-up, running environment and selection of the expander machine.

Landelle et al. [20] realize a database, that includes both qualitative and quantitative data on ORC facilities available in the ORC experimental analysis state-of-the-art. The database allows to evaluate ORC and components performances and to make a complex comparison. Figure 7.1 presents the ORC gross electric efficiency respect to the ORC gross power, distinguishing the applications of the considered data. The results show how, in a power range of 0.1 kW to 10 kW the most diffuse applications are solar and waste heat recovery, while the coupling with biomass is less common.

The ORC performance depends on operating conditions of source and sink, the size of components and working fluid. Therefore, the selection and sizing of expansion machine is fundamental, due to the strong influence on the whole system performance. The technology choice depends on the operating conditions, on the working fluid and on the size of the system. The selection and size of expander depends on several criteria, such as technical limitations, its performance, reliability, compactness [92]. However, in micro power devices, also economic, technical or operational considerations may often prove to be more important than efficiency. Also noise, vibration and dimensions aspects have to be taken into account.

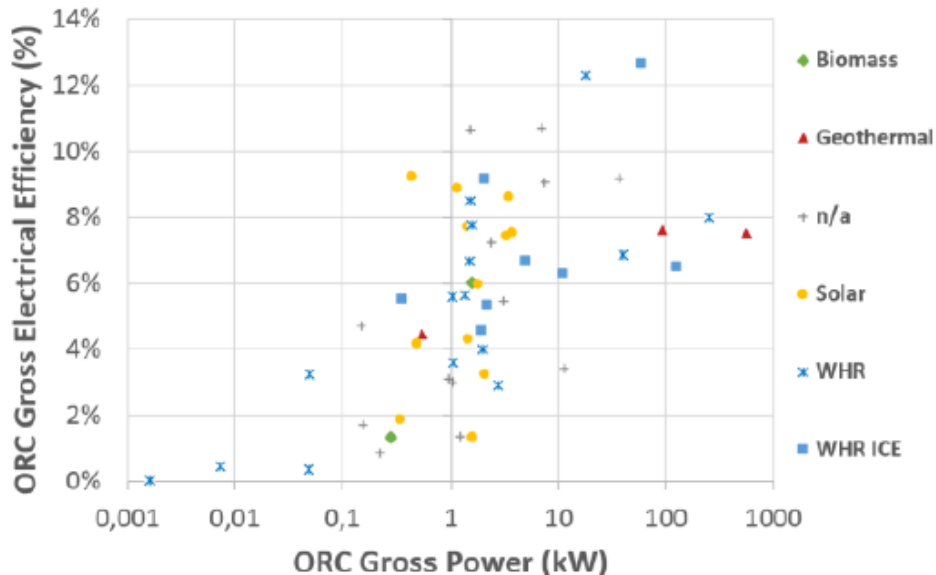


Fig. 7.1: ORC function of power output [20].

The following sections present the expander technologies applied in the micro-scale ORC, with particular interest on the piston machines, object of the experimental activity presented in Chapter 8. The typical losses and operational maps are introduced and discussed.

7.1 Expanders for small scale Rankine cycles

Generally, ORC expanders are classified into velocity based expanders (i.e. turbines) and volume based expanders (i.e. volumetric expanders). More in details, the ORC turbine could be an axial or a radial turbine. However, turbines are not suitable for small size ORC systems (less than 50 kW_{el}), mainly because rotational speed increases dramatically with decreasing output power and consequently the cost increases.

The volumetric expanders, otherwise called positive displacement expanders, are more appropriate in small scale ORC units (typically power lower than 150 kW_{el}), due to [3, 9, 92, 93]:

- low flow rates and rotational speed (generally 1500 rpm to 3000 rpm on a 50 Hz electric grid);
- ability to operate under large pressure ratios;
- good performance;
- tolerance of liquid phase presence during expansion in some operating conditions;
- good isentropic efficiency (scroll and screw expanders better accepts liquid fraction than piston expanders).

In a volumetric expander the decrease of the pressure is caused by an increase of the volume of the expansion chambers. It usually comprises a stator and one or several rotors connected to the expander shaft: their relative position, which varies with the shaft rotating angle, defines a series of working chambers in which the fluid is trapped. The high-pressure fluid forces the rotors to move and a moving boundary work is done by the fluid on the rotors. The volume of working chambers increases and the pressure decreases: energy transferred, under the form of mechanical work, results in a decrease of the fluid energy [3, 9, 92].

ORC turbomachines comparison

Axial turbines are generally used in combination with high molecular weight working fluids, large mass flow rate and low pressure ratio. Using organic fluids, the enthalpy drop during the expansion is low, and consequently few stages are required. Even single stage turbines can be employed for low or medium temperature ORC cycles. Moreover, the low speed of sound, characteristic of organic fluids, is reached much sooner in an ORC than in a water steam cycle. This fact is a limitation as high Mach numbers are related to higher irreversibilities and lower turbine efficiencies.

Meanwhile, radial inflow turbines are designed for high pressure ratios and low working fluid flow rates. Their geometry allows higher peripheral speeds and higher enthalpy drop per stage than axial turbines. Moreover, the radial turbines maintain an acceptable efficiency over a large range of part load conditions, but it is difficult to assemble several stages in series [9].

There exists a large panel of positive displacement expanders. The most popular technologies are piston, twin-screw, scroll and vane, while less common are roots and single-screw expanders. Moreover, each technology gathers a large number of variants. Their classification is based on: (i) technology of stator and rotors, (ii) type of mechanism used to create variation of the working chambers volume and (iii) timing of the various phases (suction, expansion and discharge). Figure 7.2 shows the classification of the most diffuse expander technologies. The timing of each phase could be imposed by the geometry of the machines or, in the case of piston expanders, by valves. Generally, the absence of valves simplifies the design and increases the reliability of the machine. Moreover, the expanders could be classified as open-drive, semi-hermetic or hermetic, if it is possible to access to the connection between mechanical shaft and electric generator. A difficulty associated with the use of a positive displacement machine is its lubrication, due to the contact between moving elements, which can be liquid or solid, less common because compatible only with adequate materials. Oil can be circulated with the working fluid through the entire ORC system or be separated and driven back to the expander supply by an external circuit (less compact solution and not adapted for mobile applications). The design of some synchronized machines, as some scroll and screw expanders, prevents any contact between the moving elements and an oil-free operation is suitable. This solution is beneficial for the overall ORC, but a penalty for the expander itself, due to larger tolerances between moving parts: the presence of oil guarantees the sealing of the leakage paths (generally piston expanders show lower internal leakage than scroll and screw expander) [9, 3, 92].

Generally, volumetric expander technologies are compared based on technical and performance parameters. The main parameters are following introduced and described:

- **rotational speed** (N in [rpm]) of the expander;
- **displacement**, V_s [m^3] is the machine swept volume. Generally, it is a fraction

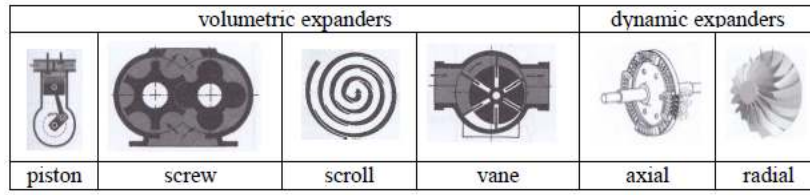


Fig. 7.2: Classification of volumetric expanders according to the type of motion of the rotors [94].

of the stroke displacement;

- **displaced flow rate** is function of the displacement, the rotational speed and the working cycle frequency i , as shown in eq. (7.1):

$$\dot{V}_s = i \cdot N \cdot V_s \quad (7.1)$$

- **Built-in Volume Ratio**, BVR , is defined as the ratio between the volume at the end of the expansion process (V_{ex}) and the volume at the end of the suction process (V_{su}):

$$BVR = \frac{V_{ex}}{V_{su}} \quad (7.2)$$

- **pressure ratio**, β , is the ratio between the pressure at the end of the suction process p_{su} and the pressure at the end of the expansion process p_{ex} :

$$\beta = \frac{p_{su}}{p_{ex}} \quad (7.3)$$

- **isentropic effectiveness or efficiency** is the ratio between the power produced by the expander (P could be a shaft or electric power) and the power it would produce if the expansion of the fluid was isentropic (evaluated as the product between the mass flow rate and the isentropic enthalpy variation) as shown in eq. (7.4):

$$\eta_{iso} = \frac{P}{\dot{m} \cdot \Delta h_{iso}} \quad (7.4)$$

- **filling factor** Φ is defined as the ratio between the displaced flow rate entering the expander and the theoretical displaced flow rate, as shown in eq. (7.5). The value of this parameter is affected by the internal leakages, supply pressure drop, heat transfer and clearance volume.

$$\Phi = \frac{\dot{V}_s}{\dot{V}_{s,th}} \quad (7.5)$$

The following part introduces the most widely used volumetric expansion devices, with particular interest on reciprocating piston expanders, presented in Section 7.2. Section 7.1.5 introduces the main performance parameters and compares performance of expansion typologies.

7.1.1 Scroll expanders

Scroll expanders are growing in popularity, due to their operational simplicity, relatively small number of components and low production and maintenance costs. Generally, scroll expanders are compressors rotating in reverse direction. Scroll expanders belong to the family of orbiting machines. They are composed of two involutes, one being the central symmetry of the other Figure 7.3(a). Generally, one involute is fixed while the other one shows an orbiting movement *Fixed Scroll* and *Orbiting Scroll* in Figure 7.3(b). Their relative position defines a series of chambers, most of them having a crescent-shape layout. These chambers act as suction, expansion or discharge chambers [3].

Figure 7.3(b) displays the evolution of the fluid inside the machine. The suction chamber located in the center of the machine and in communication with the suction port is at its minimal volume (i.e. the clearance volume). From this position, its volume increases over one entire shaft revolution. The fluid at the supply pressure fills the chamber through the supply port. Then the suction chamber divides itself into three chambers: two of them become expansion chambers and form two different expansion paths; the third one forms the new suction chamber whose volume is the clearance volume. Since the fluid pressure inside the clearance volume is equal to the supply pressure, this clearance volume does not impact the machine performance. The pair of expansion chambers exists for at least a fraction of one full revolution but it can also take several turns to disappear. The number of full revolutions during which the pair of expansion chambers exists is closely related to the built-in volume ratio of the machine. As shown Figure 7.3(b), several pairs of expansion chambers can simultaneously exist. During their existence, the volume of the expansion chambers increases, so that the fluid pressure decreases. At the end of the expansion process expansion chambers become discharge chambers. This happens when expansion chambers open up to the exhaust line. The pressure at the end of the expansion process is either equal (perfect expansion), higher (under-expansion), or lower (overexpansion) than the exhaust pressure. In the two latter cases, some fluid has to leave or enter the machine to equalize the pressure. The associated irreversibility decreases the isentropic effectiveness of the machine. For a last full shaft revolution, the volume of the discharge chambers will slightly increase first and finally decrease towards zero. The fluid, at the exhaust pressure (in the absence of pressure losses), is expelled inside the carter of the machine and exits through the exhaust port [3].

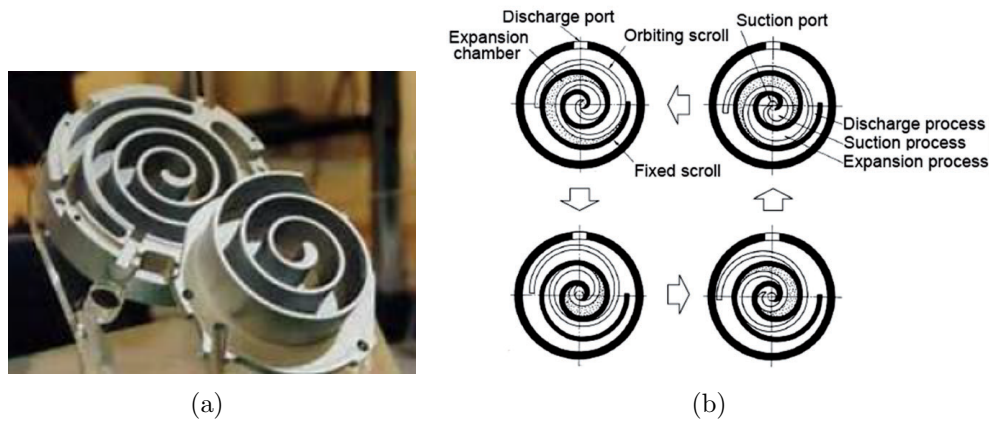


Fig. 7.3: Scroll expander [95] (7.3(a)) and its principle of operation [96] (7.3(b)).

7.1.2 Screw expanders

Screw expanders originate from screw compressors and they are capable of gas expansion. A screw expander acts as a screw compressor with a reversed direction of rotation. Screw expanders are available on the market as single or twin-screw expanders. Currently, most of the screw expanders are twin-screw machines, visible in Figure 7.4a. Scientific and technical literature also mentions the use of single-screw expanders but to a lesser extent [3]. In more details, a twin-screw expander is made up of two intermeshing helically toothed rotors (the male and the female rotors) housed in a casing. The rotors and the casing delimit a series of working chambers that evolve from one extremity of the rotors to the other one. The casing comprises a suction port and a discharge port, located at both extremities of the rotors. The location and the shape of the two ports allow for the communication of the chambers with the supply and the discharge lines respectively. The same chamber becomes, successively, a suction chamber, an expansion chamber, and finally a discharge chamber. At the initial angular position of the machine shaft, the chamber volume is equal to zero. A screw expander presents no clearance volume. As the male rotor rotates, the volume of the chamber increases until reaching a maximum value and then decreases towards zero. The built-in volume ratio is equal to the ratio between the maximum volume and the expander swept volume. The volume ratio is not a function of the geometry of the rotors. It depends on the angular position of the high-pressure control edge. Lower angular position of the control edge means larger built-in volume ratio and smaller swept volume. Hence, for given rotor dimensions, a compromise has to be found between increasing the swept volume and the built-in volume ratio.

A single-screw expander is made up of a central rotor with helical grooves meshing with two toothed gate rotors, as shown in Figure 7.5. This meshing delimits a working chamber on each side of the rotor, resulting in symmetrical and simultaneous evolution of the fluid with respect to the central rotor rotation axis. Consequently, a better

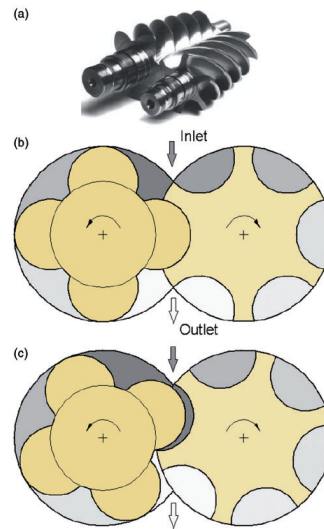


Fig. 7.4: Photo of the screw-shaped components of the expander (Figure 7.4(a)) and the cross section of a screw expander with a symmetric profile during operation (Figure 7.4(b), Figure 7.4(c)) [96].

balance of radial and axial loads is achieved, increasing the bearing lifespan. Currently, most of the screw expanders used in ORCs are twin-screw machines, but single-screw expanders are also available on the market [3].

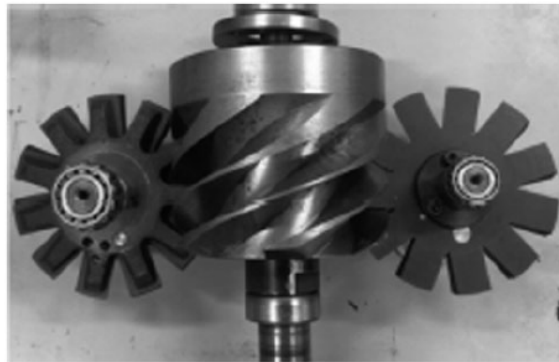


Fig. 7.5: Single-screw expander[96].

The rotor profile plays an important role in the reduction of leakage and frictional losses and overall performance of expander [93]. Early used screw compressor had asymmetric profile which creates significant leakage path due to the large blow-hole area when they are restructured to work as an expander. Later on, the rotor profile was modified into an asymmetric shape which has a lower blow-hole area but offers high frictional losses. An example is the Lysholm asymmetric profile, also named as Lysholm screw expander, reported in Figure 7.6. Its design is based on superchargers used in forced induction systems for internal combustion engines. Such expanders are also characterized by long life and their ability to handle wet steam [96].

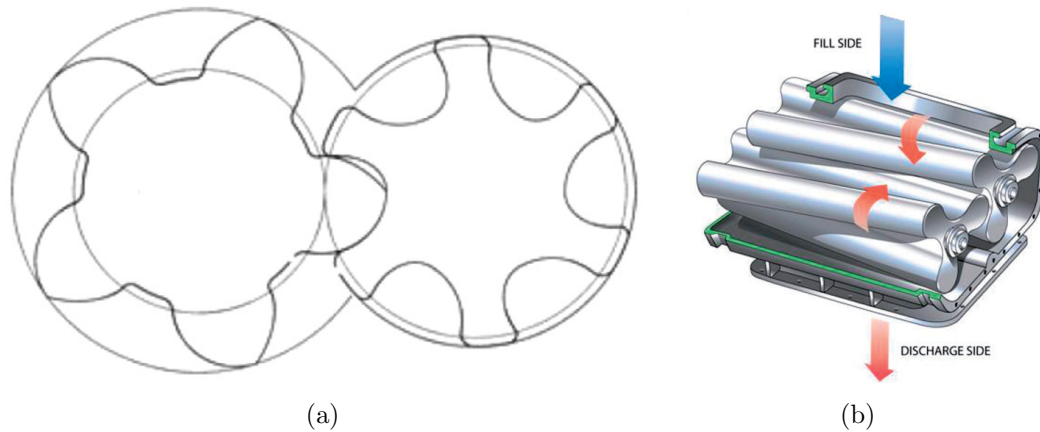


Fig. 7.6: Lysholm asymmetric profile [93] (7.6(a)) and working principle of Lysholm screw expander [96] (7.6(b)).

7.1.3 Vane expanders

The vane expander is a relatively simple machine. The most complex part is the vane mechanism. This kind of expander consists in a cylindrical housing (stator or housing in Figure 7.7) in which a cylindrical rotor is in motion. The rotor is offset from the center of the housing. Slots are spread out all over the rotor and allow the insertion of vanes that are pushed out by a spring or similar mechanisms. The vanes are pressed against the housing and define chambers. Two mechanisms exist: the vane position is maintained either by a spring or by the working fluid pressure. Spring-assisted vane expanders show better volumetric performance because the vane is always pushed against the housing but the friction losses are higher than in the pressure-assisted expander, decreasing the isentropic efficiency. The chamber in communication with the admission port is referred to as the suction chamber. When that chamber is no longer in contact with the suction port, the expansion process begins and ends when the chamber faces the exhaust port, becoming then a discharge chamber [3].

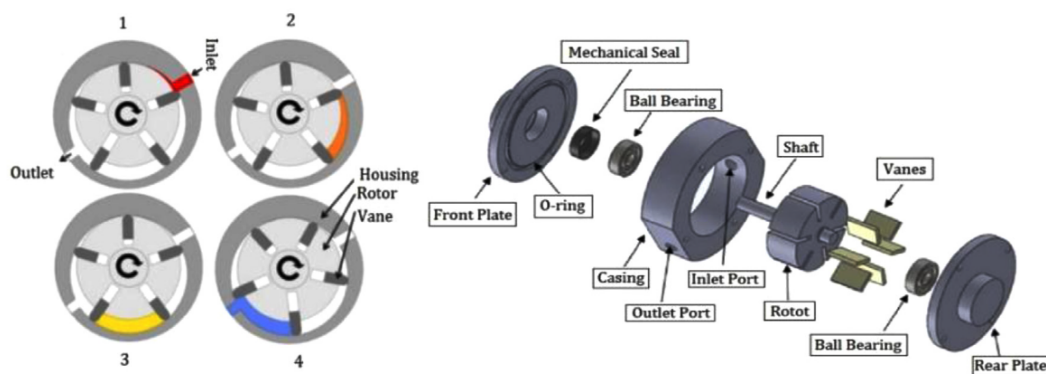


Fig. 7.7: Working principle and components of vane expander [93].

7.1.4 Piston expanders

Piston expanders are based on the solutions drawn from a range of technical areas, primarily from automotive, energy, and petrochemical industries. They can be divided into several groups which differ fundamentally from each other. When operating as expansion devices in cogeneration ORC systems, the following types of piston expanders are the most frequently encountered [96]:

- reciprocating piston expanders;
- rotary piston expanders (in literature sometimes identified in the group of *trochoidal expanders*);
- gerotor expanders (in literature sometimes identified in the group of *trochoidal expanders*);
- rolling/swing piston expanders;
- free piston expanders;

The reciprocating piston expander is made up of the piston and the cylinder arrangement similar to an automotive engine (as better described in Section 7.2). Even though traditional piston expanders can be applied in ORC systems, this has not yet become common practice due to several factors such as a complex construction which is directly related to their high production costs, noisy operation, high vibration levels, high friction losses, the necessity to use a lubricant, and low efficiency in relation to other expansion devices [96].

Rotary piston expanders, also known as Wankel rotary engine, could be applied in ORC applications. The diagram of such expander, in Figure 7.8(a), presents a far fewer parts than a regular reciprocating piston engine. Due to the contact between the edges of the rotating piston and the casing, rotary piston expanders are characterized by continuous, intensive friction resulting in relatively rapid wear of the mating surfaces. Such expanders also struggle with problems of ensuring tightness which, in combination with the above-mentioned friction and difficulties with lubrication, causes that these machines have low potential for achieving high efficiencies. In order to obtain acceptable levels of efficiency, the design parameters and operating conditions need to be carefully optimized. Their best qualities are: small overall dimensions, low weight, low vibration, and quiet operation [96].

The name of gerotor expander derives from *generated rotor*. Such expander consists of an inner and outer component. During operation, the rotating piston moves inside its surrounding component and the inner component always has one less tooth than the outer component as in Figure 7.8(b). The elements are mounted eccentrically, which causes the creation of chambers with changing volumes, allowing the expansion of a working medium [96]. Such expanders are also characterized by a rather simple design,

low production costs and they do not need additional lubrication. Such machines have the potential to become viable alternatives to other types of expanders.

Figure 7.8(c) shows the working principle of a rolling piston expander. The expander operation is based on the rolling of the round piston along the interior surface of the casing (which has a larger inner diameter than the piston diameter). This allows the expansion of the gas in the closed space, and its volume grows as the piston moves. The core component of this expander is a sealing vane, which maintains continuous contact with the piston and is used to prevent gas from leaking out of the working volume, while the piston rolls within the vane it retracts into the cylinder, enabling a smooth start of the next operating cycle [96]. Rolling piston expanders are characterized by low values of expansion ratio and the possibility of using vapor at very high pressures. Rolling piston expanders feature low production costs due to their simple design. The main drawback is the relatively strong friction occurring between a piston and a sealing vane, and difficulties with providing appropriate leak tightness [96].

Free piston expanders are suitable for low flow rate and has lower leakage and frictional losses as compared to the rest of volumetric expanders. The free piston expander are used in CO₂ refrigeration cycle. The working principle of a free piston expander is shown in Figure 7.8(d): the free piston expander can be designed as two kinds of structures, the single acting free piston and the double acting one. Owing to the symmetrical feature, the double acting free piston can always come back if the expander piston can run through the forth stroke. In the single acting free piston expander, the piston is driven to move through the back stroke by the mechanical spring, which absorbs the energy in the forth stroke [97].

7.1.5 Comparison between volumetric expander typologies

Figure 7.9 provides the turbine volumetric expansion ratio values, i.e. the volumetric expander built-in volume ratio (see eq. (7.2)) of existing or tested ORC systems adopting volumetric expanders, radial or axial turbines, respect to the power size. The presented values have been evaluated by Branchini et al. [6] by means of data found in different literature sources examining ORC expanders or provided by expander producers. As previously introduced, the volumetric expander are generally applied for low power size.

Figure 7.10 and Figure 7.11 show a comparison between volumetric expanders technologies, produced by Lemort and Legros [3], considering a sample of 67 machines described in literature. From Figure 7.10, it can be observed that scroll and piston expanders approximately cover the same range of power; twin-screw expanders cover larger powers and fill the gap between turbomachineries and other expander technologies, while single-screw machines cover a smaller range of power; vane and trochoidal expanders compete with scroll ad piston. Figure 7.11 presents the range of maximal rotational speeds achieved for each technology: most of the expanders operate at speed lower than 6000 rpm; twin screw and roots expanders can achieve much larger ranges, which

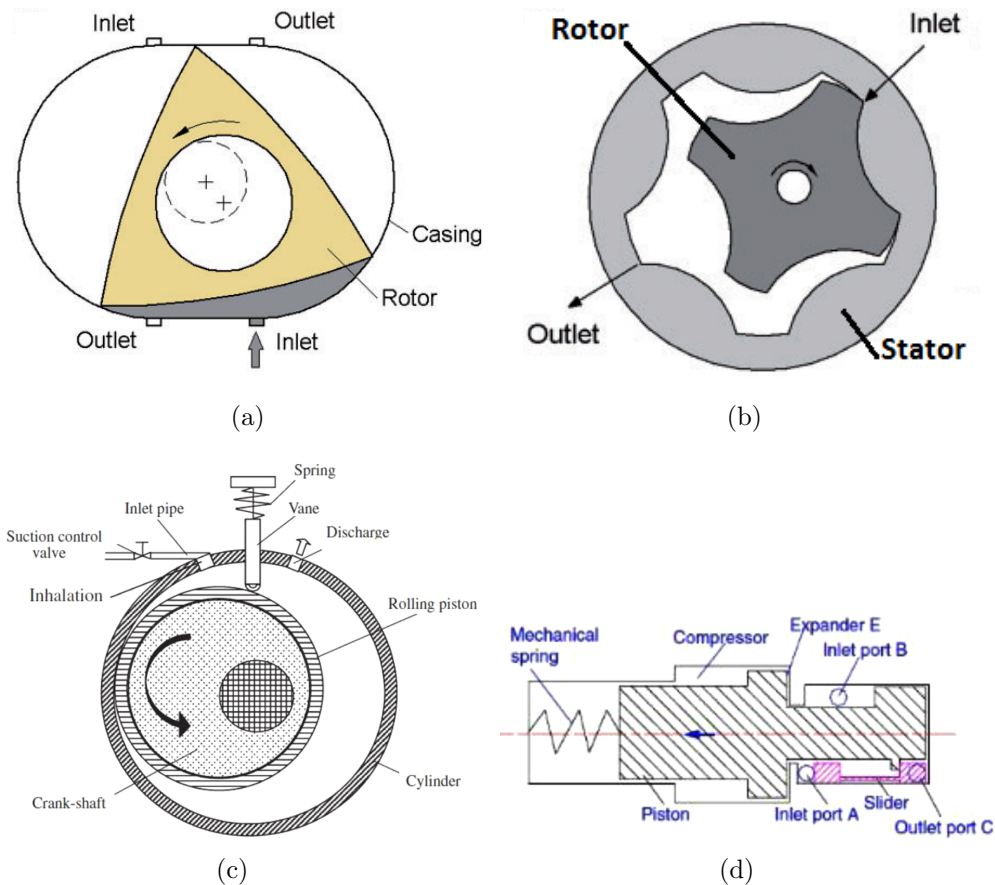


Fig. 7.8: Diagram of a rotary piston expander [96] (7.8(a)), gerotor [96] (7.8(b)), rolling [93] (7.8(c)) and free [97] (7.8(d)) piston expanders.

tends to increase the compactness of machine. Piston expanders present low rotational speed (600 rpm to 2000 rpm): these values eliminate the need of speed reduction gearbox [3, 93].

From the database realized by Landelle et al. [20] a comparison between the isentropic efficiency of ORC expanders as function of power size and technology is available.

Lemort et al. [92] compare piston, screw and scroll expanders and list the technical constrains inherent to each machines, as displacement, pressure ratios, maximum temperatures and volumetric expansion ratios, based on open technical and scientific literature. The displaced flow rate of piston expanders typically range from 1.25 l s^{-1} to 75 l s^{-1} , similar as those of internal combustion engine cylinders; while screw expanders range approximately from 25 to 1100 l s^{-1} . The internal volume ratios of piston expanders could be large and it is limited by the specific work of the machine. The values usually achievable ranges between 6 up to 14. Meanwhile, with screw expander, 5 is typical value, but large values (for instance equal to 8) are reported in literature. Scroll compressors show volume ratios ranging from 1.5 to 3.5, while values of 4 are achieved

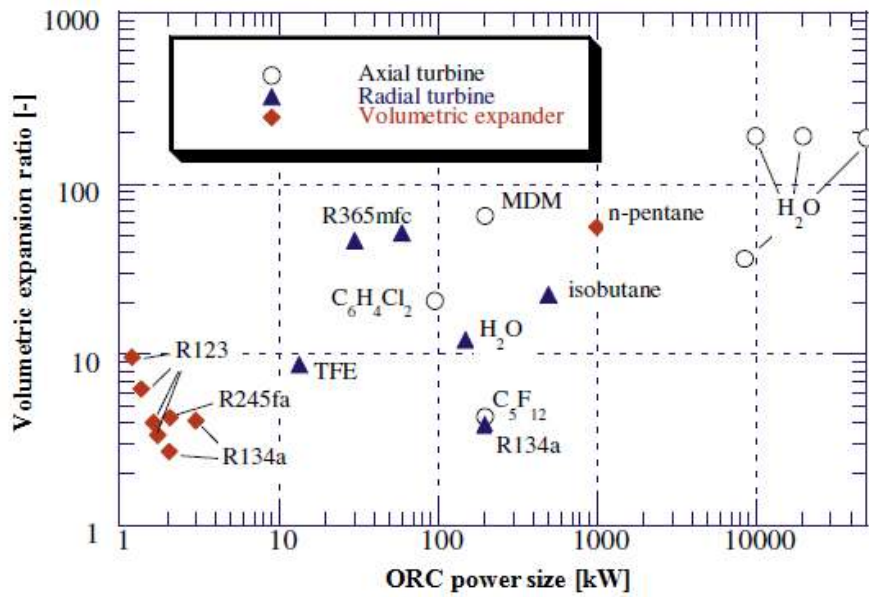


Fig. 7.9: Turbine volumetric expansion ratio values of existing ORC turbines of different technology and with specified fluids [6].

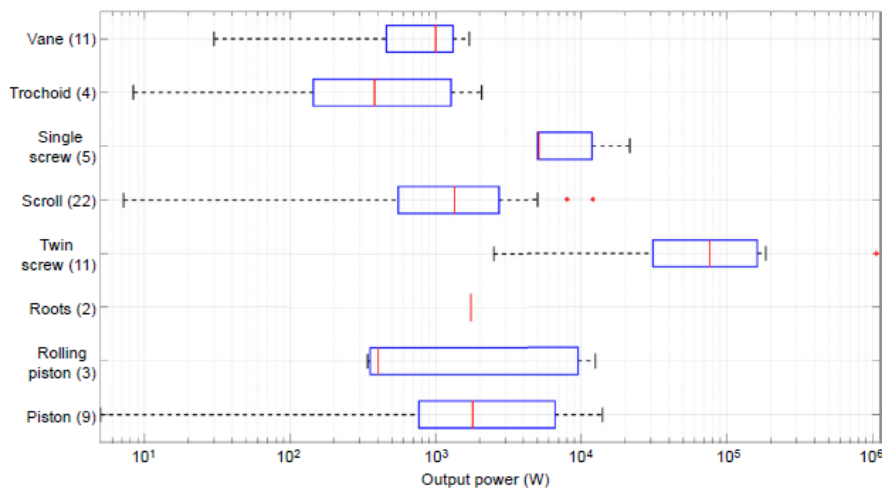


Fig. 7.10: Power ranges of major volumetric expander technologies [3].

with air compressors. The volume ratio values are constrained by performance and costs considerations. However, larger values could be reached by associating expanders in series. Scroll compressors pressure ratios are typically lower than 11, but in expander mode, the maximum value is equal to 15. These values are listed in Table 7.1, where the missing data have been sourced in [93]. No values of pressure ratios are available, but typically piston expanders can operate under large pressure ratios with reasonable efficiencies, because of their larger internal volume ratios. The operating pressure and

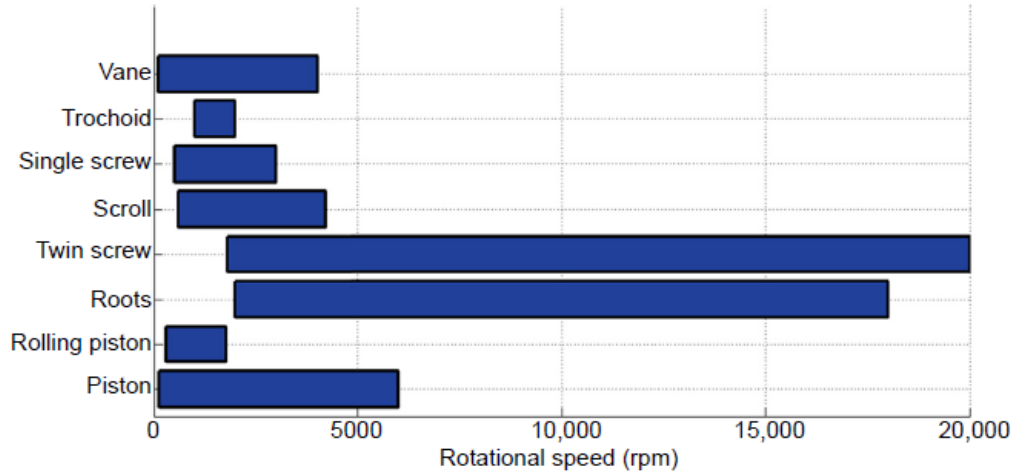


Fig. 7.11: Rotational speeds ranges of major volumetric expander technologies [3].

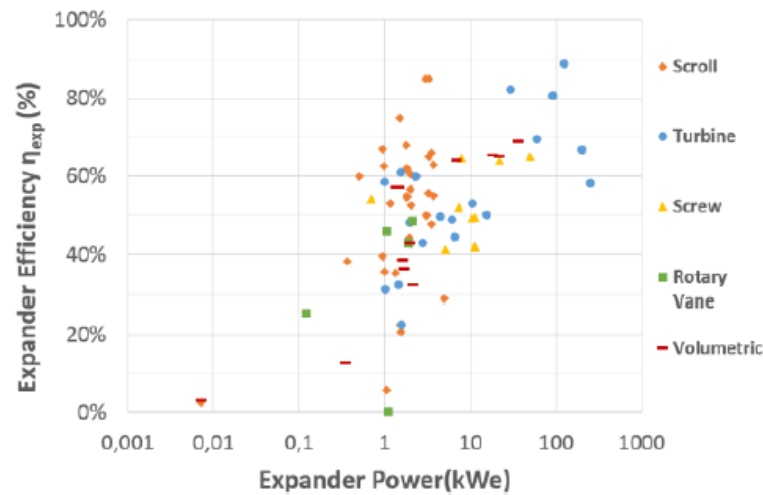


Fig. 7.12: ORC and expander efficiency function of power output [20].

temperature can reach 9 MPa and 380 °C to 560 °C respectively.

Table 7.1: Technical constrains inherent piston, screw and scroll expanders [93, 92].

Type	Piston	Screw	Scroll
Displaced flow rate [l s^{-1}]	1.25 to 75	25 to 1100	1.1 to 49
Built-in volume ratio [-]	6 to 14	2 to 8	1.5 to 3.5
Pressure ratio [-]		2 to 10	<10

Moreover, Imran et al.in [93] conclude that the screw expanders have higher performance compared to others; the vane expanders have lowest performance, due to higher leakage and friction losses, low rated power and lower isentropic efficiency. The screw expanders

are not suitable commercially for power production less than 25 kW, as the cost will be very high due to sensitive design and fabrication. Therefore, in the range 1 kW to 25 kW, the most suitable are the scroll expanders, due to simple structure, ability to operate in two phase expansion, low cost and relatively high isentropic efficiency. Although piston expanders provide larger expansion ratio and high isentropic efficiency, they have complex structures, can not handle the wet expansion, subjected to flow oscillation/vibrations during operation and needs balancing. Piston expanders can be classified into reciprocating and rolling piston expanders on the basis of the motion and rolling piston expanders have relatively simple structure, low leakage and frictional losses [93].

Another expanders performance comparative assessment available is through the using of non-dimensional parameters. Generally, specific speed N_s and specific diameter D_s are used for selection of an expansion machines. More in detail, these parameters are given as shown in eqs. (7.6) and (7.7) [98, 99].

$$N_s = N \cdot \sqrt{\frac{\dot{V}}{(\Delta h_{is})^{3/2}}} \quad (7.6)$$

$$D_s = \frac{D \cdot (\Delta h_{is})^{1/4}}{\sqrt{\dot{V}}} \quad (7.7)$$

N is the expander rotational speed [rad s^{-1}], D is the characteristic diameter of the expander [m], \dot{V} is the expander outlet volumetric flow rate [$\text{m}^3 \text{s}^{-1}$], while Δh_{is} is the isentropic enthalpy variation across the expander [J kg^{-1}]. The definition of these non-dimensional parameters is based on the concept of similarity. The concept of similarity is convenient because it allows to reduce the number of parameters needed to describe the machines characteristics: through the dimensional analysis, only four parameters are sufficient to describe completely, and consequently compare, the performance of geometrically similar machines. These parameters are: (i) specific speed number, (ii) specific diameter, (iii) Reynolds number and (iv) suction specific speed or Mach number. However, it is difficult to present the performance of any machine as a function of four parameters at one time. Fortunately, two of these variables, i.e. Reynold number and Mach number, have only a secondary effect on the expander performance, as demonstrated by Barber and Prigmore [100], and they can be ignored. Therefore, the expander performance can be represented as a function of only the specific speed N_s and the specific diameter D_s , previously introduced. With the International System of units used in this report, specific speed and specific diameter are truly dimensionless. The values for these parameters, however, are often quoted with different units of measure [99]. Based on the similarity concept, Balje [101] used the available information on expander performance data to compute the optimal geometry and maximum obtainable efficiencies at the design point operation for various types of expander and he presented these information in a N_s - D_s diagram presented in Figure 7.13 [98], where the similarity parameters are considered with different units of measure [102, 99]. More in detail,

N_s and D_s are evaluated through eqs. (7.6) and (7.7) considering: N in [rpm], V in cubic feet per second, Δh_{is} in foot-pounds per pound and D in feet. Therefore, the dimensionless values of specific speed and specific diameter in eqs. (7.6) and (7.7) can be converted to the corresponding values in these U.S. customary units by multiplying by 129 and 0.420, respectively [99]. Moreover, other information required to classify an expander is the ratio between the suction specific speed S and the diameter D , as shown in Figure 7.13, in order to identify the expander properly operational curve. The figure shows also how expanders with similar geometry will have the same efficiency for same specific speed. In case of piston expanders, the operational curves are in the lowest speed zone, with $N_s < 1$ and $3 < D_s < 60$.

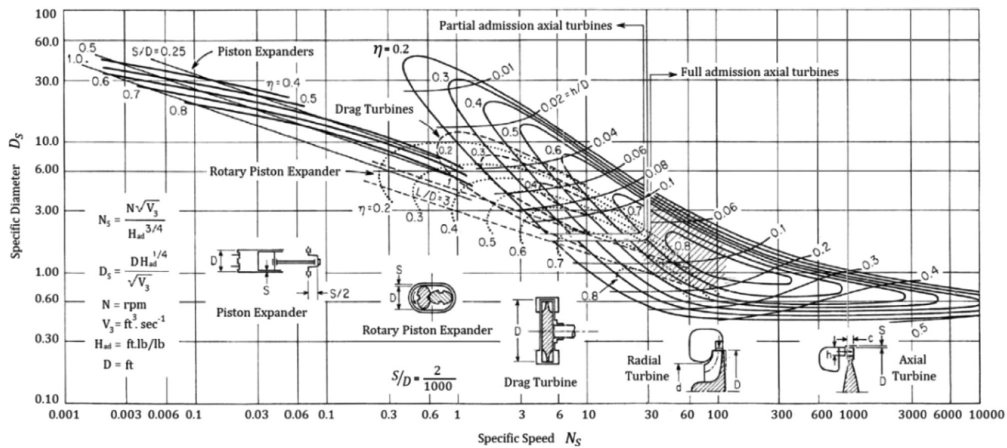


Fig. 7.13: Performance map for different types of expander [98].

The following section describes the reciprocating piston expander technology and models available in literature, with particular interest on the advantages and limitations, conventional performance indicators, operation values and classification of typical losses.

7.2 Reciprocating piston expanders

A piston expander is made up of one or several cylinders in which pistons move in a reciprocating fashion from the Top Dead Center (TDC) to the Bottom Dead Center (BDC). Reciprocating pistons are classified into radial piston and axial piston expander: the axial piston expanders are compact in size and had relatively less noise than radial piston expanders. Fluid enters and leaves the cylinder through orifices equipped with valves, that made this kind of expander more structurally complex compared to other positive displacements expanders. Main valves types are poppet, sleeves and rotary valves. For discharge also exhaust ports could be used, that allow to lead lower mass flow rate and larger compression work, because the fluid is recompressed earlier.

Figure 7.14 presents the theoretical indicator diagram (pressure drops neglected) in the pressure-volume plane of a piston expander, where *suc* and *des* indicate the suction and

discharge orifices and the volume between the TDC and BDC is the stroke displacement or named maximal displacement ($V_{S,max}$ in the figure). The fluid flow configuration inside the cylinder of a piston expanders can be *uniflow* (on left in Figure 7.14), when the supply port is located close to the head, while the exhaust port is at the opposite extremity; or *crossflow* (right diagram in Figure 7.14), where both the ports are located at the cylinder head. The fact that suction and discharge do not occur in the same location limits the suction heat transfer, which has a positive impact on the volumetric performance of the machine [93, 3].

nomenclature [R] V_S Stroke Displacement [m³] The various phase of the diagram are fol-

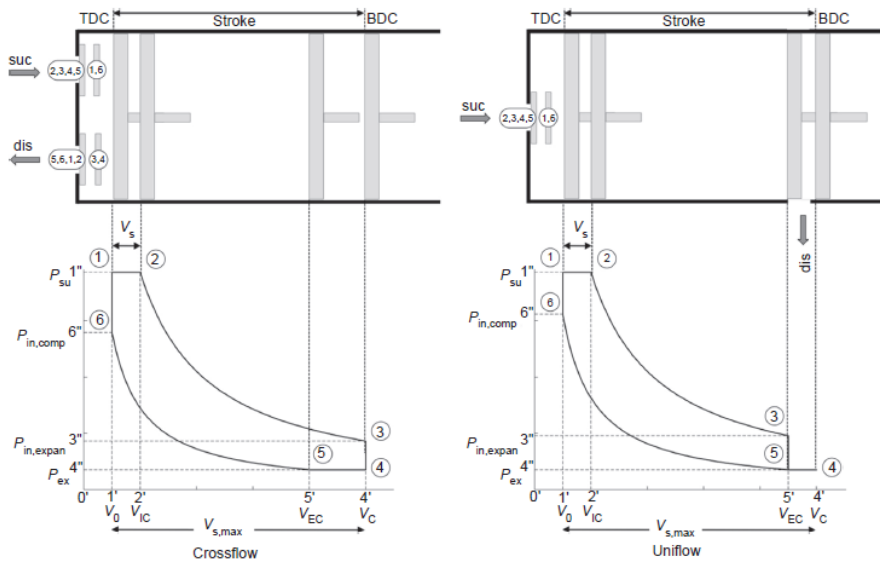


Fig. 7.14: Indicator diagram of piston expanders [3].

lowing described [3]:

- position 1, the cylinder volume is minimal (piston at TDC) and equal to the clearance volume V_0 ;
- from 1 to 2 represents the admission process, the piston starts its downward stroke (from TDC to BDC); since the supply port is open, the fluid at the supply pressure enters the cylinder; the volume increase is equal to the expander displacement V_S ;
- position 2, the volume is equal to V_{IC} (Inlet Closing) and the supply valve closes;
- from 2 to 3 is the expansion phase, the mass of fluid trapped inside the cylinder behaves as a closed system and the fluid pressure decreases from the supply pressure P_{su} to the pressure at the end of the expansion $P_{in,expan}$;
- position 3, the exhaust port opens;

- from 3 to 5 is the discharge process, the piston begins the movement from the TDC to the BDC (the the position of point 3 is different and it distinguishes different situations deeply described following);
- from 5 (V_{EC}) to 6 is the compression process, the pressure is increased from P_{ex} to $P_{in,comp}$. The pressure at the end of this process can be lower (over compression), equal (perfect compression) or higher (under compression) than the supply pressure;
- position 6, the inlet valve opens;
- from 6 to 1, fluid enters into cylinder yielding an increase of the pressure.

More in detail, from position 3 to 5 two scenarios can occurs [3], as shown in Figure 7.14:

- *under-expansion*, it corresponds to evolution from position 3 to 4 in Figure 7.14 left. The pressure at the end of the expansion $P_{in,expan}$ is higher than the pressure in the exhaust pipe P_{ex} ; therefore, some fluid leaves the machines to decrease its pressure and the piston has just reached the BDC and starts to move upward. The fluid remaining inside the cylinder is pushed out (from 4 to 5). Usually, this phenomenon occurs when the expander internal volume ration is lower than the system specific volume ratio;
- *over-expansion*, correspondent to evolution from 3 to 5 in Figure 7.14 right. In this case, the pressure $P_{in,expan}$ is lower than P_{ex} and the piston continues its descent towards BDC (position 4) and moves again towards TDC (from 4 to 5). It occurs when the internal volume ratio imposed by the expander is higher than the system specific volume ratio [9, 3].

These two effects can reduce the efficiency of the expansion process and the most common being under-expansion and this is the reason because volumetric expanders are generally less adapted to high expansion ratios.

7.2.1 Losses in piston expanders

The actual indicator diagram results a deformation of the theoretical one, previously introduced, because the presence of losses. In particular, the major losses in the piston expanders, penalizing the overall isentropic effectiveness, are the under or over expansion losses, under or over compression losses, internal leakages supply / exhaust pressure losses and heat transfer. For instance, there are pressure gradients across leakage paths resulting from clearances between moving elements and the fluid can leak through the piston rings. In uniflow configurations, the leakage flow can be recovered in the exhaust pipe. Fluid can also leak through the valves from the supply pipe into the cylinders and it can leak along the poppet valve stems.

Moreover, the fluid exchanges heat with the physical boundaries, as expander casing or chamber walls, causing a temperature increase or decrease. If the working fluid is a vapor, it could also condensate. In the absence of adequate insulation, the expander casing exchanges heat with the environment and cannot be considered as adiabatic. These phenomena have not a significant impact on the indicator diagram or on the internal work, but they only influences the fluid discharge temperature.

In piston expanders, as explained in the previous section, recompression may occur when the exhaust valve closes before reaching the TDC: as a function of the pressure at the end of recompression phase, under or over compression losses occur.

Also during suction and discharge processes pressure drops take place: they decrease the pressure at the beginning of the expansion process and increase it at the beginning of the discharge phase. Therefor, the area of the actual indicator diagram results smaller than in the theoretical one and the power production decreases. More in details, the pressure drops are related to the flow restrictions in supply and exhaust ports, as the valves opening or closing characteristics [3].

The model proposed by Glavatskaya et al. [103], a steady-state semi-empirical model of a reciprocating expander, considers all the losses described and it could be useful to better understand the piston expander behavior. A semi-empirical, or grey-box, model is characterized by low computational time and good numerical robustness respect to empirical and deterministic models, because it is based on a limited set of equations. It allows for partial extrapolation of the performance with variation of the operating conditions and design characteristics, due to the physical meaning of the model parameters. This kind of model is typically used for the design of ORC systems based on steady-state modeling [92]. Figure 7.15 presents the piston expander model, that assumes that the fluid evolution inside the expander can be split into several consecutive steps:

- from su to $su,1$, the fluid encounters a pressure loss during the suction process (δP_{su} in Figure 7.15);
- from $su,1$ to $su,2$, the fluid is cooled down (Q_{su}) by the contact with the metal housing of the machine;
- the expansion phase is between 2 to 4 . It undergoes isentropic expansion (from 2 to 3) and an expansion at constant machine volume (from 3 to 4). During this phase under and over expansion losses occur;
- evolution from 5 to 1 represents the partial compression of the residual mass of fluid trapped inside the cylinders at the end of the discharge process, due to the presence of the clearance volume;
- during the discharge phase the fluid undergoes a pressure loss (δP_{ex} between $ex,3$ and $ex,2$) and it exchanges heat (Q_{ex} between $ex,2$ and $ex,1$) with the metal housing of the machine;

- evolution from $su,2$ to ex represents the internal leakage flow, directly linked from the expander supply to its exhaust.

Q_{amb} in Figure 7.15 represents the exhaust heat losses to the ambient and its value depends on the ambient and expander wall temperature. Meanwhile, W_{loss} are the mechanical losses lead to the heating of the expander envelope, therefore its given by the sum of Q_{su} , Q_{ex} and Q_{amb} and it influences the final value of the net power output (W_{sh} in Figure 7.15).

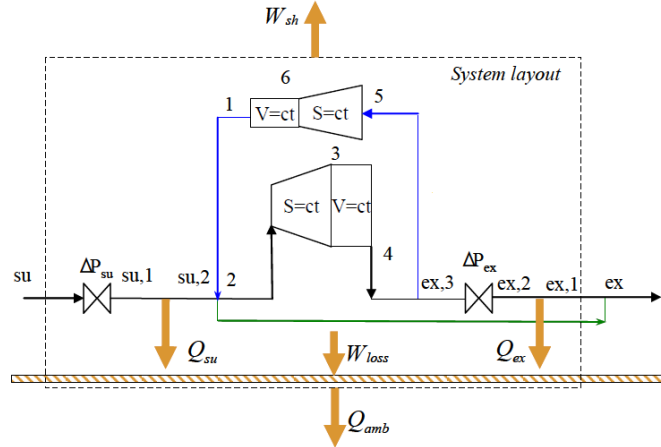


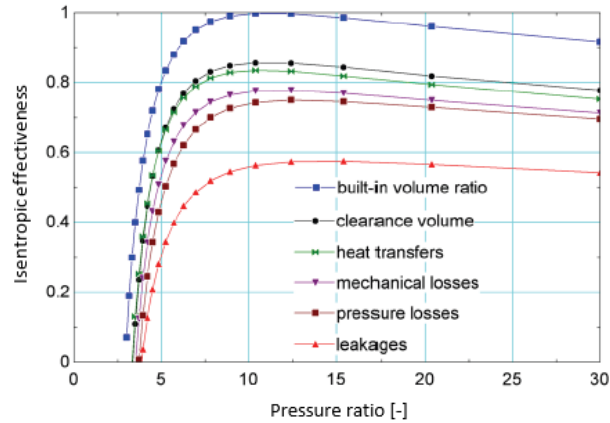
Fig. 7.15: Schematic representation of the overall expander model [103].

For example, the presented model has been used by Lemort et al. in [92] and by Oudkerk et al. in [104] to evaluate the impact of the losses on the expander isentropic effectiveness. This parameter is defined as the ratio between the power produced by the expander and the power produced if the fluid expansion was isentropic.

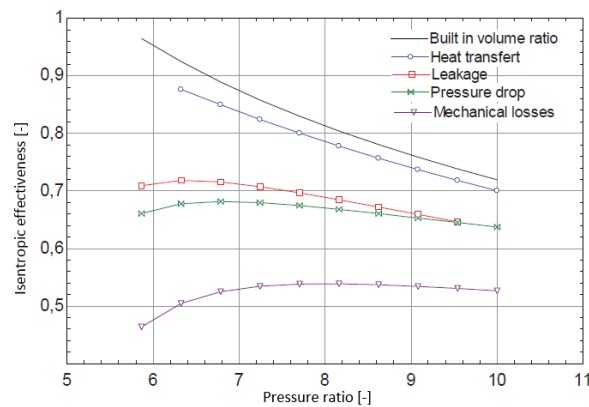
Figure 7.16(a) presents the impact of the various losses on the expander isentropic effectiveness with the pressure ratio, considering water as working fluid, a supply pressure equal to 30 bar, a supply temperature equal to 300 °C and a rotational speed of 3500 rpm (more details available in [92]). The figure shows as the major losses are due to the compression of the mass trapped inside the clearance volume and the internal leakages. Over expansion losses also decrease the isentropic effectiveness in the case of over expansion regime (i.e. in presence of a low pressure ratio).

Figure 7.16(b) shows the same diagram obtained for a piston expander integrated into an ORC cycle using R245fa as working fluid. The system has been tested for an exhaust pressure of 3 bar, supply pressure varying from 18 bar to 30 bar and rotational speed from 1000 to 4000 rpm. Figure 7.16(b) shows disaggregation of different losses: the built-in volume ratio leads to a decrease of the isentropic efficiency with the pressure ratio due to under expansion losses; for a pressure ratio of 5.8, the work to compress the fluid trapped into the clearance volume becomes equal to the work produced during the expansion and then the expander cannot produce anymore power and different sources

of losses are added; heat transfers slightly decrease the performances; the leakages have a strong impact on the efficiency and flatten the curve because they have more impact at low pressure ratios. The pressure drop does not impact much more the efficiency because the power and the flow rate decrease in the same time, but it affects more the compactness of the expander. Meanwhile, the mechanical losses decrease the efficiency and have more impact for low pressure ratios [104].



(a)



(b)

Fig. 7.16: Impact of the different losses on the evolution of the isentropic effectiveness with the pressure ratio [92, 104].

In addition, Quoilin et al. [105] built operating maps based on the expander and fluids limits for scroll and screw technologies considering a few typical ORC working fluids. Those maps are defined in the evaporating and condensing coordinate system and for a given expander technology and working fluid, the operating map shows a triangular shape. The upper limit corresponds to the working fluid critical temperature; the left side limit is defined by the limitation on the under expansion losses, while the right side limit is related to the value coefficient, i.e. the ratio of the expander displacement to

the delivered power. Figure 7.17 shows the operating map of piston expanders in terms of condensation temperature and pressure (the maximal volume ratio set equal to 10) [92].

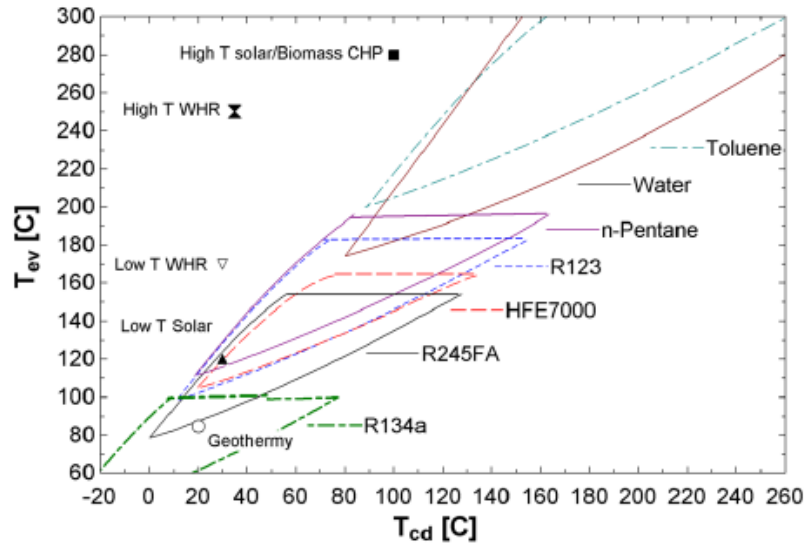


Fig. 7.17: Operating maps for piston expanders [92].

CHAPTER 8

Experimental test facility

***Summary.** The test rig developed in laboratory is described in this chapter. The internal ORC layout and the water supplies are introduced. The main parameters and information about each components are presented to understand the test bench operation and actual condition. The ORC expander is a key component, but few operational information are available, due to its prototypical nature.*

Figures 8.1 and 8.2 show the layout of the developed test facility. More in details, Figure 8.1 presents the internal layout of the micro-ORC under investigation, while Figure 8.2 shows the external circuits, realized in the laboratory in order to test the ORC system. Figure 8.3 is the simplified scheme of the connection between ORC system and cold and hot water supplies.

The ORC internal components have been originally provided by StarEngine company, while the instrumentation and the ORC external circuits of the test facility have been implemented for this experimental study. The ORC system is based on a recuperative configuration and it currently operates with R134a as working fluid. The organic fluid is mixed with an appropriate oil to lubricate the movable elements of the expander (the organic fluid percentage has to be between 95-99%) [106]. The ORC main components are: evaporator, expander, recuperator, pump and condenser, described in Section 8.1. The considered system is rated for an electrical power output up to 3kW, assuming an ORC efficiency close to 9%, as declared by the manufacturer, and a nominal input thermal power around 30kW. Figure 8.1 also shows the presence of several manual valves (VM) installed generally at the inlet and outlet of each component for inspection in case of breakage. Moreover, a normally closed valve (VNC1) and normally open valves (VNO2 and VNO2') are installed at the outlet of evaporator: during the ORC start-up and shut-down operation, the fluid flows through the external casing of the expander (branch 1-2'), by-passing the expander cylinders (branch 1-2). The by-pass branch presence allows to increase the temperature of the expander surfaces, avoiding thermal and mechanical stresses possible during a cold start-up. When the desired temperature and pressure conditions are reached at the expander inlet, the VNC1 valve can be opened, in order to admit the fluid inside the expander. Moreover, a safety valve is installed at the outlet of the evaporator (point 1 in Figure 8.1) to avoid unexpected overpressure (maximum pressure value is set at 26 bar). The fluid exiting from the expander is sent to the recuperator through point 3 both in operative and by-passing mode. In the recuperator, the residual heat from the expander outlet stream is used to preheat the liquid prior to the evaporator inlet, in order to improve the overall cycle efficiency. Subsequently, the fluid flows to the condensations branches: the first branch

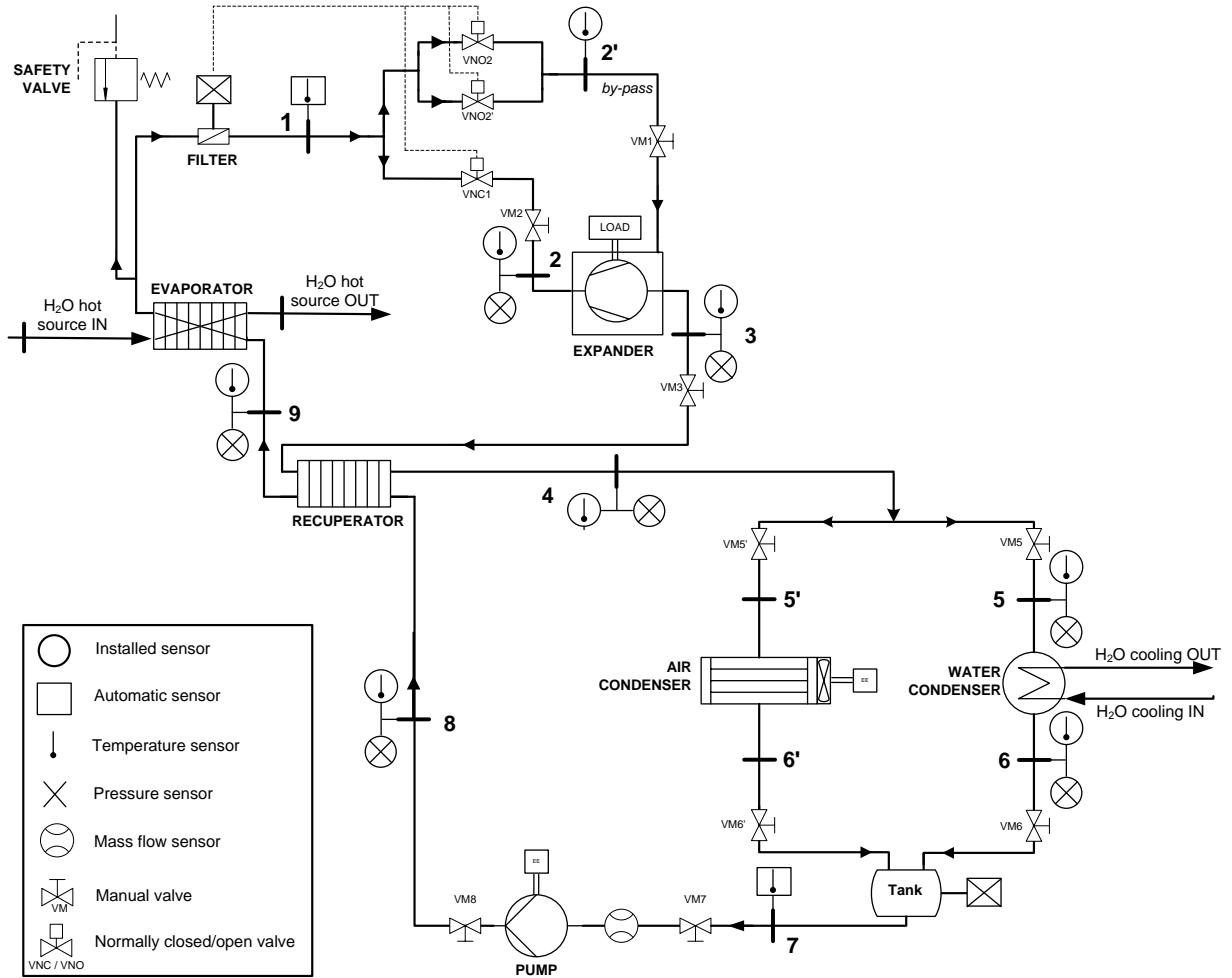


Fig. 8.1: The micro-ORC internal layout.

presents an air condenser, while the second one is a shell and tube condenser, coupled with the cold water cycle shown in Figure 8.2. Generally, during the experimental activities the air branch is maintained closed, through the VM5' and VM6' valves. The condensers outlet are collected in a tank, placed in the cycle between sections 6 and 7 (see Figure 8.1). During the tests, the collecting tank facilitates the presence of a liquid phase before the ORC pump (a gear pump with variable rotational speed, better described in Section 8.1.4) and consequently avoid problems. Meanwhile, during the maintenance operations, the fluid could be extracted from all sections and collected in it. Moreover, new fluid could be pumped in the tank during the refill procedures. In Figure 8.1 is also visible the presence of a filter (branch 1) to avoid the circulation of solid impurity. The cycle presents default temperature and pressure sensors, placed in sections 1 and 7, to measure the evaporation and condensation values. The system is also equipped with a front panel, that allows to open/close the by-pass branch, vary the pump rotational speed and display the measurement values. Furthermore, the evaporation and

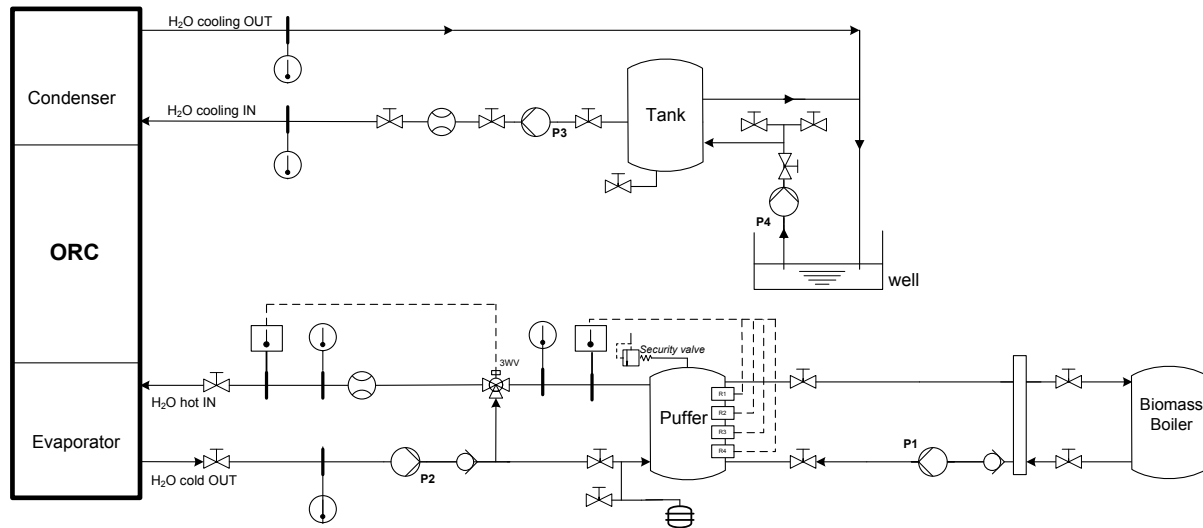


Fig. 8.2: The hot and cold water supply lines.

condensation pressure values control the automatic shut-down of the system in case of too high values.

Figure 8.4 presents the three dimensional layout of the micro-ORC under investigation, to better compare size and positions of the different components.

More sensors have been installed in the ORC system, as described in Chapter 9, to characterize the entire ORC system and identify the behavior of each component.

Figure 8.2 shows the hot and cold water supply lines. The project includes the heat input provided to the ORC by a biomass boiler producing hot water, model Tatano Kalorina 2204. The heat is supplied to the ORC evaporator via a circulation pump (P1) and an intermediate hot water storage puffer (model PFB, visible in Figure 8.5). It presents an internal plain tube heat exchanger, made of carbon steel and insulated with flexible polyurethane [107]. This tank is also equipped with four electric copper resistances (orange in Figure 8.5(a) and named R1-R4 in Figure 8.2). Each resistance absorbs an electric three-phase power equal to 8kW. The resistances are useful to compensate the boiler load variations or, if necessary, to completely replace the boiler thermal output. Tables 8.1(a) and 8.1(b) list the boiler and puffer main characteristics.

Figure 8.2 shows the presence of two thermostats installed in the hot water circuit: the first one is placed at the puffer outlet and it acts on the resistances switching on/off, while the second one is situated at the ORC evaporator inlet and it can control the

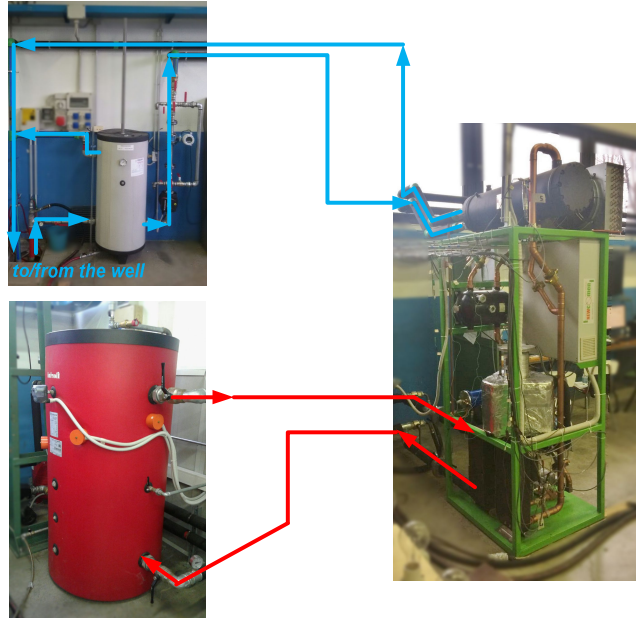


Fig. 8.3: Pictures and scheme of the test bench layout.

motor-driven three way valve (3WV in Figure 8.2). The valve control loop allows to decrease the evaporator inlet water temperature, by mixing the evaporator inlet with the return water. Due to the thermostats sensibility, actually they are bypassed and the resistances switching on/off is manually regulated. Moreover, a circulation pump, named P2, is installed in the return line.

The cold water is provided by a well available in the laboratory, as shown in Figure 8.2. A tank is installed in the line to compensate the well water variations and it presents an emptying system directly connected to the well. Moreover, two pumps are placed in the cold water circuit: the first one (P3) allows the water circulation in the condenser tool, while the second one (P4) draws water from the well. The cold water could be provided also by an external sources, through the valve installed between the pump P4 and the tank, as visible in Figure 8.2.

The model of pumps P1, P2 and P3 is a Grundfos Magna1 40-180F, characterized by various operational and control mode to change the water volumetric flow. Figure 8.6 shows the pump characteristic curves. More in details:

- the orange lines PP1, PP2 and PP3 represent the proportional pressure control

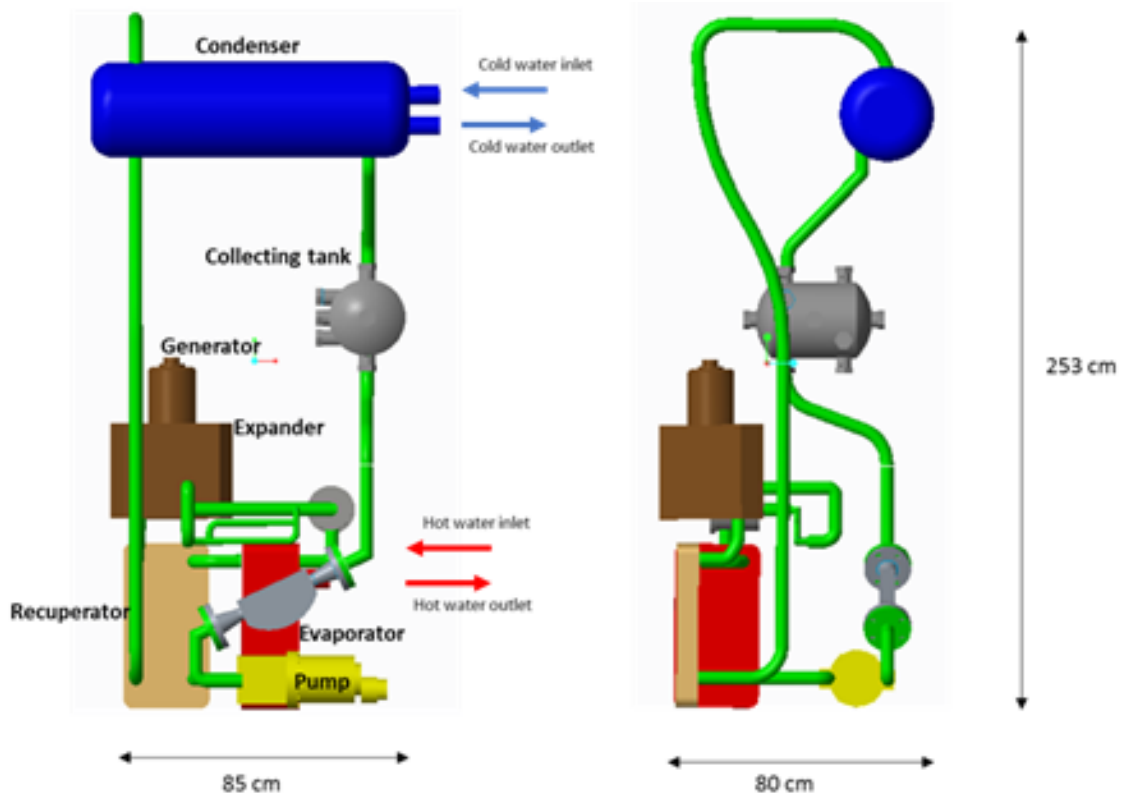


Fig. 8.4: ORC system 3D layout and size: frontal and lateral views.

mode, in which the pump performance are adjusted to the actual heat demand in the system;

- the red lines CP1, CP2 and CP3 represent the constant pressure control. This control adjusts the pump performance to the actual heat demand in the system;
- the blue curves I, II and III represent the constant speed operation. The pump runs at constant speed, independent of the actual flow demanded by the system. curve.

8.1 ORC prototype: main components

8.1.1 Evaporator and recuperator

The evaporator and recuperator are brazed plate heat exchangers, model ONDA S202, suitable for refrigerant fluids. The evaporator recovers heat from a hot water source to produce superheated organic fluid vapor, while the recuperator aims to recover the residual heat from the expander outlet stream to preheat the liquid prior to the evaporator inlet, in order to improve the overall cycle efficiency. More in details, the evaporator

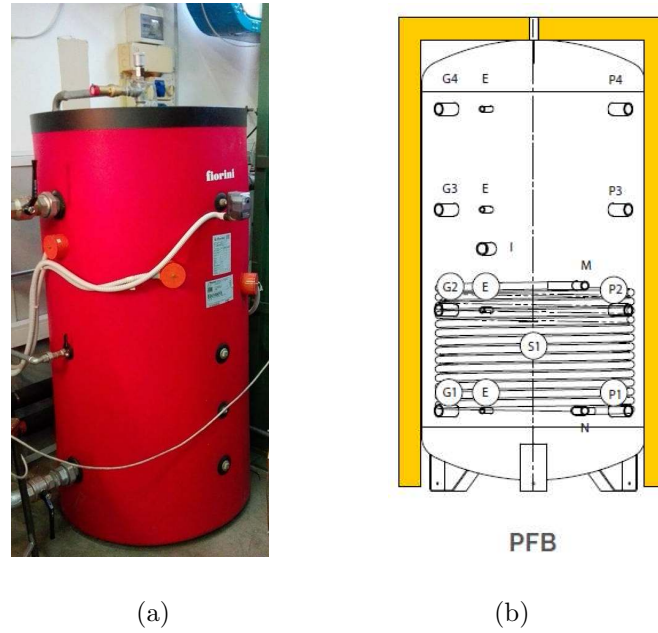


Fig. 8.5: PFB puffer picture fig. 8.5(a) and internal structure fig. 8.5(b).

presents 64 plates, while the recuperator 19. Figure 8.7 and Table 8.2 present the layout and the specifications of the heat exchangers [108]. The plates material is stainless steel 316L, with a thickness of 0.30 mm and the brazing material is copper. Considering Figure 8.7, for the evaporator W1 and W2 correspond to the hot water inlet and outlet, respectively; while BW1 and F2 correspond to the ORC fluid inlet/outlet (i.e. point 9 and 1 in Figure 8.1). In case of recuperator, F2 and F1 represent respectively the refrigerant vapor flow inlet and outlet (point 3 and 4), while the liquid flow enters in W2 and exits from W1 (point 8 and 9). On both heat exchangers, there is a layer of insulated material, in particular an expanded reticular polyethylene foam with a thickness of 8 mm. The working temperature of this material can vary between -50°C to 105°C [108].

8.1.2 Condenser

The water condenser is a shell and tube heat exchanger model ONDA CT 292. The condenser materials are compatible with refrigerant fluid, as HCFCs, HFCs, NH_3 . Commonly, the material of this kind of condensers consists of: headers made in cast-iron or carbon steel, tubesheets, shell, baffles and refrigerant connections in carbon steel and tubes in copper [109]. More specifications are presented in Table 8.3 and Figure 8.8. Another parameter indicated by the manufacture is the fouling factor, essential for the condenser operation, in particular after several operating hours. In [109] is indicated a fouling factor equal to $0.000\,043\text{ m}^2\text{ K W}^{-1}$ for normal city water and equal to

Table 8.1: Tatano Kalorina 2204 biomass boiler (8.1(a)) and storage puffer (8.1(b)) characteristics.

(a)		(b)	
Biomass boiler		Storage	Heat exchanger
Nominal heat output	46 kW	Max pressure	5 bar
Max pressure	3 bar	Max temperature	90 °C
Max temperature	85 °C	Volume	500 l
Water content	116 l	Surface	2.1 m ²
Rated voltage	230 V	Weight	80 kg
Rated current	4.7 A		
Rated frequency	50-60 Hz		
Rated input power	680 W		

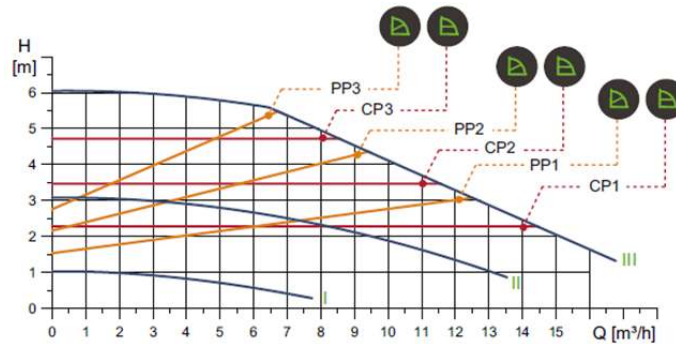


Fig. 8.6: Grundfos Magna1 40-180F operational curves.

$0.000\,086\text{ m}^2\text{ K W}^{-1}$ for river water. In the considered layout, the condenser uses cold water extracted from a well or an external source.

8.1.3 Expander

The expansion machine is a volumetric three pistons radial expander. The pistons are located at 120° and they work alternately to each other; this configuration allows to reduce mechanical block problems. A bigger model than the machine installed in laboratory has been patented by the manufacturer and some information about the machine are available in [106].

The bore and the stroke displacement of each cylinder are equal to 46 mm and the displacement of the expander results equal to 230 cm. The model available in the ORC under investigation presents a fixed valve timing (different from the new patented model) and the intake port results open during all the expansion phase (in the new model the intake port is closed 5 mm before the BDC). More in detail, the volumetric expander

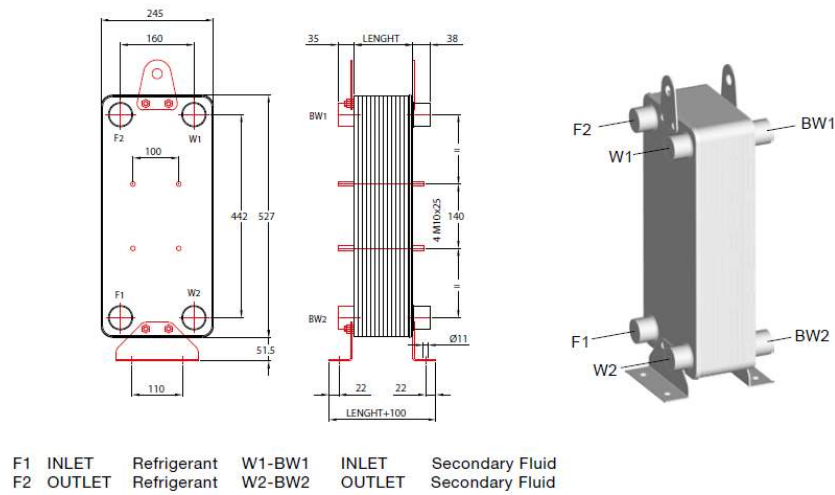


Fig. 8.7: Schematic layout of evaporator and recuperator heat exchangers.

Table 8.2: Evaporator and recuperator heat exchanger specifications.

Specifications	model S202	Evaporator	Recuperator
Pressure range [bar]	Vacuum to 30	Vacuum to 30	Vacuum to 30
Temperature range [°C]	-100 to +120	-100 to +120	-100 to +120
Maximum flow rate [m ³ h ⁻¹]	50.62	50.62	50.62
Volume per channel [l]	0.254	0.254	0.254
Dimensions [mm]	245 x 527	245 x 527	245 x 527
Plates number	N	64	19
Length [mm]	N x 2.35 + 10	160.4	54.65
Weight [kg]	N x 0.35 + 9.2	31.6	15.85

Table 8.3: Water condenser heat exchanger specifications [109].

Specifications		CT 202	
Using city water			
		Size [mm]	
Capacity [kW]	292	A	2145
Flow rate [m ³ h ⁻¹]	16.8	B	273
Pressure drop [kPa]	36	C	2000
Max flow rate [m ³ h ⁻¹]	30.5	D	275
Passes [-]	4	F	1500
Refrigerant side volume [l]	76.7	G	280
Water side volume [l]	28	R	100
Weight [kg]	158	S	88
		T	14

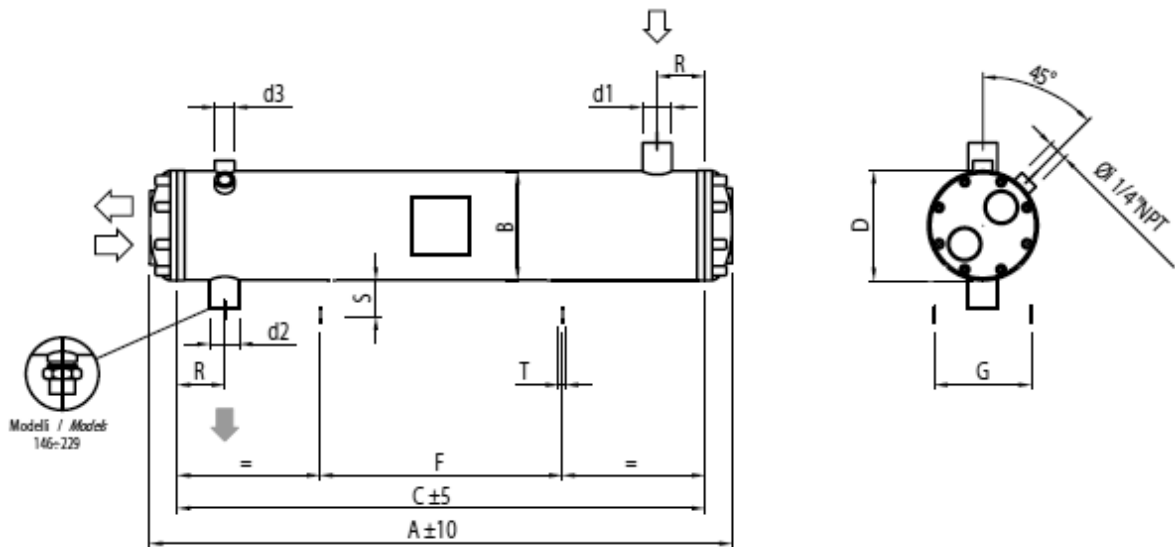


Fig. 8.8: Schematic layout of evaporator and recuperator heat exchangers [109].

comprises one jacket or cylinder (5 in Figure 8.9) housing an activate element (6) suitable for defining, in cooperation with said jacket, a variable volume expansion chamber (7). Further, the volumetric expander comprises a transmission element (37) connected, at one side, to the active element and, at the other side, to a main shaft (11). Such connection enables the active element to determine the rotation of the main shaft and therefore to convert the thermal power of the working fluid in mechanical power. The jacket (5) has an inlet and outlet (8 and 9), useful to introduce and discharge the working fluid from the expansion chamber (7). The inlet communicates with the evaporator and the outlet with the recuperator heat exchanger. Moreover, the volumetric expander comprises a valve (10), located outside the expansion chamber and it defines the head of the jacket (5). In this manner the main shaft rotates around his axis. Alternating the introduction, expansion and discharge conditions, the valve moves the active element inside the jacket with an alternate sliding due to the piston expander model. The expander defines two-stroke engine executing a complete cycle of introduction and discharge in just one revolution of the main shaft. The valve, to ensure the movement of the shaft, must synchronize the expansion conditions. In particular, Figure 8.10 presents the valve construction scheme, the jacket (5) comprises a cylinder shaped seat (22) inside which is a plunger-type piston (23). This piston has also a cylinder shape and it is slidingly-movable, giving the definition of alternate-type to the volumetric expander. The expander defines a radial or star cylinders expander, wherein the cylinder are according to radial lines, around the main shaft. In the consider case, the radial expander consist of only one star, formed by three radial cylinders. The valve comprises a distribution body (28), located in the valve body (24) and configured to follow a rotation inside the housing seat and to define the introduction, expansion and discharge conditions of the volumetric expander. Consequently, it defines the movement of the

active element (6) (i.e. the piston (23)) inside the jacket. In order to maximize the obtainable work, the discharge pressure at the outlet of the expander must be equal to the condenser pressure. If the pressure of the working fluid at the BDC is greater than the condensation pressure, there is a useful lost heat at the outlet of the expander which will be lost at the condenser, with a the production of a negative work, and consequently the reduction of efficiency and power production [106].

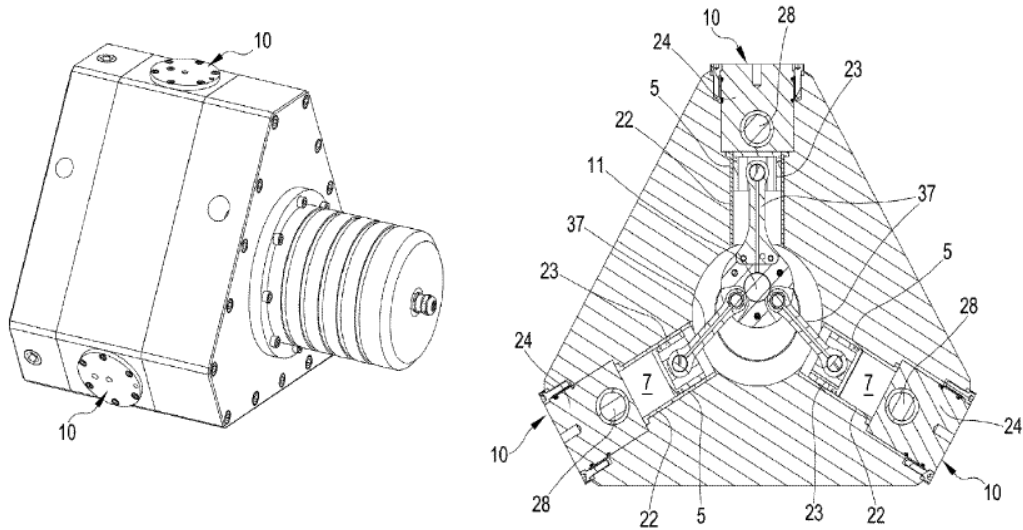


Fig. 8.9: Expander schemes, available in [106].

Figure 8.12(a) shows the kinematic connection between main shaft and rotating valve. This mechanism includes gears, pinions and idler gears. More in detail, the valves have to be able to rotate in synchronism with the displacement motion of piston, so that the suction or inlet is open when the piston is in a pre-established position (typically when the piston reaches an angles relative to the TDC), which depends on the operating pressure ratio, and it can be closed after a pre-defined fraction of time before the piston reaches the BDC [110].

On the expander surface, a layer of insulating material has been applied. More in details, the material is rockwool between two layers of silver foil, to avoid problem with humidity and eventual spills of fluid or oil (Figures 8.11(a) and 8.11(b)). To verify the good insulation, two thermocouples have been installed: the first one is placed between the expander surface and the insulating material, while the second one is on the external surface of that material.

The expander is directly connected with an electric AC generator, as visible in Figure 8.12(b), with the rated characteristics listed in Table 8.4. It is a synchronous phase generator and it has permanent magnets. Moreover, the generator presents a closed

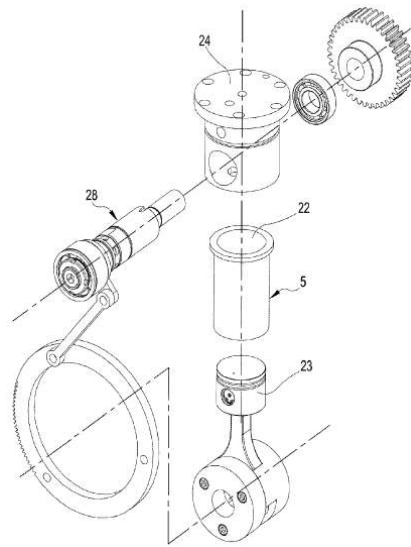


Fig. 8.10: Expander valve scheme [110].

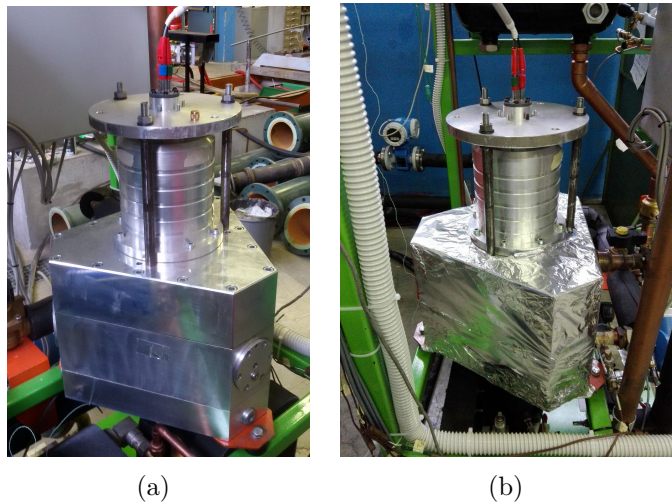


Fig. 8.11: The expander without (8.11(a)) and with (8.11(b)) the insulation material.

cooling system using R134a as fluid [111]. The electric load implemented in laboratory is a variable resistive load, able to dissipate the produced electric power, with different set point up to 3 kW, with steps equal to 600 kW.

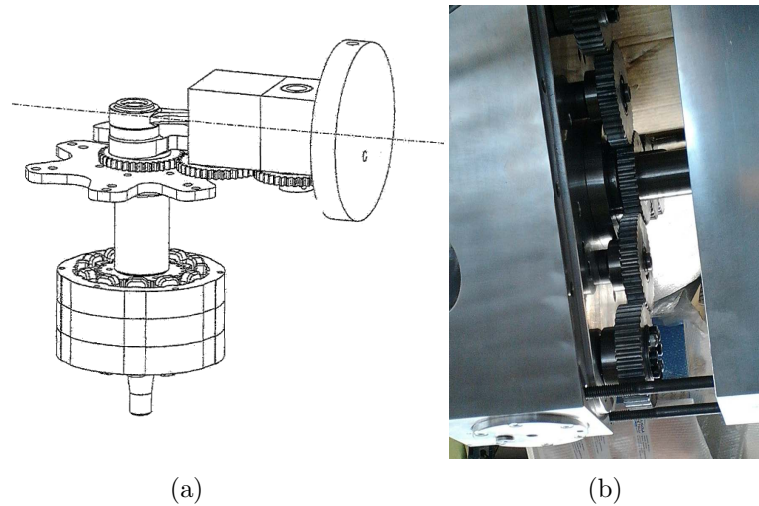


Fig. 8.12: Kinetic mechanism scheme fig. 8.12(a) and a detail of the kinetic mechanism in the considered expander fig. 8.12(b).

Table 8.4: Design specifications provided by the manufacturer for the electric generator.

Model	NGB 145 M-SA
Nominal electric power	3 kW
Efficiency (hot operation)	90 %
Nominal current	5.2 A
Nominal voltage phase-phase	380 V
Nominal frequency	120 Hz
Nominal rotational speed	1800 rpm
Nominal couple	17.8 N m
Poles number	8

8.1.4 Pump

The organic fluid recirculation pump is a volumetric external gear pump, normally operated with variable speed, by means of an inverter, in order to control the mass flow of R134a through the cycle. More informations are not available, because the pump is a prototype not yet patented. The electric generator connected to the pump is the same used for the expander (see Table 8.4). Using a gear pump is a good choice, because it is able to operate also with quality lower than 1.

Gear Pump

External and internal gear pumps are similar in pumping action and two gears come into and out of mesh to produce flow. However, the external gear pump uses two identical gears rotating against each other: one gear is driven by a motor and

it, in turn, drives the other gear. Each gear is supported by a shaft with bearings on both sides of the gear. The below figure on left presents the operational steps of an internal gear pump. More in details:

1. as the gears come out of mesh, they create expanding volume on the inlet side of the pump. Liquid flows into the cavity and is trapped by the gear teeth as they rotate;
2. liquid travels around the interior of the casing in the pockets between the teeth and the casing, it does not pass between the gears;
3. finally, the meshing of the gears forces liquid through the outlet port under pressure.

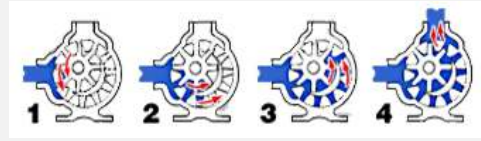
Because the gears are supported on both sides, external gear pumps are quiet-running and are routinely used for high-pressure applications such as hydraulic applications. With no overhung bearing loads, the rotor shaft can not deflect and cause premature wear [112].

Internal gear pumps are exceptionally versatile. They can operate with wide viscosity and temperature range . This is due to the single point of end clearance (the distance between the ends of the rotor gear teeth and the head of the pump). This clearance is adjustable to accommodate high temperature, maximize efficiency for handling high viscosity liquids, and to accommodate for wear. Moreover, they can run dry for short periods. They are also bi-rotational, meaning that the same pump can be used to load and unload vessels. Because internal gear pumps have only two moving parts, they are reliable, simple to operate, and easy to maintain. The figure on right shows the typical operational steps of a internal gear pump:

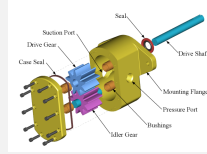
1. liquid enters the suction port between the rotor (large exterior gear) and idler (small interior gear) teeth. The arrows indicate the direction of the pump and liquid;
2. liquid travels through the pump between the teeth of the "gear-within-a-gear" principle. The crescent shape divides the liquid and acts as a seal between the suction and discharge ports;
3. the pump head is now nearly flooded, just prior to forcing the liquid out of the discharge port. Intermeshing gears of the idler and rotor form locked pockets for the liquid which assures volume control;
4. rotor and idler teeth mesh completely to form a seal equidistant from the discharge and suction ports. This seal forces the liquid out of the discharge port [113].



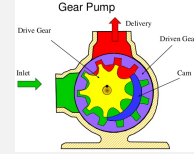
External gear pump operation [112].



Internal gear pump operation [113].



An exploded view of an external gear pump.



Components of an internal gear pump

CHAPTER 9

The test bench instrumentation and acquisition system

Summary. This chapter presents the sensors installed in the test bench, both on ORC and water sides, and the measure chain realized in the laboratory. An acquisition system is developed in Labview environmental to monitor the system behavior in real time and the parameter and the performance indexes evaluated from the measured quantities are introduced and described.

9.1 Selected and installed sensors

In order to collect data on the operation of the system, the test bench has been instrumented with temperature and pressure sensors. The measurements of temperature are made through 8 T-type and 8 K-type thermocouples, placed in the ORC and in the water cycle respectively, as indicated in Figures 8.1 and 8.2. Thermocouples have been individually calibrated at the laboratory in a thermostatic bath against a reference temperature sensor (a resistance thermometers PT100), connected to an acquisition system model Microcal 200, both visible in Figure 9.1. Thus, a first order linear calibration curve is obtained in the range 300 K to 395 K (more details available in Chapter B). The accuracy of these sensors is estimated as equal to ± 0.5 K.

The organic fluid pressure is measured by ceramics pressure transducers (Honeywell FP2000 model visible in Fig.9.2(a)) with a total error band equal to ± 0.25 %FS. Pressure transducers have different characteristics according to the high and low pressure branches (see Table 9.1) and they have been also calibrated in the laboratory. The low pressure sensors have been calibrated between 0 bar to 10 bar, while the high pressure sensors in the range 0 bar to 20 bar, due to the upper limit of the calibration system. The pressure taps are flush mounted, thus measuring the static pressure. The pressure and temperature sensors are placed in the same positions, as shown in Figure 9.2(a), at the inlet and outlet of each ORC component. This arrangement allows to characterize, besides the entire cycle, also each component, evaluating for instance physical states, pressure drops and thermal exchanges.

After the sensor installation, the system has been pressurized with air to check for the leakages. It has been observed that most of the minor leakages occurred at instrumentation joints with the pipes, Teflon has been used for gaskets or sealing purpose or torque adjustment in threads. After ensuring the air tight sealing of the test rig, vacuum

pump has been attached in the piping loop. Then working fluid has been charged to the receiver tank of the test rig. The ORC mass flow rate measure is a Coriolis unit (Endress+Hauser Promass 80E model visible in Figure 9.2(b)), located downstream the working fluid tank and upstream the gear pump. This placement: (i) allows to fill always the tube, avoiding measurement problems; (ii) reduces the induced-vibration due to the gear pump operation and (iii) it is the correct placement in terms of straight pipe lengths. The signal output is a 4 mA to 20 mA current output, corresponding to 0 g s^{-1} to 1400 g s^{-1} (Table 9.1). This sensor can measure three parameters at the same time: the other available parameters are fluid density and temperature.

Regarding hot and cold sources flow sensors, on the hot water side it is measured by an electromagnetic volumetric flow sensor model Endress+Hauser Promag 50P (Figure Figure 9.3(a)), placed in the evaporator water inlet branch (see Figure 8.2). Also in the cold water side an electromagnetic volumetric flow sensor (model Endress+Hauser Promag 10D in (Figure Figure 9.3(b))) is installed, placed after the pump P2. The output signals are 4 mA to 20 mA. The measurable flow values range has been set between 0 l s^{-1} to 4 l s^{-1} in both the flowmeters.

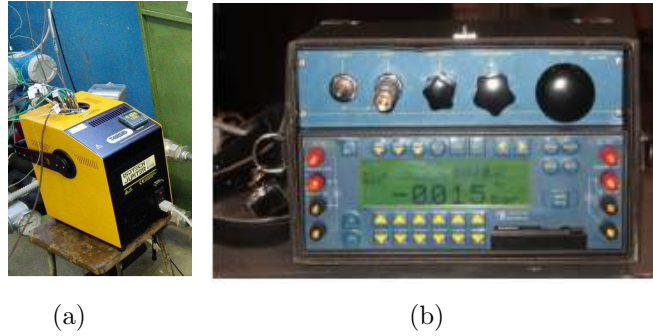


Fig. 9.1: Thermostatic bath, reference temperature sensor Figure 9.1(a) and acquisition system Figure 9.1(b) used during calibration procedure.

Table 9.1 lists the main characteristics of the described sensors with the specification of the ORC layout point where they are placed.

Table 9.1: ORC sensors main data.

	Pressure transducer		T-type	ORC mass	ORC fluid
	High Pressure	Low Pressure	thermocouples	flow sensor	density
ORC layout point	2, 8, 9	3, 4, 5, 6	2,2',8, 9, 3, 4, 5, 6	7	7
Output signal	0-5 V	0-5 V	$\pm 8 \text{ mV}$	4-20 mA	4-20 mA
Measurement range	0-30 bar	0-10 bar	-270-400 °C	$0-1400 \text{ g s}^{-1}$	$10-1400 \text{ kg m}^{-3}$
Accuracy	0.25 % FS	0.25 % FS	$\pm 0.5 \text{ K}$	0.2 % R	$\pm 0.02 \text{ g cm}^{-3}$

A Printed Circuit Board (PCB) has been connected to the expander electric generator. The PCB allows to measure the current and voltage values of each phase, through three volt transducers and three current transducers, visible in Figure 9.4. The elaboration

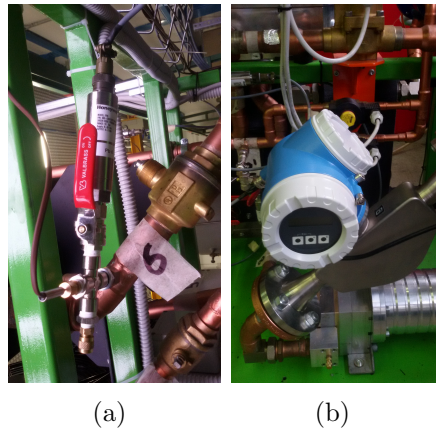


Fig. 9.2: Pressure and temperature sensors placed in the ORC [9.2(a)] and Coriolis mass flow rate measure [9.2(b)].

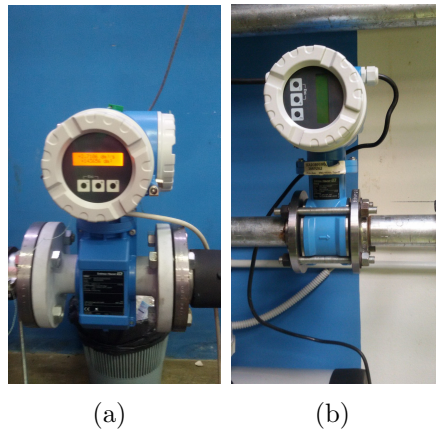


Fig. 9.3: Electromagnetic volumetric flow sensors placed in the hot water [9.3(a)] and in the cold water sides [9.3(b)].

of these signals lets to evaluate the three phase electric power produced by the ORC. A similar circuit has been connected to the pump, placed between the inverter and the pump engine, to evaluate the pump electric power consumption. Table 9.2 presents the relation between the voltage signals sent to the acquisition system and the voltage/current values of each phase set in the expander and pump PBC (at the present state the signal from the pump PCB is not elaborated).

Table 9.2: PCBs settings.

	Expander		Pump	
	<i>measure</i>	<i>signal</i>	<i>measure</i>	<i>signal</i>
voltage measurement	100 V	1 V	100 V	1 V
current measurement	1 A	400 mV	1 A	1 V

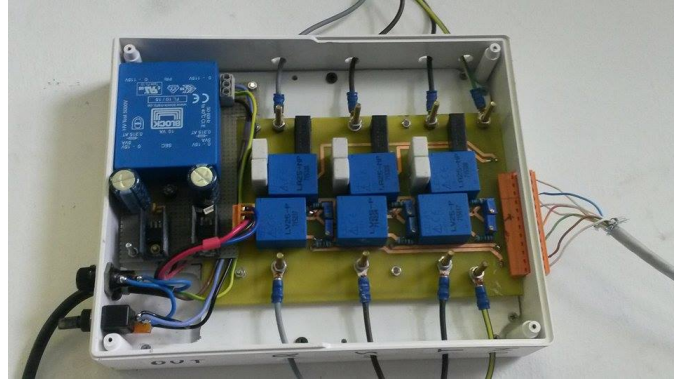


Fig. 9.4: Printed circuit board installed.

Electric power calculation

The generator electric power and the pump electric power consumption, following named P_{el} and $P_{PUMP,el}$ respectively, are three phases values. They are evaluated from the elaboration of volt $v(t)$ and current $i(t)$ signals of each phase, sampled with a velocity equal to 10 kS. More in details, the phases power values $P_1(t), P_2(t), P_3(t)$ are evaluated as following:

$$P_1(t) = v_1(t) \cdot i_1(t)$$

$$P_2(t) = v_2(t) \cdot i_2(t)$$

$$P_3(t) = v_3(t) \cdot i_3(t)$$

The sum of the averaged values, considering a time step equal to 1 s, $\bar{P}_1, \bar{P}_2, \bar{P}_3$ corresponds to the three phases power production P_{el} or, in case of the pump power consumption, $P_{PUMP,el}$.

9.2 Developed acquisition system

The test bench is also endowed with a data acquisition system. A real-time microcontroller, namely a National Instrument CompactRIO system [114], has been used to acquire signals from the installed sensors. It consist of two separable parts and consequently two processing targets: (i) a real-time processor for communication and signal processing and (ii) a user-programmable FPGA (Field Programmable Gate Array) to implement high-speed control and custom timing and triggering directly in hardware. The chassis embedded available in laboratory is a NI cRIO 9114 model (see Figure 9.5(a)) with 8 slots [115], while the controller Real Time is a NI cRIO 9022 (Figure 9.5(b)) [116]. The cRIO presents various modules, selected based on the sensors output signals. In particular:



Fig. 9.5: Chassis NI c-RIO 9114 [9.5(a)] and controller NI c-RIO 9022 [9.5(b)].

- a NI 9213 input module reads the voltage thermocouples signals [117];
- a NI 9207, an analog voltage and current input module, elaborates the signals from the flow and pressure sensors [118];
- two NI 9201, analog input modules provide 8 channels of ± 10 V with 500 kS/s sample rate, suitable to manage electric quantities [119].

Figure 9.6 presents the scheme of the entire chain of measure, highlighting the signals typologies and the acquisition system structure. Table 9.3 lists the main specifications about the entire sensors apparatus.

An acquisition software and a display panel have been realized in the laboratory computer (*HOST* in Figure 9.6), both developed in LabVIEW environment. Data have been acquired with a time step equal to 1 s. The fluid library properties CoolProp [120] has been integrated in the developed acquisition software, in order to obtain the thermodynamic state of each ORC section and to evaluate the overall performances. The evaluated states are used to instantly realize the ORC thermodynamic cycle, displayed in real time on temperature/entropy and pressure/enthalpy diagrams.

Figure 9.7 presents the thermodynamic cycle of the system on the T,s diagram. The thermodynamic states reported have been evaluated from the pressure and temperature values visible in Figure 9.8. Both these diagrams (and others do not shown in the chapter) are uploaded every second, based on the measured data.

The front panel developed shows in real time the evolution of various parameters, evaluated as following described.

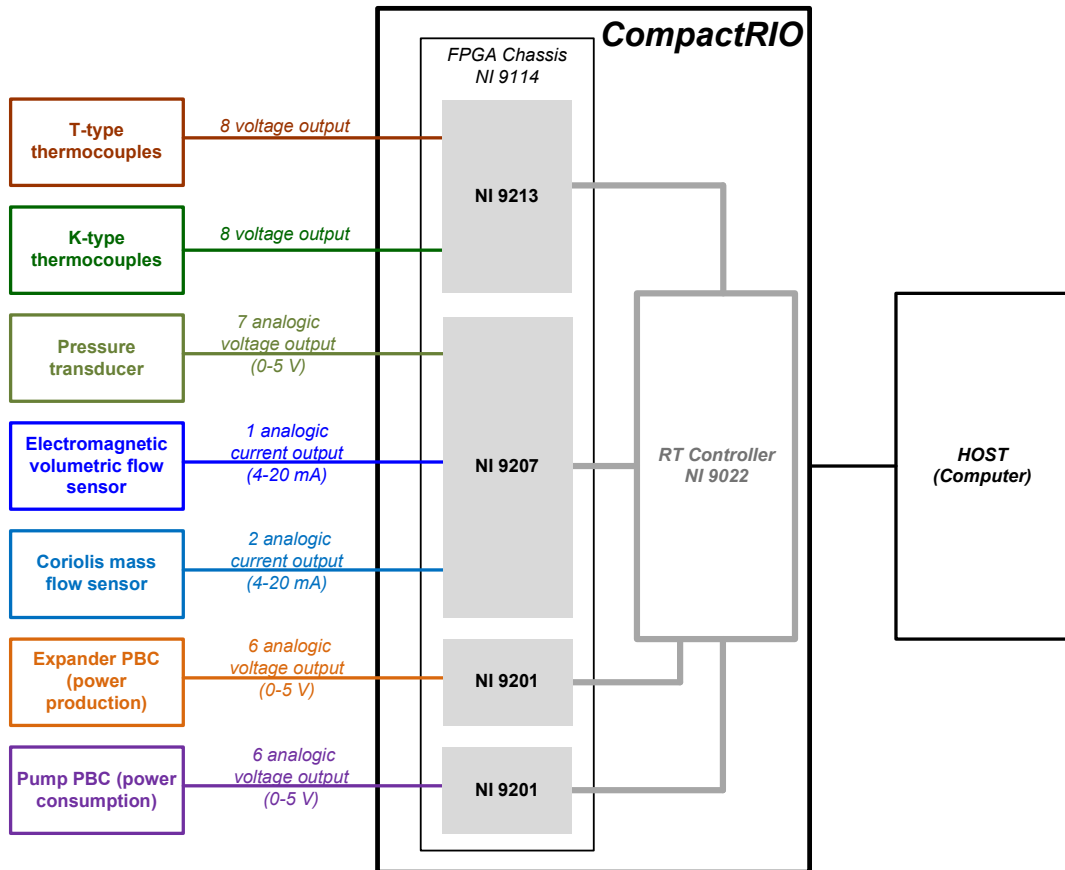


Fig. 9.6: Scheme of the measure chain in the realized test bench.

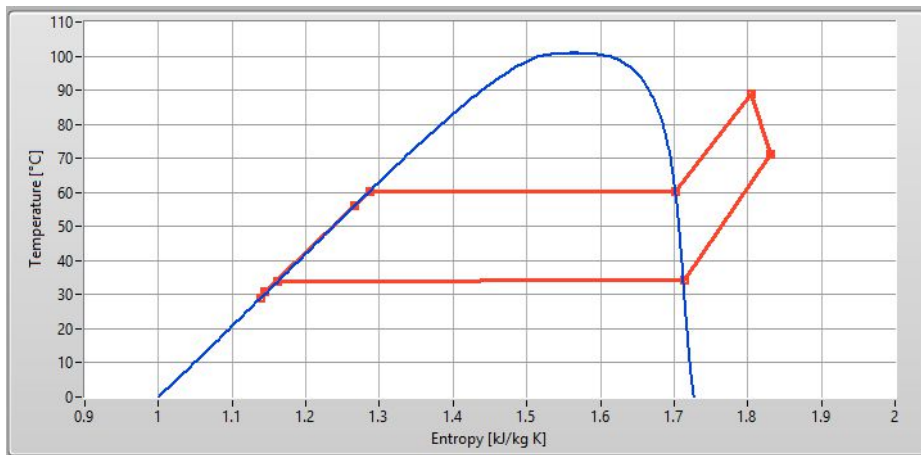


Fig. 9.7: The T,s diagram updated in real-time, based on the acquired temperature and pressure values measured.

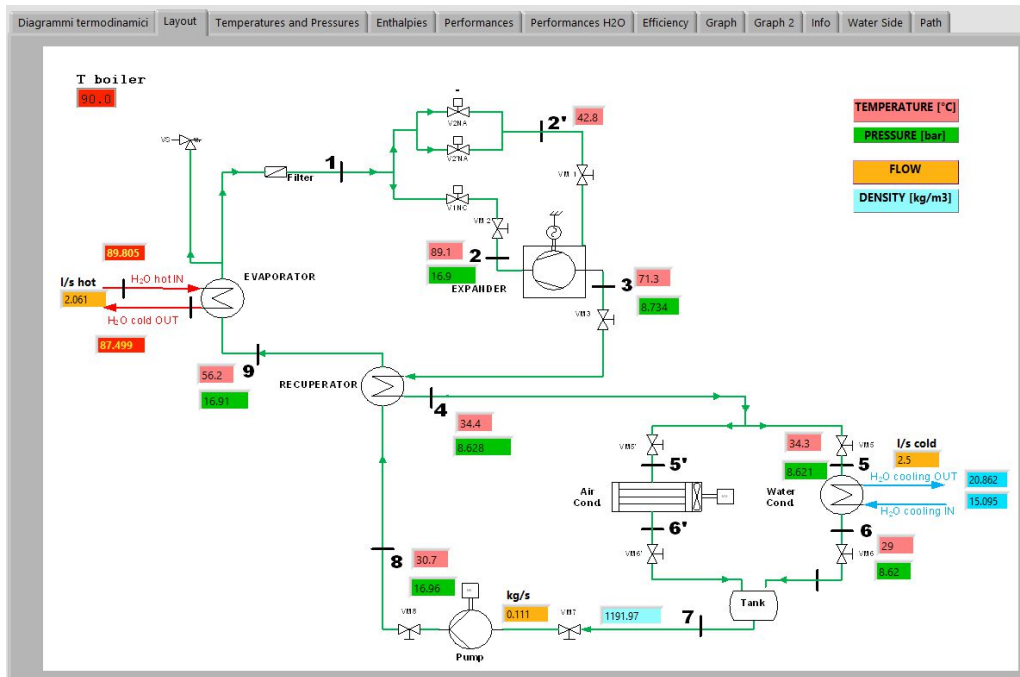


Fig. 9.8: Sensors measurement and positions on the system layout (picture extracted from the implemented real-time visualization panel).

Coolprop

CoolProp is an open-source thermophysical property library. This library is written in C++, with wrappers available for the majority of programming languages and platforms. It includes 110 pure and pseudo-pure fluids, as well as properties of 40 incompressible fluids and humid air [120].

The temperature and pressure values allow to identify the physical state of each ORC point through the use of this library. Therefore, the values of enthalpy, entropy, density and quality are available in all the measured points of the systems. Moreover, the saturation conditions, as temperature or enthalpy values, are evaluated setting the pressure equal to pressure measure and the quality equal to 0 or 1, depending on the phase of the considered stream. Tillner-Roth and Baehr in [121] estimate the accuracy of state equations (based the most accurate measurements of pressure, density, temperature, speed of sound, heat capacity and vapour pressure) for R134a in a range between 170 K to 455 K and pressure up to 70 MPa. Typical accuracy are $\pm 0.05\%$ for density, $\pm 0.02 - \pm 0.5\%$ for vapour pressure and $\pm 1\%$ for the heat capacity. R134a results as one of the fluids for which the thermodynamic properties are known at a superior level of accuracy. the following figure presents the bloc diagram of Coolprop

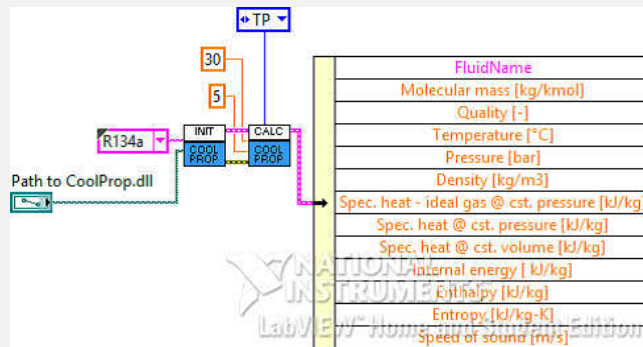
Table 9.3: Acquisition system specifications.

Physical quantity	Layout quantity	Sensor	Calibration range	Output signal	Accuracy Accuracy	Input module
ORC Temperatures	$T_2, T_2, T_3, T_4, T_5, T_6, T_8, T_9$	T-type thermocouple	0-90 °C	±80 mV	0.5 K	NI9213
ORC Pressures	p_2, p_8, p_9 p_3, p_4, p_5, p_6	Pressure transducer	0-20 bar 0-10 bar	0-5 V	0.25 %FS	NI9207
ORC mass flow rate	\dot{m}_{ORC}	Coriolis mass flow meter	0-0.5 kg s ⁻¹ *	4-20 mA	0.2 %R*	NI9207
ORC density	ρ		10-1300 kg m ⁻³ *	4-20 mA	0.02 g cm ⁻³ *	
Hot water temperatures	$T_{in, EVAP}, T_{out, EVAP}$	K-type thermocouple		±80 mV	0.5 K	NI9213
Cold water temperatures	$T_{in, COND}, T_{out, COND}$		±80 mV	0.5 K		
Hot water flow rate	$\dot{q}_{H_2O, hot}$	Magnetic flow meter	0-6.41 s ⁻¹ *	4-20 mA	0.5 %R *	NI9207
Cold water flow rate	$\dot{q}_{H_2O, cold}$	Magnetic flow meter	0-9.81 s ⁻¹ *	4-20 mA	0.5 %R *	
Electrical output power	P_{el}	PCB	0-400 V 0-5 A	0-4 V	0.1 %R 0.2 %R	NI9201

* Provided by manufacturer

in Labview environment. In figures the selected quantity are temperature and pressure (respectively equal to 30 °C and 5 bar), used as input to evaluate the physical state of R134a at that conditions. In the developed acquisition system, Coolprop is used to evaluate physical state at the inlet and outlet of each ORC component from pressure and temperature as input. It is used to evaluate saturation conditions from quality and pressure values. The figure shows also the list of physical quantity available as output. Moreover, Coolprop allows to obtain the saturation curves of the selected fluid. More information are available in Chap-

ter C.



Coolprop Block Diagram in Labview environment.

9.3 Performance parameters

Various power quantities are calculated based on thermodynamic analysis, as shown in eq. (9.1)-eq. (9.8), using the thermodynamic state of each section of the ORC system, . More in details:

- Q_{evap} and Q_{in} are the thermal power exchanged by the working fluid with the hot and cold sources, respectively in the evaporator (sections 9 and 2) and in the condenser (5 and 6). These parameters are evaluated as the product between the organic fluid mass flow rate (\dot{m}_{ORC}) and the enthalpy variation. Both these thermal powers are considered as positive flows.

$$Q_{in} = \dot{m}_{ORC} \cdot (h_2 - h_9) \quad (9.1)$$

$$Q_{out} = \dot{m}_{ORC} \cdot (h_5 - h_6) \quad (9.2)$$

- $Q_{H_2O,hot}$ and $Q_{H_2O,cold}$ are the thermal power exchanged into the evaporator and condenser, considering the water side. They are given by the product between the hot/cold water volumetric flow rate ($\dot{q}_{H_2O,hot}$ or $\dot{q}_{H_2O,cold}$), the temperature variations, the water density (ρ_{H_2O}) and the specific heat at constant pressure (c_{pH_2O}) (both evaluated at the inlet temperature through the Coolprop library).

$$Q_{H_2O,hot} = \dot{q}_{H_2O,hot} \cdot \rho_{H_2O} \cdot c_{pH_2O} \cdot (T_{in,EVAP} - T_{outT,EVAP}) \quad (9.3)$$

$$Q_{H_2O,cold} = \dot{q}_{H_2O,cold} \cdot \rho_{H_2O} \cdot c_{pH_2O} \cdot (T_{out,COND} - T_{in,COND}) \quad (9.4)$$

- $Q_{REC,v}$ and $Q_{REC,l}$ represent the heat exchanged in the vapor (3 and 4) and liquid side (8 and 9) of the recuperator (both considered positive).

$$Q_{REC,v} = \dot{m}_{ORC} \cdot (h_3 - h_4) \quad (9.5)$$

$$Q_{REC,l} = \dot{m}_{ORC} \cdot (h_9 - h_8) \quad (9.6)$$

- $P_{EXP,fluid}$ is the thermodynamic power of the fluid during the expansion phase, considering the expander as a black-box. It is calculated as the product between the ORC working fluid and its enthalpy decreasing during the expansion phase. This value will be affected by the characteristic losses of expander.

$$P_{EXP,fluid} = \dot{m}_{ORC} \cdot (h_2 - h_3) \quad (9.7)$$

- P_{PUMP} is the pump consumption, evaluated as the product between the ORC mass flow and the pressure variation respect to the density at the pump inlet (ρ_7 measured trough the Coriolis sensor).

$$P_{PUMP} = \frac{\dot{m}_{ORC} \cdot (p_8 - p_6)}{\rho_7} \quad (9.8)$$

The evaluation of the system and components performance is possible from the previously defined quantities. The performance indexes introduced as key indicator of the ORC system are presented in eq. (9.9)-eq. (9.14). In particular:

- $\eta_{ORC,gross}$ represents the ORC gross efficiency, given by the ratio between the electric power production (P_{el} , i.e. the generator power output) and the thermal power inlet the ORC (evaluated on the ORC side).

$$\eta_{ORC,gross} = \frac{P_{el}}{Q_{in}} \quad (9.9)$$

- $\eta_{ORC,net}$ is the ORC net efficiency. Respect the $\eta_{ORC,gross}$ value, the generator power output is reduced of the pump power consumption.

$$\eta_{ORC,net} = \frac{P_{el} - P_{PUMP}}{Q_{in}} \quad (9.10)$$

- $\eta_{iso,EXP,el}$ represents the electrical isentropic efficiency of the expander, i.e. the ratio between the electric power output and the power produced if the fluid expansion was isentropic from the supply to the discharge pressure. In particular, $h_{3,iso}$ is the fluid specific enthalpy evaluated at pressure equal to p_3 and entropy equal to s_2 . This parameter is affected by the losses occurring during the expansion phase.

$$\eta_{iso,EXP,el} = \frac{P_{el}}{\dot{m}_{ORC} \cdot (h_2 - h_{3,iso})} \quad (9.11)$$

- FPR , i.e. the Fluid Power Ratio, allows to evaluate how much of the power available in the fluid is transformed in electric power. The introduction of this parameter is due to the absence of sensors to measure the internal pressure of each cylinder.

$$FPR = \frac{P_{el}}{P_{EXP,fluid}} \quad (9.12)$$

- η_C and $\eta_{C,tot}$ are the Carnot efficiencies, considering the ORC internal temperature values or the external sources temperature values (in K), respectively.

$$\eta_C = 1 - \frac{T_6}{T_2} \quad (9.13)$$

$$\eta_{C,tot} = 1 - \frac{T_{in,COND}}{T_{in,EVAP}} \quad (9.14)$$

The presented parameters are used in the following sections to characterize the behavior of the ORC system and of each component.

CHAPTER 10

Test campaign

Summary. This chapter presents the test campaign carried out on the ORC prototype system installed in the laboratory. The ORC behavior is described and from the collected data a primary identification of steady state conditions allows to analyze and compare averaged data. The aim of the test campaign is realize operational maps to characterize the ORC prototype system and its components.

The aim of the experimental test campaign carried out is the investigation on the micro-ORC behavior and its thermodynamic performances in different operating conditions. The test campaign has been executed at different thermal power from the hot sources and varying the ORC mass flow. In more details, the resistances switching on and off in the hot water line has been controlled to maintain the average hot source temperature value equal to the set point, while the ORC pump rotational speed has been varied through the inverter regulation. Figure 10.1 presents the entire layout of the test rig.

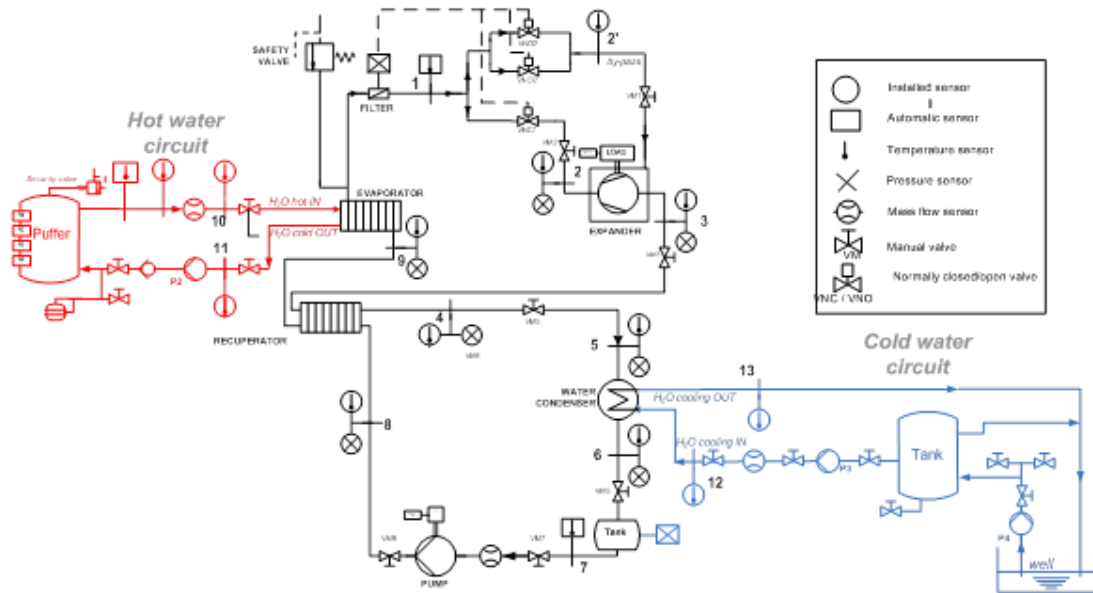


Fig. 10.1: ORC simplified layout.

10.1 Steady state operational windows preliminary identification

Several experimental tests are considered and examined in this thesis to analyze different ORC conditions. Based on the experimental experience, the relation between the various ORC parameters have been observed, with the aim to identify the fundamental parameters to described the ORC behavior. During the test campaign, the system has been operated to obtain steady states. Therefore, limited time windows are considered in this thesis and the steady state operations are manually identified if the following conditions are satisfied at the same time:

1. on the hot water side $T_{in,EVAP} \approx constant$ and $\dot{q}_{H_2O,hot} \approx constant$;
2. on the cold water side $T_{in,COND} \approx constant$ and $\dot{q}_{H_2O,cold} \approx constant$;
3. $\dot{m}_{ORC} \approx constant$;
4. $P_{el} \approx constant$;
5. $N_{EXP} \approx constant$.

Conditions 1 and 2 are related to the thermal power exchanged between the ORC system and the external sources. The hot source condition influences the maximum temperature of the cycle (T_2) and the range of pressure values allowable through the pump rotational speed variation. Consequently, this condition affects the evaporation temperature and superheating degree. Meanwhile, the cold source temperature and flow rate have an effect on the condensation pressure, on the subcooling degree and consequently on the enthalpy variation through the expander.

Conditions 3, 4 and 5 are related to the ORC behavior. The working fluid mass flow rate depends on the pump rotational speed and this value is related to the ORC maximum pressure p_2 . The electric power production is influenced by the maximum and minimum pressure values and mass flow rate. The expander rotational speed N_{EXP} (condition 5) influences the temperature and pressure at the expander discharged, caused by the expander frequency variability. The expander works at variable rotational speed and the temperature and pressure conditions at the outlet depend on the internal behavior, actually not completely defined due to the prototypical nature of the expander. As example, Figure 10.2 presents some data collected during a test. The hot water temperature at the evaporator inlet ($T_{in,EVAP}$) has been set equal to 65 °C, the frequency of the pump has been varied from 25 Hz to 30 Hz and the cold source temperature ranges between 17 °C to 17.9 °C.

In particular, Figure 10.2(a) shows the ORC mass flow rate behavior, Figure 10.2(b) presents the thermal power supplied by the hot and cold sources, related to the conditions 1 and 2. Figure 10.2(c) presents the electric power generated. Meanwhile,

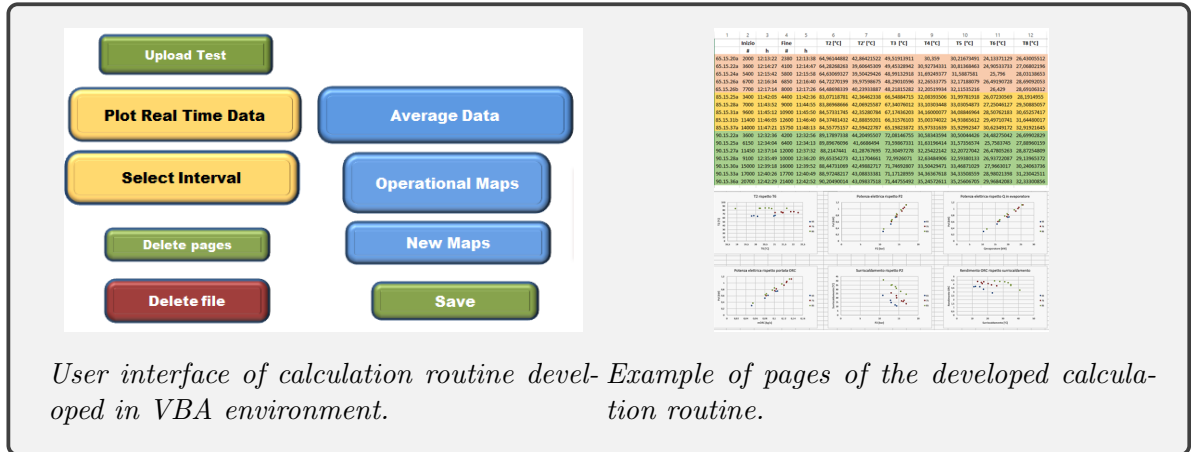
Figure 10.2(d) reports the behavior of expander rotational speed and Figure 10.2(e) the enthalpy variations at the expander outlet. In these figures the areas at the beginning and at the end of the test (in gray stripes) correspond to the start-up and shut-down phases of the ORC system. Moreover, the variation of pump rotational speed is highlighted (nearly at 600 s) and the effect are appreciable from the reported quantities. The stability of selected quantities imply the steady state of the system. As example Figures 10.3(a) and 10.3(b) report the heat exchange at the recuperator (on vapour and liquid sides) and the ORC gross efficiency $\eta_{ORC, gross}$. From the considered test the interval selected are 350 s to 420 s and 730 s to 800 s, highlighted in the figures as gray areas.

Once identified the ORC steady state conditions, the measured quantities and calculated performance have been averaged to identify an operational point. The data obtained are shown and analyzed in the following section.

The steady state preliminary identification is useful to understand and observe the ORC system behavior and to identify the relation between the several quantities measured and calculated. However, the proposed identification method could be improved based on methods and examples available in literature, as Woodland et al. [122], that propose a standard for ORC steady state measurement detection based on temperature, pressure, mass flow rate and rotational speed values variations. Other methods are F-test [123], t-tests [124], T^2 tests [125]. Kim et al. [126] propose an algorithm based on the evaporator superheat and condenser subcooling values, identified as sufficient parameters to determine the onset of steady state [127].

Calculation Routine

A calculation routine has been realized in VBA environment, with the aim to reduce the data computational time. This code allows to graph the parameters, divided by typology and system zone, recorded during a test or during a part of that. It allows to compare data from different test and to identify measurement problems or calculation mistakes. Moreover, the code can evaluate the averaged data for selected time interval and identify the maximum and minimum value of each quantity. Finally, the averaged data of various tests can be automatically plotted and compared on operational maps. The maps presented in the following sections have been obtained through the use of this calculation routine. The following figures presents the user interface and some pages realized.



10.2 Results and operational maps

This section presents the ORC system operational maps based on the experimental data obtained during test campaign. From these data an analysis has been conducted and the results are exposed and discussed. The coordinates of the maps correspond to the performance indexes and quantities evaluated as described in Section 9.3.

The ORC module was tested under various conditions, as presented in Table 10.1: the hot water temperature was varied and set at three different steps; the cold and hot volumetric flow rates were imposed at the maximum values; the cold water source temperature cannot be strictly controlled, because influenced by external conditions. However, it has been maintained lower than 19 °C in all the considered tests. Under the presented conditions, the pump frequency f_{PUMP} and consequently the rotational speed has been manually varied, influencing the ORC mass flow rate and evaporation.

Table 10.1: Tests operating conditions.

$Test$ $name$	$T_{in,EVAP}$ [°C]	$\dot{q}_{H_2O,hot}$ [l s ⁻¹]	$\dot{q}_{H_2O,cold}$ [°C]	$T_{in,COND}$ [l s ⁻¹]	f_{PUMP} [Hz]
A1	65	2.6	2.8	16.5 ÷ 18.5	18,25,30
B1	75	2.6	2.8	17 ÷ 19	25,30,35,38,40
C1	85	2.6	2.8	16.5 ÷ 18	18,25,30,35,40

Figure 10.4(a) presents hot source temperatures as function of cold source temperatures during the steady state operational points. Figure 10.4(b) shows the behaviors of ORC evaporation and condensation temperatures (T_{ev} and T_{cd} respectively). T_{ev} and T_{cd} have been evaluated as saturation temperature at pressure p_2 and p_6 , respectively. Nevertheless different cold water temperature $T_{IN,cond}$ values, the condensation temperatures results comparable, while the evaporation conditions depends on the rotational speed imposed on the pump.

Figure 10.5(a) presents the ORC maximum and minimum pressures behavior as function of the ORC mass flow rate. The p_2 value, related to the evaporation temperature T_{ev} , is imposed by the pump rotational speed and it is proportional to the working fluid mass flow rate. The figure shows also how higher values of $T_{in,EVAP}$ allow to reach higher \dot{m}_{ORC} values. The expander pressure ratio p_2/p_3 and the expander rotational speed N_{EXP} also result directly proportional to the mass flow rate (Figures 10.5(b) and 10.5(c)). Figure 10.5(d) shows the behavior of the superheated as function of the ORC mass flow rate. The superheated ΔT_{SH} is evaluated as difference between the ORC maximum temperature (T_2) and T_{ev} . The ΔT_{SH} decreasing is related to the increasing of T_2 and p_2 and consequently to the increasing of \dot{m}_{ORC} , as shown in the figure.

Figure 10.6(a) presents the electric power characterization. The electric power generation has an increasing trend in function of pressure ratio. Regarding the ORC electrical gross efficiency presented in Figure 10.6(b), it quickly grows with the pressure ratio up to be attenuated. Figures 10.6(c) and 10.6(d) report the behavior of the same quantities as function of organic fluid superheated ΔT_{SH} . In these figures the curves are translated each other, but the trends are similar. The increasing of the pump power consumption P_{PUMP} with the increasing of the pressure ratio is visible in Figure 10.7(a). The consumption of the pump is considered in the evaluation of the ORC net electric efficiency, presented in Figure 10.7(b). A maximum electrical power production equal to 1.12 kW has been observed during test named C1, corresponding to a pressure ratio equal to 2.67 and an ORC mass flow rate of 0.13 kg s^{-1} . This operational point has also the highest value of gross and net ORC efficiency, equal respectively to 4.42 % and 3.95 %.

The detail of the electric isentropic efficiency of the expander is presented in Figure 10.8(a). It decreases with increasing pressure ratio trough the expander. This trend is confirmed in literature, as just presented in Section 7.2.1. The maximum value equal to 40.85 % has been observed at pressure ratio of 1.81, while the minimum value 36.89 % has been obtained at pressure ratio equal to 2.67. These operational points correspond to the minimum and maximum of the electric generation. Figure 10.8(b) shows the behavior of the index FPR as function of the expander rotational speed N_{EXP} . The increase of the expander rotational speed (directly proportional to the pressure ratio) allows to better exploit the thermodynamic power of the fluid. The highest values have been obtained with the highest water temperatures at the evaporator.

Figure 10.9 addresses the thermal power characterization of the ORC system under investigation. Figure 10.9(a) presents the thermal power recovered Q_{in} (evaluated at the ORC side) and the thermal power discharged Q_{out} by the ORC. These quantities present a direct relationship. With the increasing of the power production, the difference between inlet and outlet sources temperatures increases. Figures 10.9(b) and 10.9(c) present the thermal balance at the evaporator and condenser heat exchanger, comparing the thermal power captured or discharged by the organic fluid to the thermal power discharged or captured by the external sources. Figure 10.9(d) compares the thermal power exchanged in the recuperator, showing a $Q_{REC,v}$ higher than $Q_{REC,l}$ in all the presented operational point. These figures allow to identify the thermal losses occurred

in the heat exchangers under the operational conditions. The heat balance in each diagram results higher in the hottest stream side.

Figure 10.10(a) shows the thermodynamic cycle of the operational point at maximum power production and efficiency. Meanwhile, Figures 10.10(b) to 10.10(d) report the thermal exchanged diagrams evaluated at recuperator, condenser and evaporator. The maximum organic fluid temperature at evaporator outlet is close to the hot source temperature. Moreover, these diagrams allows to evaluate the heat losses in all the heat exchangers.

10.2.1 Assessment of irreversibility

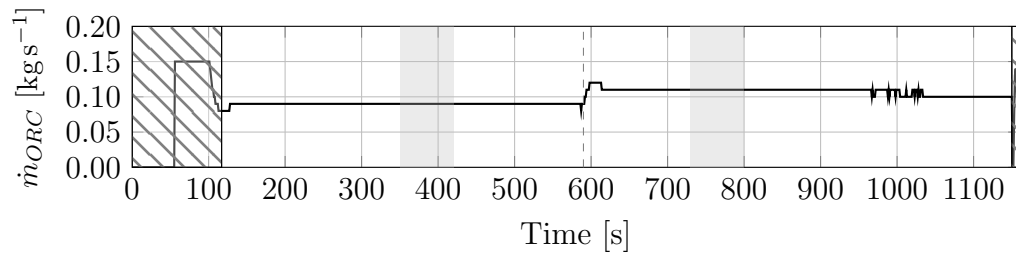
On the basis of previous literature, other parameters could be introduced to evaluate the ORC losses. Bianchi and De Pascale introduce in [5] the parameter η_{rr} , defined as following:

$$\eta_{rr} = 1 - \frac{T_{min}}{T_{max} - T_{min}} \cdot \ln \frac{T_{max}}{T_{min}} \quad (10.1)$$

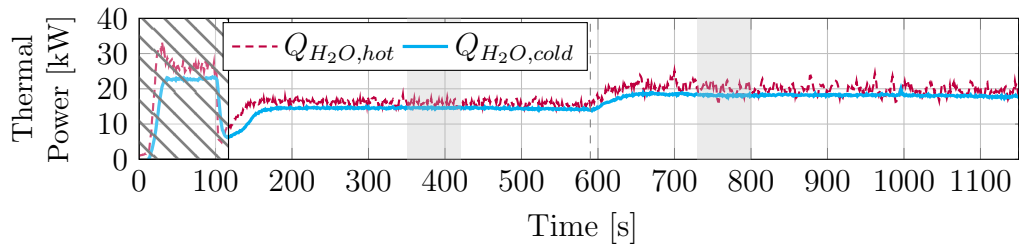
It represents the efficiency of an ideal reversible recuperation cycle, made up of a isobaric heat absorption, an isentropic expansion and an isothermal compression, as shown in Figure 10.11. In this cycle, during the process of heat exchange with the evolving fluid at constant pressure, the hot source temperature decreases from T_{max} to T_{min} . The ratio between the ORC efficiency and η_{rr} is named irreversibility recuperation cycle η_{II} , as shown in eq. (10.2). This parameter represents a measure of the distance of the thermodynamic cycle under investigation from the ideal cycle in which heat is exchanged with a finite, variable temperature, heat source.

$$\eta_{II} = \frac{\eta}{\eta_{rr}} \quad (10.2)$$

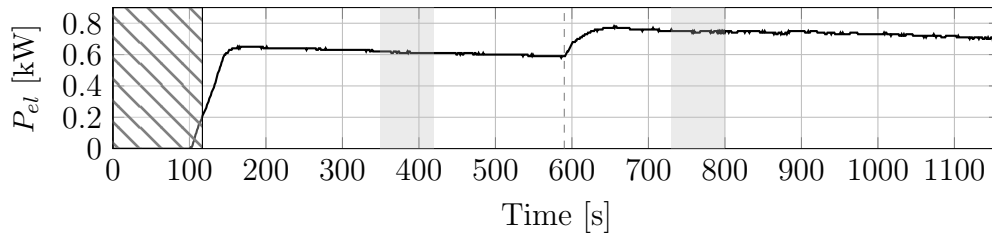
Figure 10.12(a) shows the plotted values from literature η_{rr} in function of the hot source temperature T_{max} , considering a T_{min} variable between 15 °C to 20 °C. The operational data obtained during the test campaign results inside the highlighted area. Figure 10.12(b) presents the values of the η_{II} parameter obtained from the experimental data: with the increasing of the hot source temperatures, the irreversibilities of the ORC under investigation increase. The data are compared to the irreversibility recuperation cycle efficiency obtained from data of ORC available in literature [5]. In the considered operational temperature range the prototype ORC under investigations presents higher values of η_{II} .



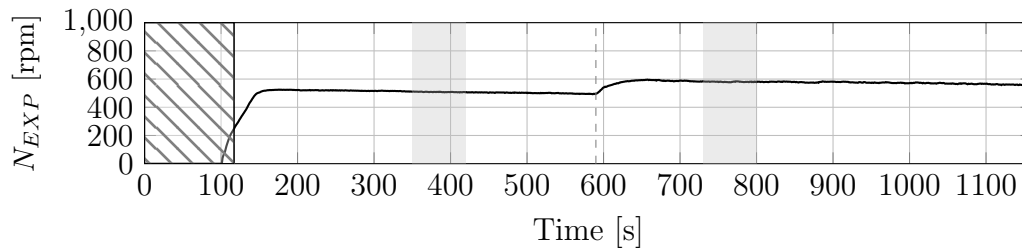
(a) Organic fluid mass flow rate



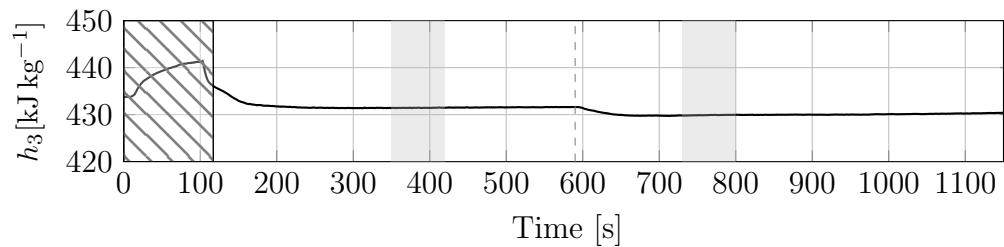
(b) Thermal power evaluated at the hot and cold sides



(c) Electric power production

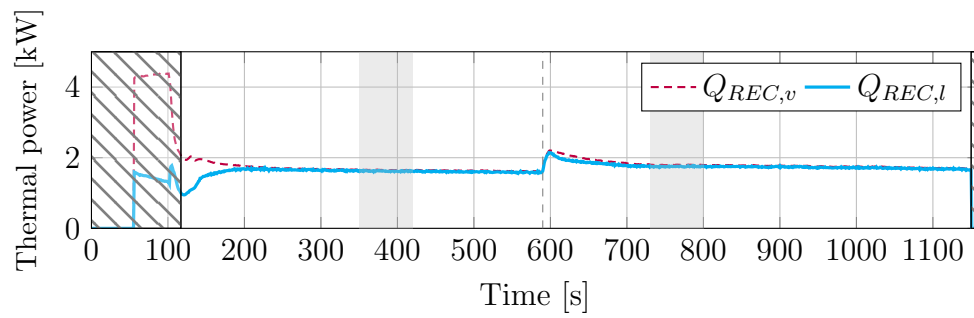


(d) Expander rotational speed

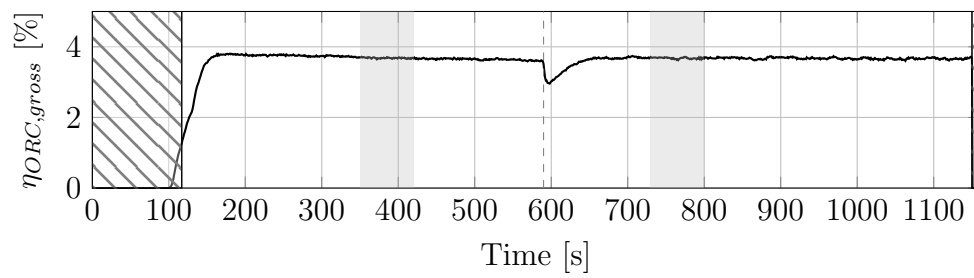


(e) Enthalpy variations at the expander outlet

Fig. 10.2: Quantities variations during a carried out test.

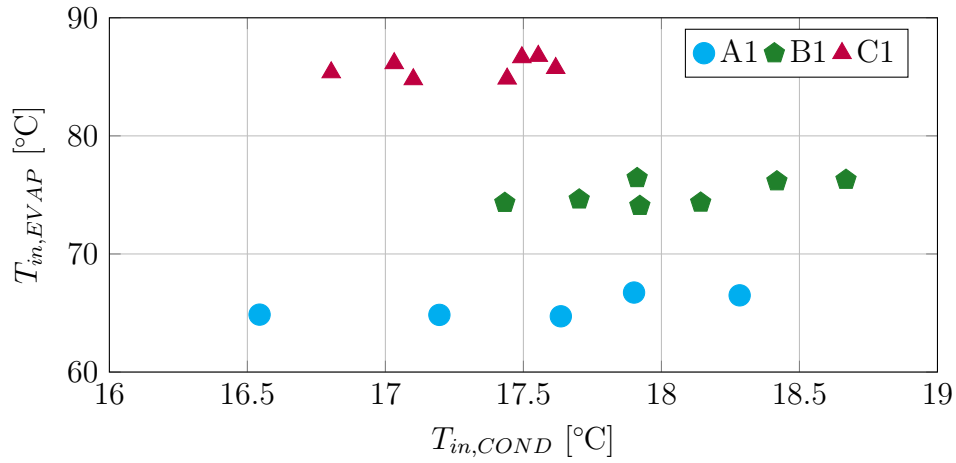


(a)

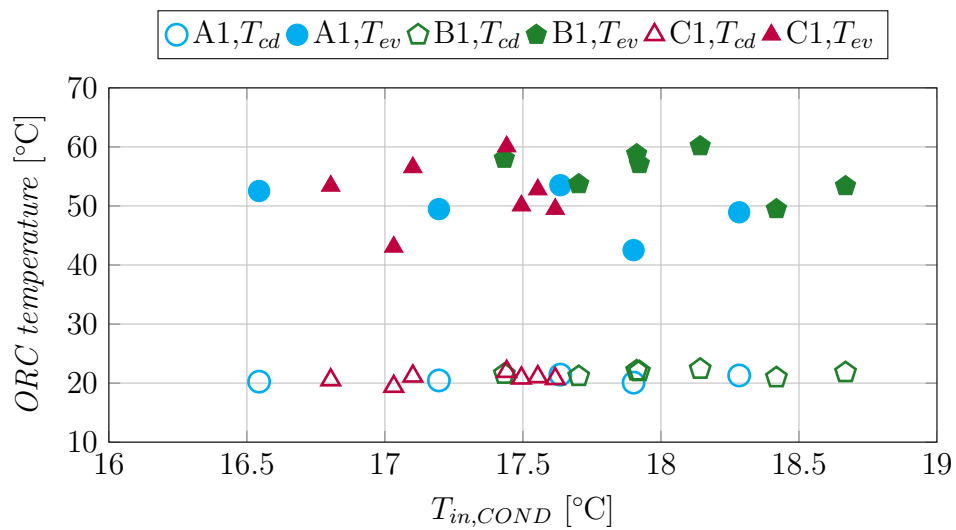


(b)

Fig. 10.3: Recuperator heat exchange (10.3(a)) and ORC gross efficiency (10.3(b)) behavior during a carried out test.



(a)



(b)

Fig. 10.4: Operating point obtained during steady state conditions: hot sources temperature (10.4(a)) and ORC evaporation and condensation temperatures (10.4(b)) versus cold sources temperature.

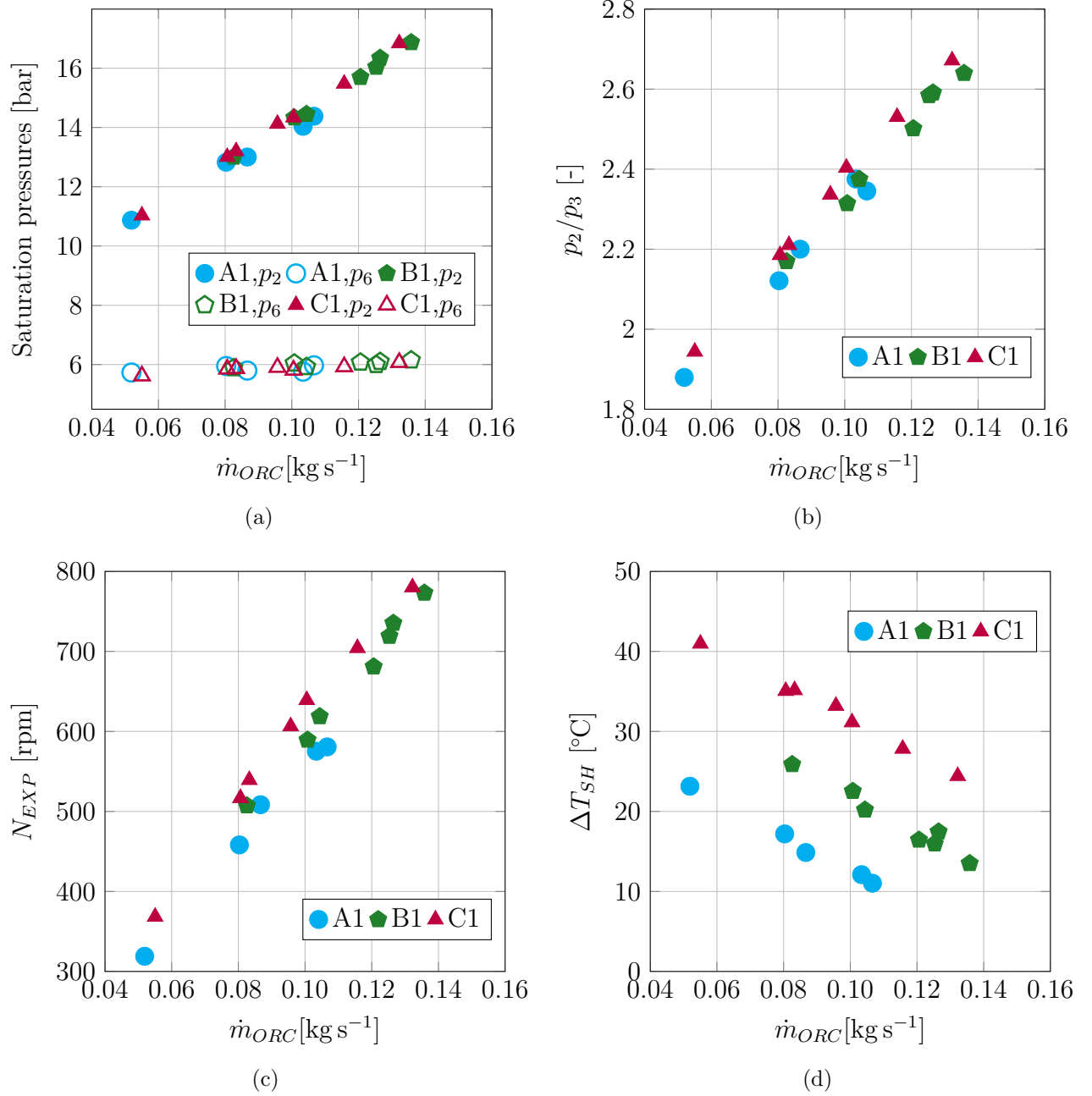


Fig. 10.5: ORC maximum and minimum pressures, p_2 and p_6 , (10.5(a)) and expander pressure ratio p_2/p_3 (10.4(b)) behavior versus the working fluid mass flow rate.

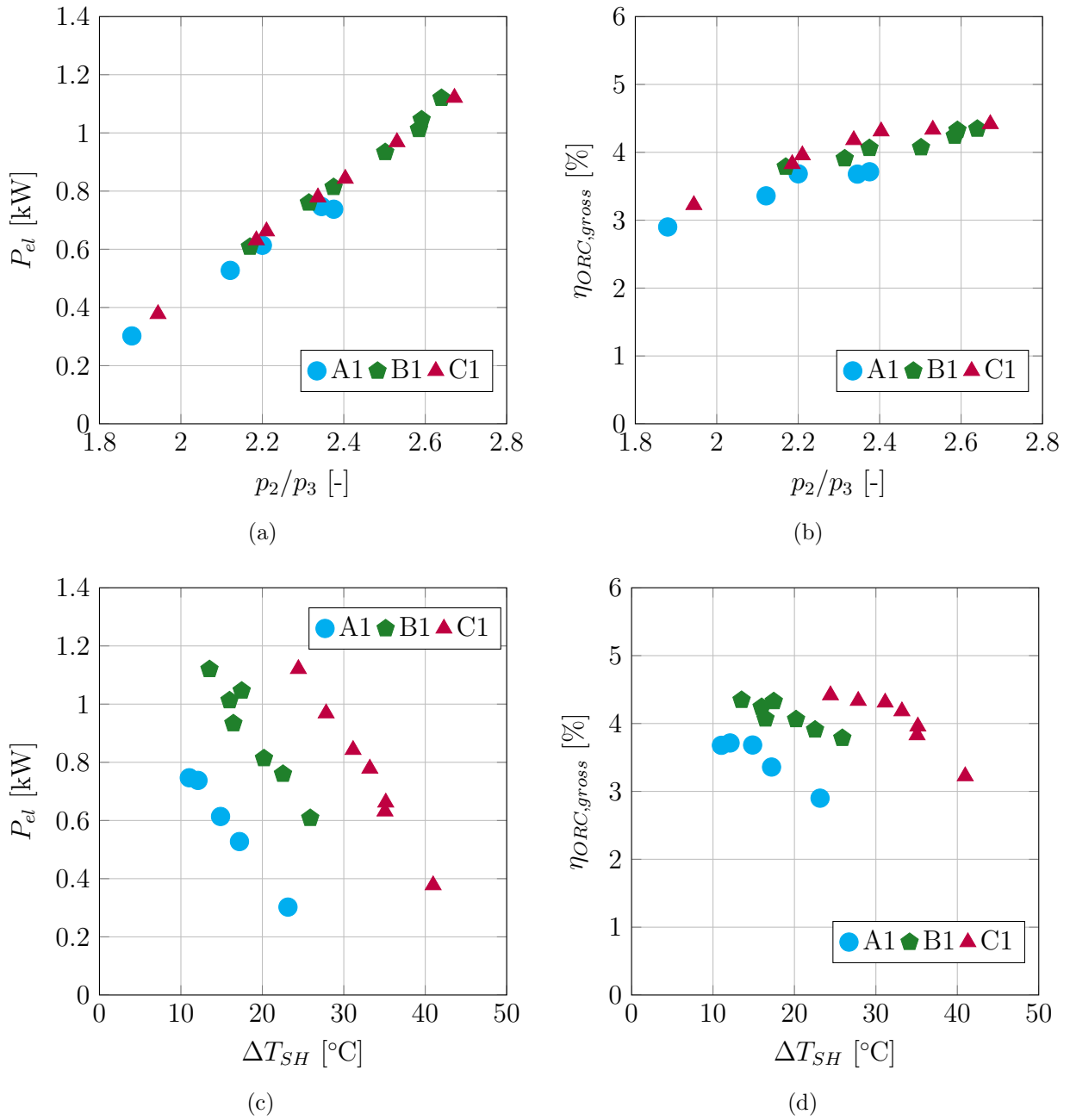


Fig. 10.6: Electric power production (10.6(a)) and ORC gross efficiency (10.6(b)) versus expander pressure ratio p_2/p_3 ; electric power production (10.6(c)) and ORC gross efficiency (10.6(d)) versus superheated ΔT_{SH} ;

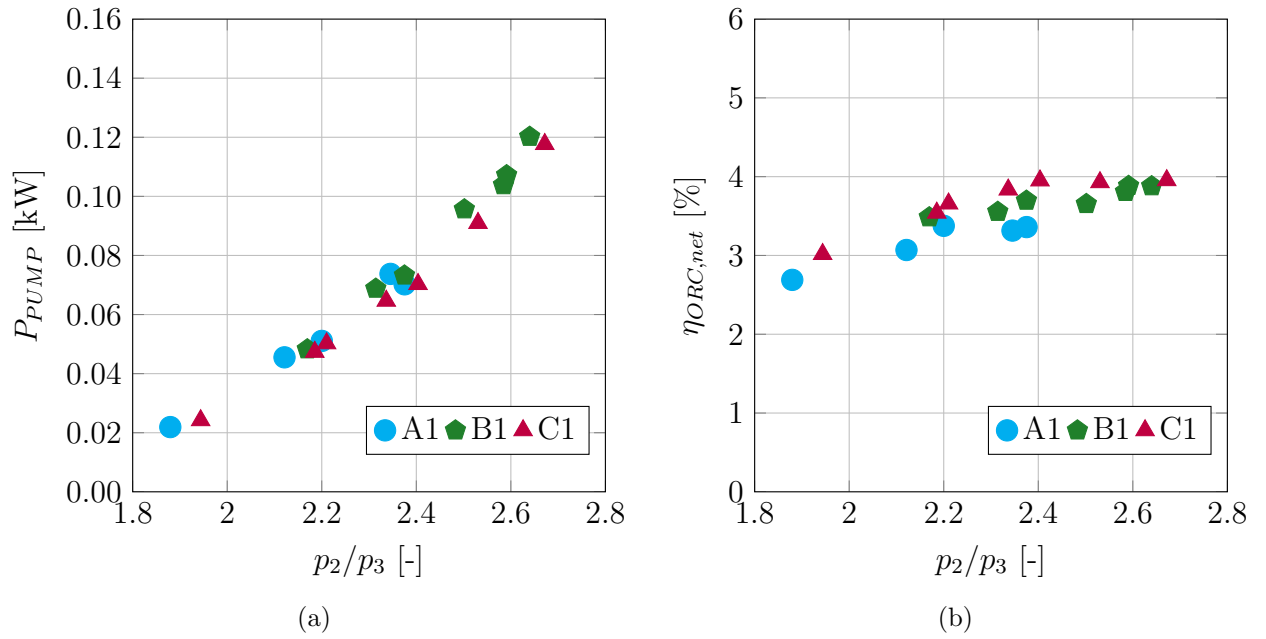


Fig. 10.7: ORC pump consumption (10.7(a)) and ORC net efficiency (10.7(b)) behavior versus expander pressure ratio p_2/p_3 .

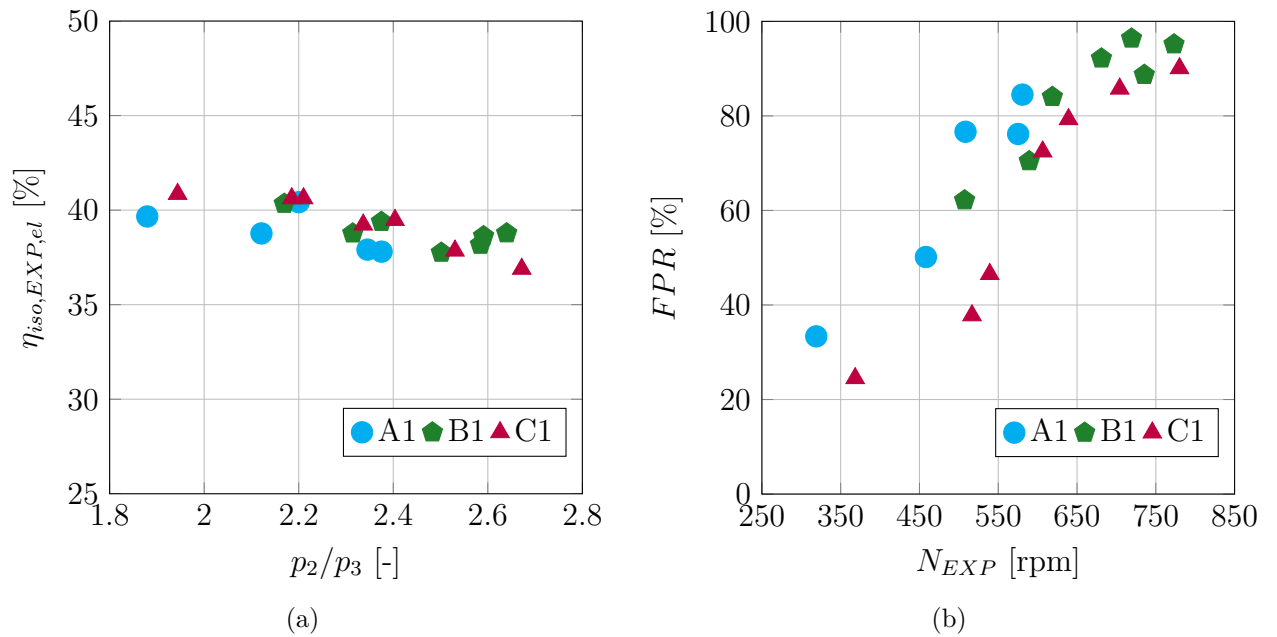


Fig. 10.8: Expander characterization: electrical isentropic efficiency behavior versus the expander pressure ratio (10.8(a)); fluid power ratio versus the expander rotational speed N_{EXP} .

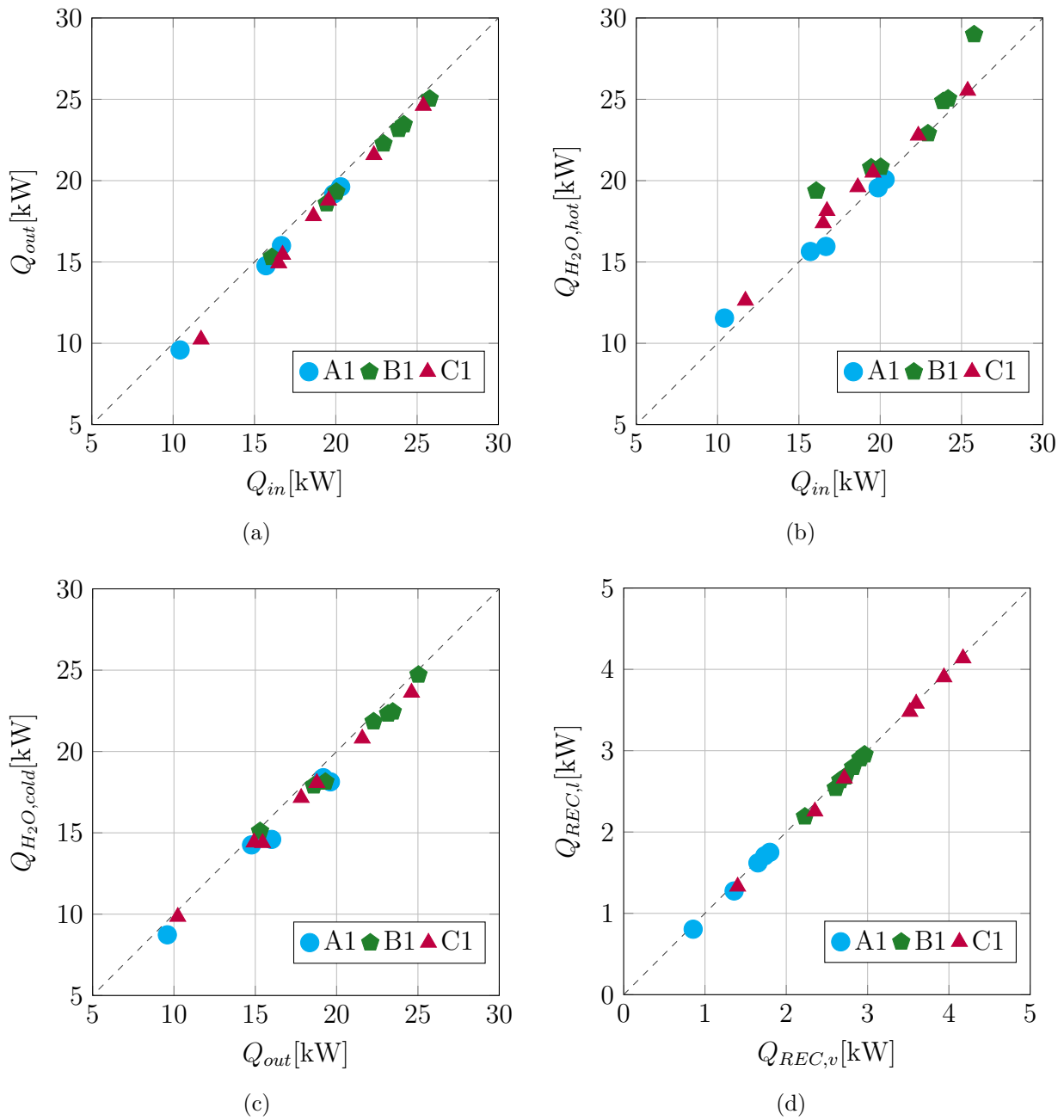


Fig. 10.9: ORC thermal power characterization: comparison between inlet and outlet thermal power (10.9(a)); heat exchange at evaporator (10.9(b)) and condenser (10.9(c)); heat exchange at recuperator (10.9(d)).

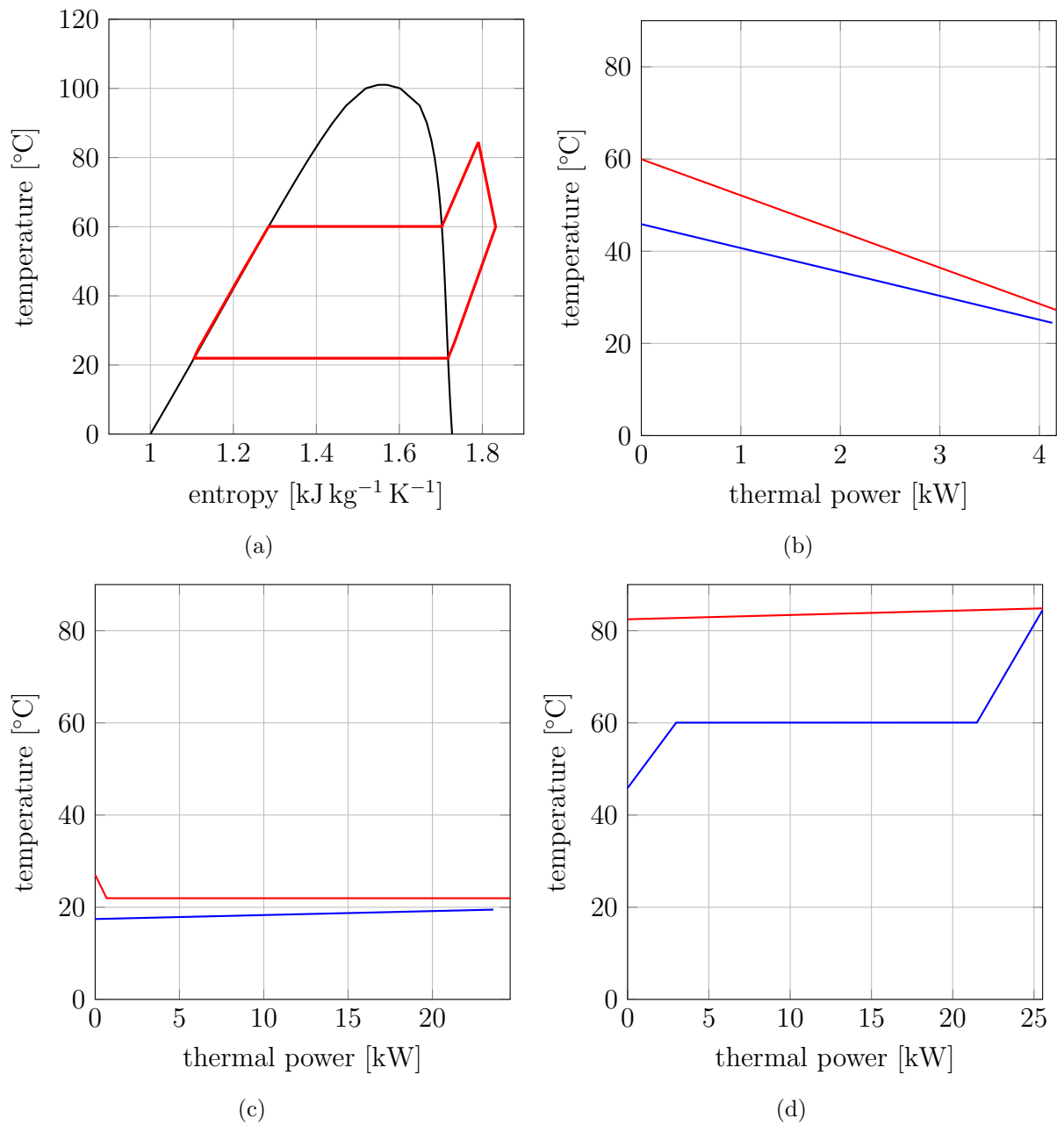


Fig. 10.10: Thermodynamic cycle (10.10(a)) and heat exchanged diagram in recuperator (10.10(b)), condenser (10.10(c)) and evaporator (10.10(d)) of the operating point at maximum electric power production.

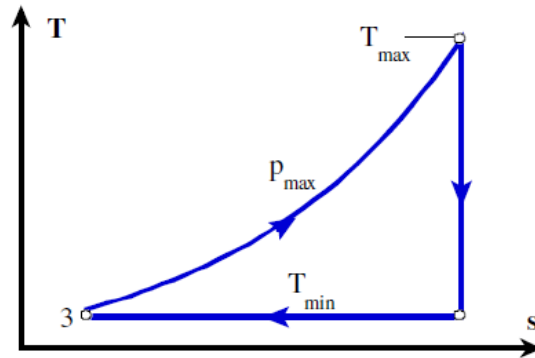


Fig. 10.11: Schematic representation of the overall expander model [5].

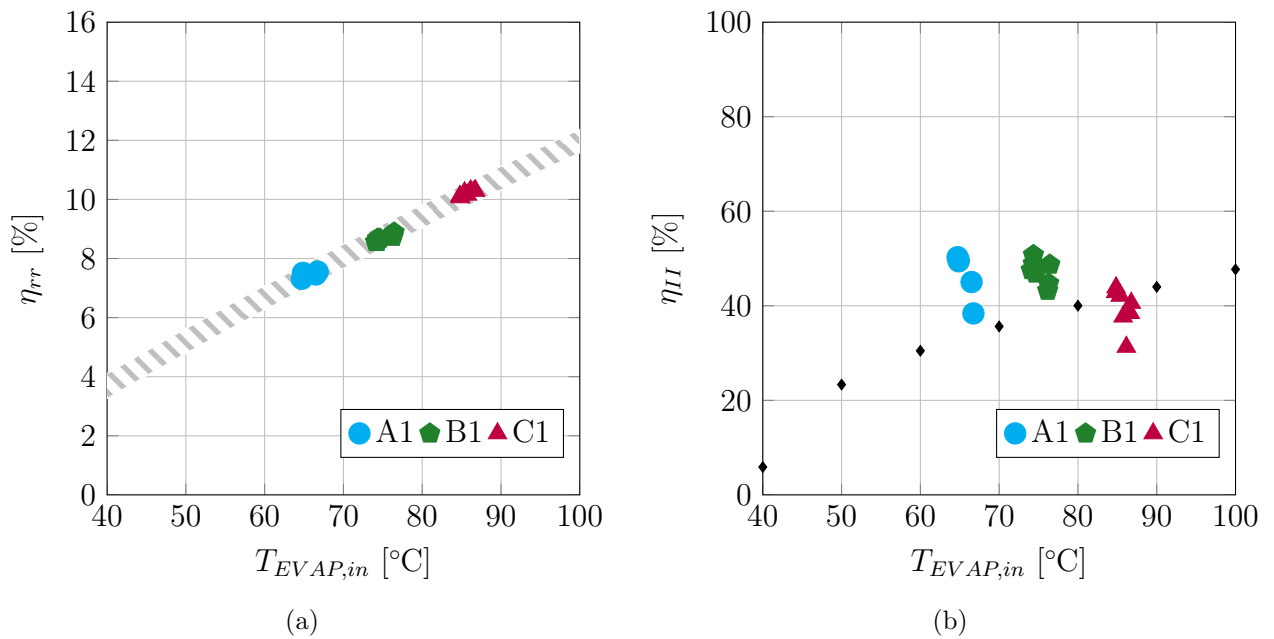


Fig. 10.12: Efficiency of the ideal reversible recuperation cycle (10.12(a)) and irreversibility recuperation cycle efficiency (10.12(b)) for the operational data.

Conclusions

Organic Rankine Cycle (ORC) is a technology that can convert thermal energy into electricity. This technology is based on conventional water steam cycle configuration, using working fluids with organic nature. This characteristic opens up the possibility to exploit low-grade heat, at low temperature ranges between 50 to 400 °C, that otherwise would be wasted. Therefore, this technology can play an important role to improve the energy efficiency of new or existing energy-intensive applications.

From a worldwide capacity installations analysis, the diffusion of ORC technology results mainly related to the renewable heat sources applications, in particular geothermal and biomass. However, the diffusion of ORC application as waste heat recovery system is increasing, due to the growing interest to the environmental impact and to the efficiency improvement. The heat recovery market is still at an early stage but has long passed the demo/prototype phase. The most suitable processes for ORC waste heat recovery application result cement, glass, steel and oil and gas industries and this trend is confirmed by the market. In this context interest in exploring and investigating ORC innovative applications has growing and this thesis aims to identify advantages and problems of ORC application in unusual sectors.

In particular, the carried out research activity is focused on the waste heat recovery application of ORC systems in innovative power scenarios, describing cases from the biggest to the lowest scale. Both industrial and residential applications are considered. In both applications, the installation of a subcritical and recuperated ORC system is examined and the heat recovery is considered in absence of an intermediate heat transfer circuit. This solution allows to improve the recovery efficiency, but requiring safety precautions. Possible integrations of ORC systems with renewable sources are also presented and investigated to identify the advantages of ORC installation.

The offshore oil and gas sector has been selected as a promising industrial large-scale ORC application. The analyzed scenario consists in a novel offshore power system for oil and gas platforms. More in detail, the power system on board consists of three gas turbines each one equipped with an organic Rankine cycle turbogenerator. Wind mills are also connected to the stand-alone electric grid to reduce the fuel consumption and pollutants. The platform considered as case study has a nominal electric power demand of 30 MW and it is located in the North Sea. A dynamic model of the power system, based on design specification, has been developed in the Modelica language using component models from validated libraries. The first aim of this analysis is the evaluation of maximum allowable wind power for which the stability of the platform electric grid is not compromised. The considered wind turbines have a design capacity of 5 MW and they are sized and modeled on NREL offshore reference generators. The performed simulations suggest that the wind mills should cover not more than one third

of the power consumption in nominal conditions. Moreover, a thermodynamic analysis of the novel offshore power system has been performed, with the aim to observe how the wind power variations influence the performance of single components and the overall integrated system. Due to the unpredictability of the wind turbines power production, two wind scenarios are observed and compared. The obtained results show how the gas turbines and ORC combined cycle efficiency in off-design conditions swings around the design efficiency value, due to the action of the ORC control system. Furthermore, the ORC efficiency increases with the decreasing of the recovered thermal power. Different cogenerative configurations are also considered and estimated: the available thermal power into the exhausted gas and in the condenser are used to evaluate the thermal efficiency of the innovative combined cycle under the wind power variation effect. The electric and thermal performance of the combined cycle are compared to simpler plant configurations consist of gas turbines or gas turbines integrated with a wind farm. The comparison of the performance shows how the most complex power plant presents the highest electric efficiency, but a lower thermal efficiency, although the possibility of thermal power recovery from gas turbines exhausted gas and from the ORC condenser. The developed model allows also estimating the fuel consumption and the CO₂ emissions of the considered configurations. The net present value method demonstrates the economic feasibility of the waste heat recovery units and wind mills. On the electric side aspect, the results suggest that the use of the ORC units enables reducing the electric frequency fluctuations of the standalone grid caused by the variability of the wind production, compared to the installation of the gas turbines alone. Conversely, the waste heat recovery system makes the plant slower to adapt to the variations, due to inertia of the heat transfer equipment.

An experimental test facility has been developed to evaluate the micro-ORC potential as small-scale waste heat recovery system in domestic or industrial sector. Small and micro-scale ORC units are quite different from big sized units. Generally they are not equipped with a dynamic turbine, but with volumetric expanders. Volumetric expanders presents advantages over turbines, as low cost, lower rotational speeds and ability to handle a liquid phase, characteristic particularly interesting for Rankine cycle applications. The state of the art of different available technologies are introduced and compared. The technical constraints inherent to each machine are listed and the performance mentioned in the open technical and scientific literature is presented. A focus on the piston expander technology is presented and the most important parameters to characterized pistons expander behavior are introduced. Moreover, literature examples are presented to identify the typical trend of the performance of these volumetric machines.

The components of the developed test rig are described, as the cold and hot water supply circuits installed in the laboratory. The project includes the heat input provided to the ORC by a biomass boiler producing hot water. The specifications of the main elements are listed. Moreover, the layout of the micro-ORC prototype system under investigation is presented. Information on its main components is presented. In order to collect data on the operation of the system, the test bench has been instrumented with temperature, pressure sensors and flow meters. The measurements of temperature

have been made through T-type and K-type thermocouples, placed in the ORC and in the water cycle respectively, while the organic fluid pressures are measured by ceramics pressure transducers. Sensors have been individually calibrated at the laboratory to improve their accuracy. Regarding flow sensors, on the hot and cold water sides the volumetric flow rates are measured by electromagnetic volumetric flow sensor placed in the evaporator and condenser water inlet branches, to evaluate the thermal power exchanged between the ORC fluid and external sources. Meanwhile, the ORC flow rate measurer is a Coriolis unit, that allows to measure the organic fluid mass flow rate and density. Moreover, a Printed Circuit Board (PCB) is connected to the expander electric generator, to measure the current and voltage values of each phase, through three volt transducers and three current transducers. The elaboration of signals lets to evaluate the three phase electric power produced by the ORC and the rotational speed of the expander. The test bench have been also endowed with a data acquisition system. A real-time microcontroller is used to acquire signals from all the installed sensors. Various modules are selected based on the sensors output signals. An acquisition software and a display panel are realized in the laboratory computer, both developed in LabVIEW environment. The fluid library properties CoolProp has been selected and integrated in the developed acquisition software, in order to obtain the thermodynamic state of each ORC section and to evaluate the overall performances. The evaluated states are used to instantly realize the ORC thermodynamic cycle, displayed in real time on thermodynamic diagrams. Various indexes have been identified in literature or introduced, based on the available measures, to evaluate the performance of the ORC under investigation. All these quantities are evaluated and shown in real-time by the developed display panel. The experimental test campaign carried out is presented. It aims to investigate the ORC behavior and thermodynamic performances in different operating conditions. In particular, the test campaign is executed at different thermal power from the hot sources and varying the ORC mass flow rate. The collected data, represent the dynamic behavior of the ORC, have been analyzed to identify ORC steady states conditions and several operational point are obtained. The operational maps realized show the relations between the main parameters and the evaluation of the irreversibility of the cycle respect data available in literature. The maximum electrical power production observed is equal to 1.12 kW, correspondent to the maximum heat power input. Moreover, this operational point allowed the highest value of gross and net ORC efficiency, respectively equal to 4.42 % and 3.95 %.

Prospective

In the future, the presented approach, applied in oil and gas offshore sector to couple gas turbines, ORCs and wind farm, could be used in different scenarios to coupled renewable sources and conventional systems. It could be used for onshore applications or to integrate power plant with renewable sources, as solar fields or wind farm, considering from big to small and micro-power size.

From the experimental activity, the characterization curves of the ORC prototype could be extracted and used to develop a dynamic model. Particular interesting could be model the expander and pump machines, due to their prototypical natures, and validate the models with the available experimental results. The model of the systems could be used to analyze the coupling with various kind of users, as a residential building or exploiting the low-temperature waste stream from industrial processes, analyzing the economic and environmental aspects with the net present value method presented. Moreover, in the developed test rig, other micro-ORC or small scale power system could be tested.

APPENDIX A

Appendix not available in the on-line version.

APPENDIX B

Sensors calibration

The following table reports the calibration curves obtained for each sensors. In case of thermocouple, the reported curves transform signal from the sensors to temperature values (x and y in $^{\circ}\text{C}$), respectively), while in case of the pressure sensors, the signal (x in $[\text{V}]$) is transformed through the reported curves in a pressure value (y in $[\text{bar}]$). The sensors names reported in the table are related to the ORC layout sections, previously presented in Chapter 8. Moreover, the subscripts used in the case of pressure sensors distinguish between Low (LP) and High Pressure (HP).

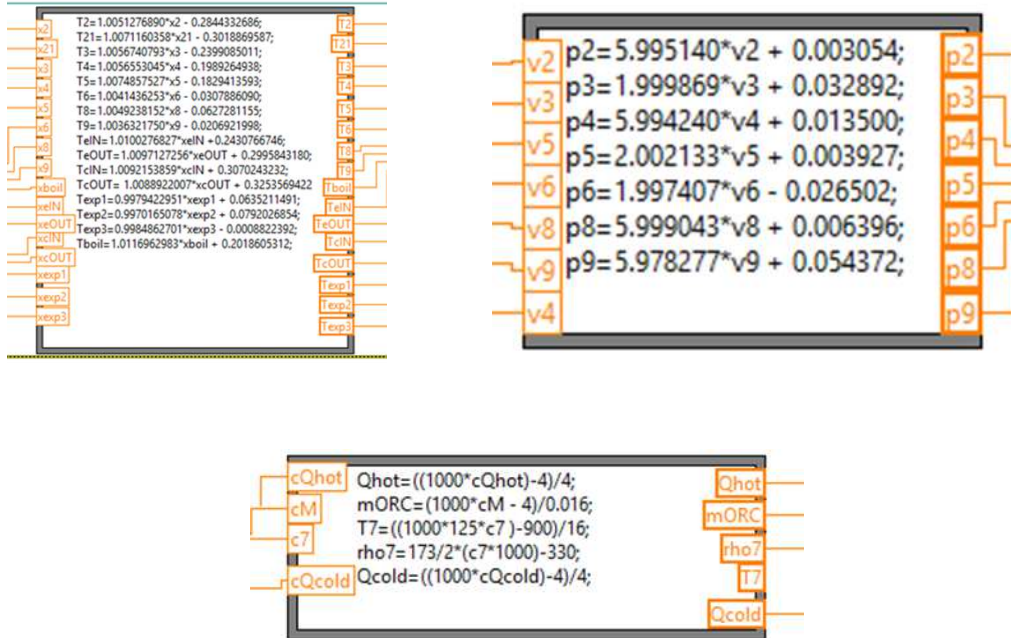
Temperature curves		Pressure curves	
T2	$y = 1.0051276890x - 0.2844332686$	p2 _{HP}	$y = 5.995140x + 0.003054$
T2'	$y = 1.0071160358x - 0.3018869587$	p3 _{LP}	$y = 1.999869x + 0.032892$
T3	$y = 1.0028065430x - 0.0966052694$	p4 _{HP}	$y = 5.994240x + 0.013500$
T4	$y = 1.0056740793x - 0.2399085011$	p5 _{LP}	$y = 2.002133x + 0.003927$
T5	$y = 1.0074857527x - 0.1829413593$	p6 _{LP}	$y = 1.997407x - 0.026502$
T6	$y = 1.0041436253x - 0.0307886090$	p8 _{HP}	$y = 5.999043x + 0.006396$
T8	$y = 1.0049238152x - 0.0627281155$	p9 _{HP}	$y = 5.978277x + 0.054372$
T9	$y = 1.0036321750x - 0.0206921998$		

Meanwhile, the following table reports the calibration curves related to the hot and cold water circuits. Moreover, three surface K-type thermocouples are presented in the test bench: the first thermocouple measures the expander surface temperature under the surface of the insulate material (*in*), the second one measures the expander surface temperature on the surface of the insulate material (*ex*) and the third one is located on a wall surface, to evaluate the ambient temperature.

Thermocouple K	Curves
boiler outlet	$y = 1.0116962983x + 0.2018605312$
evaporator inlet	$y = 1.0100276827x + 0.2430766746$
evaporator outlet	$y = 1.0097127256x + 0.2995843180$
condenser inlet	$y = 1.0092153859x + 0.3070243232$
condenser outlet	$y = 1.0088922007x + 0.3253569422$
expander surface (in)	$y = 0.9979422951x + 0.0635211491$
expander surface (ex)	$y = 0.9970165078x + 0.0792026854$
ambient surface	$y = 0.9984862701x - 0.0008822392$

The following figures report the formula nodes, where the equations listed in the previous tables are introduced in the control system realized in LabVIEW environment. The last

figure presents the equations introduced to elaborate the signal from the other sensors, i.e. the hot and cold volumetric flow meters and the Coriolis sensors. The equations have been obtained from the settings values presented in Chapter 9.

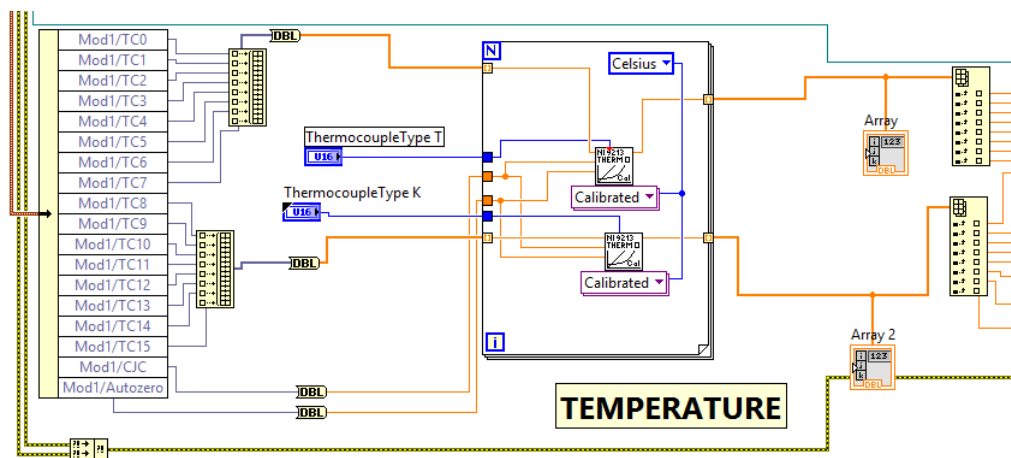


APPENDIX C

Developed acquisition system

The acquisition system, developed in Labview environment, consists of the *real-time* project and the *host* project. In the first project, the sensors signals are transduced and the calibration curves are implemented (as shown in Chapter B). Some examples of the realized structures and blocks are here presented.

The following figure shows the loop implemented to elaborate the signal from the temperature sensors.



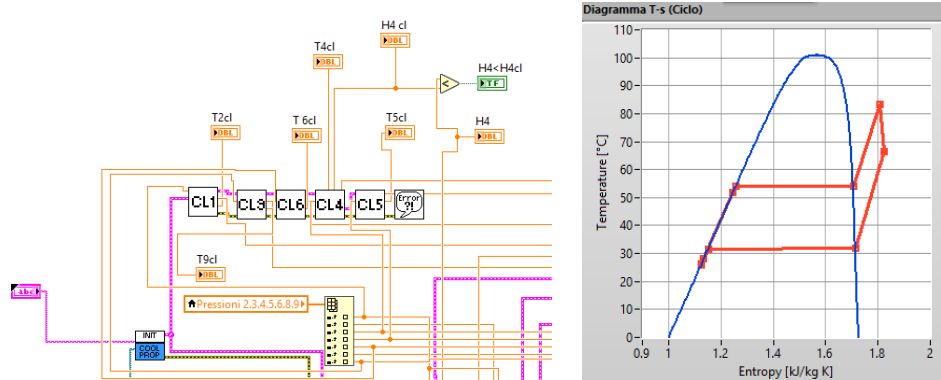
Transducer loop for temperature sensors.

Meanwhile, in the *host* project, all the measured quantity are elaborated to evaluate the performance parameters. For instance, the loop realized to plot the ORC thermodynamic (closed) cycle, upload every 1 s (in real time), is presented. To realize it, the evaluation of evaporation and condensation condition are needed: the *CL* blocks, specifically developed, allow to evaluate the thermodynamic state of the ORC section on the saturation curves.

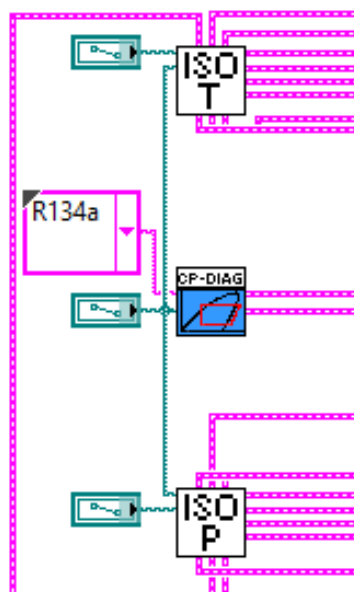
Moreover, the loop developed in Labview environment to trace the vapor and liquid curves on the T-s diagram through the specific Coolprop block is shown.

The *formula node* presented allows to evaluate, through the shown formulas, the ORC performance indexes and parameters, as enthalpy variations, exchanged thermal powers, pressure drops, efficiencies, superheating, etc..

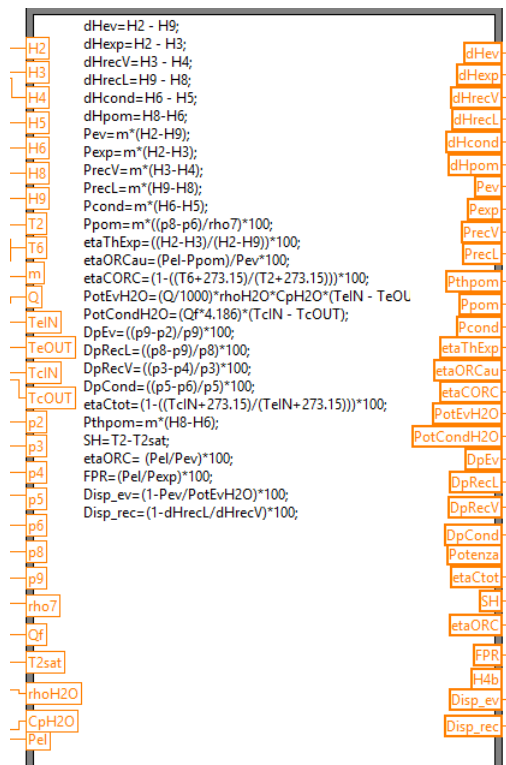
The last figures shows the structure implemented to save data in an excel file, then elaborated through the calculation routine developed as a VBA code.



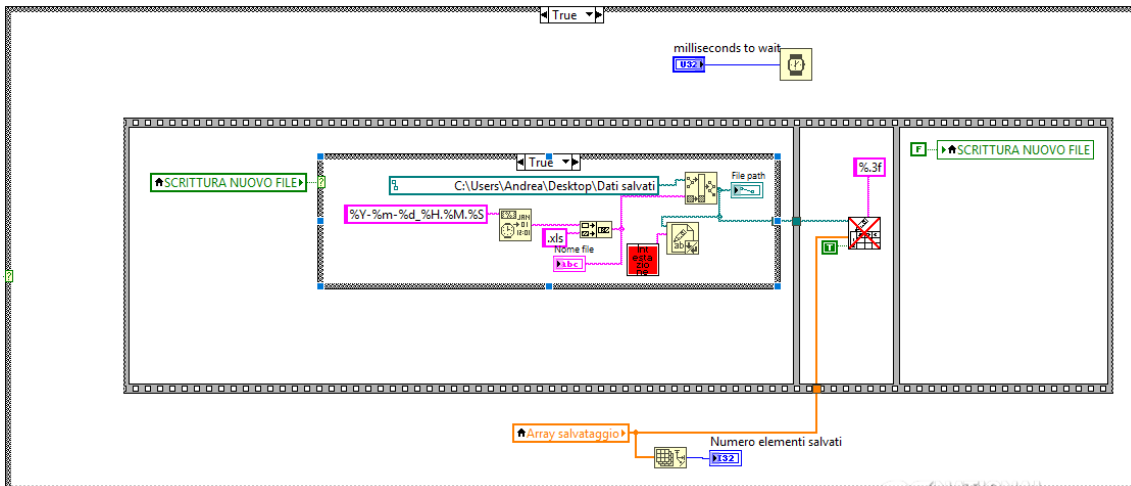
Loop to plot the ORC thermodynamic cycle on T-s diagram in real time.



Loop to plot saturation curves.



Performance Formula Node.



Case Structure to save data.

APPENDIX D

Performed test- operational data

Table D.1: ORC data operation, case A1

$T_{in,EVAP}$	°C	66.73	66.50	64.84	64.72	64.86
$T_{in,COND}$	°C	17.90	18.28	17.20	17.64	16.54
T_2	°C	65.67	66.12	64.33	64.54	64.63
T_3	°C	39.39	41.34	42.63	41.46	40.74
T_4	°C	22.39	23.89	22.87	23.98	23.22
T_5	°C	22.42	23.78	22.89	23.87	23.20
T_6	°C	19.90	21.03	20.09	20.97	19.78
T_8	°C	21.54	22.83	21.48	22.65	21.85
T_9	°C	32.40	33.93	34.55	34.13	33.42
\dot{m}_{ORC}	kg s ⁻¹	0.05	0.08	0.09	0.11	0.10
p_2	bar	10.87	12.83	13.00	14.38	14.04
p_3	bar	5.78	6.05	5.91	6.13	5.91
p_4	bar	5.74	5.96	5.80	5.98	5.77
p_5	bar	5.74	5.96	5.80	5.98	5.76
p_6	bar	5.73	5.95	5.80	5.97	5.76
p_8	bar	10.90	12.87	13.04	14.43	14.09
p_9	bar	10.91	12.88	13.04	14.43	14.09
P_{el}	kW	0.30	0.53	0.61	0.75	0.74
N_{EXP}	rpm	319.02	458.16	508.44	580.67	575.27
ρ_7	kg m ⁻³	1226.71	1222.37	1225.60	1222.43	1226.27

Table D.2: ORC data operation, case B1

$T_{in,EVAP}$	°C	76.16	76.29	74.62	74.08	74.33	76.43	74.35
$T_{in,COND}$	°C	18.42	18.67	17.70	17.92	17.43	17.91	18.14
T_2	°C	75.35	75.90	73.90	73.55	73.98	76.25	73.64
T_3	°C	52.73	52.62	51.37	49.86	49.62	51.02	47.59
T_4	°C	24.79	25.87	24.90	25.62	25.47	26.73	26.69
T_5	°C	24.74	25.72	24.80	25.46	25.31	26.65	26.50
T_6	°C	21.36	22.03	21.03	21.46	21.42	21.86	22.25
T_8	°C	22.96	23.99	22.93	23.73	23.45	24.47	24.86
T_9	°C	41.25	41.36	40.39	39.79	39.51	40.57	38.55
\dot{m}_{ORC}	kg s ⁻¹	0.08	0.10	0.10	0.12	0.13	0.13	0.14
p_2	bar	13.01	14.33	14.45	15.70	16.04	16.34	16.87
p_3	bar	6.00	6.19	6.08	6.27	6.21	6.31	6.39
p_4	bar	5.89	6.05	5.93	6.08	6.00	6.11	6.16
p_5	bar	5.89	6.05	5.93	6.08	6.00	6.10	6.16
p_6	bar	5.89	6.04	5.92	6.08	5.99	6.10	6.15
p_8	bar	13.04	14.38	14.50	15.76	16.11	16.42	16.95
p_9	bar	13.05	14.37	14.49	15.75	16.10	16.42	16.93
P_{el}	kW	0.61	0.76	0.81	0.93	1.01	1.05	1.12
N_{EXP}	rpm	507.28	589.33	618.70	680.94	719.16	735.38	773.09
ρ_7	kg m ⁻³	1224.15	1221.08	1223.28	1220.69	1222.29	1219.88	1219.30

Table D.3: ORC data operation, case C1

$T_{in,EVAP}$	°C	85.37	84.79	84.84	86.14	85.74	86.65	86.76
$T_{in,COND}$	°C	16.80	17.10	17.44	17.03	17.62	17.49	17.55
T_2	°C	84.54	84.36	84.49	84.04	84.54	85.21	85.98
T_3	°C	62.30	61.38	59.95	48.17	53.85	58.10	63.71
T_4	°C	25.18	26.09	27.25	21.77	23.68	24.41	25.65
T_5	°C	25.10	25.98	27.05	21.78	23.54	24.29	25.56
T_6	°C	20.20	20.85	21.65	18.91	20.24	20.50	20.70
T_8	°C	22.38	23.33	24.46	20.64	22.08	22.23	23.05
T_9	°C	46.72	46.39	45.87	37.43	41.37	44.15	47.82
\dot{m}_{ORC}	kg s ⁻¹	0.10	0.12	0.13	0.06	0.08	0.08	0.10
p_2	bar	14.34	15.48	16.84	11.03	13.01	13.20	14.12
p_3	bar	5.97	6.12	6.30	5.67	5.95	5.97	6.04
p_4	bar	5.82	5.94	6.08	5.63	5.86	5.87	5.92
p_5	bar	5.81	5.93	6.07	5.63	5.86	5.87	5.91
p_6	bar	5.81	5.93	6.07	5.62	5.85	5.87	5.91
p_8	bar	14.38	15.54	16.93	11.06	13.04	13.23	14.17
p_9	bar	14.38	15.53	16.92	11.07	13.04	13.24	14.16
P_{el}	kW	0.84	0.97	1.12	0.38	0.63	0.66	0.78
N_{EXP}	rpm	639.18	704.16	780.10	368.40	516.69	539.27	606.37
ρ_7	kg m ⁻³	1224.57	1223.05	1220.47	1228.97	1224.82	1223.86	1223.53

Bibliography

- [1] Bertrand F. Tchanche, Gregory Lambrinos, Antonios Frangoudakis, and George Papadakis. Low-grade heat conversion into power using organic rankine cycles—a review of various applications. *Renewable and Sustainable Energy Reviews*, 15(8):3963–3979, 2011.
- [2] European Commission. Integrated pollution prevention and control reference document on economics and cross-media effects, July 2006.
- [3] Ennio Macchi and Marco Astolfi. *Organic Rankine Cycle (ORC) Power Systems: Technologies and Applications*. Woodhead Publishing, 1 edition, 2017.
- [4] Huijuan Chen, D. Yogi Goswami, and Elias K. Stefanakos. A review of thermodynamic cycles and working fluids for the conversion of low-grade heat. *Renewable and sustainable energy reviews*, 14(9):3059–3067, 2010.
- [5] Michele Bianchi and Andrea De Pascale. Bottoming cycles for electric energy generation: Parametric investigation of available and innovative solutions for the exploitation of low and medium temperature heat sources. *Applied Energy*, 88(5):1500–1509, 2011.
- [6] Lisa Branchini, Andrea De Pascale, and Antonio Peretto. Systematic comparison of orc configurations by means of comprehensive performance indexes. *Applied Thermal Engineering*, 61(2):129–140, 2013.
- [7] Junjiang Bao and Li Zhao. A review of working fluid and expander selections for organic rankine cycle. *Renewable and Sustainable Energy Reviews*, 24:325–342, 2013.
- [8] Tzu-Chen Hung, T.Y. Shai, and S.K. Wang. A review of organic rankine cycles (ORCs) for the recovery of low-grade waste heat. *Energy*, 22(7):661–667, 1997.
- [9] Sylvain Quoilin, Martijn Van Den Broek, Sébastien Declaye, Pierre Dewallef, and Vincent Lemort. Techno-economic survey of organic rankine cycle (orc) systems. *Renewable and Sustainable Energy Reviews*, 22:168 – 186, 2013.
- [10] Carlo Carcasci, Riccardo Ferraro, and Edoardo Miliotti. Thermodynamic analysis of an organic rankine cycle for waste heat recovery from gas turbines. *Energy*, 65:91–100, 2014.
- [11] P.S. Bundela, Vivek Chawla, et al. Sustainable development through waste heat recovery. *American Journal of Environmental Sciences*, 6(1):83–89, 2010.

- [12] Fredy Vélez, José J Segovia, M. Carmen Martín, Gregorio Antolín, Farid Chejne, and Ana Quijano. A technical, economical and market review of organic rankine cycles for the conversion of low-grade heat for power generation. *Renewable and Sustainable Energy Reviews*, 16(6):4175–4189, 2012.
- [13] Steven Lecompte, Henk Huisseune, Martijn van den Broek, Bruno Vanslambrouck, and Michel De Paepe. Review of organic rankine cycle (ORC) architectures for waste heat recovery. *Renewable and Sustainable Energy Reviews*, 47:448–461, 2015.
- [14] Filippo Cataldo, Rita Mastrullo, Alfonso William Mauro, and Giuseppe Peter Vanoli. Fluid selection of organic rankine cycle for low-temperature waste heat recovery based on thermal optimization. *Energy*, 72:159–167, 2014.
- [15] Jason R. Juhasz and Luke D. Simoni. A review of potential working fluids for low temperature organic rankine cycles in waste heat recovery. In *The third edition of the International Seminar on ORC Power Systems (ASME ORC 2015), Brussels*, volume 12, 2015.
- [16] Dongxiang Wang, Xiang Ling, Hao Peng, Lin Liu, and LanLan Tao. Efficiency and optimal performance evaluation of organic rankine cycle for low grade waste heat power generation. *Energy*, 50:343–352, 2013.
- [17] Young-Jin Baik, Minsung Kim, Ki-Chang Chang, Young-Soo Lee, and Hyung-Kee Yoon. Power enhancement potential of a mixture transcritical cycle for a low-temperature geothermal power generation. *Energy*, 47(1):70–76, 2012.
- [18] J.L. Wang, Li Zhao, and X.D. Wang. A comparative study of pure and zeotropic mixtures in low-temperature solar rankine cycle. *Applied Energy*, 87(11):3366–3373, 2010.
- [19] Kiyarash Rahbar, Saad Mahmoud, Raya K. Al-Dadah, Nima Moazami, and Seyed A. Mirhadizadeh. Review of organic rankine cycle for small-scale applications. *Energy Conversion and Management*, 134:135–155, 2017.
- [20] Arnaud Landellea, Nicolas Tauverona, Philippe Haberschille, Rémi Revellinc, and Stephane Colassona. Performance evaluation and comparison of experimental organic rankine cycle prototypes from published data. 2016.
- [21] Leilei Dong, Hao Liu, and Saffa Riffat. Development of small-scale and micro-scale biomass-fuelled chp systems—a literature review. *Applied thermal engineering*, 29(11):2119–2126, 2009.
- [22] Francesco Campana, Michele Bianchi, Lisa Branchini, Andrea De Pascale, Antonio Peretto, Marco Baresi, Alessandro Fermi, Nicola Rossetti, and Riccardo Vescovo. ORC waste heat recovery in European energy intensive industries: Energy and GHG savings. *Energy Conversion and Management*, 76:244–252, 2013.

- [23] Thomas Tartière. ORC market : A world overview.
- [24] Nicola Rossetti. Report preliminare sulle potenzialità di recupero di effluenti per valorizzazione elettrica mediante sistemi ORC (Organic Rankine Cycle) a livello nazionale, H-REII Annex 1. 2010.
- [25] International Finance Corporation (IFC). Environmental, health, and safety guidelines for offshore oil and gas development. 2007.
- [26] Lars Jakob Alveberg and Eldbjørg Vaage Melberg. The norwegian petroleum sector, 2013.
- [27] Commission of the European Communities. Europe's climate change opportunity. 2008.
- [28] EY. Global oil and gas tax guide 2013.
- [29] Rakesh K. Bhargava, Michele Bianchi, Lisa Branchini, Andrea De Pascale, Francesco Melino, Andrea Peretto, and Elisa Valentini. Thermo-economic evaluation of ORC system in off-shore applications. In *Proceedings of ASME Turbo Expo 2014*, Düsseldorf, Germany, June 2014.
- [30] Leonardo Pierobon, Rambabu Kandepu, and Fredrik Haglind. Waste heat recovery for offshore applications. In *ASME 2012 International Mechanical Engineering Congress and Exposition*, pages 503–512. American Society of Mechanical Engineers, 2012.
- [31] Tuong-Van Nguyen, Leonardo Pierobon, Brian Elmegaard, Fredrik Haglind, Peter Breuhaus, and Mari Voldsund. Exergetic assessment of energy systems on North Sea oil and gas platforms. *Energy*, 62(0):23–36, 2013.
- [32] Iñigo Martínez de Alegría, Jose Luis Martín, Iñigo Kortabarria, Jon Andreu, and Pedro Ibañez Ereño. Transmission alternatives for offshore electrical power. *Renewable and Sustainable Energy Reviews*, 13(5):1027–1038, 2009.
- [33] Temesgen M. Haileselassie, Marta Molinas, and Tore Undeland. Multi-terminal VSC-HVDC system for integration of offshore wind farms and green electrification of platforms in the North Sea. In *Proceedings of Nordic Workshop on Power and Industrial Electronics*, Espoo, Finland, June 2008.
- [34] Peter Jones, Lars Stendus, and ABB Sweden. The challenges of offshore power system construction. Troll A, electrical power delivered successfully to an oil and gas platform in the North Sea. In *Proceedings of European Wind Energy Conference & Exhibition*, Athens, Greece, February-March 2006.
- [35] Jens Hetland, Hanne Marie Kvamsdal, Geir Haugen, Fredrik Major, Vemund Kårstad, and Göran Tjellander. Integrating a full carbon capture scheme onto

- a 450MW_e NGCC electric power generation hub for offshore operations: Presenting the Sevan GTW concept. *Applied Energy*, 86(11):2298–2307, 2009.
- [36] Henriette Undrum, Olav Bolland, and Eivind Aarebrot. Economical assessment of natural gas fired combined cycle power plant with CO₂ capture and sequestration. In *Proceedings of the 5th International Conference on Greenhouse Gas Control Technologies*, Cairns, Australia, August 2000.
- [37] Pal Kloster. Energy optimization on offshore installations with emphasis on offshore combined cycle plants. In *Proceedings of Offshore Europe Conference*, Aberdeen, Great Britain, September 1999.
- [38] Leonardo Pierobon, Fredrik Haglind, Rambabu Kandepu, Alessandro Fermi, and Nicola Rossetti. Technologies for waste heat recovery in off-shore applications. In *ASME 2013 International Mechanical Engineering Congress and Exposition*. American Society of Mechanical Engineers, 2013.
- [39] Olav Bolland, M. Førde, and B. Hånde. Air bottoming cycle: use of gas turbine waste heat for power generation. *Journal of Engineering for Gas Turbines and Power*, 118:359–368, 1996.
- [40] Leonardo Pierobon and Fredrik Haglind. Design and optimization of air bottoming cycles for waste heat recovery in off-shore platforms. *Applied Energy*, 118:156–165, 2014.
- [41] Alberto Benato, Leonardo Pierobon, Fredrik Haglind, and Anna Stoppato. Dynamic performance of a combined gas turbine and air bottoming cycle plant for off-shore applications. In *Proceedings of the 12th Biennial Conference on Engineering Systems Design and Analysis*, Copenhagen, Denmark, June 2014.
- [42] Rakesh K. Bhargava, Michele Bianchi, and Andrea De Pascale. Gas turbine bottoming cycles for cogenerative applications: Comparison of different heat recovery cycle solutions. In *ASME 2011 Turbo Expo: Turbine Technical Conference and Exposition*, pages 631–641. American Society of Mechanical Engineers, 2011.
- [43] Andrea Burrato. Oregon: Ge waste heat recovery system to reduce co2 emissions and increase plant efficiency. *General Electric, Technology Insights*, 2013.
- [44] Lisa Branchini and Horacio Perez-Blanco. Computing gas turbine fuel consumption to firm up wind power. In *ASME Turbo Expo 2012: Turbine Technical Conference and Exposition*, pages 735–741. American Society of Mechanical Engineers, 2012.
- [45] Lisa Branchini and Horacio Perez-Blanco. Handling wind variability using gas turbines. In *ASME Turbo Expo 2012: Turbine Technical Conference and Exposition*, pages 727–734. American Society of Mechanical Engineers, 2012.

- [46] Statoil. www.statoil.com, 2009.
- [47] LORC Knowledge. www.lorc.dk/offshore-wind-farms-map/bard-offshore-1, 2012.
- [48] Atle Rygg Årdal, Tore Undeland, and Kamran Sharifabadi. Voltage and frequency control in offshore wind turbines connected to isolated oil platform power systems. *Energy Procedia*, 24(0):229–236, 2012.
- [49] Jorun I. Marvik, Eirik V. Øyslebø, and Magnus Korpås. Electrification of offshore petroleum installations with offshore wind integration. *Renewable Energy*, 50:558–564, 2013.
- [50] Wei He, Gunnar Jacobsen, Tiit Anderson, Freydar Olsen, Tor D Hanson, Magnus Korpås, Trond Toftevaag, Jarle Eek, Kjetil Uhlen, and Emil Johansson. The potential of integrating wind power with offshore oil and gas platforms. *Wind Engineering*, 34(2):125–138, 2010.
- [51] Rakesh K. Bhargava, Michele Bianchi, Lisa Branchini, Andrea De Pascale, and Valentina Orlandini. Organic rankine cycle system for effective energy recovery in offshore applications: A parametric investigation with different power rating gas turbines. In *ASME Turbo Expo 2014: Turbine Technical Conference and Exposition 2015, GT2015-42292*. American Society of Mechanical Engineers.
- [52] Piero Colonna, Emiliano Casati, Carsten Trapp, Tiemo Mathijssen, Jaakko Larjola, Teemu Turunen-Saaresti, and Antti Uusitalo. Organic Rankine cycle power systems: From the concept to current technology, applications, and an outlook to the future. *Journal of Engineering for Gas Turbines and Power*, 137(10):1–19, 2015.
- [53] E.H. Wang, H.G. Zhang, B.Y. Fan, M.G. Ouyang, Y. Zhao, and Q.H. Mu. Study of working fluid selection of organic rankine cycle (orc) for engine waste heat recovery. *Energy*, 36(5):3406–3418, 2011.
- [54] Wendy C. Andersen and Thomas J. Bruno. Rapid screening of fluids for chemical stability in organic Rankine cycle applications. *Industrial & Engineering Chemistry Research*, 44(15):5560–5566, 2005.
- [55] Leonardo Pierobon, Tuong-Van Nguyen, Ulrik Larsen, Fredrik Haglind, and Brian Elmegaard. Multi-objective optimization of organic Rankine cycles for waste heat recovery: Application in an offshore platform. *Energy*, 58:538–549, 2013.
- [56] Jason Mark Jonkman, Sandy Butterfield, Walter Musial, and George Scott. Definition of a 5-MW reference wind turbine for offshore system development. Technical report, National Renewable Energy Laboratory, 2009.
- [57] Simon-Philippe Breton and Geir Moe. Status, plans and technologies for offshore wind turbines in Europe and North America. *Renewable Energy*, 34(3):646–654, 2009.

- [58] Francesco Casella and Alberto Leva. Modelling of thermo-hydraulic power generation processes using Modelica. *Mathematical and Computer Modeling of Dynamical Systems*, 12(1):19–33, Feb. 2006.
- [59] Francesco Casella, Tiemo Mathijssen, Piero Colonna, and Jos van Buijtenen. Dynamic modeling of organic Rankine cycle power systems. *Journal of Engineering for Gas Turbines and Power*, 135(4):042310, 2013.
- [60] Joachim Kurzke. *Component map collection 2, Compressor and turbine maps for gas turbine performance computer programs*. Germany, 2004.
- [61] F. Carchedi and G. R. Wood. Design and development of a 12:1 pressure ratio compressor for the Ruston 6-MW gas turbine. *Journal for Engineering for Power*, 104:823–831, 1982.
- [62] Joachim Kurzke. How to create a performance model of a gas turbine from a limited amount of information. In *Proceedings of ASME Turbo Expo 2005*, Reno-Tahoe, Nevada, June 2005.
- [63] Aurel Stodola. *Dampf- und Gasturbinen: Mit einem Anhang über die Aussichten der Wärmekraftmaschinen*. Springer Berlin, Berlin, Germany, 1922. ISBN: 7352997563.
- [64] Meinhard Schobeiri. *Turbomachinery flow physics and dynamic performance*. Springer Berlin, Berlin, Germany, 2005. ISBN: 9783540223689.
- [65] Sergio Mario Camporeale, Bernardo Fortunato, and Antonio Dumas. Dynamic modelling of recuperative gas turbines. *Proceedings of the Institution of Mechanical Engineers, Part A: Journal of Power and Energy*, 214(3):213–225, 2000.
- [66] Fredrik Haglind and Brian Elmegaard. Methodologies for predicting the part-load performance of aero-derivative gas turbines. *Energy*, 34(10):1484–1492, 2009.
- [67] Leonardo Pierobon, Krishna Iyengar, Peter Breuhaus, Rambabu Kandepu, Fredrik Haglind, and Morten Hana. Dynamic performance of power generation systems for off-shore oil and gas platforms. In *Proceedings of ASME Turbo Expo 2014*, Düsseldorf, Germany, June 2014.
- [68] Frank P. Incropera, David P. DeWitt, Theodore L. Bergman, and Adrienne S. Lavine. *Fundamentals of Heat and Mass Transfer*. John Wiley & Sons, Inc., Jefferson City, United States of America, 2007. ISBN: 9780470501979.
- [69] Joseph P. Veres. Centrifugal and axial pump design and off-design performance prediction. Technical report, NASA, Sunnyvale, United States of America, 1994. Technical Memorandum 106745.

- [70] Signe Schløer, Henrik Bredmose, and Harry B. Bingham. The influence of fully nonlinear wave forces on aero-hydro-elastic calculations of monopile wind turbines. *Marine Structures*, 50:162 – 188, 2016.
- [71] Jakob Mann. Wind field simulation. *Probabilistic engineering mechanics*, 13(4):269–282, 1998.
- [72] International Electrotechnical Commission - IEC. Wind turbines - part 1: Design requirements. Technical report, International Electrotechnical Commission, 2005.
- [73] Stig Øye. Flex4 simulation of wind turbine dynamics. In *Proceedings of the 28th IEA Meeting of Experts Concerning State of the Art of Aeroelastic Codes for Wind Turbine Calculations*, Kongens Lyngby, Denmark, April 1996.
- [74] Norwegian Technology Centre. Electrical systems NORSOK STANDARD E-001. Technical report, Norwegian Technology Centre, 2007.
- [75] Michael Grottke, Hairong Sun, Ricardo M. Fricks, and Kishor S. Trivedi. Ten fallacies of availability and reliability analysis. pages 187–206, 2008.
- [76] Jorge Luis Romeu. *Understanding series and parallel systems reliability*, volume 11.
- [77] Jesús María Pinar Pérez, Fausto Pedro García Márquez, Andrew Tobias, and Mayorkinos Papaelias. Wind turbine reliability analysis. *Renewable and Sustainable Energy Reviews*, 23:463 – 472, 2013.
- [78] Simon Frost Martin Wall, Richard Lee. Offshore gas turbines (and major driven equipment) integrity and inspection guidance notes. Technical report, ESR Technology Ltd, 2006.
- [79] Kapsali Marina and John K. Kaldellis. Offshore wind power basics. *Comprehensive Renewable Energy*, Volume 2:431–468, 2012.
- [80] European Union. Directive 2004/8/EC on the promotion of cogeneration based on a useful heat demand in the internal energy market and amending directive 92/42/EEC, February 2004.
- [81] Directive 2004/08/EC of the European Parliament and of the Council. Official Journal of the European Union, February 2004.
- [82] Ministry of the Environment. www.regjeringen.no, October 2012.
- [83] Douglas-Westwood. Offshore wind assessment for Norway: Final report. Report, The Research Council of Norway, 2010.
- [84] Robert Beith. *Small and micro combined heat and power (CHP) systems: advanced design, performance, materials and applications*. Elsevier, 2011.

-
- [85] Stefano Clemente, Diego Micheli, Mauro Reini, and Rodolfo Taccani. Bottoming organic rankine cycle for a small scale gas turbine: A comparison of different solutions. *Applied Energy*, 106:355 – 364, 2013.
- [86] Costante Invernizzi, Paolo Iora, and Paolo Silva. Bottoming micro-Rankine cycles for micro-gas turbines. *Applied thermal engineering*, 27(1):100–110, 2007.
- [87] Yousef S.H. Najjar and Abdulhaiy M. Radhwan. Cogeneration by combining gas turbine engine with organic rankine cycle. *Heat Recovery Systems and CHP*, 8(3):211–219, 1988.
- [88] Yousef SH Najjar. Efficient use of energy by utilizing gas turbine combined systems. *Applied Thermal Engineering*, 21(4):407–438, 2001.
- [89] Paola Bombarda, Costante Invernizzi, and Claudio Pietra. Heat recovery from diesel engines: A thermodynamic comparison between kalina and orc cycles. *Applied Thermal Engineering*, 30(2):212–219, 2010.
- [90] Iacopo Vaja and Agostino Gambarotta. Internal combustion engine (ICE) bottoming with organic Rankine cycles (ORCs). *Energy*, 35(2):1084–1093, 2010.
- [91] Kalyan K. Srinivasan, Pedro J. Mago, and Sundar R. Krishnan. Analysis of exhaust waste heat recovery from a dual fuel low temperature combustion engine using an organic rankine cycle. *Energy*, 35(6):2387–2399, 2010.
- [92] Vincent Lemort, Ludovic Guillaume, Arnaud Legros, Sébastien Declaye, and Sylvain Quoilin. A comparison of piston, screw and scroll expanders for small scale rankine cycle systems. In *Proceedings of the 3rd International Conference on Microgeneration and Related Technologies*, 2013.
- [93] Muhammad Imran, Muhammad Usman, Byung-Sik Park, and Dong-Hyun Lee. Volumetric expanders for low grade heat and waste heat recovery applications. *Renewable and Sustainable Energy Reviews*, 57:1090–1109, 2016.
- [94] Andreas P. Weiß. Volumetric expander versus turbine—which is the better choice for small ORC plants? In *ASME ORC 2015, 3th International Seminar on ORC Power Systems*, 2015.
- [95] Saeedeh Saghatoun, Weilin Zhuge, and Yangjun Zhang. Review of expander selection for small-scale organic Rankine cycle. In *ASME 2014 4th Joint US-European Fluids Engineering Division Summer Meeting collocated with the ASME 2014 12th International Conference on Nanochannels, Microchannels, and Minichannels*. American Society of Mechanical Engineers, 2014.
- [96] Grzegorz Zywica, Tomasz Zygmunt Kaczmarczyk, and Eugeniusz Ihnatowicz. A review of expanders for power generation in small-scale organic Rankine cycle systems: Performance and operational aspects. *Proceedings of the Institution of*

- Mechanical Engineers, Part A: Journal of Power and Energy*, 230(7):669–684, 2016.
- [97] Bo Zhang, Xueyuan Peng, Zelong He, Z Xing, and P Shu. Development of a double acting free piston expander for power recovery in transcritical CO₂ cycle. *Applied Thermal Engineering*, 27(8):1629–1636, 2007.
- [98] O. Badr, P.W. O’callaghan, M. Hussein, and S.D. Probert. Multi-vane expanders as prime movers for low-grade energy organic Rankine-cycle engines. *Applied Energy*, 16(2):129–146, 1984.
- [99] Arthur J. Glassman and Warner L. Stewart. Use of similarity parameters for examination of geometry characteristics of high-expansion-ratio axial-flow turbines. 1967.
- [100] R. Barber and D. Prigmore. Solar-powered heat engines. *Solar Energy Handbook*, Kreider, J., and Kreith, F., eds. McGraw Hill Book Company, pages 22–1, 1981.
- [101] O.E. Balje. A study on design criteria and matching of turbomachines: Part asimilarity relations and design criteria of turbines. *Journal of Engineering for Power*, 84(1):83–102, 1962.
- [102] K.E. Nichols. *How to select turbomachinery for your application*. Arvada Barber Nichols Eng. Company.
- [103] Yulia Glavatskaya, Pierre Podevin, Vincent Lemort, Osoko Shonda, and Georges Descombes. Reciprocating expander for an exhaust heat recovery rankine cycle for a passenger car application. *Energies*, 5(6):1751–1765, 2012.
- [104] Jean-François Oudkerk, Rémi Dicks, Olivier Dumont, and Vincent Lemort. Experimental performance of a piston expander in a small-scale organic rankine cycle. In *IOP Conference Series: Materials Science and Engineering*, volume 90, page 012066. IOP Publishing, 2015.
- [105] Sylvain Quoilin, Sébastien Declaye, Arnaud Legros, Ludovic Guillaume, and Vincent Lemort. Working fluid selection and operating maps for organic rankine cycle expansion machines. In *Proceedings of the 21st international compressor conference at Purdue*, page 10, 2012.
- [106] Closed-cycle plant, US2016032786 (A1), https://world-wide.espacenet.com/publicationdetails/originaldocument?cc=us&nr=2016032786a1&kc=a1&ft=d&nd=4&date=20160204&db=epodoc&locale=en_e_p, 04 – 02 – 2016.
- [107] Sistemi per acqua calda (in italian).

- [108] Onda S.p.a. Advanced heat transfer solutions: brazed plate heat exchangers, <http://pdf.directindustry.com/pdf/onda/brazed-plate-heat-exchangers/21365-76747.html>.
- [109] Onda S.p.a. Shell and tube condensers, <http://pdf.directindustry.it/pdf-en/onda/ct-condensers/21365-76752.html>.
- [110] Integrated Rankine-cycle machine, US2012267898 (A1), 25-10-2012.
- [111] *Dati di targa generatore sincrono trifase a magneti permanenti tipo NGB 145 M-SA (in Italian)*, 15-03 2013.
- [112] External gear pumps, <http://www.pumpschool.com/principles/external.asp>.
- [113] Internal gear pumps, <http://www.pumpschool.com/principles/internal.asp>.
- [114] National Instruments. CompactRIO, <http://www.ni.com/compactrio/whatis>.
- [115] National Instruments. Chassis NI cRIO-9114, <http://www.ni.com/pdf/manuals/375079e.pdf>.
- [116] National Instruments. NI cRIO-9022, <http://www.ni.com/datasheet/pdf/en/ds-202>.
- [117] National Instruments. NI 9213, <http://www.ni.com/pdf/manuals/374916a02.pdf>.
- [118] National Instruments. NI 9207, <http://www.ni.com/pdf/manuals/375206a02.pdf>.
- [119] National Instruments. NI 9201, <http://www.ni.com/pdf/manuals/373783a02.pdf>.
- [120] Ian H. Bell, Jorrit Wronski, Sylvain Quoilin, and Vincent Lemort. Pure and pseudo-pure fluid thermophysical property evaluation and the open-source thermophysical property library coolprop. *Industrial & Engineering Chemistry Research*, 53(6):2498–2508, 2014.
- [121] Reiner Tillner-Roth and Hans Dieter Baehr. An international standard formulation for the thermodynamic properties of 1, 1, 1, 2-tetrafluoroethane (HFC-134a) for temperatures from 170 K to 455 K and pressures up to 70 MPa. *Journal of Physical and Chemical Reference Data*, 23(5):657–729, 1994.
- [122] Brandon J Woodland, James E Braun, Eckhard A Groll, and W Travis Horton. Experimental testing of an organic rankine cycle with scroll-type expander, [http://www.ey.com/publication/vwluassets/2013_globaleil_and_gas_tax_guide/\\$file/eyoila_nd_gas_2013.pdf](http://www.ey.com/publication/vwluassets/2013_globaleil_and_gas_tax_guide/$file/eyoila_nd_gas_2013.pdf).
- [123] Songling Cao and R Russell Rhinehart. An efficient method for on-line identification of steady state. *Journal of Process Control*, 5(6):363–374, 1995.
- [124] Bihrat Önöz and Mehmetcik Bayazit. The power of statistical tests for trend detection. *Turkish Journal of Engineering and Environmental Sciences*, 27(4):247–251, 2003.

- [125] S Narasimhan, Chen Shan Kao, and RSH Mah. Detecting changes of steady states using the mathematical theory of evidence. *AIChE journal*, 33(11):1930–1932, 1987.
- [126] Minsung Kim, Seok Ho Yoon, Piotr A Domanski, and W Vance Payne. Design of a steady-state detector for fault detection and diagnosis of a residential air conditioner. *International journal of refrigeration*, 31(5):790–799, 2008.
- [127] Steven Lecompte. *Performance evaluation of organic Rankine cycle architectures: application to waste heat valorisation*. PhD thesis, Ghent University, 2016.